Preliminary Study of an Intra-operative PET Imaging Probe System

by

Sam Seoung Huh

A dissertation submitted in partial fulfillment
of the requirements for the degree of
Doctor of Philosophy
(Biomedical Engineering)
in The University of Michigan
2011

Doctoral Committee:

Research Professor Neal. H. Clinthorne, Co-Chair
Emeritus Professor W. Leslie Rogers, Co-Chair
Professor Jeffrey A. Fessler
Professor Zhong He

Dedicated to my parents

ACKNOWLEDGEMENTS

I would like to thank Prof. W. Leslie Rogers and Prof. Neal H. Clinthorne for supporting me financially over the years and keeping motivating me to do my research. Their feedback on my research also enriched my research and catalyzed me to find solutions. I also would like to thank Prof. Jeffrey Fessler and Prof. Zhong He for their valuable comments on my dissertation and being on my dissertation committee. I would like to thank Prof. Rogers again for making precious comments on my dissertation. I also would like to thank Prof. Charles A. Cain and Prof. Jeffrey Fessler for serving on my qualifying oral examination committee.

I am thankful to former lab colleges Dr. Lisha Zhang, Dr. Sang-June Park, and Dr. Li Han for discussing matters academically and personally. I am also thankful to colleges Dr. Don Burdette, Dr. Eric Cochen, and Mr. Shane Smith from the Ohio State University for helping me build my experimental set-up. I am also thankful to Mr. Jim Berry from the Department of Nuclear Engineering for helping build my experimental set-up.

I am grateful to Mrs. Linda Brandt and Mr. Charles Schneider from PET Chemistry Center for helping with my activities in my lab. I am also thankful to other colleges and friends for their support through the years. I am also thankful to Mr. Bobby Glushko from the U of M Copyright Office for advice on the copyright law.

Table of Contents

List of Figures

FIGURE

List of Tables

TABLE

ABSTRACT

Preliminary Study of an Intra-operative PET Imaging Probe System

by

Sam Seoung Huh

Co-Chairs: W. Leslie Rogers and Neal H. Clinthorne

PET imaging has gained widespread acceptance in cancer imaging because Positron Emission Tomography can identify physiological changes due to cancer. Nevertheless conventional PET imaging has difficulty detecting tumors less than 1cm in diameter in clinical use due mainly to background radiation, statistical noise, resolution loss due to lack of depth interaction resolution in detectors, and annihilation photon acolinearity.

Conventionally if detected tumors are surgically removable, surgeons locate and remove the tumors during surgery based on the preoperative scans. One of the drawbacks of relying solely on preoperative imaging is that tumor locations could be displaced during surgery due to patient's movement.

In this dissertation, a preliminary study of an intra-operative PET imaging probe system is presented. The proposed probe system consists of a low resolution partial ring detector and a high resolution imaging probe that is equipped with a position tracker. The high resolution probe operates in coincidence with the partial ring detector. The high resolution imaging probe and its proximity to target lesions contribute to the localization of small tumors. In addition, the probe system can be used to detect occult tumors. The ultimate goal is to provide incremental 3-dimensional reconstructed images that are re-projected in real time onto a plane whose orientation is driven by the tracking device.

A prototype of the PET imaging probe system was built to test the feasibility of the intra-operative PET imaging probe system. Coincidence detection efficiency of about 0.00012% was observed. A variant of 3-dimensional one-pass list-mode maximum likelihood algorithm (OP-LML) was developed to reconstruct images from the measured data. A row-action maximum likelihood algorithm was integrated with the OP-LML. To speed up image reconstruction by a factor of 30-40, the proposed algorithm was parallelized and was run on a graphics processing unit.

Reconstructed images from simulated data with no intrinsic blurring showed resolution of 1.0mm~1.5mm FWHM. However as we expected, reconstructed images from the experimental set-up with limitations failed to separate two Na-22 point sources 1.5mm apart. Experimental resolutions of 4mm FWHM in the longitudinal direction and 2mm FWHM in the transverse direction were obtained for the two point sources.

Chapter 1
Introduction

1 .1 Cancer Statistics

According to statistics, a quarter of deaths in the United States are due to cancer [1]. As expected, prostate cancer shows the highest incidence rate for men and women are most likely to be attacked by breast cancer.

From 1970 thru 2006, prostate cancer had been the leading diagnosis for males and breast cancer had been the leading diagnosis for females [1]. The incidence rates of lung cancer and colon cancer have been roughly downwards over 20 years from 1975 to 2003 for males. For women, the colon cancer incidence rate has been abating over the same time, but the lung cancer incidence rate increased.

However, lung cancer became the highest death rate for both males and females by 1990 [1]. Prostate cancer and colon cancer followed lung cancer in death rates for males. Breast cancer death rates followed lung cancer death rates for females.

1 .2 Tumor Metabolism

It was found that cancer cells tend to metabolize glucose by glycolysis even in an environment of sufficient O_2 [2]. This preference for glycolysis rather than oxidative

phosphorylation may be due partially to the hypoxia [2] [3]. Since the oxygen supply is below the consumption level [4], cancer cells may tend to up-regulate the glycolysis [2].

1 .3 Imaging Modalities for Cancer Detection

1. 3 .1 Diagnostic Ultrasound Imaging

Diagnostic ultrasound is capable of presenting cross-sectional anatomy in a completely noninvasive way [5]. Ultrasound is patient-friendly compared to MRI, X-ray, or PET. The difference in acoustic impedance reflects and refracts incident sound waves [6].

1. 3 .2 X-Ray Imaging (Computerized Tomography)

X-ray imaging is based on the transmission of incident energy rather than reflection [7]. Interactions of X-ray photons in the patient's body are shown in Figure 1-1. Photoelectric effect, Rayleigh scattering, and Compton scattering are briefly described in Figure 1-1.

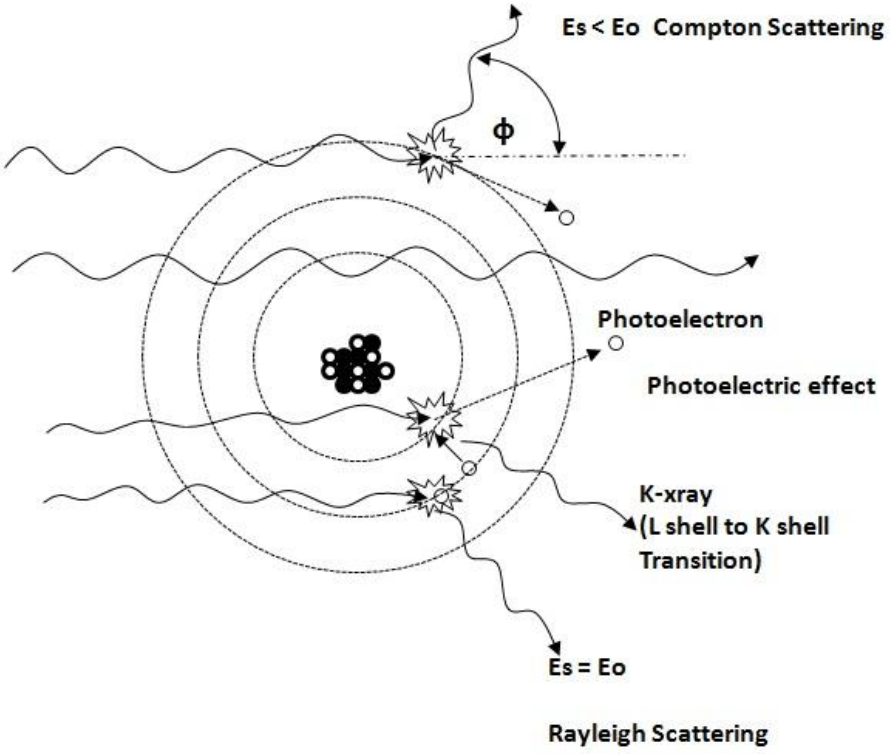

Figure 1-1. Interactions of X-ray photons in body. This picture was adapted from [7].

1. 3 .3 **MRI Imaging**

The excess number of spins aligned with the external magnetic field results in macroscopic magnetization M_0 [8]. The relaxation rate then depends on the *molecular environment* of protons [8]. The relaxation rate is acquired by measuring the RF photons (signal) in the RF coil.

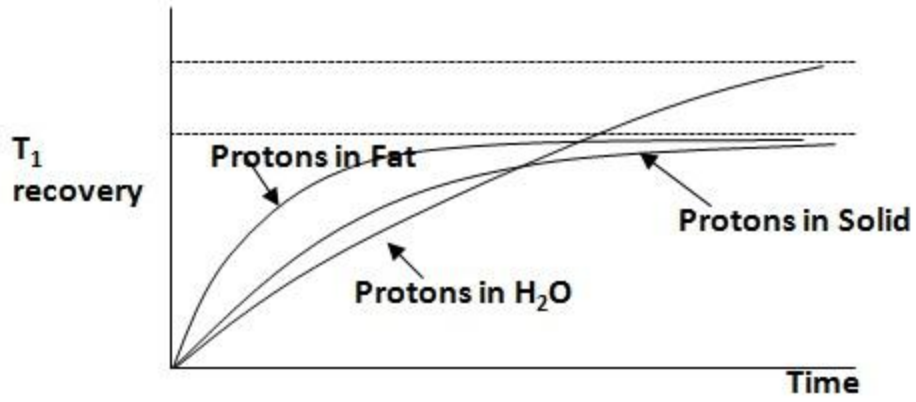

Figure 1-2. Longitudinal relaxation measurement of fat, solid, and water. This picture was adapted from [9].

1 .4 Positron Emission Tomography Imaging

1. 4 .1 Introduction to PET Imaging

In diagnostic ultrasound imaging, since the detection of abnormal tissues depends on the difference of acoustic impedance of adjacent tissue types, lesions without minimal acoustic impedance difference are undetectable. For X-ray, even though X-ray imaging can convey high resolution information on anatomical changes caused by cancer, conventional X-ray imaging lacks of acquiring information on biological changes. MRI imaging can also provide high resolution anatomical information without exposure to radiation. However, it has a limited capability in conveying biological information.

On the contrary, positron emission tomography (PET) can convey biological changes (functional information) caused by cancer. The functional information is acquired with the help of radiotracers.

1.4.1.1 Typical Radio-labeled tracers

Typical positron emitting radiotracers for PET imaging are ^{18}F-FDG (110 minutes half life time) for soft tissue, ^{11}C-choline (half life time 20 min), and ^{11}C-acetate. ^{18}F-FDG is intravenously administered. ^{18}F-FDG is circulated in the vascular system and actively transported into the cells by glucose transporter proteins (GLUTs) [10]. It is then phosphorylated by hexokinases (HK-II) [11]. Most of the resulting ^{18}F-FDG-6-phosophates, which are anions, are trapped since cells have no anion transporter. ^{18}F-FDG-6-phosophates are also metabolically isolated in the cells; FDG-6-P is no longer subject to the glycolytic pathway [12]. The high glucose uptake of malignant tumors is mainly due to the over-expression of GLUTs and increased hexokinase activity [12]. For example, GLUT I is over-expressed in primary lung tumors.

Another metabolic marker is choline. High choline phospholipid metabolites in tumors have been detected [13]. Phosphatidylcholine is one component of cell membranes [14] and choline is the precursor for phosphatidycholine synthesis. However the metabolism of ^{11}C-choline is not clearly understood. ^{11}C-choline has been used for studying carcinoma of the brain, prostate, and esophageal [15]. C-11 labeled acetate has shown high uptake in prostate carcinoma [16]; however the reasons for this observation have not been clearly explained.

1.4.1.2 Typical Conventional PET Scanners

The early staging of tumors that have high ^{18}F-FDG (^{18}F-labeled 2-deoxy-2-fluoro-D-glucose) uptake has been studied using FDG-PET (Positron Emission Tomography) imaging. Basics of PET imaging are briefly described. A positron emitted

from a radio-labeled tracer loses its kinetic energy mostly through the ionization process, the excitation process, and Bremsstrahlung. Usually after losing its kinetic energy, the positron annihilates with a nearby electron. This electron-positron annihilation results in two 511keV photons that are emitted in opposite directions. The deviation from the exact opposite direction, which is termed acolinearity, is due to residual positron-electron momentum [17].

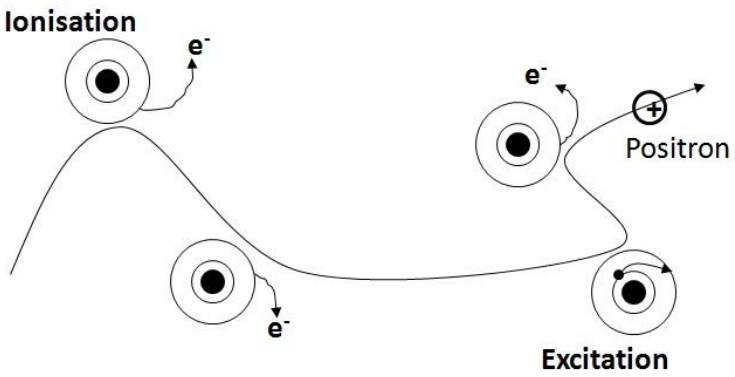

Figure 1-3. Ionization and excitation processes by positrons. This picture was adapted from [18].

The annihilation photon acolinearity is illustrated in Figure 1-4. We can see that the positron emitter can be approximately localized to a line by detecting a pair of annihilation photons. We need to detect the annihilation photons at different angles to localize tumors. If we detect positrons, we can localize positron emitters within its positron range.

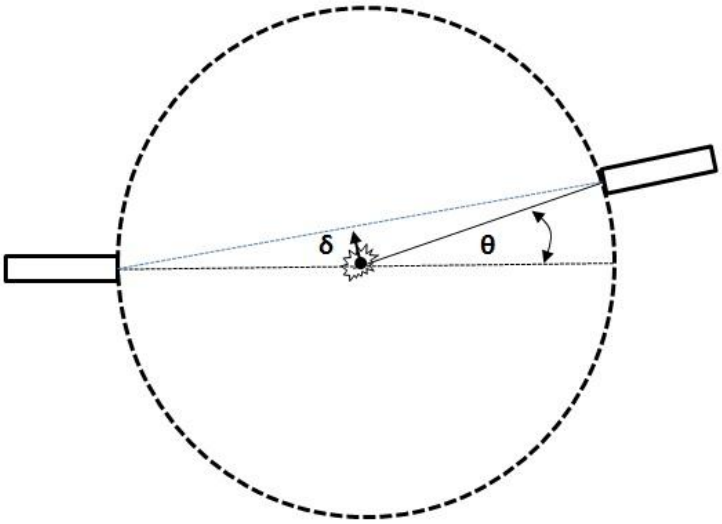

Figure 1-4. Illustration of annihilation photon acolinearity. The FWHM of θ is roughly 0.5º [17]. This picture was adapted from [19].

Some typical characteristics of conventional PET scanners are briefly described here [20] [21]. Generally whole body PET scanners have ring diameters large enough to accommodate a range of patient bodies. In turn, the large ring diameter results in resolution degradation due to photon acolinearity.

Precise detection of annihilation photon pairs is one of the most important tasks in PET scanners. A simplified PET scanner is shown in Figure 1-5. The line with two arrow ends indicates a possible trajectory of a pair of annihilation photon pairs.

Incident gamma rays are detected in detector elements. From Figure 1-5, it is clear that width of the detection element roughly determines a lower limit on spatial resolution. Also the gamma ray energy and scintillator stopping power will also have an effect on spatial resolution and sensitivity. The characteristics of detection materials play key roles in PET scanners.

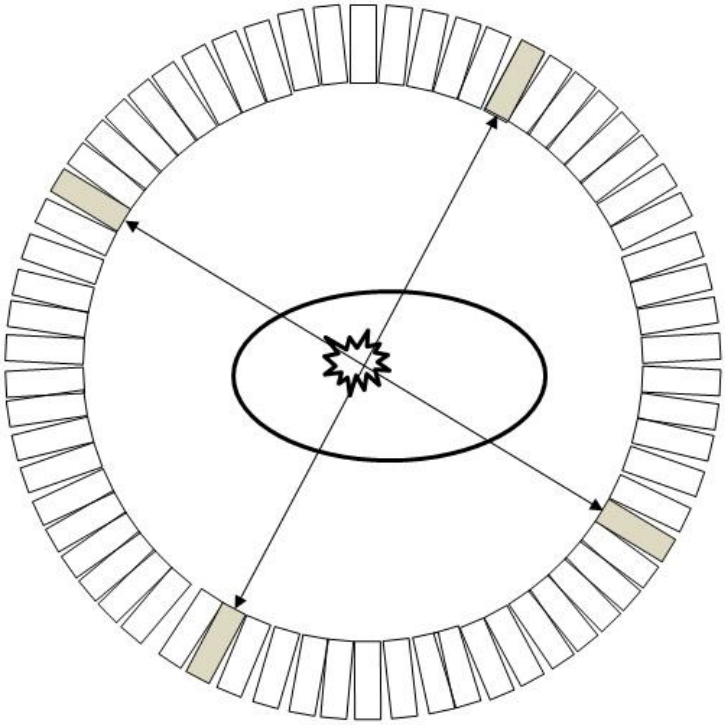

Figure 1-5. Illustration of a typical PET scanner showing lines-of-response.

1. 4 .2 **Motivation for the Intra-operative PET imaging probe**

Positron Emission Tomography (PET) is one of the effective diagnostic imaging methods for identifying and locating tumors. PET imaging can convey function information rather than anatomical information. Based on the preoperative diagnostic scanning, surgeons make decisions whether or not the tumors are surgically removable. Conventionally if the tumors are surgically removable, surgeons locate and remove the tumors during surgery based on the preoperatively acquired diagnostic images. One of the drawbacks of solely relying on preoperative imaging is that tumor locations can be displaced due to patient's change of position. As a result, surgeons must pay extraordinary attention to locate lesions that were identified by various imaging methods prior to surgery. Even after surgeons locate lesions, the complete removal of tumors is

difficult because the tumor margin is difficult to delineate. It is important to identify the margin in order to preserve healthy tissue as much as possible without leaving any residual tumor.

Another important issue during surgery is to discover small tumors that are not detected in preoperative imaging procedure. Occult tumors that survive surgery can grow after surgery. It is well known that early detection of tumors can increase the life span and the quality of life of patients. Reliable detection of tumors that are less than 1 cm in diameter, however, remains a challenge in conventional whole-body PET imaging. Even though the on-axis intrinsic resolution of current PET devices can be ~5 mm FWHM, this figure is rarely achievable in clinical use because of background radiation in nearby tissue due to undesired uptake in normal tissue, statistical noise, and poor depth resolution in the PET systems. In addition, the relatively large ring diameter (~850mm) of whole-body PET scanners tends to further reduce the spatial resolution due to annihilation photon acolinearity. Figure 1-6 shows correctly localized lesions versus lesion size from a phantom study [22]. For 6 different PET imaging systems, whole body PET scanners revealed difficulty detecting small tumors in the study.

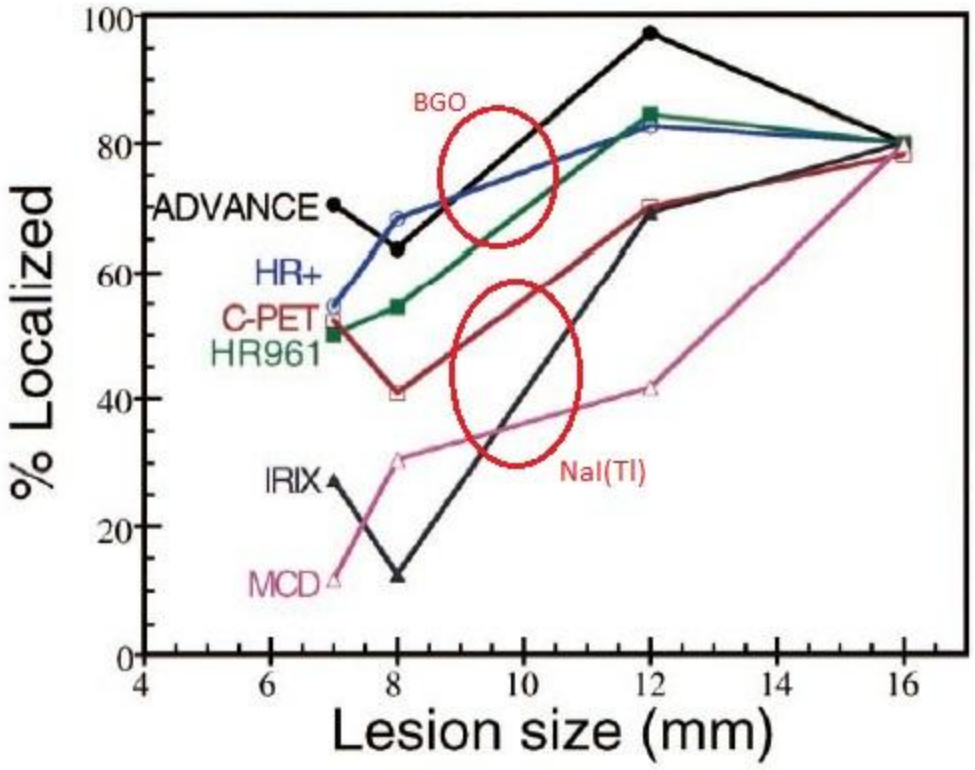

Figure 1-6. Correctly localized lesions versus lesion size. This picture is from [22]. Advance, HR+, and HR981 consists of BGO. C-PET, IRX, and MCD consists of NaI(Tl). All the PET systems are whole body scanners.

Non-imaging intra-operative probes have demonstrated effective tumor detection during surgical removal of lymph nodes. In order to locate small tumors and the residuals of tumor dissection more effectively, intra-operative *imaging* probes are preferred because imaging probes can display 2-dimensioal images so that surgeons or clinicians spend less time locating legions. 2-dimensional imaging can take advantage of characteristics of beta emitting radio-tracers.

One scenario is to directly detect beta particles from radio-isotopes emitting positron particles. Positron particles with short ranges can be used to achieve high spatial resolution. Although this is attractive from a viewpoint of reducing effects of 511 keV

background from elsewhere in the body due to the positron-electron annihilation, positron particles have short ranges which limit the method's utility in detecting deep seated, small tumor foci below the surface of exposed tissue. The positron ranges of some radio-tracers are shown in Figure 1-7.

To detect deep seated tumors, gamma-ray sensitive imaging probes are more suitable than positron sensitive imaging probes. However, use of single photon detection typically at either 140keV or 511keV results in a wide point-spread function due to the long attenuation length in virtually all materials that are used for collimation. The 511keV photons in water have the mean free path of approximately 10cm [23].

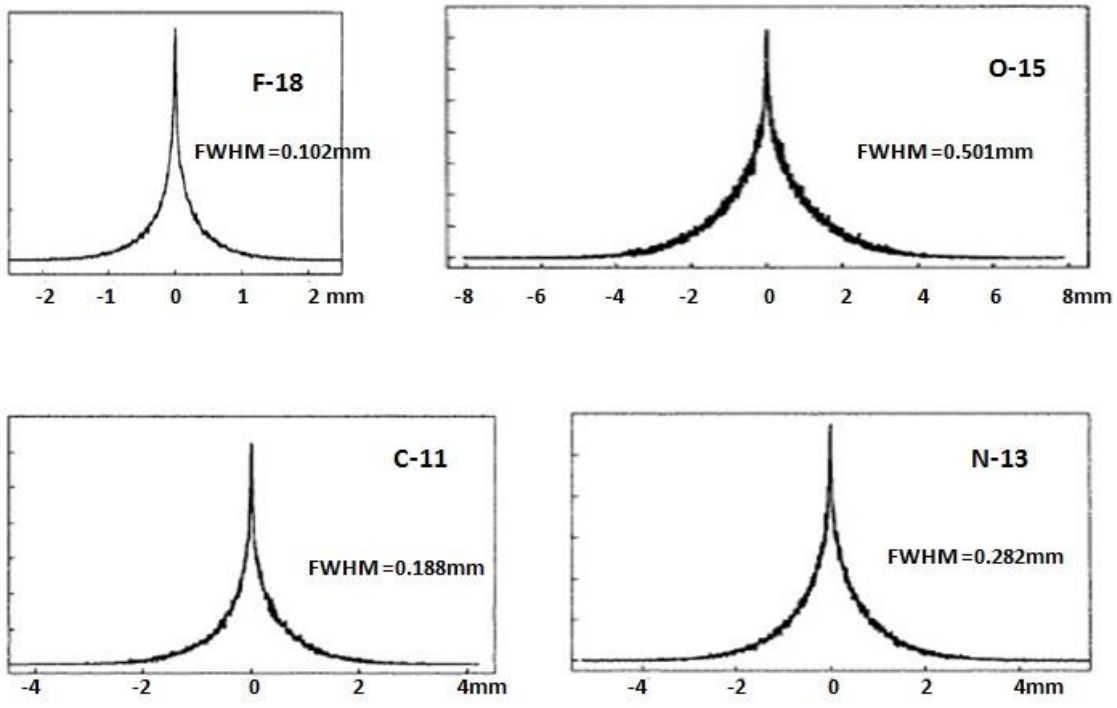

Figure 1-7. Positron ranges of F-18, C-11, N-13, and O-11. These pictures were adapted from [24]. Notice that the x-axis of the positron range is not in the same scale.

1.4.2.1 **Non-Imaging Probes**

An early intra-operative approach was to use a small size hand-held *non-imaging* gamma ray detector in order to localize tumors during surgery after the radiotracer administration. In the work of Oredipe *et al*., 10^5 cells and 10^4 cells were detected by labeling these cells with ^{125}I-antibody; the approximate volume of these cells wass less than $1mm^3$ [25] [26].

One early example of localization of tumors using radiotracers is the work by Atiken *et al* [27]. In their work, ^{131}I labeled caricinoembryonic-antigen (CEA) antibody was injected into xenografted mice that had tumors expressing CEA. A gamma ray sensitive probe with appropriate shielding was then moved by hand to detect 364keV photons from tumor sites and control sites. Higher counts from tumor sites were observed. However, the CEA antibody was not widely used. For intraoperative gamma probes, background gamma ray detection was an issue. In order to reduce the background contamination, Saffer *et al*. proposed coincidence detection of two photons, which have no angular correlation, (171keV and 245keV) from ^{111}In [28]. Random coincidences due to high activity from the tumor sites were a problem for the study.

Kraig *et al*. studied sentinel lymph node biopsy using an intra-operative gamma ray sensitive non-imaging probe and technetium-99m-antimony-trisulfide colloid [29]. The technique continues to be successfully applied. FDG for single-gamma detection was also tested as a radiotracer for intra-operative imaging because FDG often shows a high tumor to background ratio in FDG-PET imaging [30].

1.4.2.2 **Imaging Probes**

As the surgical non-imaging probes using single photon (gamma ray) detection were accepted as useful tools for aiding surgery, high spatial resolution *imaging* probes were studied. Direct positron detection of ^{18}F-FDG was investigated to obtain high spatial resolution for superficially located tumors. The FWHM of typical positrons is shown in Table 1-1.

Positrons from positron emitting radiotracers in superficially located tumors such as colon cancer and brain cancer can be detected for tumor localization. Two typical types of imaging probes for direct positron detection are briefly reviewed. One is a phoswich type imaging probe [31]. The front layer consists of a plastic scintillation detector (rise time ~1ns and decay time ~10ns) for detecting positrons, and the back-to-back coupled layer is comprised of a gadolinium silicate (GSO) doped with cerium scintillation detector (decay time ~30-60ns) for detecting one of the 511keV annihilation photon pair from positron-electron annihilation in the front layer. The GSO also serves as a light guide for emission photons from the plastic scintillator. The positron and gamma-ray interactions are differentiated based on signal shapes. If the two signals are detected within a timing window, the interaction location is then estimated.

Table 1-1. FWHM of typical positrons in water. This table was adapted from [24].

	F-18	C-11	N-13	O-15
FWHM of positron range	0.102mm	0.188mm	0.282mm	0.501mm

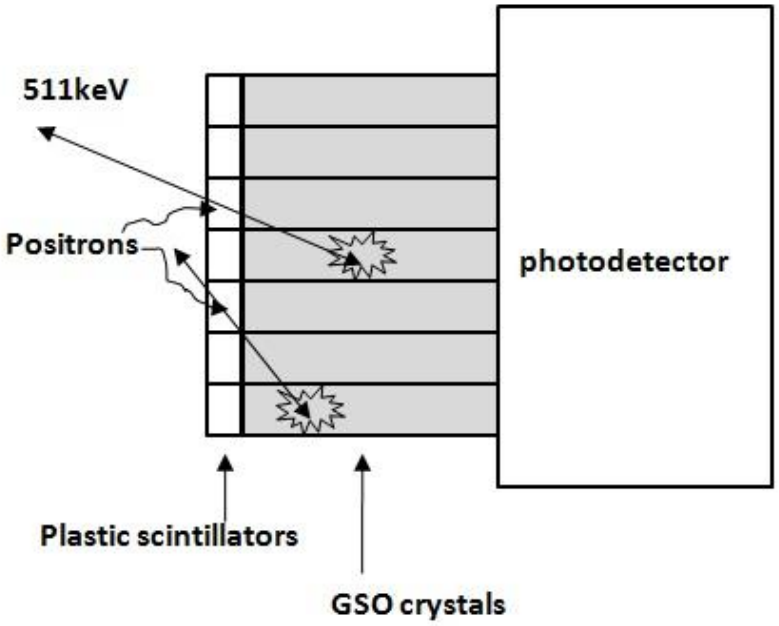

Figure 1-8. Typical phoswich imaging probe. This picture was adapted from [31].

Another type of probe consists of a double-sided strip silicon detector. P+ strips on one side and n+ strips on the other side, orthogonal to each other, form two-dimensional (2D) pixels [32]. The pitch is 1mm and the strip width is 0.8mm. For silicon, roughly 1 electron-hole pair/3.79eV is generated [33]. In contrast, the scintillation efficiency of the plastic detector is roughly 1 light photon/100eV [34]. Therefore we can get better signal detection in the silicon detector because we can achieve higher energy resolution.

Another type of imaging probe, which can be considered as an ancestor of the PET imaging probe system, was investigated by Zhang *et al*. They investigated the idea of an intra-rectal imaging device based on a Compton camera [35]. Their Monte Carlo simulation studies demonstrated that the prostate-specific Compton imaging probe significantly outperformed conventional SPECT. Figure 1-9 shows the illustration of the

Compton imaging system. Figure 1-10 shows the sagittal view of the Compton imaging probe system.

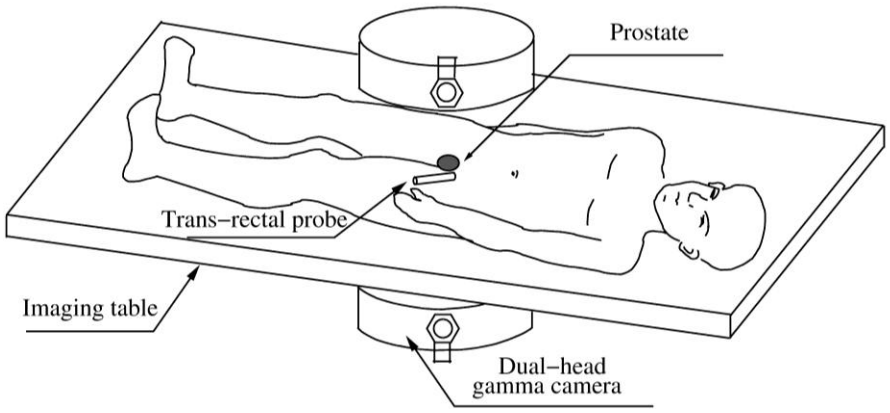

Figure 1-9. Illustration of the Compton imaging probe system. This picture is from [35].

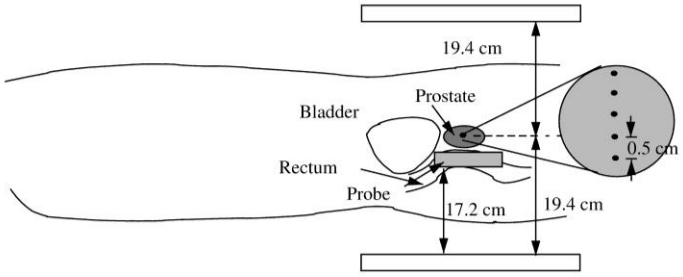

Figure 1-10. Sagittal view of the Compton imaging probe system. This picture is from [35].

Figure 1-11 shows the principle of Compton camera image reconstruction. The scattering angle is obtained by Equation (1.1). The origin of the disintegration is then one of the points on the cone. By overlapping many ovals or circles on the image plane, the position of disintegration is obtained. Figure 1-12 shows the cone back-projection on an image plane.

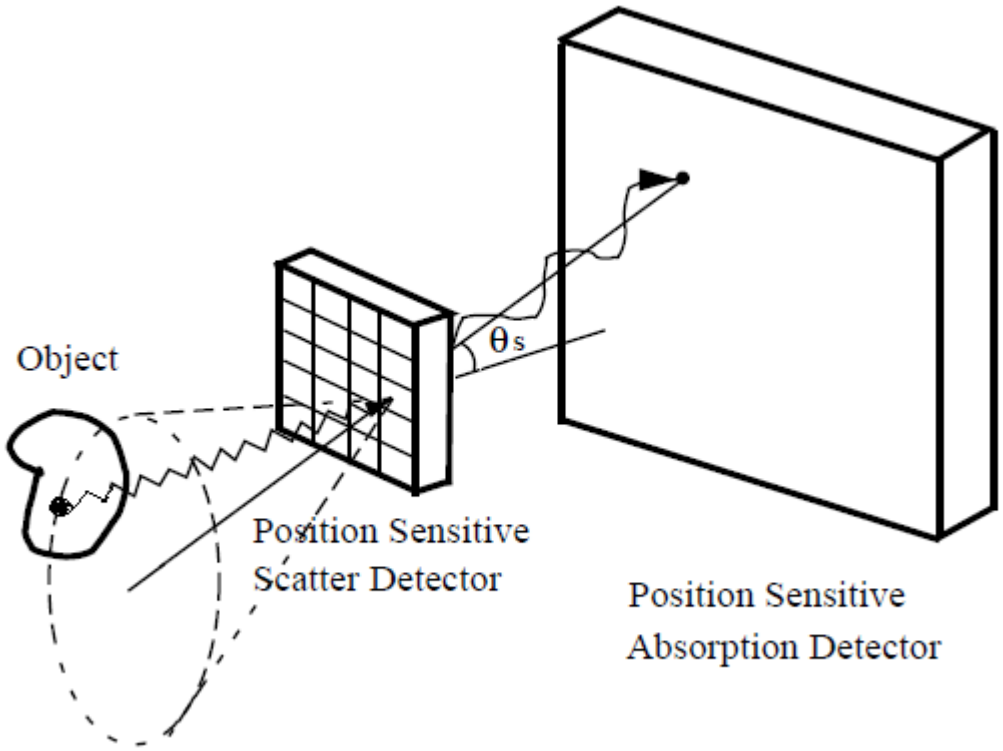

Figure 1-11. Principle of Compton Camera. This picture was adapted from [ch1-52].

$$cos\theta_{scatter} = 1 - \frac{m_e c^2 E_{rec}}{E_0 E_s} \tag{1.1}$$

where $E_s = E_0 - E_{rec}$ and E_{rec} is the recoil electron kinetic energy. E_s is the scatter photon energy.

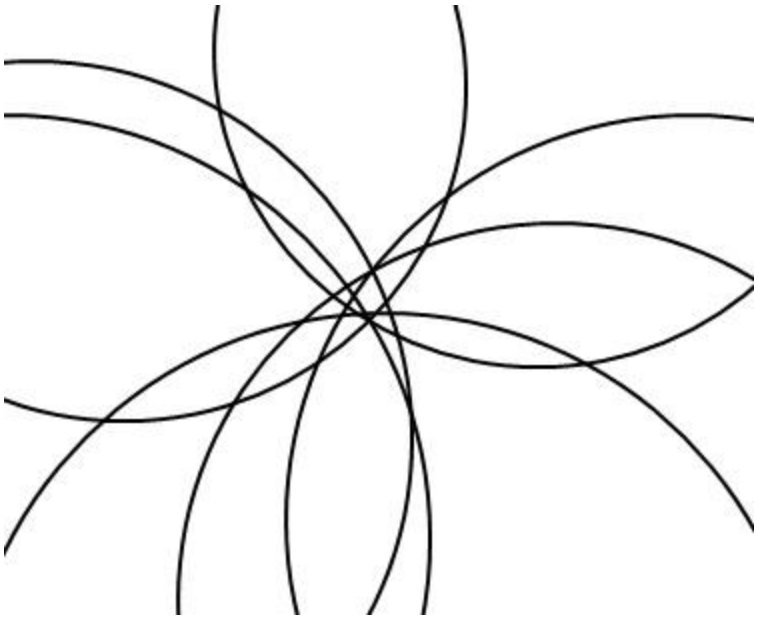

Figure 1-12. Cone back-projection on an image plane.

1.4.2.3 **Intra-operative PET Imaging Probe**

To overcome the drawbacks of gamma-ray sensitive non-imaging probes and positron sensitive imaging probes, we have been investigating a small, high resolution PET imaging probe that operates in coincidence with a segment of a conventional PET scanner. The high spatial resolution intra-operative PET imaging probe can help surgeons determine locations and the extent of primary tumor during surgery and identify tumors that spread out beyond primary tumors, for example extra-capsular existence of prostate cancer or spreading of breast cancer to lymph nodes.

1 .5 **Goals**

In this study, we present a preliminary study of an intra-operative positron emission tomography (PET) imaging probe system that provides reconstructed images in real time. The proposed imaging system consists of a low resolution partial ring detector

and a high resolution imaging probe that is equipped with a position tracker. The PET imaging probe operates in coincidence with the partial ring detector. The high resolution imaging probe and its proximity to target lesions contribute to the localization of small tumors. Our ultimate goal is to provide incrementally updated 3-D reconstructed images that are re-projected in real time onto a plane whose orientation is driven by the tracking device. To make progress to our ultimate goal, we have three specific goals to implement.

First, we propose a variant of the one-pass list-mode ordered subsets maximum likelihood. For image reconstruction, the line connecting two end-points of the two annihilation photons, called LOR (line of response), is considered individually in list mode. A one-pass list-mode ML algorithm goes through the ordered subsets once and only once. The modified one-pass list-mode algorithm is based on a row-action maximum likelihood algorithm (RAMLA). One interesting characteristic of the RAMLA is that it is a *convergent* ordered subsets ML algorithm. The variant of one-pass list-mode ML algorithm will divide the incoming LORs into subsets temporally on the fly and update the reconstructed image for each incoming subset.

The second goal was to implement and test the proposed image reconstruction algorithm using parallel computing. Parallel computing can significantly reduce the image reconstruction time. We used a parallel programming language called CUDA (Compute Unified Device Architecture) and a graphical processing unit (GPU) with 128 streaming processors (SP).

The third goal was to build a prototype of the intra-operative PET imaging system. The prototype system consists of BGO block detectors with low spatial resolution and a pixelated NaI(Tl) probe with higher spatial resolution. The prototype

system was built on a VMEbus system. In order to streamline the experiments, an on-line data acquisition/analysis program was also developed.

1 .6 A New Intra-operative PET Imaging Probe System: My Contributions

The PET imaging probe system consists of a high spatial resolution (~2mm) imaging probe equipped with a position tracker and a partial ring detector that operates in coincidence with the probe.

The intra-operative PET imaging probe system can provide high spatial resolution images during surgery at low cost compared to conventional whole body PET systems. Probe resolution is substantially higher than whole body PET especially in the transverse direction. An integral part of our ultimate goal is to provide incrementally reconstructed images in real time.

1. 6 .1 Simulation Studies for the Intra-operative PET Imaging Probe

We used the GEAT4 simulation tool kit for simulation studies. In the simulation studies, the intra-operative PET imaging probe system is comprised of a pixelated LSO crystal detector and a BGO partial ring detector. The pixelated LSO probe operates in coincidence with the BGO partial ring detector. LSO has comparable emission light compared to NaI(Tl) and has higher stopping power than BGO.

From these simulation studies, we could obtain simulated data before we built a prototype of the PET imaging probe system. The simulated experiment can keep track of each gamma ray trajectory and secondary particles from the gamma ray. Since the simulated data are almost ideal, we can remove any position error or measuring error that is inevitable in real measurement systems.

In addition, we incorporated an anthropomorphic Zubal phantom [36] into the PET imaging probe system. Scattering in the phantom was observed to evaluate the effect of scattered gamma rays on imaging quality.

1. 6 .2 Sliding Window Ordered Subsets List Mode ML Algorithm

The intra-operative PET imaging probe system is designed to provide reconstructed images in real time. In order to reconstruct images on the fly, we confined the number of lines-of-response (LORs) within a subset to a very small number. In addition, row-action ML algorithm (RAMLA) is integral to the proposed iterative image reconstruction algorithm. In RAMLA, the number of projection views per subset can be set to one. However, a small number of projection views per subset can result in low signal to noise ratio in conventional OSEM algorithms.

One pass list mode OS EM (OPL ML) is also integral to the proposed image reconstruction algorithm. The final reconstructed image is obtained after the first iteration in OPL ML algorithm. Because the proposed PET imaging probe system intends to provide reconstructed images in real time, minimizing the number of iterations is required.

We also used a Gaussian back-projection kernel instead of a strip that connects two endpoints of a line-of-response. This Gaussian back-projection kernel was adapted from the original list-mode ML algorithm.

This algorithm was termed “sliding window ordered subsets list-mode ML algorithm”. The proposed algorithm was used for both simulation studies and measured data studies in this dissertation.

1. 6 .3 **Parallel Image Reconstruction Using a Graphics Card**

A variant of one-pass list-mode ML algorithm for the PET imaging probe system requires intensive computation even though we confine the number of LORs within a subset to a small number. We used a graphics card (nVidia Geforce 9800GTX+) to speed up image reconstruction. The graphics card has a graphics processing unit (GPU) with 128 streaming processors (SPs). The GPU was designed to implement fast parallel computation. The speed-up of image reconstruction by using GPUs is significant compared to that of quad core CPUs.

We parallelized our list-mode ML algorithm using CUDA in order to run it on the GPU. The image space was set to a 64×32×32 array of voxels for simulation studies. Each voxel measured $0.5\times0.5\times0.5mm^3$. We assigned 2×128 thread blocks. A 16×16 array of threads comprises a thread block. As a result, the number of assigned threads is the same as that of voxels in image space. Therefore one thread in CUDA code corresponds to one voxel in image space.

For measured data study, we used a 128×64×64 array of voxels. Each voxel measured $0.25\times0.25\times0.25mm^3$ for the measured data study. The speed-up of image reconstruction not only reduced the image reconstruction time, but also streamlined studies on image reconstruction because it reduced the cycles of debugging and verification.

1. 6 .4 A First-Generation Prototype of the Intra-operative PET Imaging Probe System

We have designed and constructed a first-generation prototype of the intra-operative PET imagining probe system. The prototype system consists of a pixelated NaI(Tl) crystal detector and an array of BGO block detectors. A module of pixelated NaI(Tl) crystals was coupled to a Hamamatsu H8500 position sensitive PMT with an 8×8 array of anodes. A charge division circuit (CDC) was used to convert the 8×8 array of PSPMT anode outputs to a set of 4 outputs. The 4 outputs were routed to a peak-sensing ADC and were digitized for position estimation.

Each BGO block detector has 4 PMT outputs. The BGO outputs were also routed to the peak-sensing ADC. A VME FPGA board was used to build a coincidence circuit. The coincidence events were acquired using a custom data acquisition program. The custom data acquisition program was designed to take the coincidence events and display outcomes of position estimation on the fly.

A small Na-22 source disks was used to test the prototype system. A double source disk with 1.5mm source separation was imaged, but the two point sources were not distinguished in reconstructed images. However the theoretical spatial resolution of the prototype was not enough to separate the two Na-22 point sources. In addition, the elongation of the reconstructed images in the longitudinal direction due to limited angle tomography was not severe. This mitigated effect of limited angle tomography in the PET imaging probe system was predicted in simulation studies.

1 .7 **Dissertation Overview**

In this dissertation, a prototype of an intra-operative PET imaging probe system was investigated and developed. In addition, an iterative image reconstruction algorithm for real time image reconstruction was investigated and tested using parallel computing. This dissertation is organized as follows. Chapter 2 describes (1) the system configuration of the intra-operative PET imaging probe system and (2) Monte Carlo simulations of background radiation. Chapter 3 describes a proposed iterative image reconstruction algorithm. A variant of the one-pass list-mode ML algorithm was developed for real time image reconstruction. The row-action ML algorithm was infused into a one-pass list-mode OSEM algorithm. The number of LORs within a subset was confined to a small number. A Gaussian kernel was also integral to the proposed algorithm. Chapter 4 describes parallel image reconstruction using a graphics processing unit (GPU). The proposed image reconstruction algorithm was parallelized using CUDA. Chapter 5 describes the prototype of the intra-operative PET imaging probe system that we built in order to obtain real data. A pixelated NaI(Tl) detector and a bank of BGO block detectors comprised the prototype system. Conclusions and future work are discussed in Chapter 6.

Chapter 2
Intra-operative PET Imaging Probe System and Monte Carlo Simulations on the Effects of Background Radiation

In this chapter, the general description of the intra-operative PET imaging probe system is presented in the first half of this chapter. In addition to the general description, advantages and disadvantages of the intra-operative PET imaging probe system are discussed. In the second half of this chapter, a simulation study of the effects of background radiation is presented.

2 .1 Review of Motivations

Before introducing an intro-operative PET imaging probe system, we briefly review the motivations of the study. Conventional whole-body PET systems have relatively big radii enough to blur reconstructed image due to annihilation photon acolinearity. As a result, there is a limitation on achievable spatial resolution from conventional PET imaging systems. In order to overcome the limitation, the intra-operative PET imaging probe system was designed to place an imaging probe very close to target lesions.

In addition, the intra-operative PET imaging probe system requires fewer resources than a possible very-high-resolution whole-body PET system. In the proposed

PET imaging probe system, the high resolution imaging probe operates in coincidence with a low resolution partial ring detector.

Pre-surgical diagnostic images can be used to located tumor sited during surgery. However it is a difficult task to locate tumor sites during surgery due to patient's change of position. On the contrary, the intra-operative PET imaging probe system aims to provide real time images during surgery. We investigated a variant of one-pass list mode ML algorithm in order to reduce the number of iterations to obtain final reconstructed images. We also investigated the use of GPU to speed up image reconstruction. Since this real time processing can help surgeons or clinicians identify tumor sited on the fly, we expect that we can improve the efficiency of surgery for removing tumors.

The proposed imaging probe system, however, suffers limited angle data collection. The effects of limited angle tomography were observed when we used the proposed image reconstruction algorithm. In the proposed algorithm, new estimates are updated on the basis of projection-by-projection.

2 .2 **Intra-operative PET Imaging Probe System**

2. 2 .1 **Detecting Small Tumors with High Resolution PET Imaging Systems**

As a result of recent advances in detector materials and photo multipliers, high spatial resolution PET imaging systems became more feasible [37] [38]. For instance, Rouze *et al*. used position sensitive PMTs and a 0.87mm-pitch array of LSO crystals for a small animal PET scanner [38]. This high resolution PET imaging system could be scaled up to whole body PET systems. However, the cost to build the extraordinary high

resolution whole body PET scanner would be unjustified for clinical use. In addition, the spatial resolution is not linearly proportional to the size of detector crystals.

A few factors affecting spatial resolution of a ring PET system are discussed. The approximate intrinsic spatial resolution at the center of a PET ring detector (in FWHM) is given in Equation (2.1) [39] [40]. All the units are in millimeters.

$$\Gamma = 1.25\sqrt{(w/2)^2 + (0.0022D)^2 + R^2 + b^2} \qquad (2.1)$$

where w is the crystal width, $\boldsymbol{D}$ is the ring diameter, and R is the effective positron range. The numerical factor 1.25 is from the interpolation and back-projection in the image reconstruction, and the numerical factor 0.0022 = 0.5×*tan(0.25°)* is due to annihilation photon acolinearity. The term b is determined by the coupling between crystals and photo-detectors.

Figure 2-1 shows the PMT quadrant sharing of light from a set of crystals. Four PMTs (A, B, C, and D) share the light from pixilated crystals.

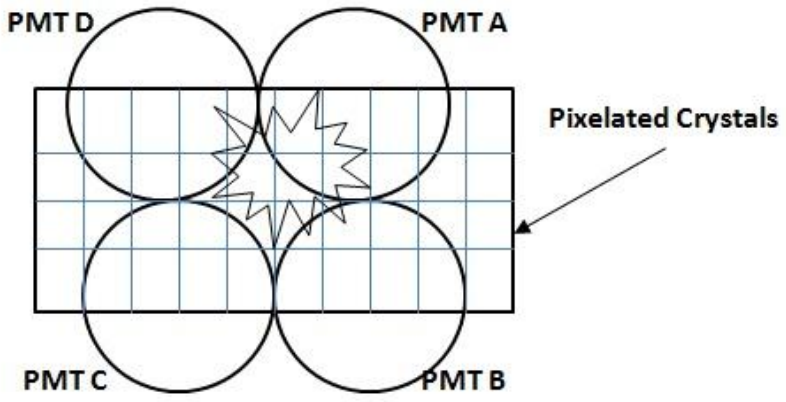

Figure 2-1. PMT quadrant sharing scheme. This picture was adapted from [41].

On the other hand, Figure 2-2 shows the one-to-one coupling of crystals and avalanche photo-diodes (APDs). Light photons from each crystal are routed only to a single coupled APD. In a similar way, one crystal can be coupled to a single PMT. If a crystal has the one-to-one coupling between the crystal and a photo-detector, the term *b* is zero. The term *b* is non-zero for the light-sharing coupling.

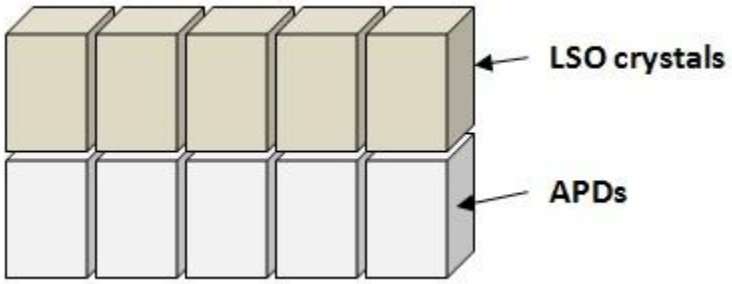

Figure 2-2. One-to-one coupling of an array of APDs and an array of LSOs. This picture was adapted from [42].

Table 2-1 shows effective positron ranges of some typical radio-tracers. F-18 FDG is widely used for PET scans. From Equation (2.1), the intrinsic spatial resolution from two different systems [39], assuming the term *b* is zero, is shown in Table 2-2. The effective positron range (2.35×*rms*) of F-18 is due to the long tail of the positron range distribution.

Table 2-1. Effective positron ranges. The term *r* is the effective FWHM. The table is from [43].

Isotope	F-18	C-11	Ga-68	Rb-82
Maximum Kinetic Energy (MeV)	0.64	0.96	1.90	3.35
FWHM (mm)	0.13	0.13	0.31	0.42
FWTM (mm)	0.38	0.39	1.6	1.9
r =235×rms (mm)	0.54	0.92	2.8	6.1

Table 2-2. Intrinsic spatial resolution of two different systems. This table was adapted from [39].

	detector diameter	F-18 effective positron range	Resolution(Γ)
3mm crystal width	350mm	0.5mm	2.2mm
2mm crystal width	350mm	0.5mm	1.8mm

For more realistic estimation of the spatial resolution of whole body PET scanners, we could include the non-zero *b* term, which is the crystal identification uncertainty, and a linear sampling term [37].

$$\Gamma = 1.25\sqrt{(w/2)^2 + (0.0022D)^2 + R^2 + b^2 + (d \times s)^2} \qquad (2.2)$$

where the term b is non-zero and the term $d \times s$ is for the linear sampling. The term *d* is the crystal pitch and the term *s* is a sampling factor.

The term *b* can be removed if the coupling between a crystal and a photo-detector is one-to-one. The linear sampling rate was carefully considered when relatively big crystals were used, for example 20mm-by-20mm crystals roughly have the intrinsic spatial resolution of 10mm [44].

Albeit small size detectors are used, the linear sampling is still an important factor in high spatial resolution PET systems because higher spatial resolution is required to detect smaller lesions. Linear sampling that does not meet the Nyquist sampling requirement results in blurring in reconstructed images [45] [40]. Figure 2-3 shows the definition of the sampling distance [45]. In general, the embedded sampling distance is the crystal pitch. Usually the crystal pitch is greater than the crystal width. Since the sampling distance is larger than the detector intrinsic resolution (*w/2)*, the Nyquist

sampling requirement is not satisfied. Therefore the oblique LORs are included to reduce the sampling distance in half.

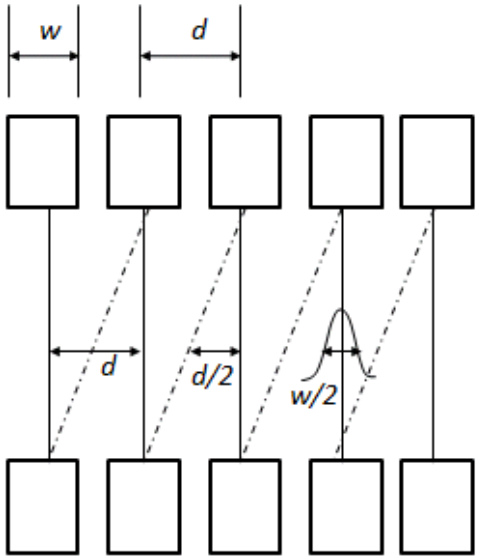

Figure 2-3. Illustration of the detector intrinsic resolution and the sampling distance at the center of a ring PET scanner. The term ***d*** is the crystal pitch, the term ***d / 2*** is the linear sampling distance, the term *w* is the crystal width, and the term ***w/2*** is the intrinsic detector resolution. This picture was adapted from [45].

Table 2-3 shows estimated spatial resolution for an 850mm diameter system as a function of detector width and the isotope. Equation 2.2 was used to calculate the estimates. The term b was set to 1mm. It is interesting that the spatial resolution of the 2mm crystal system is 3.11mm, which is greater than the width of the crystal. From the estimates, it is clear that achievable FWHM resolution greater than the crystal width except for the 4mm crystal with S=0. Table 2-4 shows the spatial resolution of an 85cm diameter PET scanner when the crystal position uncertainty was set to zero and F-18 was the isotope of interest. The spatial resolution is still below the crystal sizes.

Table 2-3. Spatial resolution of an 85cm diameter PET scanner with respect to the detector width and the isotope. The term *b* was set to 1mm. The sampling factor was included. This table is from [37].

Isotope	Linear sampling factor	Detector widths (mm)		
		2	3	4
F-18	S = 0	3.04	3.40	3.82
	S = 0.25	3.11	3.52	4.02
	S = 0.5	3.29	3.88	4.56

Table 2-4. Spatial resolution of an 85cm diameter PET scanner when the term b is set to zero. F-18 is the isotope of interest.

Linear sampling factor	Detector widths (mm) 2	3	4
S= 0.25	2.8	3.2	3.7
S = 0.5	3.0	4.6	4.29

2. 2 .2 General Description of the Intra-operative PET Imaging Probe System

The proposed intra-operative PET imaging probe system consists of a small, high spatial resolution imaging probe that can be placed close to lesions during surgery and a low resolution partial ring detector as shown in Figure 2-4. The high resolution imaging probe is comprised of either LSO or LYSO:Ce crystals. The low resolution partial ring detector consists of BGO crystals, for example 5×5×30 mm^3 crystals. The PET imaging probe is equipped with a position tracker. The position tracker provides imaging probe's position and orientation. The coincidences between the imaging probe and the partial ring detector are collected in list mode for image reconstruction as shown in Figure 2-5.

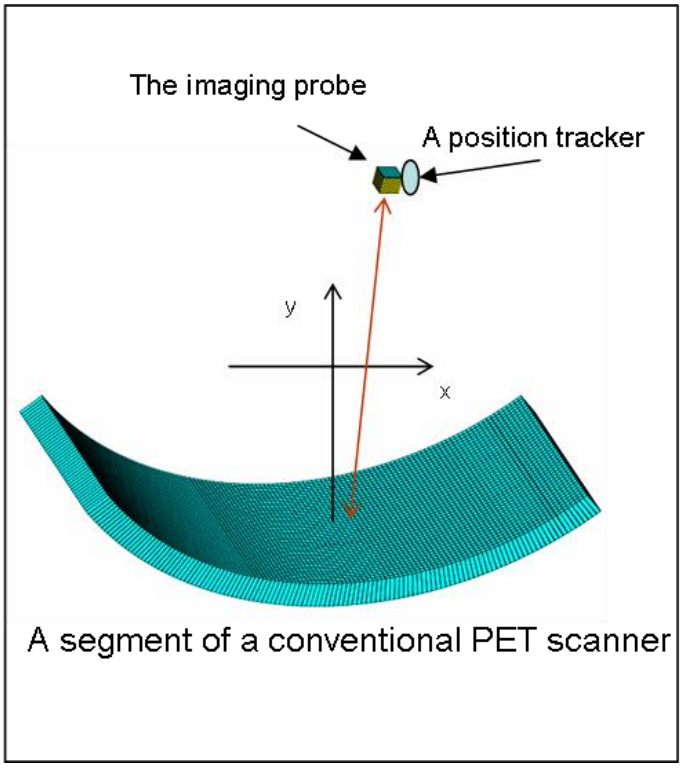

Figure 2-4. Illustration of the intra-operative PET imaging probe system.

Figure 2-6 illustrates the intra-operative PET imaging probe system used with an anthropomorphic phantom. The anthropomorphic phantom is one section of the Zubal phantom [46]. A segment of a conventional PET scanner is beneath the anthropomorphic phantom. The small PET imaging probe in the surgical opening is also shown in the illustration. A position tracker is not included in the illustration for simplicity's sake. In order to obtain a joint solid angle as large as possible, the PET imaging probe is placed very close to suspicious lesions. Since the probe is so much closer to the tumor sites than the ring detector segment that probe intrinsic resolution largely determines the image resolution. The position tracker will be integrated in one of final versions of the PET imaging probe system.

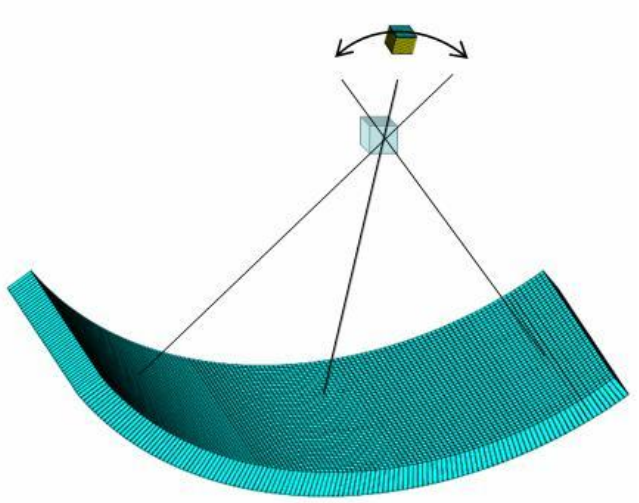

Figure 2-5. Coincidence data (LORs) between the imaging probe and the partial ring detector.

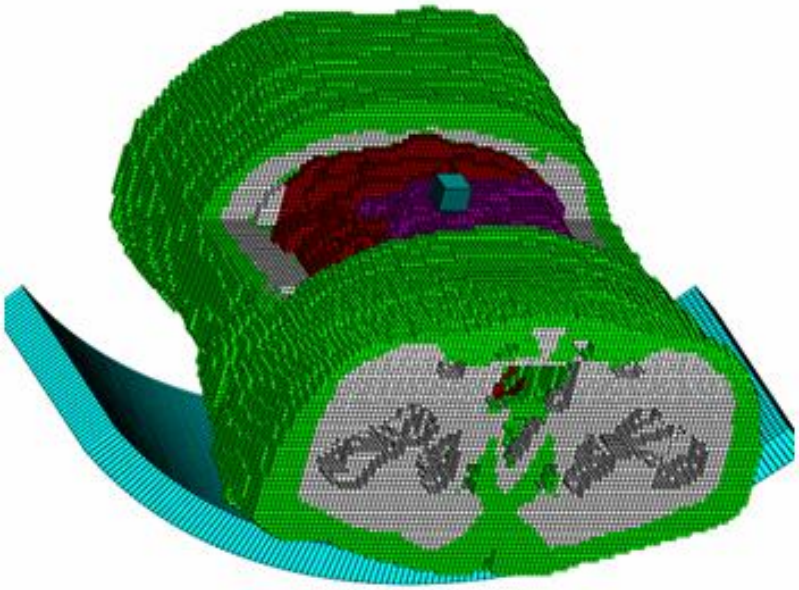

Figure 2-6. Intra-operative PET imaging probe system with Zubal Phantom. The imaging probe is in the surgical opening.

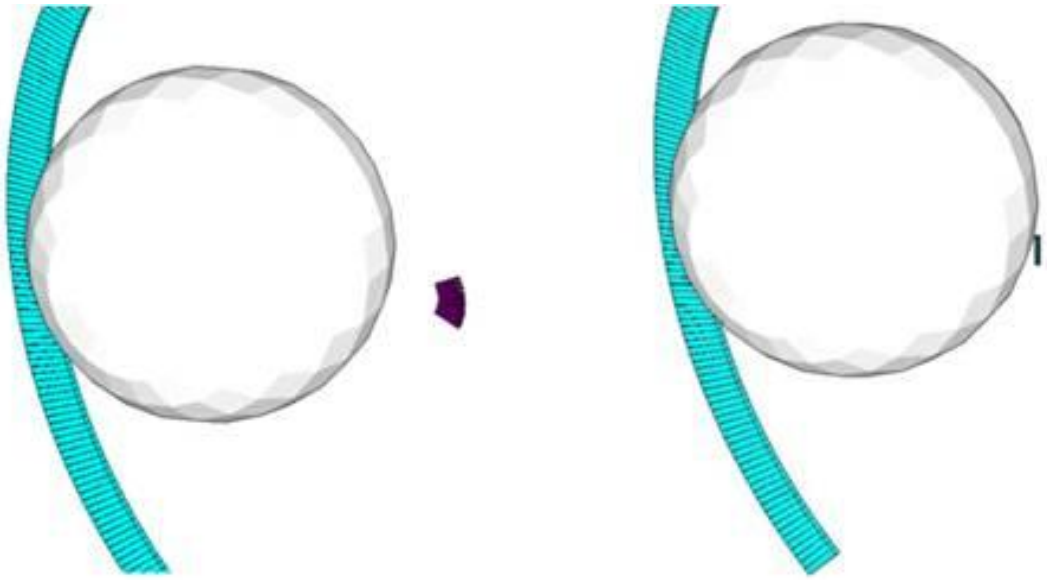

Figure 2-7. Two potential types of imaging probes. A fan-shaped probe (on the left) and a parallel stacked probe (on the right).

We can consider at least two types of imaging probes; a parallel stacked imaging probe and a fan shaped imaging probe. The two types of the imaging probes are shown in Figure 2-7. The fan-shaped imaging probe can contain thick crystals and achieve high detection efficiency under the assumption that a target lesion is at the focal point of the fan-shaped probe. On the other hand, the parallel stacked probe can minimize the effect of loss of depth of interaction (DOI) information by using relatively thin crystals. One drawback of the parallel stacked type is low detection sensitivity.

2. 2 .3 **Irregular Sampling PET Systems**

The PET imaging probe system has a different sampling scheme than that of conventional PET scanners. Two irregular sampling PET systems are reviewed briefly to avoid radical transition from conventional PET scanners to the PET imaging probe system.

2.2.3.1 **Compact PET for Prostate Imaging**

Since the prostate is small and its location is known, two banks of detectors are used in order to put the detectors close to prostate [ch2-11, 47]. Figure 2-8 shows an illustration of the compact PET for prostate imaging.

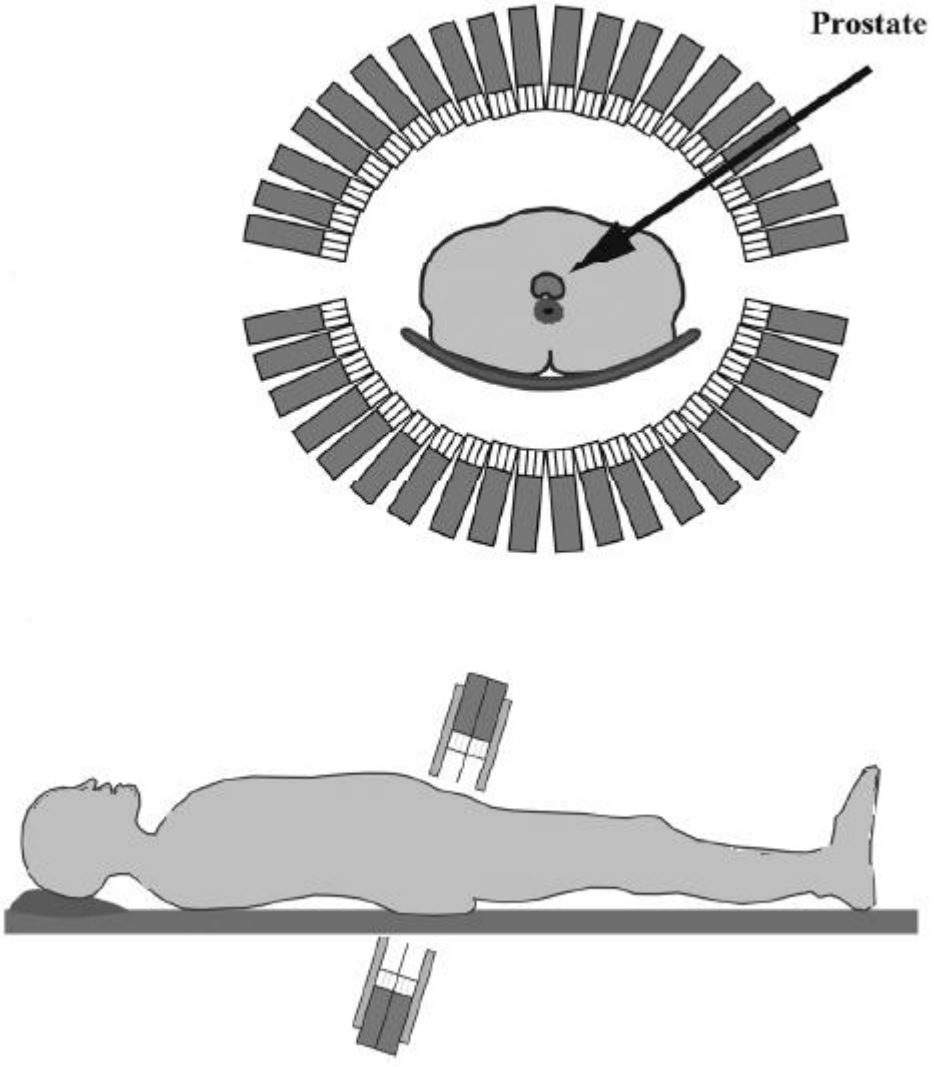

Figure 2-8. Illustration of the compact PET for prostate imaging system. This picture is from [47].

We can notice that two banks of detectors do not sample the whole 360° over a patient's body. Figure 2-9 shows the missing elements in a sonogram due to the missing detector elements.

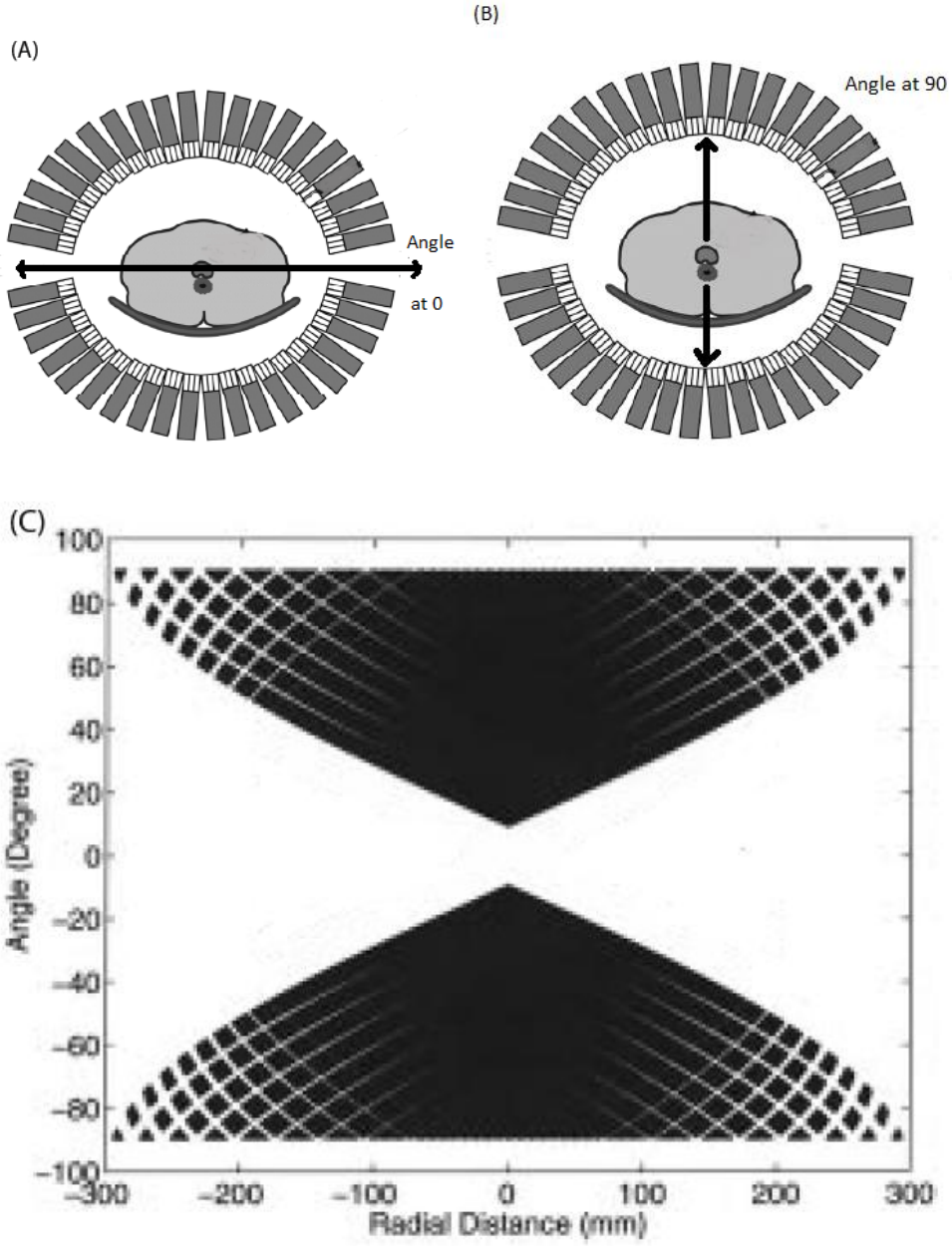

Figure 2-9. Irregular sampling. These pictures were adapted from [47].

As illustrated in Figure 2-9 there are no lines of response in the 20-degree interval at 0 degree because of the missing detectors. On the other hand, many LORs are available at 90°. As a result, we see some empty region in the sinogram. In order to augment the sinogram, the LORs between detectors of the same bank are allowed as shown in the upper picture in Figure 2-10. The augmented sinogram is also shown in Figure 2-10.

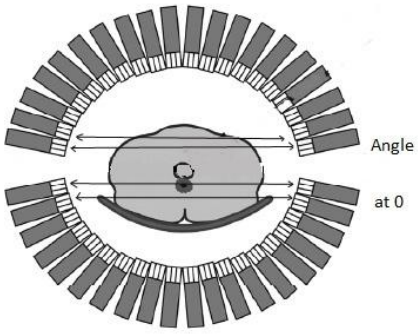

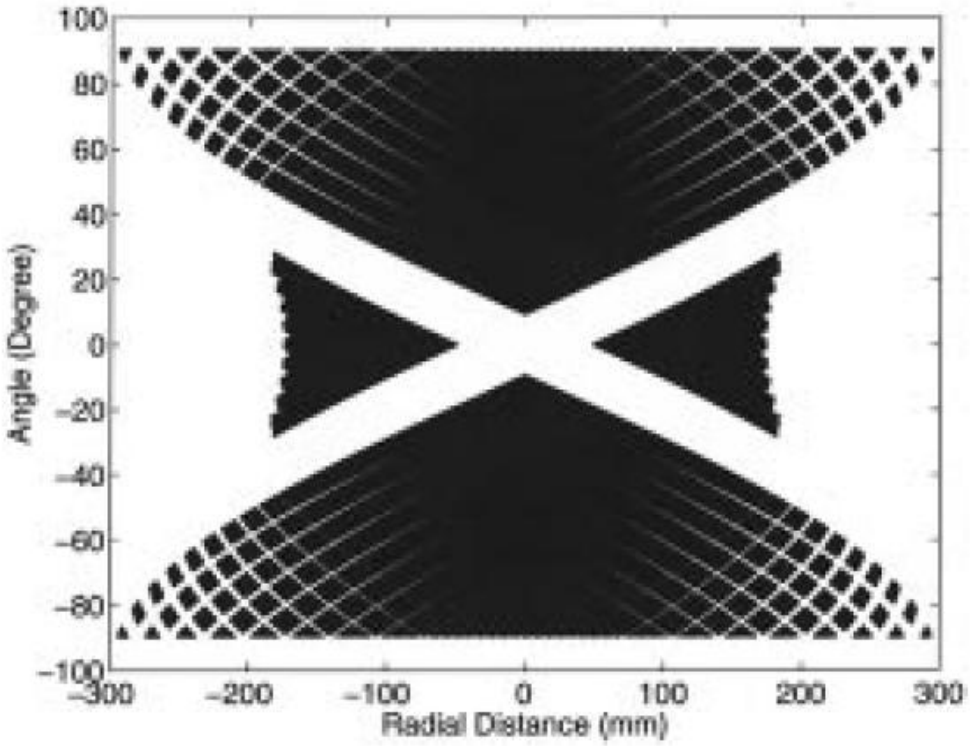

Figure 2-10. Augmented sonogram. This picture is from [47].

Figure 2-11 shows the compact PET scanner that consists of two banks of detectors. One reconstructed image from the compact PET scanner is shown in Figure 2-12. The phantom consists of two cylinders. The inner cylinder has 3 times higher source activity than the outer cylinder. Note that image elongation along the vertical center line.

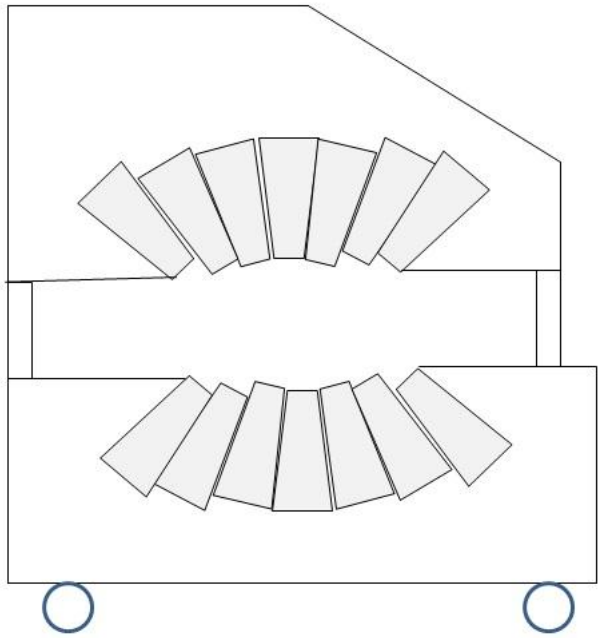

Figure 2-11. Illustration of an implemented Compact PET scanner. Not to scale. This was adapted from [48].

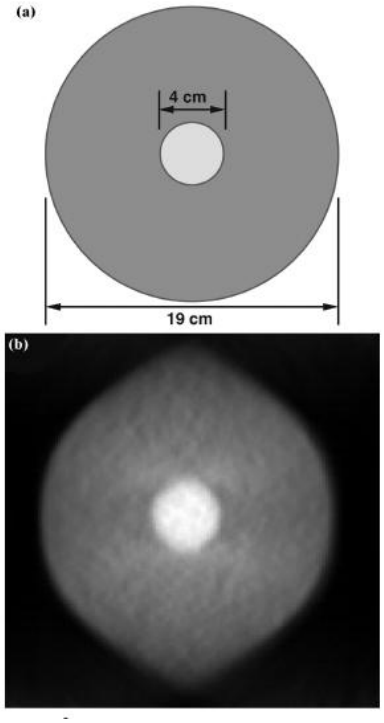

Figure 2-12. Reconstructed image from the compact PET. This picture is from [48].

2.2.3.2 **PEM-PET**

A positron emission mammography – positron emission tomography (PEM-PET) system is dedicated to breast imaging [49]. The rectangular PEM-PET system is shown in Figure 2-13. The PEM-PET system has capability of obtaining depth of interaction because crystal elements are sandwiched between an array of photodiodes and a PMT. Each bank of detectors operates in coincidence with three other banks of detectors. As a result, the rectangular PET system has 172 million possible LORs.

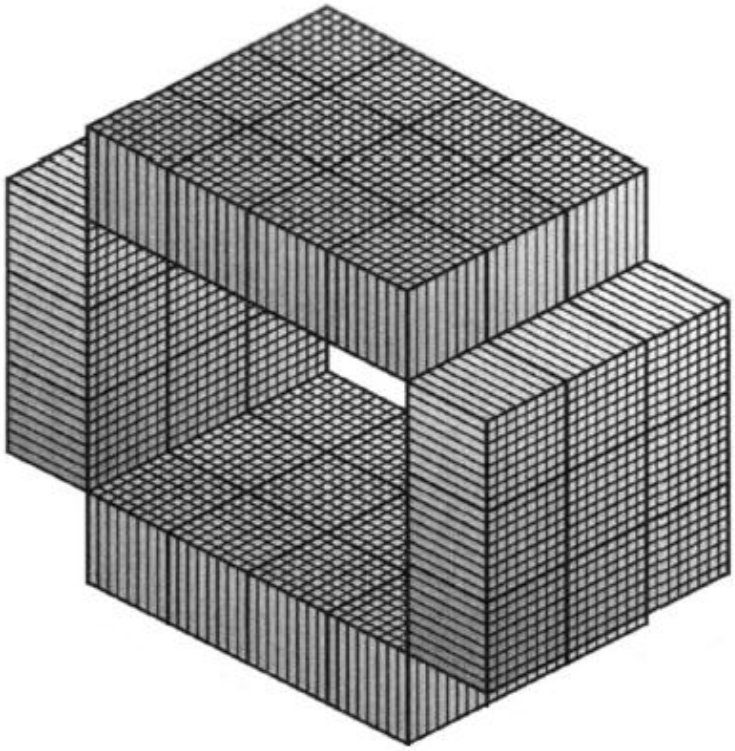

Figure 2-13. Rectangular PET system. This picture is from [49].

Since detector elements are not in a circular array, angular sampling intervals are not the same. All the oblique LORs that have different depth of interaction are collected and processed.

A local impulse response of the system was used for system analysis [50]. The local impulse response was measured at the center of the rectangular PET system. Figure 2-14 shows transaxial, coronal, and sagittal contour plots of the local impulse response. Due to the irregular sampling, we can see the contours are not symmetric. However contours near the center resembles ovals. The ovals indicate distortion due to irregular sampling is alleviated near the center.

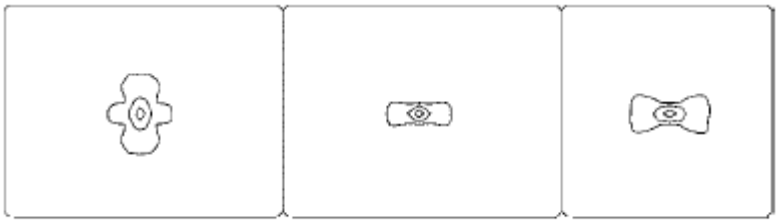

Figure 2-14. Measured local impulse response at the center. Transaxial, coronal, and sagittal views (from the left). This picture is from [49].

2. 2 .4 **Advantages of the Intra-operative PET imaging Probe System**

As shown in Table 2-3, it is unlikely to achieve high spatial resolution from whole-body PET systems just by using small crystals. This spatial resolution limitation is due mainly to the limited linear sampling and annihilation photon acolinearity. In this dissertation, a high resolution PET imaging probe is placed very close to the target lesions. The imaging probe's proximity to lesions and small size crystals in the imaging probe are main sources of high spatial resolution. We can roughly calculate the intrinsic spatial resolution of a pair of mismatching detectors using a coincidence aperture function (CAF).

The coincidence aperture function (CAF) from a pair of detectors can be calculated as shown in Figure 2-15 [45]. The sum of the angle α and β at a given position represents the value of CAF at the position. Equation (2.3) is for inside the dashed lines joining the opposite extremities of the two crystals. Equation (2.4) is for outside the dashed lines.

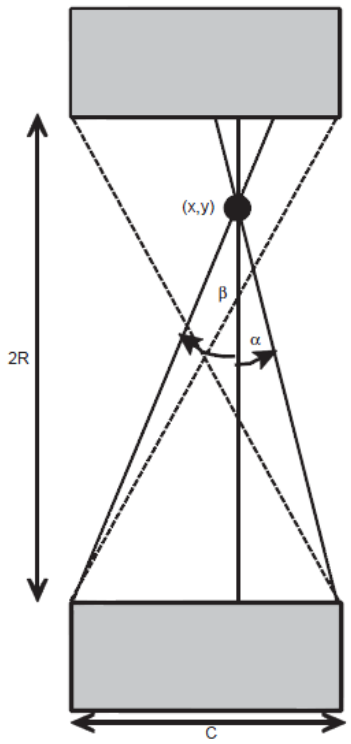

Figure 2-15. Joint angle calculation to draw a coincidence response function. The illustration is from [45].

$$\alpha = \tan^{-1}\frac{(\frac{C}{2} - |x|)}{(R + |y|)}, \qquad \beta = \tan^{-1}\frac{(\frac{C}{2} + |x|)}{(R + |y|)} \tag{2.3}$$

$$\alpha = \tan^{-1}\frac{(\frac{C}{2} - |x|)}{(R + |y|)}, \qquad \beta = \tan^{-1}\frac{(\frac{C}{2} - |x|)}{(R + |y|)} \tag{2.4}$$

The geometrical coincidence response function with respect to the coordinates (*x*, *y*) is visualized in Fig. 2-16.

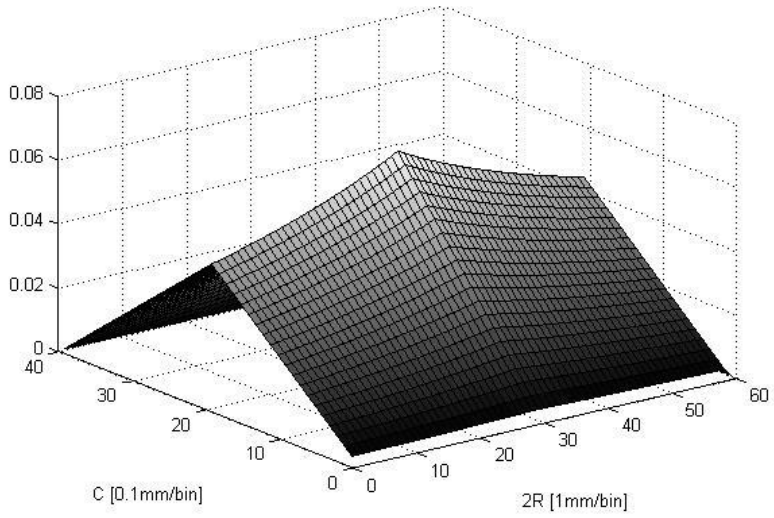

(a)

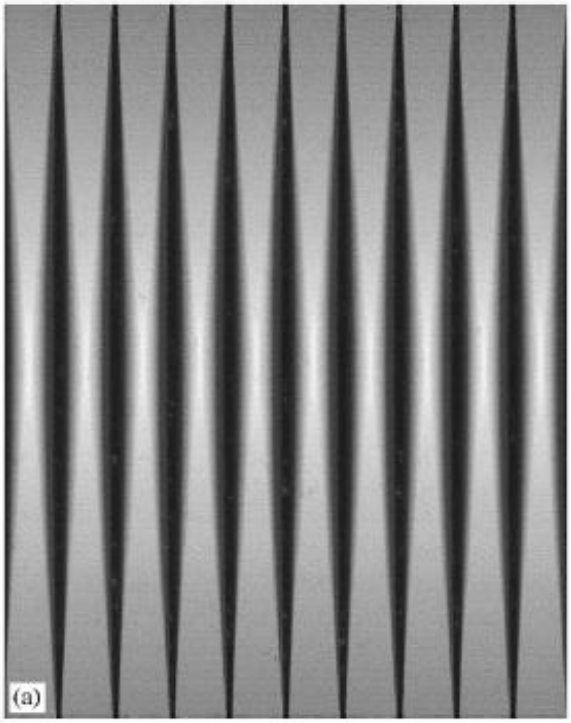

(b)

Figure 2-16. Visualization of the geometrical coincidence aperture functions of pairs of crystals. (a) CAF between two crystals. (b) 2-dimensional plot of CAFs of several detector pairs. This picture is from [45].

The upper drawing shows a coincidence response function between a pair of crystals by using Equation (2.3) and (2.4). We can see the response function has a narrower width at the middle point. The lower picture shows CAFs of 10 pairs of crystals.

In the intra-operative PET imaging probe system, detector crystals in a pair are different in width. For example, the small crystal is 2mm in width and the other crystal is 4mm in width as shown in Fig. 2-17. The separation between the two different size crystals was set to 30mm.

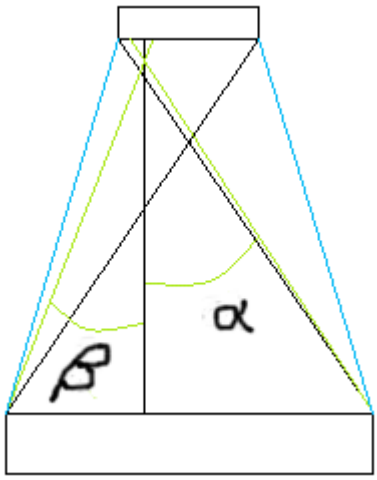

Figure 2-17. Joint angle made by two crisscrossing lines. The joint angle is the sum of α and β. The crisscrossing lines represent the angular limit that both detectors see when a source is located at the crisscrossing point. Outside the two boundary lines, true coincidence is zero.

The joint angle γ along the horizontal line was calculated as shown in Fig. 2-18. The estimated angle was drawn with respect to the position along the horizontal line in Fig. 2-19. The FWHM of the coincidence response function along the horizontal line is smaller than the width of the small crystal as shown in Fig. 2-19.

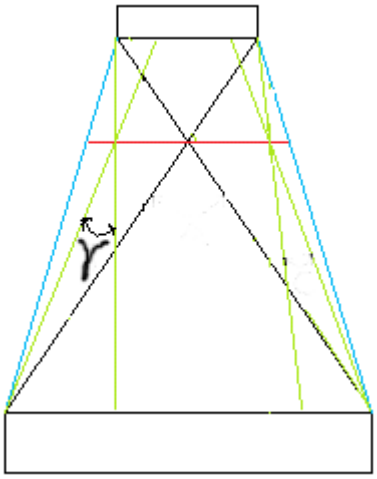

Figure 2-18. Joint angle outside the crisscrossing lines joining the opposite extremities of the two crystals. The joint angle is γ.

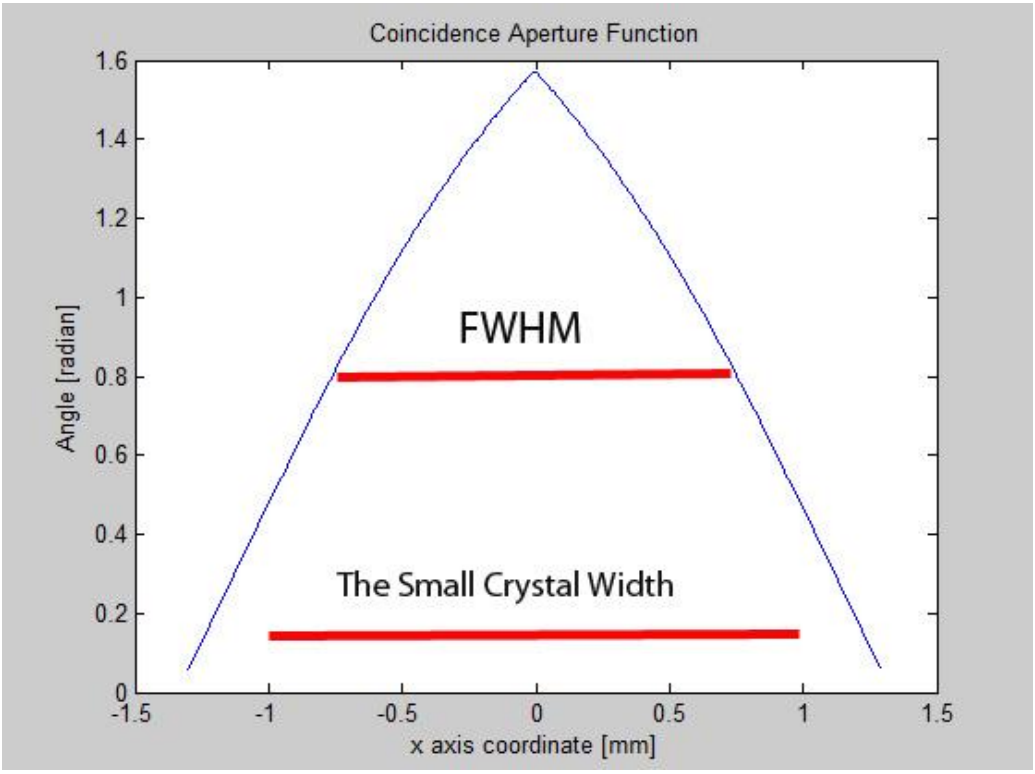

Figure 2-19. Coincidence aperture function (γ with respect to locations) along the horizontal line in Fig. 2-18. The separation distance from the horizontal line to the small crystal was set to 10mm.

In the intra-operative PET imaging probe system, the intrinsic spatial resolution near the imaging probe is determined by the crystal width of the PET imaging probe. Therefore the FWHM of the coincidence response function of the PET imaging probe is set to *w*, the width of small crystals, though it is actually less than *w* near the imaging probe. Equation (2.2) was rewritten into Equation (2.5).

$$\Gamma = 1.25\sqrt{(w)^2 + (0.0022D)^2 + R^2 + b^2 + (d \times s)^2} \qquad (2.5)$$

The ROI of the intra-operative PET imaging probe system is very small and very close to the imaging probe rather than the partial ring detector. Fig. 2-20 shows two pairs of different size detectors. The position-electron annihilation location is set to the origin (0,0). The pair with wide separation has larger position error (Δy) due to annihilation photon acolinearity than the pair with smaller separation. We are interested in the pair with smaller separation. The detector on the left-hand side is located at 280mm to the left of the origin. The position error (Δy) with respect to the distance Δx is shown in Fig. 2-21. The position error at Δx=40mm is roughly 0.3mm as shown in Fig. 2-21. The error due to annihilation photon acolinearity is less than the effective positron range of ^{18}F. The term 0.0022*D* is replaced with 0.3 in Equation (2.6).

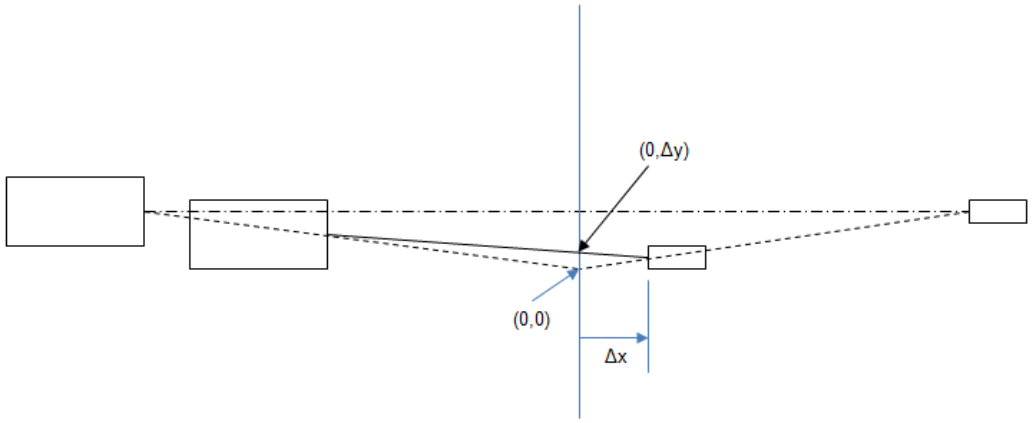

Figure 2-20. Position error due to annihilation photon acolinearity. This drawing is not to scale.

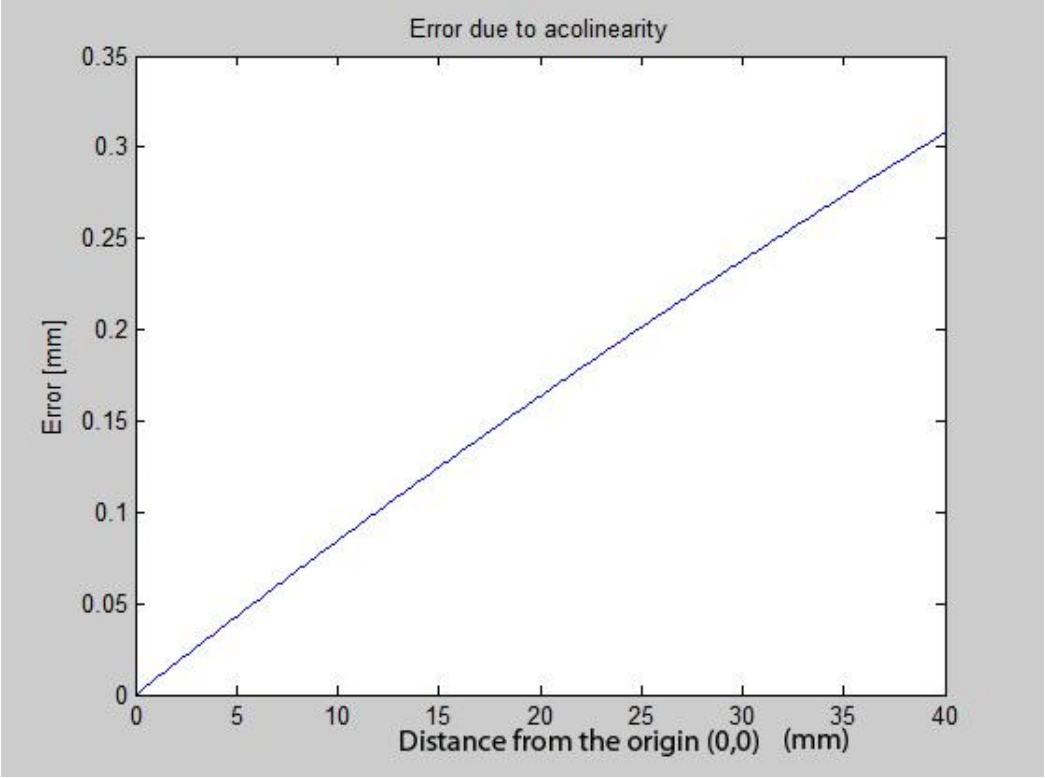

Figure 2-21. Position error with respect to Δx measured in millimeter.

$$\Gamma = 1.25\sqrt{(w)^2 + 0.3^2 + R^2 + b^2 + (d \times s)^2} \qquad (2.6)$$

In addition, the one-to-one coupling of the crystals and photo-detectors is much more feasible on account of the small size of the PET imaging probe. Therefore the term *b* can be set to zero as shown in Equation (2.7).

$$\Gamma = 1.25\sqrt{(w)^2 + 0.3^2 + R^2 + zero + (d \times s)^2} \qquad (2.7)$$

Another characteristic of the intra-operative PET imaging probe system is its affinities to the fan-dichotomic sampling scheme [51]. The fan-dichotomic sampling scheme is shown in Fig. 2-22. In the fan-dichotomic sampling scheme, the two split rings have one missing detector element. The half ring is rotated by *d*/2 to obtain finer sampling. The fan-beam LORs are then collected rather than parallel beam LORs in order to minimize the sampling distance at the center [52].

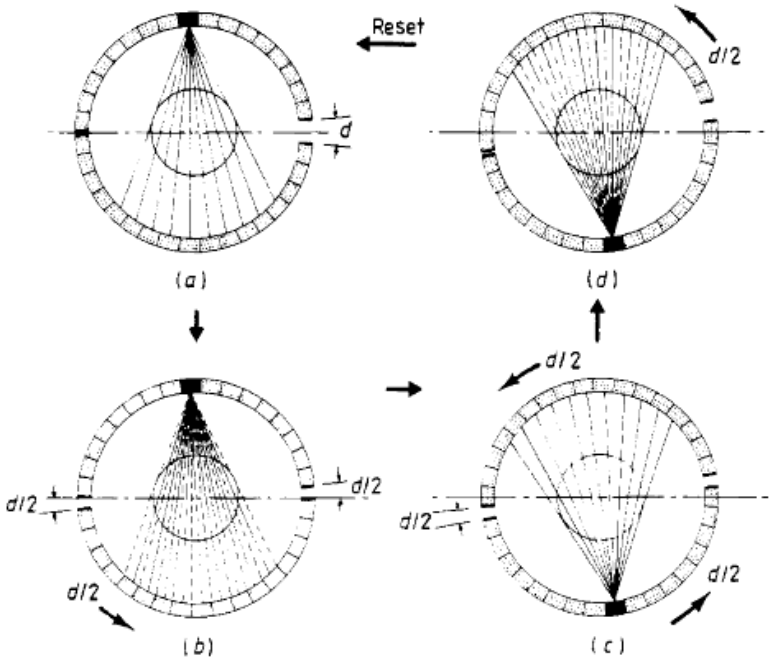

Figure 2-22. Fan-beam LORs in the fan-dichotomic sampling scheme. This picture is from [51].

Kouris *et al.* reported that finer radial sampling was more important than finer angular sampling [53] for stationary PET scanners. Therefore translation in the tangential direction as well as curvilinear motion is also desirable.

The upper drawing in Fig. 2-23 shows possible LORs between pairs of the same size crystals of a stationary PET system. The lower drawing shows possible LORs between pairs of different size crystals. In theory, the PET imaging probe can be moved because it is equipped with a position tracker. Fig. 2-24 shows the displacement of a bank of smaller crystals in the vertical direction. New possible LORs are superimposed on the proceeding LORs in Fig. 2-24. We note that position error from position trackers as well as crystal widths is inevitable in real measurements.

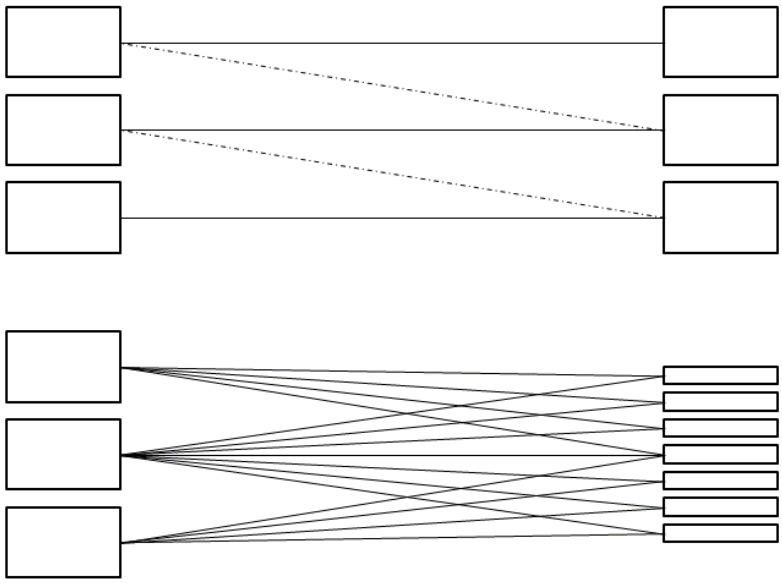

Figure 2-23. Possible LORs between pairs of crystals.

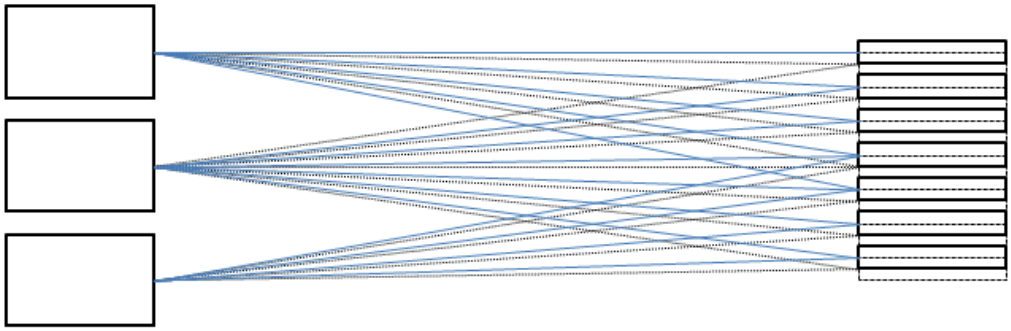

Figure 2-24. Finer radial sampling by moving the small probe vertically. LORs are superimposed.

By translating the PET imaging probe incrementally, the sampling distance can be made as small as desired. Position uncertainty of the position tracker depends on the type of tracker used. Table 2-5 shows a few position tracker modalities. Optical trackers show high accuracy and high resolution.

Table 2-5. Position tracker modalities. This table is from [54].

	Mechanical	Optical	Magnetic	Acoustic
Accuracy	0.1~2.5mm	0.1~0.5mm	~5mm	~1mm
Resolution		Best~0.01mm		~0.1mm
Bandwidth	>3000Hz	100~2500Hz	20~100Hz	500~1000Hz
Interference Sources	Physical occlusion	Heat, occlusion	Ferrous objects, magnetic fields	Temp., humidity, occlusion
Example	Faro Arm, NeuroNavigator	Optotrak 3020, Flashpoint	Polhemus, Flock of Birds	Sonic Wand
Contact / Non-contact	Direct Contact	Contact with targets	Contact with targets	Contact with targets
Passive /Active	Passive	Active	Active	Active

In theory, very fine sampling is feasible. Therefore the term $d \times s$ can be set to zero. Equation (2.7) is rewritten into Equation (2.8).

$$\Gamma = 1.25\sqrt{(w)^2 + 0.3^2 + R^2 + zero + zero} \quad (2.8)$$

As a result, the spatial resolution is determined by the detector width, position error due to photon acolinearity, the effective positron range, and the blurring from image reconstruction as shown in Equation (2.9). Table 2-6 shows the comparison of the spatial resolution of two different PET systems. Crystal size of 1mm slightly deteriorates spatial resolution of the PET imaging probe system. Equation (2.9) for the intra-operative PET imaging system is valid only in the transverse direction. The spatial resolution in the longitudinal direction is affected by limited angle tomography.

$$\Gamma = 1.25\sqrt{(w)^2 + 0.3^2 + R^2} \quad (2.9)$$

Table 2-6. Comparison of the intrinsic spatial resolution.

	Crystal width	*Scanner diameter*	*F-18 Positron range*	*Crystal uncertainty*	*Linear sampling factor*	*Γ* (spatial resolution)
Conventional PET system	2mm	850mm	0.5mm	1mm	0.25	3.11mm
Intra-operative PET imaging probe system	2mm	(0.3mm)*	0.5mm	1mm	zero	2.89mm
Intra-operative PET imaging probe system	2mm	(0.3mm)*	0.5mm	zero	zero	2.60mm

*The values in parentheses represent position error due to annihilation photon acolinearity.

2. 2 .5 Limitations of the Intra-operative PET Imaging Probe System

One main drawback of the intra-operative PET imaging probe system is that it is not capable of collecting coincidence data over 360° (or 180°) around the FOV. According to the central slice theorem, reconstructed images from limited angle data will be distorted along the axis perpendicular to the front of the imaging probe. Another drawback is position error due to the portable imaging probe. The probe position and orientation are provided by a position tracker that has its own uncertainty. Patient's respiratory motion is another cause of position error. These factors are discussed briefly.

2.2.5.1 Limited Angle Tomography

Albeit angular sampling is not as critical as linear sampling at the center of stationary PET scanners [53], incomplete angular sampling around the FOV results in distorted images with a point response function that depends on angle. The same problem was addressed in a breast PET imaging study. A partial ring PET imaging system for breast cancer suffered the same image distortions due to limited angle tomography [55]. Surti and Karp investigated the possibility of reducing the effects of limited angle tomography by incorporating time-of-flight (TOF) information into image reconstruction [55]. In their study, a simulated scanner had a ring diameter of 15cm and axial length of about 15cm. A simulated phantom was a 6cm diameter by 8cm long cylinder, containing three 5mm-diameter hot spheres with the 8:1 uptake ratio. The coordinates (x, y) were (0,0), (1.8,0), and (0, -1.8) cm. It also had a cold sphere at (0, 1.8) cm.

Their simulation study showed the time of time-of-flight (TOF) information could alleviate effects of limited angle tomography. They used a three-dimensional list-mode iterative reconstruction algorithm using chronologically ordered subsets, using a relaxed

OSEM update equation (relaxation parameter λ=1) with 33 subsets. This type of image reconstruction method will be briefly discussed in Chapter 3. The crystal size of detectors measured 1×1×10 mm^3. The voxel size of the image space was 0.5×0.5×0.5mm^3.

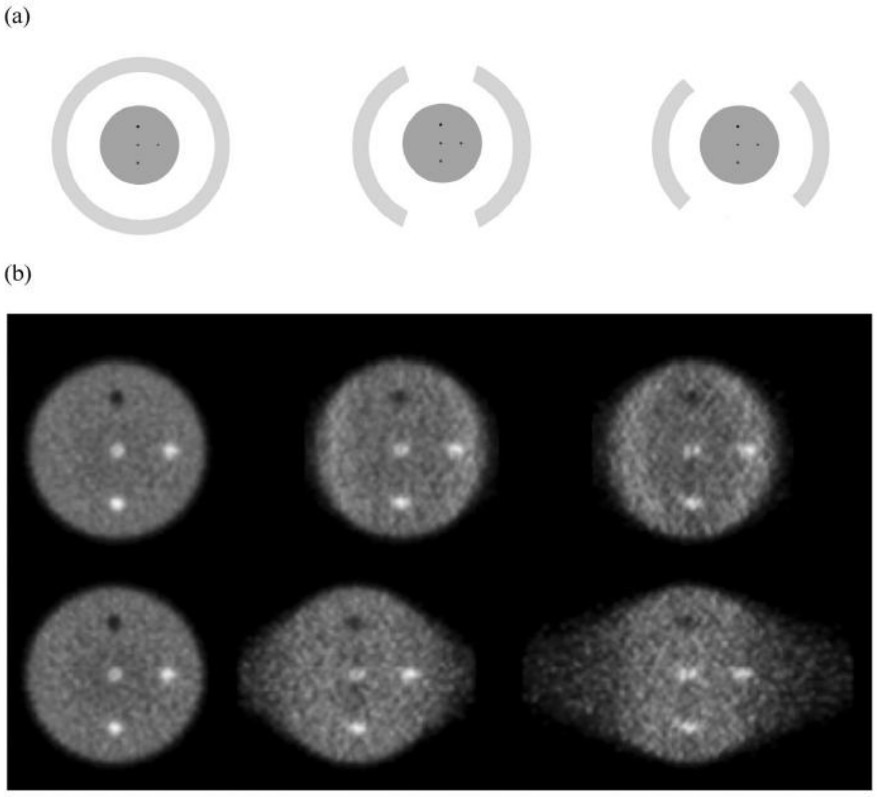

Figure 2-25. Partial ring PET imaging for breast imaging. (a) Schematic of detector arrangement for a full ring, 2/3 ring, and ½ ring scanner. (b) Reconstructed images. The top row shows TOF reconstructed images (timing resolution of 200ps). The bottom shows the non-TOF images. This picture is from [ch2-19, 55].

We note that the center source sphere is still visible without TOF information albeit it is elongated along the horizontal line perpendicular to the pair of detectors. We can expect similar image distortions caused by the intra-operative PET imaging probe system. TOF correction is beyond the scope of this dissertation.

2.2.5.2 Probe position error due to the position tracker

The position and orientation of the PET imaging probe is necessary for image reconstruction. Unfortunately, the position tracker has its own uncertainty. This uncertainty should be considered because the intra-operative PET imaging system has high intrinsic resolution as a result of its very small detector elements.

However, the effects of the position uncertainty due to the position tracker are not addressed in this dissertation but will be reported in future studies.

2.2.5.3 Respiratory Motion

Further loss of probe image resolution will result from organ movement due to respiratory motion [56]. This effect will also need to be addressed in future studies.

2. 2 .6 Ongoing Studies

There are some on-going studies by other research groups that use similar imaging geometries. Two PET systems are briefly reviewed.

2.2.6.1 PET Insert Device for a microPET system

Tai *et al*. have been working on a virtual pinhole PET geometry [57]. Fig. 2-26 shows the PET insert device for a microPET system. The PET insert device operates in coincidence with the outer ring and is rotated around the center to cover 180°.

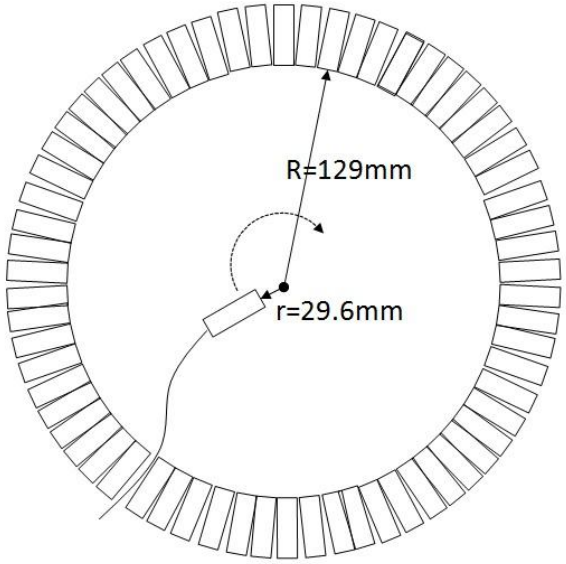

Figure 2-26. PET insert device for a microPET system. This picture was adapted from [57].

2.2.6.2 **Zoom-in mircoPET System**

Qi *et al*. have been working on a zoom-in PET system [58]. Fig. 2-27 shows the zoom-in microPET system using a single high resolution insert. The zoom-in PET system collects both LORs from the ring detector and LORs between the high resolution detector and the ring detector. By using $0.25\times0.25\times20mm^3$ LSO crystals, they claimed that acolinearity, scatters in detector crystals, and positron range would dominate intrinsic spatial resolution.

This imaging geometry was partially inspired by the study in this dissertation. However, the zoom-in microPET system does not use a positron tracker. The high resolution detector has pre-determined positions.

Fig. 2-28 shows the comparison of local impulse response functions of a conventional microPET system and the zoom-in microPET system. The local impulse response of the zoom-in microPET system shows elongation along the longitudinal

direction. However, it shows s narrower *local impulse response* function in the transverse direction.

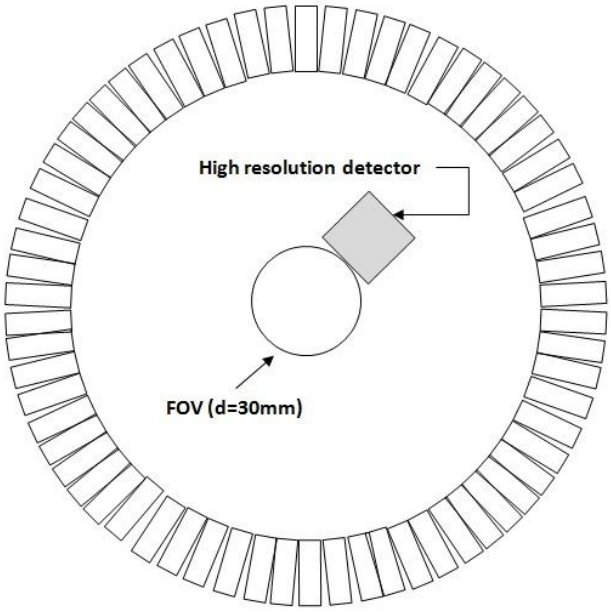

Figure 2-27. Zoom-in microPET system. This picture was adapted from [58].

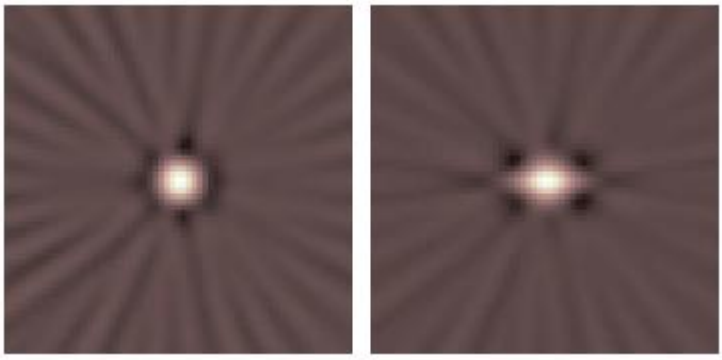

Figure 2-28. Measured *local impulse response function*. Conventional microPET (left) and zoom-in microPET (right). These pictures are from [58]. The zoom-in microPET shows a narrower local impulse response in the vertical direction. The intrinsic resolution of the high resolution detector is 0.25mm.

2. 2 .7 Summary of the intra-operative PET imaging probe system

The intra-operative PET imaging probe system consists of a high spatial resolution PET imaging probe and a relatively low resolution partial ring detector. The PET imaging probe equipped with a position tracker operates in coincidence with the partial ring detector. The PET imaging probe's proximity to the target lesions and the small crystals of the PET imaging probe mainly contribute to obtaining high spatial resolution.

Even though the probe is small, it subtends a large solid angle because it is close to the tumor. On the other hand, the partial ring detector is further away and in general will have greater loss due to attenuation even if the size of the partial ring subtends a fairly large solid angle.

Limited angle tomography is one of the drawbacks of the PET imaging probe system. However, based on local impulse response functions from irregular sampling PET systems, it is expected that the degree of distortion is not severe. Spatial resolution degradation due to limited angle tomography will be also discussed in Chapter 3 (simulated data) and Chapter 5 (measured data).

2 .3 Effects of Background Radiation

Monte Carlo simulations provide fast and efficient ways to understand the proposed imaging system. In particular, we can investigate some physical phenomena that are not easily observed in real experiments. For example, the gamma interactions in simulated phantoms and detectors are not easily observed with limited equipment. By

using Monte Carlo simulations, we can, however, virtually observe each interaction in any part of the imaging system.

We used Geant4 which is written in C++ for Monte Carlo simulations [ch2-23, 59]. We can also incorporate open C++ source codes into the Geant4. Geant4.9 versions include low energy physics for low energy gamma rays, which is useful for medical imaging system simulations.

2. 3 .1 **Monte Carlo Simulation of Positrons**

We are primarily interested in using F-18 FDG as a radio-tracer. F-18 FDG is widely used for PET imaging. The radio-tracer, F-18 FDG, emits a positron. The emitted positron annihilates with an electron nearby, resulting in a pair of two 511keV annihilation photons. The kinetic energy spectrum of positrons from F-18 is continuous because a positron shares the available energy with a neutrino. The positron decay is described in Equation (2.10). F-18 beta decay is briefly described in Equation (2.11).

$$\text{Proton} + \text{energy} \rightarrow \text{neutron} + \text{positron} + \text{neutrino} \tag{2.10}$$

$$^{18}_{9}F \rightarrow {}^{18}_{8}O + n + e^{+} + \nu \tag{2.11}$$

The energy spectra of F-18 positrons were calculated based on the Fermi theory of nuclear β decay as shown in Equation (2.12) [60]. The kinetic energy of simulated positrons was sampled from the continuous distribution at 1keV intervals. Fig. 2-29 shows the superimposition of the sampled theoretic distribution from the Fermi theory and the simulated kinetic energy distribution. The two distributions are superimposed for

comparison. The end-point energy is 635keV and the mean energy is 250keV. The FWHM positron range in water was about 0.16mm from the Monte Carlo simulation using Penelope models in GEANT4 as shown in Fig. 2-30.

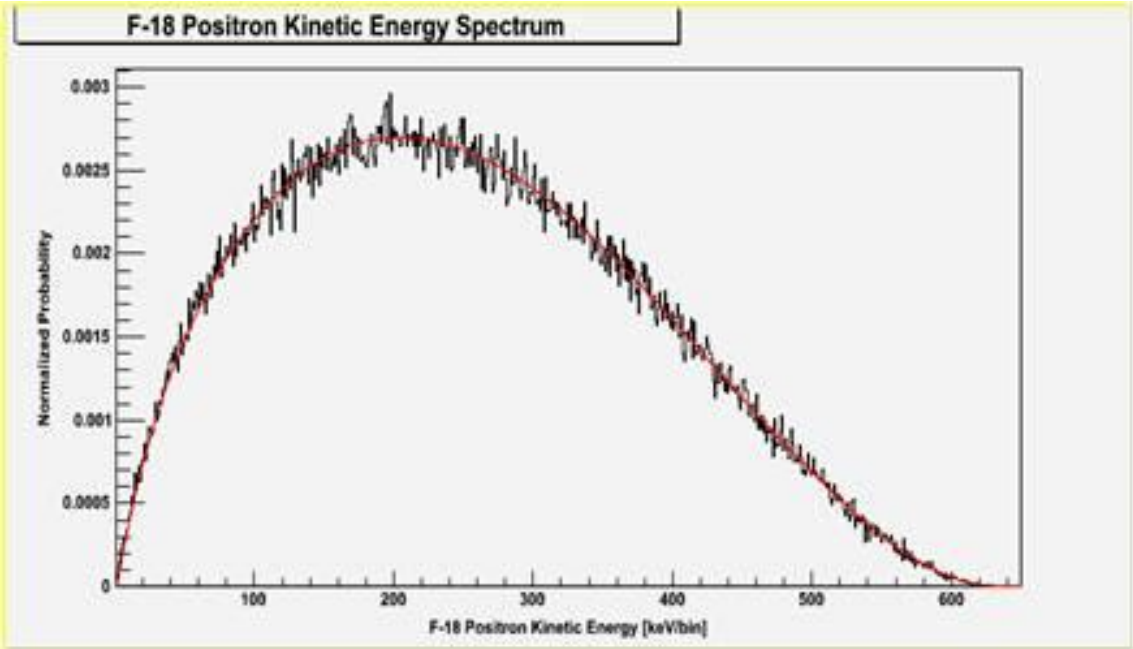

Figure 2-29. Theoretical F-18 positron kinetic energy spectrum (smooth solid line) and the simulated spectrum.

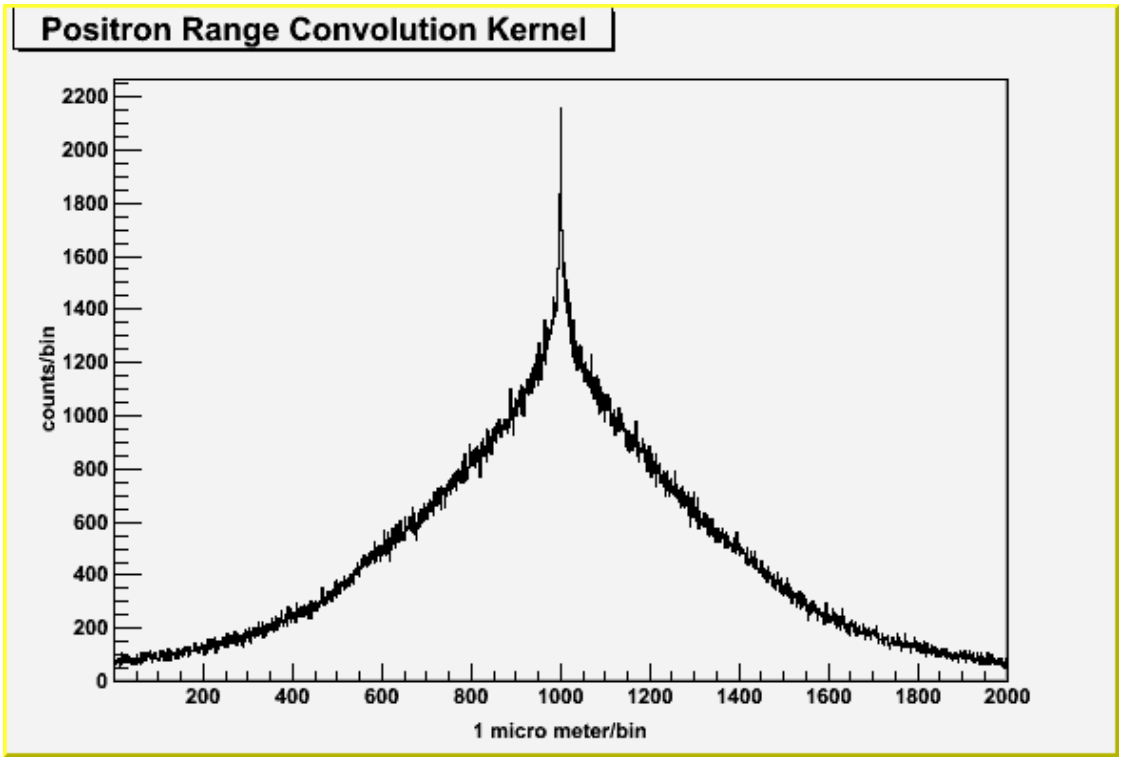

Figure 2-30. Projection of simulated F-18 annihilation locations onto an axis.

$$\frac{dN}{d\gamma} = C\frac{\gamma}{\eta}(\gamma_{max} - \gamma)^2\eta^2 F(Z,\eta) \tag{2.12}$$

where $F(Z,\eta)$ is the factor accounting for the nuclear coulomb potential, $\gamma = E/m = 1 = T/m$, T is the kinetic energy. The term m is the electron rest mass (511keV), Z is the atomic number of the daughter isotope, and C is a constant (for any given Z).

2. 3 .2 Realistic Background Simulations

The radio-tracers that are administered before PET imaging are designed to be localized in tumors. In reality, a large portion of the tracers are also taken up in normal

cells, resulting in background activity. Especially, organ tissues can contain a large portion of the radio-tracers. Furthermore this background also results in increased count rates in the detectors. Fig. 2-31 shows a typical F-18 FDG bio-distribution in the course of time. We can see that the dose ratio in organs slightly changes over time. We note that average F-18 activity (total activity/body volume) for clinical use is roughly 0.13μCi/ml (4.8kBq/ml) [48].

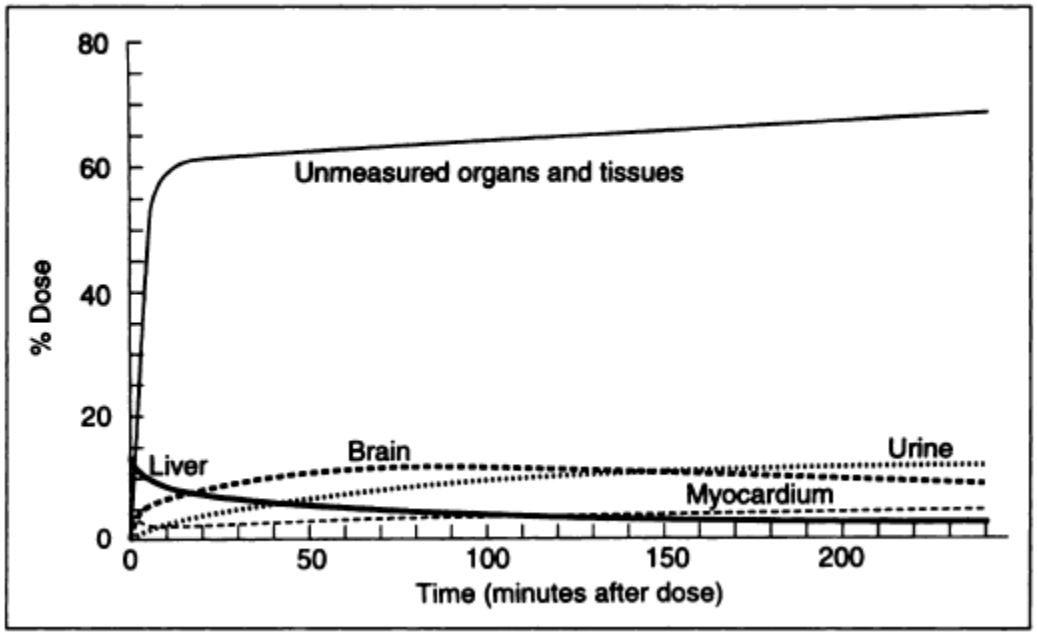

Figure 2-31. Dose percentage of FDG in the course of time. This picture is from [51].

One quantitative method to compare tracer densities is the standard uptake ratio (SUV). The SUV is defined in Equation (2.13).

$$SUV = \frac{uptake(\frac{kBq}{ml})}{injected\ dose(kBq)/patient's\ weight(g)} \tag{2.13}$$

The SUVs in different organs are shown in Table 2-7 and Table 2-8. SUVs in liver are different from the two studies. This is not surprising to researchers because many factors can affect measuring SUVs [52].

Table 2-7. FDG Standard Uptake Values in main organs. This table is from [53].

	Liver	Spleen	Bone marrow	Heart	Lung
Subjects without active malignancy	1.9±0.4	1.6±0.3	1.5±0.3	3.6±2.0	0.5±0.2
Subjects with active primary or metastatic lung cancer P values	2.1±0.4 P < 0.05	1.9±0.8 P < 0.05	1.8±0.3 P < 0.05	3.1±1.5 P = ns	0.5±0.2 P = ns

The characteristics of the gamma ray interactions in patient's body were observed using Monte Carlo simulations. Fig. 2-32 shows the transverse view of the simulation set-up. The anthropomorphic phantom with organ voxels is placed close to the ring detector. A quarter of the ring is used for the partial ring detector for the intra-operative PET imaging probe system. Three quarters of the ring is for future studies. Fig. 2-33 shows the sagittal view of the simulation set-up. Each voxel of the simulated phantom is full of water.

The PET imaging probe points to the area of inguinal lymph nodes in Fig. 2-32. Prostate cancer can spread to the inguinal lymph nodes. Simulated positrons are placed in specific organ voxels for each simulation. The interactions in the anthropomorphic are observed and the deposited energy in the detectors is recorded for analysis. Background radiation from prostate voxels and urine voxels are discussed.

Table 2-8. Standard Uptake Values in organs. This table is from [54].

Variable	Mean (Range)	Male (n=52)	Female (n=48)
Age	53.5	54.2	52.7
Weight (lbs)	131.1	134.6	126.4
FDG (mCi)	13.4	13.6	12.7
	SUV		
Nasopharynx	1.8	1.7	1.8
Tonsil	2.9	2.7	3.0
Parotid gland	1.3	1.5	1.4
Submandibular gland	1.7	1.8	1.7
Tongue	2	1.9	2
Sternocleidomastoid muscle	1.0	1.1	1.0
Thyroid	1.7	1.5	1.9
Lung	0.6	0.5	0.6
Hilum	1.1	1.0	1.2
Aorta	2.0	1.8	2.2
Inferior vena cave	1.9	1.8	2.0
Myocardium	3.0	2.4	3.7
Liver	2.8	2.7	2.9
Gall bladder	1.6	1.5	1.8
Spleen	2.3	1.8	2.0
Pancreas	1.7	1.5	1.9
Stomach	2.1	2.0	2.1
Caecum	1.9	1.6	2.3
Ascending colon	1.8	1.8	2.2
Transverse colon	1.8	1.5	2.1
Descending colon	1.6	1.5	1.8
Sigmoid colon	1.7	1.7	1.8
Rectum	2.0	1.8	2.3
Prostate	1.1 ~ 3.4	2.2	
Testis	1.5 ~ 4.6	3.0	

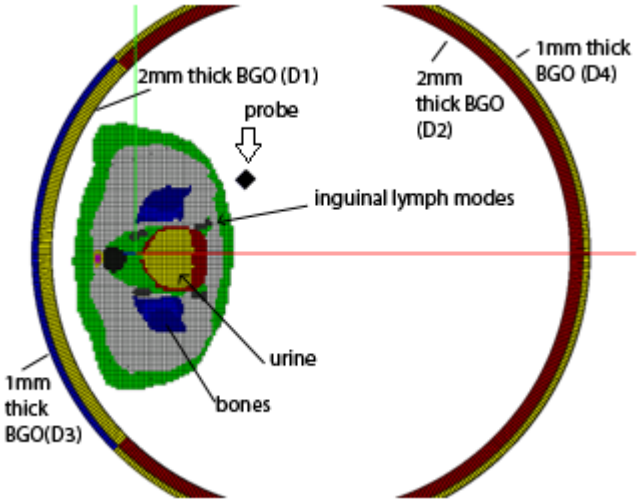

Figure 2-32. Transverse view of an anthropomorphic and the probe system. The probe points to the area of inguinal lymph nodes. D1 and D3 (a quarter of the ring detector) are for the PET imaging probe system. D2 and D4 are for the future studies. D1 is 2mm thick BGO crystals and D3 is 1mm thick BGO crystals (a total of 3mm thick).

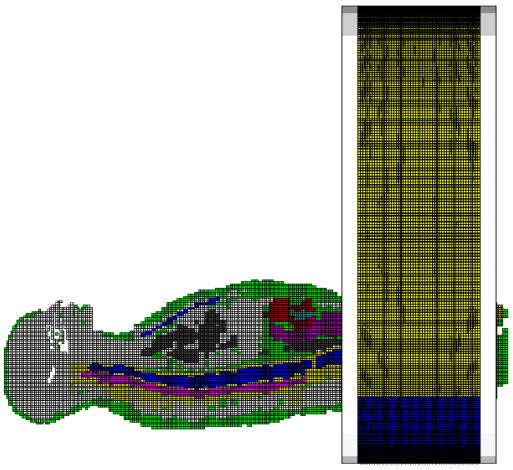

Figure 2-33. Sagittal view of the set-up. Tungsten shielding on either side of the ring detector is also included. Each tungsten shield measures 30mm thick and 30mm wide.

2.3.2.1 **Prostate Voxels**

The prostate has 438 voxels in the Zubal phantom. 10,000 simulated positrons were generated in each voxel of the prostate. The inner ring of the ring detector has 20mm thick BGO crystals. The outer ring is comprised of 10mm thick BGO crystals. The total thickness of the inner and outer rings is 30mm. We analyzed the data from detector 1 (D1) for the intra-operative PET imaging probe system. Data for 30mm thick BGO crystals can be obtained by collecting interactions both in detector 1 (D1) and in detector 3 (D3). Detector 2 (D2) and detector 4 (D4) are for future studies. The total number of positrons that are simulated is 10,000×438 (4,380,000 positrons). The total number of 511keV gamma rays from all the annihilation is 4,380,000×2 (8,760,000 gamma rays).

The interactions inside the anthropomorphic phantom were observed to categorize the data into two parts: gamma rays that are *not scattered* inside the anthropomorphic phantom and gamma rays that are *scattered* inside the simulated phantom. Scattered gamma rays refer to the gamma rays that have at least one interaction inside the phantom before escaping the phantom. Un-scattered gamma rays refer to the gamma rays that have no interaction inside the phantom before escaping the phantom.

Fig. 2-34 shows the deposited energy in D1 from gamma rays that escaped the phantom without interactions. The unscattered incident gamma rays have 511keV energy. The detector response function for BGO was not included. Not all incident gamma rays are detected in D1 because we used 20mm thick crystals that do not stop all the incident 511 keV gamma rays. Since the incoming gamma rays are 511keV, we can see the 511keV photo peak in the spectrum. Part of the detected incident gamma rays are scattered in D1. The expanded energy spectrum below 511 keV is shown in Fig. 2-35.

The two peaks to the left of the 511keV peak are K-shell X-ray escape peaks in BGO (refer to Fig. 2-36). The Compton edge is around 340keV.

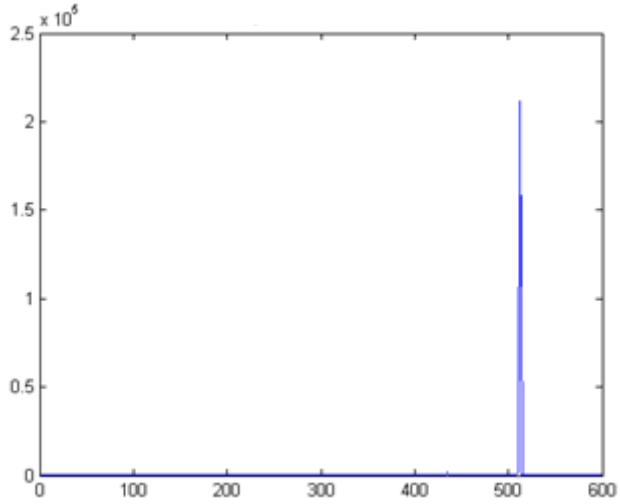

Figure 2-34. Energy spectrum in the detector 1 from detected incoming gamma rays that have no interaction before escaping the phantom. The detector response function for BGO was not included. The horizontal scale is in keV.

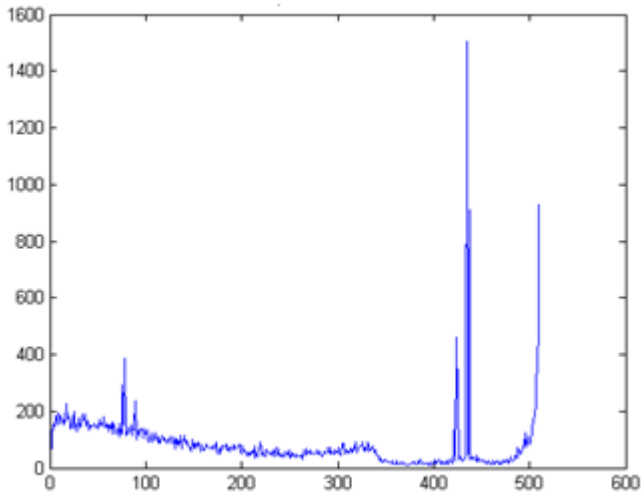

Figure 2-35. Expanded-in view of the left hand side of the photo peak (<511keV) of the energy spectrum shown in Fig. 2-34. The detector response function for BGO was not included. The horizontal scale is in keV.

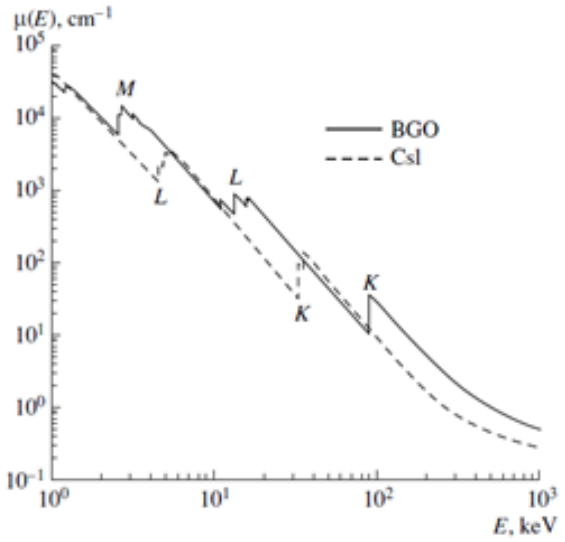

Figure 2-36. Linear radiation-absorption coefficients for BGO (solid line) and CsI (dashed line). This picture is from [65].

The deposited energy distribution in the detector 1 from the scattered-then-incoming gamma rays that have at least one interaction before escaping the phantom is shown Fig. 2-37. Since the energy of these gamma rays is less than 511keV, we do not see the 511keV photo peak. The sum of the deposited energy from scattered and un-scattered gamma rays is shown Fig. 2-38. The far left hump is due mainly to scattered incident gamma rays.

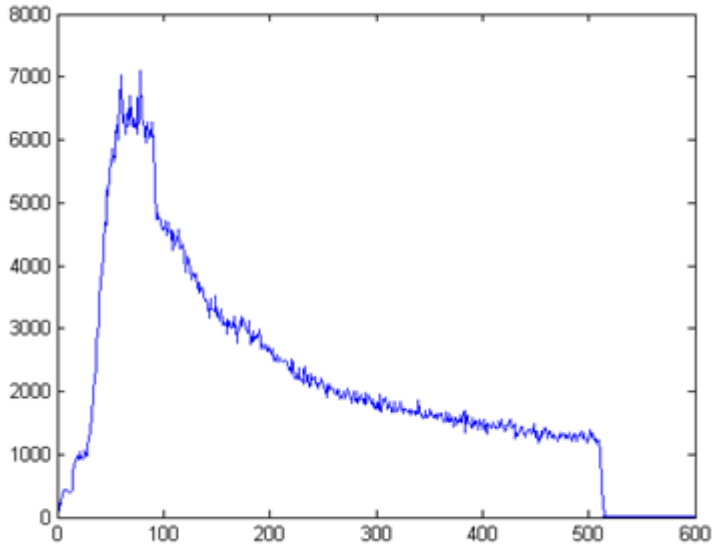

Figure 2-37. Deposited energy spectrum from detector 1 from scattered incoming gamma-rays that have at least one interaction before escaping the phantom. The horizontal scale is in keV.

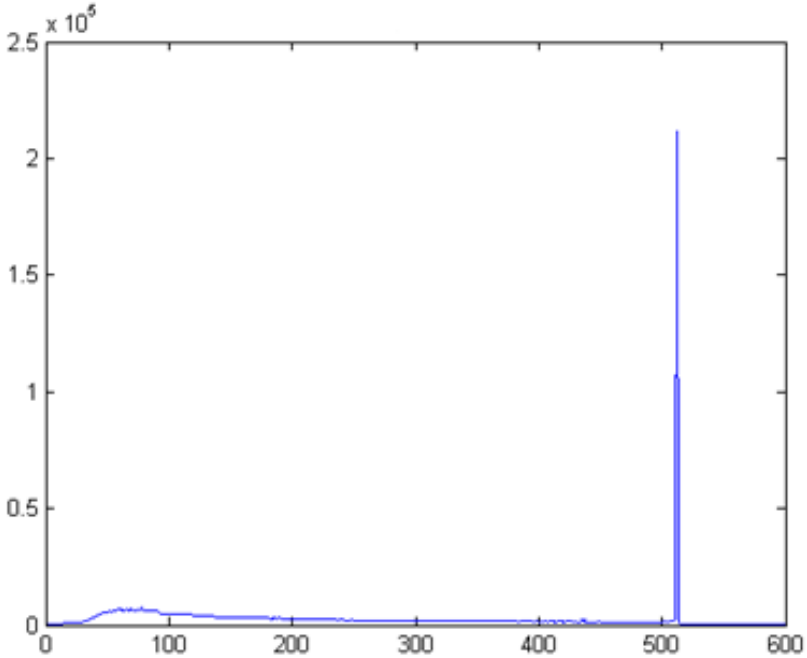

Figure 2-38. Sum energy spectrum from the detector 1 from all the gamma rays that escaped the phantom without interactions. The low energy bump is almost the same as the deposit energy spectrum in Fig 2-37. The horizontal scale is in keV.

Table 2-9 shows the detection of the unscattered incident gamma rays and scattered incident gamma rays in the detector 1. About 85% of the detected events are from gamma rays that have been scattered in phantom. The BGO detector has limited energy resolution. Typical energy resolution of BGO at 511 keV is around 10% [ch2-30, 66] and can be worse. When 10% energy resolution is used, the energy spectrum is shown in Fig. 2-39. A more realistic BGO energy resolution for a BGO PET imaging system could be as poor as 20% [67].

Table 2-9. Detected gamma rays in the BGO detector 1.

	D1	detection efficiency out of 8,760,000 gammas
Un-scattered incident gamma rays	259523 counts	2.95%
Scattered incident gamma rays	1258685 counts	14.35%
total	1518208 counts	17.3%

Table 2-10. BGO energy resolution. This table is from [68].

	NaI(Tl)	CsI(Tl)	GSO(Ce)	BGO
Desnsity (g/cm3)	3.67	4.51	6.71	7.13
Radiation length (cm) at 511keV	2.59	1.85	1.38	1.12
Decay constant (ns) (fast/slow) (ratio)	230	700/7000 (20/1)	56/600 (7/1)	60/300 (1/10)
Peak emission (nm)	415	560	430	480
Light Output (relative)	100	145	20-25	12-16
Index of refraction	1.85	1.8	1.85	2.15
Hygroscopic	strong	slight	no	no
Melting point	651	621	1900	1050
Hardness (Mho)	2	2	5.7	5
Cleavage	(100)	none	(100)	none
Radiation hardness to low energy gamma (rad)	10^{3}	10^{6-7}	10^{9}	10^{5-7}
Dopant concentration (%)	0.1 – 0.2	0.067	0.5	-
Energy resolution (%) to C-137[c]	7.0	9.0	7.8	***9.5***
Effective atomic number	51	54	59	74
Chemical formula	NaI	CsI	Gd_2SiO_2	$Bi_4(GeO_4)_3$

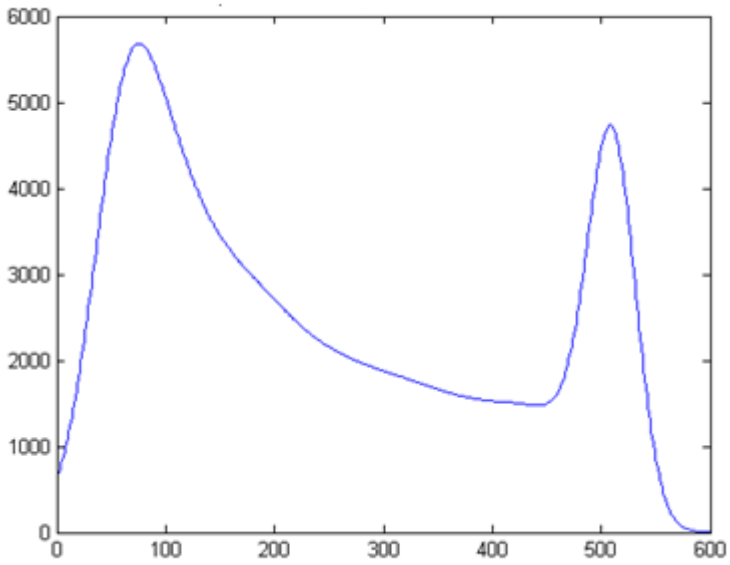

Figure 2-39. Deposited energy spectrum in detector 1. The energy resolution was set to 10%. Both scattered and unscattered gamma rays were included. The horizontal scale is in keV.

Comparing Fig. 2-37 and Fig. 2-39 indicates that the contribution of scattered gamma rays to the peak at 511keV can be estimated by extrapolating the tail of the scattered gamma ray spectrum. From this observation, we can estimate how much portion of the photo-peak is from scattered-then-incoming gamma rays.

2.3.2.2 **Urine Voxels**

The number of urine voxels in Zubal phantom is 6,596. In order to obtain gamma rays, 10,000 simulated positrons were generated in each urine voxel. Fig. 2-40 shows the deposited energy spectrum in the detector D1 from the scattered incident gamma rays. The general outline of the spectrum is almost identical to that observed for the prostate.

Fig. 2-41 shows the deposited energy spectrum in the detector D1 from urine for both scattered and unscattered gamma rays.

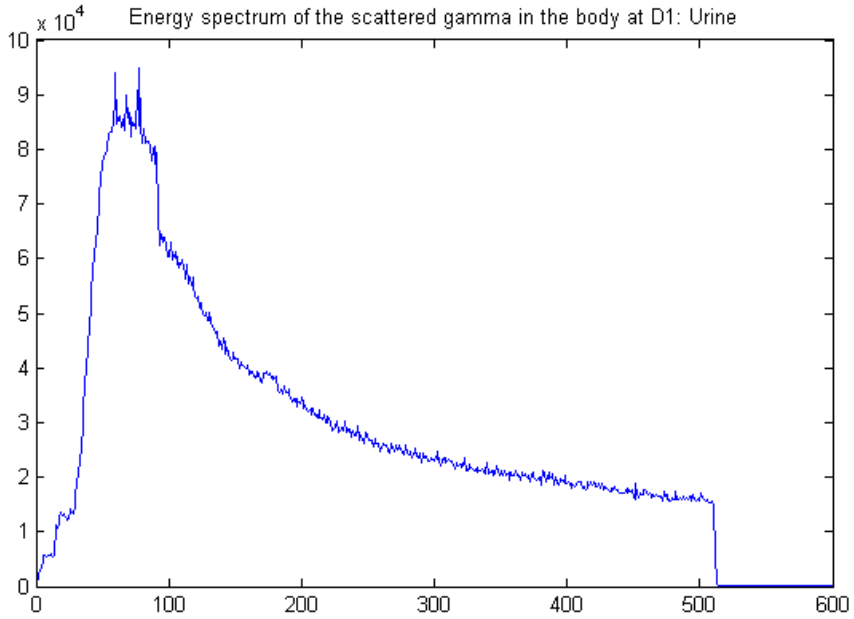

Figure 2-40. Deposited energy spectrum in the detector D1 from the scattered gamma rays. The horizontal scale is in keV.

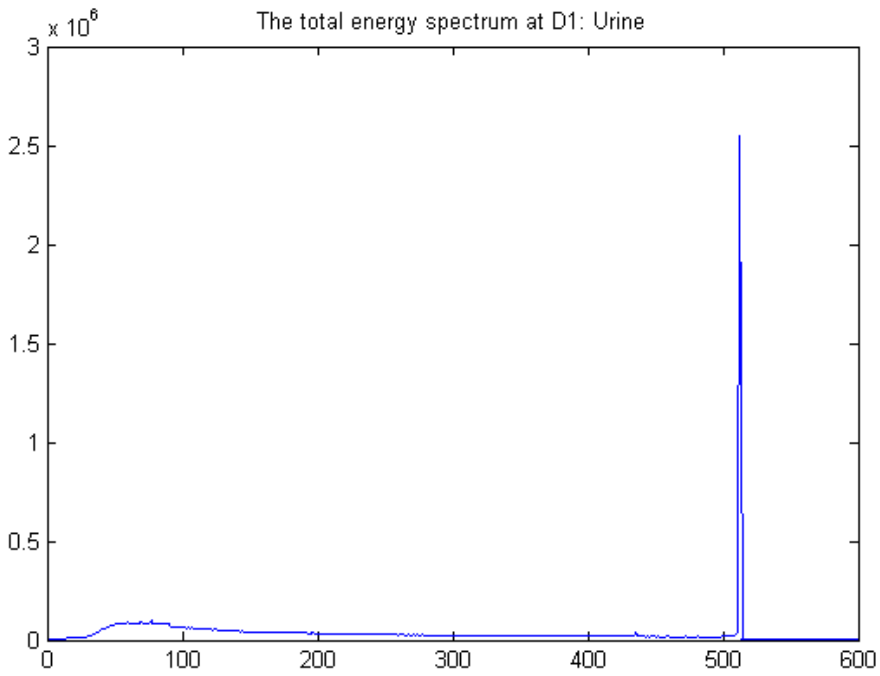

Figure 2-41. Deposited energy spectrum in the detector D1 from all the gamma rays from urine that escaped the phantom with or without interactions. The horizontal scale is in keV.

Table 2-11 shows the detected gamma rays in the detector 1 (D1). Interactions of incoming 511keV gamma rays in D1 comprise roughly 16% of all gamma ray interactions.

Table 2-11. Detected gamma rays originated from urine voxels.

	D1	detection efficiency out of 131920000 gammas
Unscattered incident gamma rays	3125156 counts	2.3%
Scattering incident gamma rays	16387500 counts	12.4%
total	19512656 counts	14.7%

2. 3 .3 **Summary of effects of background radiation**

The effect of background simulation was investigated using Monte Carlo simulations when the PET imaging probe pointed to inguinal lymph nodes. About 80 % of the detected gammy rays in the partial ring detector were comprised of gamma rays that had at least one interaction inside the phantom before escaping the phantom.

2 .4 **Summary**

In this chapter, we described the intra-operative PET imaging probe system in the first half. The proposed PET imaging probe system can obtain high spatial resolution in the longitudinal direction. However the effects of limited angle tomography should be addressed. In the second half, effects of background radiation were discussed using Monte Carlo simulations.

Chapter 3
Iterative Image Reconstruction Using a Row-Action ML Algorithm, One-Pass List-Mode Ordered Subsets EM, and a Gaussian Back-projection Kernel for Real Time Image Update.

In this chapter, a row action ML algorithm, which converges to the ML solution, is modified for real time image reconstruction. A one-pass list-mode EM algorithm is combined with the row action ML algorithm in order to minimize the number of iterations. In addition, a Gaussian back-projection kernel is integral to the image update equation. The subset size, i.e., the number of LORs in each subset, is relatively small compared to conventional OSEM. The proposed image update algorithm is tested using simulated data and a graphics processing unit (GPU). GPU programming is discussed in Chapter 4.

3 .1 Conventional Ordered Subsets MLEM for Bin-Mode Data/Sinogram

3. 1 .1 MLEM

Iterative update algorithms that include photon attenuation, scatter, and detector blurring [ch3-1, 68] became feasible as computation speed and computing algorithms are faster than before. Fig. 3-1 shows main steps for a typical iterative maximum likelihood (ML) image reconstruction algorithm.

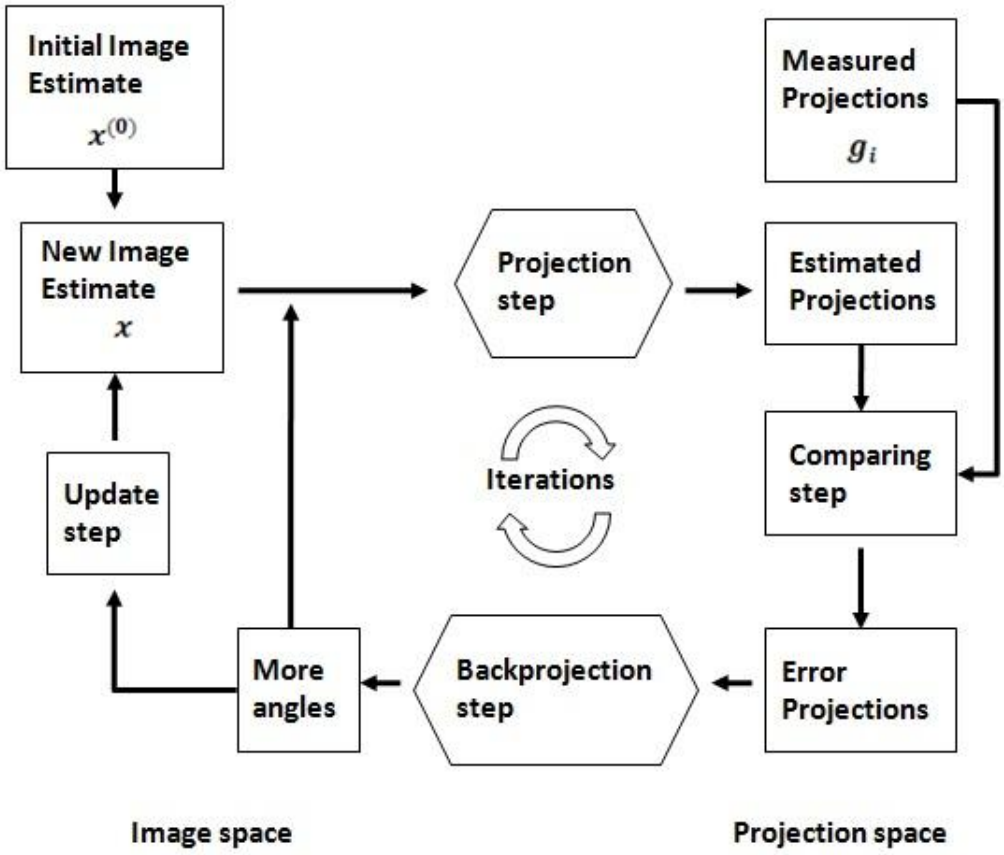

Figure 3-1. Typical iterative image reconstruction procedure. This flow diagram was adapted from [68].

3. 1 .2 **OSEM**

As can be seen in Fig. 3-2, forward projections and backward projections are performed over all the projection views in MLEM [69]. On the contrary, the projection views are divided into subsets in OSEM. Therefore each subset contains finite number of projection views. Image is then updated based on subsets. As a result, OSEM has a faster initial convergence rate than a conventional MLEM algorithm. The original OSEM algorithm is shown Fig. 3-3 [70]. We can notice that the update loop is nested in another

loop in Fig. 3-3. In conventional OSEM, each subset contains more than 1 projection view in order to avoid poor signal to noise ratios.

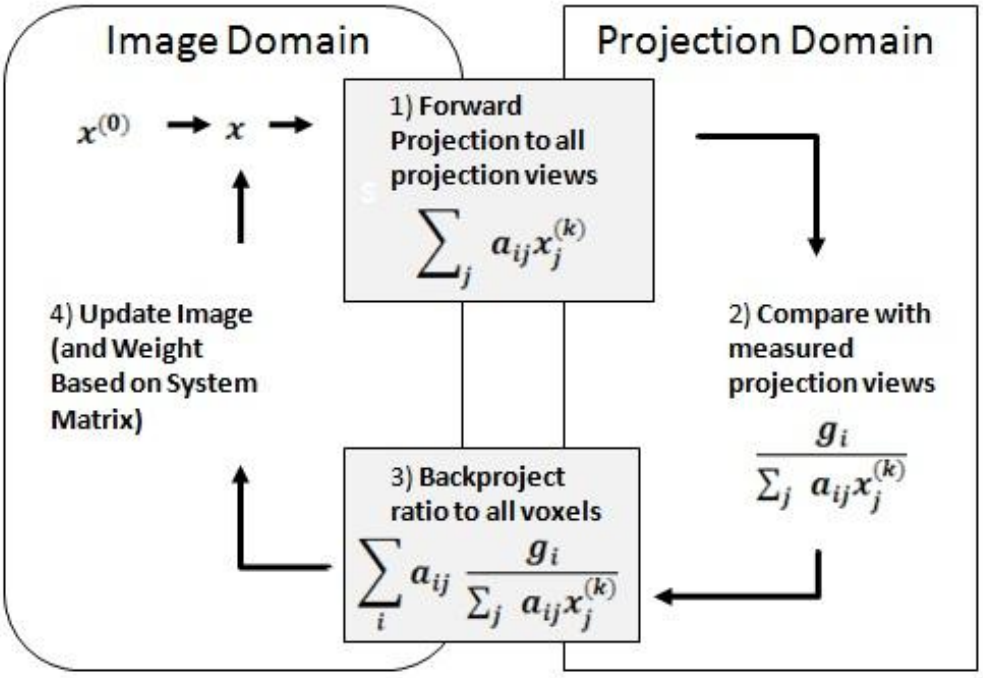

Figure 3-2. MLEM flow diagram. This picture was adapted from [69].

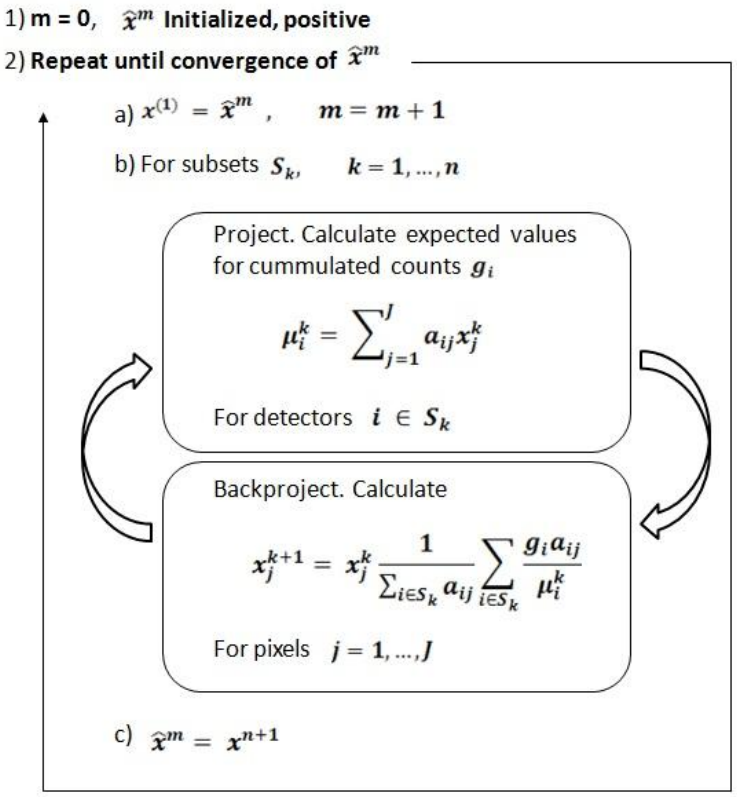

Figure 3-3. OSEM algorithm. The picture was adapted from [70].

The acceleration of convergence becomes faster as the number of subsets increases. Fig. 3-4 shows the reconstructed images of MLEM and OSEM with respect to the number of iterations. The number of iterations is not a pre-determined number, but two iterations are recommended for OSEM as the rule of thumb [68]. It was also reported that less than 4 projections in each subset could result in poor signal to noise ratio in OSEM [71] [72].

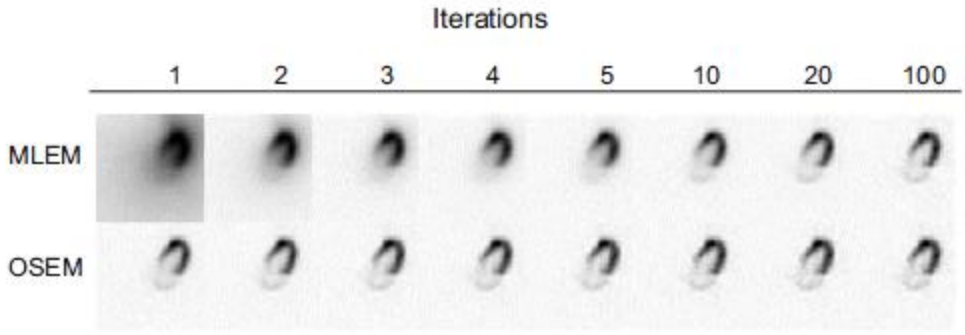

Figure 3-4. The upper row is from MLEM and the lower row is from OSEM. The number of subsets is not disclosed in [68]. The reconstructed images are shown with respect to the number of iterations. This picture is from [68].

3. 1 .3 **Convergence Problems**

Browne *et al*. used a simple *inconsistent* system to show conventional OSEM is not convergent to the ML solution [73].

$$\begin{cases} 0.5x_1 + x_2 = 1 \\ 0.5x_1 + x_2 = 2 \end{cases} \tag{3.1}$$

The likelihood function under Poisson distribution assumption is given in Equation (3.2) [74, Chapter 6].

$$\sum_{i=1}^{I}\left(\left(\sum_{j=1}^{J} a_{i,j}x_j\right) - g_i \ln\left(\sum_{j=1}^{J} a_{i,j}x_j\right)\right) \tag{3.2}$$

where $a_{i,j}$ are elements of the system matrix and the g_i are the measurement.

We take the derivative of $L(x_1, x_2) = 3ln(0.5x_1 + x_2) - 2(0.5x_1 + x_2)$ and set it to zero, resulting in Equation (3.3).

$$x_1 + 2x_2 = 3 \tag{3.3}$$

OSEM uses one equation at one time. $[2\ 1]^T$ satisfies the second equation and $[4\ 2]^T$ is then used in an attempt to satisfy Equation (3.3). However these two solutions do not satisfy Equation (3.3). As a result, the attempted solution alternates between $[2\ 1]^T$ and $[4\ 2]^T$.

3 .2 Efficient Estimates Update Considering One Measurement at One Time: Projection-by-Projection Reconstruction

Algebraic Reconstruction Techniques (ARTs) originated from the work of Kaczmarz to solve linear systems of equation. The modified ART was then applied to image reconstruction [75]. The modified ART is briefly reviewed because the row-action ML algorithm was inspired by the modified ART and the relaxed ART is relatively easier to discuss.

3. 2 .1 Relaxation Parameter

Measurements without additive noise are given by Equation (3.4) [74, Chapter 6].

$$g = Ax \tag{3.4}$$

Each equation in Equation (3.4) forms a hyper-plane H_i .

$$H_i = \{x \in R^n \mid \langle a_i, x\rangle = g_i\} \tag{3.5}$$

The Kaczmarz's algorithm to find the solution using the hyper-planes is given in Equation (3.6) [75].

$$x^{k+1} = x^k + \frac{g_i - \langle a_i, x^k\rangle}{\langle a_i, a_i\rangle} a_i \tag{3.6}$$

The hyper-planes $\langle a_i, x\rangle = g_i$ in Equation (3.5) can be scaled without modifying the hyper-planes. Strohmer and Vershunin stated that generally the sequence $\{x_k\}$ converges to the solution of $Ax = g$ [75].

Herman *et al* applied Kaczmarz's algorithm to image reconstruction. The measurement is given by Equation (3.7) [74, Chapter 6].

$$g = Ax + e \tag{3.7}$$

where the term g is the measurement vector and the term e is the error vector and the term A is the system matrix.

One possible approach, stated by Herman, is to assume that error is bounded.

$$-\epsilon_i \leq g_i - \sum_{j=1}^{J} a_{i,j}\hat{x}_j \leq \epsilon_i \tag{3.8}$$

where $a_{i,j}$ are elements of the system matrix.

We may also impose a non-negative constraint on x_j. We can then use new notations to explicitly represent x_j under the conditions of Equation (3.8) and non-negativity.

$$\sum_{j=1}^{J} n_{i,j}\hat{x}_j \leq q_i \tag{3.9}$$

where the n_i are given J-dimensional vectors and the q_i are given real numbers. $\langle n_i, n_i \rangle \neq 0$.

A question is how to find X_i given in Equation (3.10).

$$X_i = \{x \mid \langle n_i, x\rangle \leq q_i\} \tag{3.10}$$

Since a scaled ART can be used to find solution of Equation (3.11) in terms of hyper-planes H_i.

$$H_i = \{x \in R^n \mid \langle n_i, x \rangle = q_i\} \tag{3.11}$$

Herman *et al*. used a version of the scaled ART in order to obtain the solution of Equation (3.9).

$$\begin{aligned} x^{(k+1)} &= \beta_k(x, n_{ik}, q_{ik}) \\ &= \begin{cases} x^k, & if\ \langle n_{ik}, x^k \rangle \leq q_{ik}, \\ x^k + \lambda^{(k)} \dfrac{q_{ik} - \langle n_{ik}, x^k \rangle}{\langle n_{ik}, n_{ik} \rangle} n_{ik}, & otherwise \end{cases} \end{aligned} \tag{3.12}$$

Here, we can get back to the previous notations for practical purpose because we can confine the sequence $\{x^k\}$ to positive numbers during iterations and the error $(g_i - \sum_{j=1}^{J} a_{i,j} x_j)$ is implicitly restricted to a small value. The update equation using typical notiations is given Equation (3.13). Implicit assumptions of non-negativity and bounded error are embedded in Equation (3.13).

$$x_j^{(k,i)} = x_j^{(k,i-1)} + \lambda^{(k)} \frac{g_i - \sum_{v=1}^{J} a_{i,v} x_v^{(k,i-1)}}{\sum_{v=1}^{J} \left(a_{i,v}\right)^2} a_{i,j} \tag{3.13}$$

where g_i is the measurements and a_{ij} are line intersections between the measurement *i* and the pixel *j*. The term *k* is the number of iterations over the whole data.

By using the same notations, a typical MLEM algorithm is described by

$$x_j^{(k)} = \frac{x_j^{(k-1)}}{\sum_{i=1}^{I} a_{i,j}} \left(\sum_{i=1}^{I} \frac{a_{i,j}\, g_i}{\sum_{v=1}^{J} a_{i,v} x_v^{(k-1)}} \right) \tag{3.14}$$

The MLEM can be rewritten into Equation (3.11) [76].

$$x_j^{(k)} = x_j^{(k-1)} + \frac{x_j^{(k-1)}}{\sum_{v=1}^{I} a_{v,j}} \frac{\partial L_y(x)}{\partial x_j}\bigg|_{x^{(k-1)}} \tag{3.15}$$

$$\frac{\partial L_y(x)}{\partial x_j} = \sum_{i=1}^{I} a_{i,j} \left(\frac{g_i - \sum_{v=1}^{J} a_{i,v} x_v}{\sum_{v=1}^{J} a_{i,v} x_v} \right) \tag{3.16}$$

When we compare the modified ART and MLEM, we can notice the modified ART updates estimates after each measurement. The MLEM algorithm updates estimates using the whole projection views.

3. 2 .2 **Data Accessing Order**

Herman *et al*. subdivided the LORs into either parallel beam subsets or divergent beam subsets [77]. By using this subdivision, they tended to make LORs in each subset as independent as possible. However the proof of this scheme has not been explained mathematically. This data accessing order is similar to the subset ordering in conventional OSEM.

3. 2 .3 **Row-Action Methods**

We can notice we don't need the whole $a_{i,j}$ in Equation (3.13). The update equation using ART uses only non-zero $a_{i,j}$. The $a_{\mathrm{i,j}}$ is the line intersection between the measurement *i* and the pixel *j*. Roughly speaking, we need one row of the system matrix *R* to update the estimates. This is why the algorithm is called a *row-action method* [74, chapter 11].

3. 2 .4 **Review of Convergence**

The convergence of the relaxation method is briefly reviewed because this convergence is one of its unique characteristics [74, chapter 15]. In addition, it is simpler than the discussion on the convergence of row-action ML. Equation (3.13) is shown as part of the proof of convergence. For further details, refer to [74, chapter 15].

$$\lim_{k\to\infty} \left\| x^{(k+1)} - x^{(k)} \right\|^2 = 0 \tag{3.17}$$

Using the definition of Equation (3.9) and the second of Equation (3.12), we have Equation (3.18). We use the notations of n_i and q_i in order to explicitly show the assumptions of non-negativity and bounded error.

$$\begin{aligned} \langle n_{ik}, x^{(k+1)} \rangle &= \langle n_{ik}, \beta_k\left(x^{(k)}, n_{ik}, q_{ik}\right) \rangle \\ &= \langle n_{ik}, x^{(k)} \rangle \\ &+ \lambda^{(k)} \frac{q_{ik} - \langle n_{ik}, x^{(k)} \rangle}{\langle n_{ik}, n \rangle} \langle n_{ik}, n_{ik} \rangle \end{aligned} \tag{3.18}$$

$$X_i = \{x \mid \langle n_i, x \rangle \leq q_i\} \tag{3.19}$$

$$X = \bigcap_{i=1}^{P} X_i \tag{3.20}$$

The term λ is bounded as in Equation (3.21).

$$0 < \tau_1 \leq \lambda^{(k)} \leq \tau_2 < 2 \tag{3.21}$$

By using Equation (3.12), we have Equation (3.22).

$$\begin{aligned} \left\|x^{(k+1)} - x^{(k)}\right\|^2 & \\ &= \left\|\left(x^{(k)} + \lambda^{(k)} \frac{q_{ik} - \langle n_{ik}, x^{(k)}\rangle}{\langle n_{ik}, n_{ik}\rangle} n_{ik}\right) - x^{(k)}\right\| \\ &= \left\|\lambda^k \frac{q_{i,k} - \langle n_{ik}, x^{(k)}\rangle}{\|n_{ik}\|^2} n_{ik}\right\|^2 \\ &= \left(\lambda^{(k)}\right)^2 \frac{\left(q_{ik} - \langle n_{ik}, x^{(k)}\rangle\right)^2}{\|n_{ik}\|^2} \end{aligned} \tag{3.22}$$

Let θ be any vector that satisfies Equation (3.19).

$$\begin{cases} \langle n_{ik}, \theta\rangle \leq q_{ik} \\ \langle n_{ik}, x^{(k)}\rangle > q_{ik} \end{cases} \tag{3.23}$$

We use Equation (3.24) to show the sequence $\left\|x^{(k)} - \theta\right\|$ is not increasing.

$$\begin{aligned} \left\|x^{(k+1)} - \theta\right\|^2 &= \left\|x^{(k+1)} - x^{(k)} + x^{(k)} - \theta\right\|^2 \\ &= \left\|x^{(k+1)} - x^{(k)}\right\| \\ &+ 2\langle x^{(k+1)} - x^{(k)}, \quad x^{(k)} - \theta\rangle \\ &+ \left\|x^{(k)} - \theta\right\|^2 \end{aligned} \tag{3.24}$$

The second term in Equation (3.24) can be rewritten into Equation (3.25) by using Equation (3.12) and Equation (3.23).

$$
\begin{aligned}
&\langle x^{(k+1)} - x^{(k)}, x^{(k)} - \theta \rangle \\
&= \lambda^{(k)} \frac{q_{ik} - \langle n_{ik}, x^{(k)} \rangle}{\|n_{ik}\|^2} \langle n_{ik}, x^{(k)} - \theta \rangle \\
&\leq \lambda^{(k)} \frac{q_{ik} - \langle n_{ik}, x^{(k)} \rangle}{\|n_{ik}\|^2} \left(\langle n_{ik}, x^{(k)} \rangle - q_{ik} \right) \\
&= -\lambda^{(k)} \frac{\left(q_{ik} - \langle n_{ik}, x^{(k)} \rangle \right)^2}{\|n_{ik}\|} \\
&= -\frac{1}{\lambda^{(k)}} \left\| x^{(k+1)} - x^{(k)} \right\|^2
\end{aligned}
\tag{3.25}
$$

We can insert Equation (3.25) into Equation (3.24).

$$
\begin{aligned}
&\left\| x^{(k+1)} - \theta \right\|^2 \\
&\leq \left(1 - \frac{2}{\lambda^{(k)}} \right) \left\| x^{(k+1)} - x^{(k)} \right\|^2 \\
&+ \left\| x^{(k)} - \theta \right\|^2
\end{aligned}
\tag{3.26}
$$

The $\left(\frac{2}{\lambda^{(k)}} - 1 \right)$ is positive since we have Equation (3.21).

$$
\begin{aligned}
&\left\| x^{(k+1)} - \theta \right\|^2 + \left(\frac{2}{\lambda^{(k)}} - 1 \right) \left\| x^{(k+1)} - x^{(k)} \right\|^2 \\
&\leq \left\| x^{(k)} - \theta \right\|^2
\end{aligned}
\tag{3.27}
$$

From Equation (3.27), we can notice the sequence $\left\| x^{(k)} - \theta \right\|$ is decreasing. Therefore Equation (3.27) implies Equation (3.17).

3 .3 **ART for Digital Tomosynthesis**

The Algebraic Reconstruction Technique (ART) was used to reconstruct one slice of a 3D image from limited angle projections covering less than ±30° [78]. In the same way, three dimensional images from limited angle projections can be obtained in CT and this process is referred to as Tomosynthesis [79]. Fig. 3-5 shows the illustration of typical digital Tomosysnthesis.

ART with a weight matrix for ray projection was proposed [79]. The weight matrix seems to take the place of the de-blurring process of conventional Tomosynthesis algorithms. Therefore post-processing is not required in the modified ART.

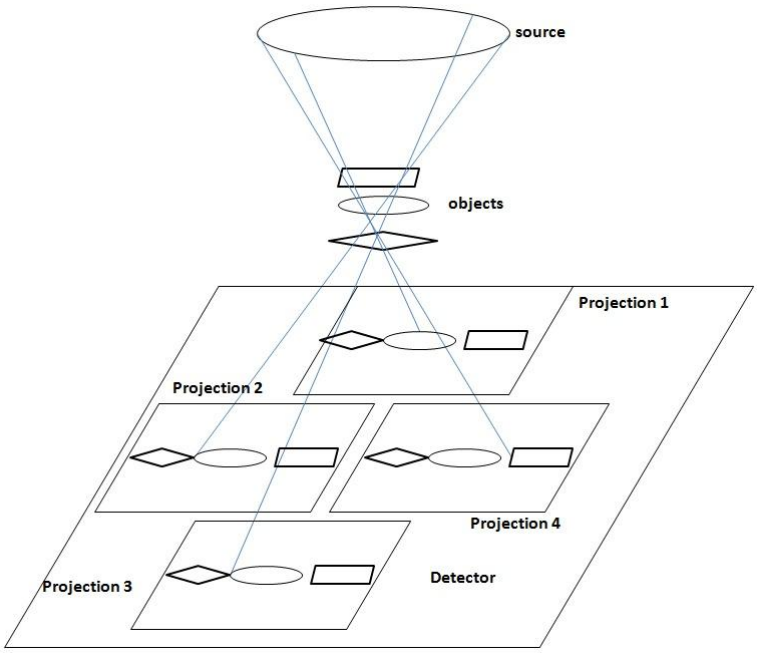

Figure 3-5. Illustration of Tomosynthesis. This picture was adapted from [79].

3 .4 One-Pass List Mode Expectation Maximization Algorithm (OPL-EM)

3. 4 .1 OPL-EM

The conventional bin mode MLEM is described in Fig. 3-6 [80]. List mode MLEM can be derived from a bin mode MLEM algorithm [81]. The term *n* is the total bin numbers in Equation (3.28). The term *j* is the number of voxels in image space. The g_i are the measured number of LORs in the bin *i*. The a_{ij} are elements of a system matrix. The current estimate term, $\sum_{j=1}^{m} a_{ij} x_j^{(k)}$, is represented as $\mu_i^{(k)}$ in Equation (3.28) [81].

$$\text{Image}^{(k+1)} = \text{Image}^{(k)} \times \text{Normalized Backprojection of} \left[\frac{\text{Measured Projections}}{\text{Projections of Image}^{(k)}} \right]$$

Figure 3-6. Interpretation of the conventional MLEM algorithm. This picture was adapted from [80].

$$x_j^{(k+1)} = \frac{x_j^{(k)}}{\sum_{i=1}^{n} a_{ij}} \left(\sum_{i=1}^{n} \frac{g_i}{\mu_i^k} a_{ij} \right), with\ \mu_i^k = \sum_{j=1}^{m} a_{ij} x_j^k \qquad (3.28)$$

The bin mode update equation in Equation (3.28) can be converted into a list mode update equation that is obtained by removing the bin term *n*. The bin *i* contains g_i LORs in Equation (3.28). Therefore we have a total of $L = \sum_{i=1}^{n} g_i$ LORs. We are interested in each LOR, rather than the number of LORs in a bin. Equation (3.28) can be rewritten as in Equation (3.29) [81].

$$x_j^{(k+1)} = \frac{x_j^{(k)}}{\sum_{i=1}^{n} a_{ij}} \left(\sum_{i=1}^{L} \frac{1}{\mu_i^k} a_{ij} \right), with\ \mu_i^k = \sum_{j=1}^{m} a_{ij} x_j^k \qquad (3.29)$$

Going through the whole LORs to update estimates takes long time. To accelerate the convergence rate, the OSEM algorithm is applied to Equation (3.29). The term *L*, the total number of LORs, is divided into *K* subsets. It means $L = \sum_{k=1}^{K} S_k$ as in Equation (3.30) [81]. It was noted that the subsets were chronologically obtained. We note that the sensitivity map ($\sum_{i=1}^{n} a_{ij}$) is challenging.

$$x_j^{(k+1)} = \frac{x_j^{(k)}}{\sum_{i=1}^{n} a_{ij}} \left(\sum_{i \in S_k} a_{ij} \frac{1}{\mu_i^{(k)}} \right), \qquad for\ k = 1, \dots, K \qquad (3.30)$$

The final image x_j^K is obtained just after one iteration over the whole data [76]. Convergence to an ML solution is not guaranteed in Equation (3.30).

3. 4 .2 **Regularization**

Smoothing was incorporated into the update equation. A Gaussian kernel was used in [81]. This kernel was used one time for each update.

$$x^{(k+1)} = x^{(k)} \times s \times (c^{(k)} \otimes \varphi), \qquad for\ k = 1, \dots, K \qquad (3.31)$$

where the symbol × denotes an element-by-element multiplication between two vectors and the symbol ⊗ denotes convolution of a 3-dimensional image with a kernel. The term *s* is for the sensitivity correction factors mainly due to scanner geometry and the term c^k

is for the multiplicative image correction values. The term c^k includes a resolution kernel ρ. The term φ is the kernel for smoothing. For more details, refer to [81].

Table 3-1 shows the comparison of reconstruction times. 3-D RP (3D FBP) time includes binning of the list-mode data into a 4-dimensional projection matrix. OPL-EM used ρ=1.0mm, φ =0mm (no regularization), and K=50 for a 54 million event data set, and ρ=1.35mm, φ=0mm, and K=75 for the 145 million event data set. The factored version of OPL-EM used simple 1-dimensional convolutions instead of truly 3-D convolution operations. A 667-MHz Alpha XP1000 workstation was used for image reconstruction. It is interesting that the reconstruction time for the factored (one dimensional kernel) OPL-EM with the smaller matrix size is less than that of 3-dimensional FBP.

Table 3-1. Comparison of reconstruction times. This table is from [81].

Events and Matrix Size	3D RP (3D FBP)	OPL-EM	OPL-EM (factored)
54 million (256×256×256)	4h 9m	7h 8m	3h 58m
145 million (256×256×512)	5h 11m	23h 45m	12h 30m

3 .5 **Row Action Maximum Likelihood Algorithm (RAMLA) for Bin Mode Data**

3. 5 .1 **Row-Action ML Algorithm**

One-pass list mode EM (OPL-EM) using OSEM showed the speed-up of list mode image reconstruction. One drawback of OSEM is that convergence to an ML solution is not guaranteed. Albeit this limitation is not critical for practical use, the

convergence is still a factor considered. A row action ML algorithm (RAMLA) is an iterative image reconstruction algorithm using subsets and is still convergent to an ML solution. The RAMLA update equation for bin mode data is shown in Equation (3.32) [73].

$$x_j^{(k,i)} = x_j^{(k,i-1)} + \lambda_k x_j^{(k,i-1)} \times \sum_{l \in S_i} a_{lj} \left(\frac{g_l}{\sum_{j=1}^{M} a_{lj} x_j^{(k,i-1)}} - 1 \right) \tag{3.32}$$

where $\lambda_k, (0 < \lambda_k \sum_{l \in S_i} a_{lj} \leq 1)$, is the relaxation parameter.

Another advantage of RAMLA is that it can be used for noisy, low count rate data. In particular, short time-resolution of consecutive images of small animal PET imaging is required to observe fast biological changes in objects [81]. The short acquisition time results in noisy, low count rate data.

For the RAMLA reconstruction algorithm, each subset can contain one projection view [81]. This loose constraint makes RAMLA suitable for the intra-operative PET image system. We reiterate that too small number of projection views per subset can result in poor signal to noise ratio. Bin mode RAMLA can be converted into list mode RAMLA that is obtained by setting g_l to 1 as shown in Equation (3.33). The subscript term *l* then means each LOR, rather than a bin.

$$x_j^{(k=1,i)} = x_j^{(k=1,i-1)} + \lambda_{k=1} x_j^{(k=1,i-1)} \cdot \sum_{l \in S_i} a_{lj} \left(\frac{1}{\sum_{j=1}^{M} a_{lj} x_j^{(k=1,i-1)}} - 1 \right) \tag{3.33}$$

3. 5 .2 **Asymptotic Convergence**

To obtain convergence to an ML solution, we need some constraints on relaxation parameters. For the proof of the asymptotic convergence, refer to [73].

$$\lim_{k\to\infty} \lambda_k = 0 \tag{3.34}$$

$$\sum_{k=0}^{\infty} \lambda_k = +\infty \tag{3.35}$$

In addition, $\sum_{l\in S_i} a_{lj}$ in Equation (3.36) is also included to limit the range of λ_k .

$$0 < \lambda_k \sum_{l\in S_i} a_{lj} \leq 1 \tag{3.36}$$

3 .6 **Real-time List Mode PET Imaging Reconstruction Using Regularized Pseudo-Inverse Matrix: Event-by-Event Reconstruction**

Before introducing a variant of OPL-ML using RAMLA, a *real-time* list mode image reconstruction algorithm using a regularized pseudo-inverse matrix is reviewed. Selivanov *et al.* proposed real time list-mode image reconstruction using a regularized pseudo-inverse of the system matrix [83].

In their proposed algorithm, a vector of measurement, g_e, is related to the radio-tracer distribution, x, as follows.

$$g_e = Ax + e \tag{3.37}$$

Where the term e is a vector of measurement error and the term P is an $N \times M$ system matrix and the term b_e is the measurement, i.e., sinogram.

The minimum-norm least-square solution (MNLS) of Equation (3.33) is given as follows.

$$x_{MNLS} = A^{+} g_e \tag{3.38}$$

where P^{+} is the Moore-Penrose pseudo-inverse matrix.

The A^{+} can be rewritten as $VD^{+}U^{T}$ assuming that $A = UDV^{+}$ and $D^{+} = diag(\mu_1^{-1}, \mu_2^{-1}, \dots, \mu_M^{-1})$. The term D^{+} is a diagonal matrix containing the reciprocals of the respective positive singular values as shown in Equation (3.39).

$$D^{+} = diag(d^{+}), \qquad d^{+} = \begin{cases} \mu_i^{-1}, & if\ \mu_i > 0 \\ 0, & if\ \mu_i = 0 \end{cases} \tag{3.39}$$

We use only the non-zero singular values for the estimation, resulting in regularization by truncating zero-valued singular values as shown in Equation (3.40). The term T is less than or equal to the term M.

$$\hat{x} = \left\{ \hat{x}_k : \hat{x}_k = \sum_{i=1}^{T} v_{ki} \mu_i^{-1} \sum_{j=1}^{N} u_{ji} g_j \right\} \tag{3.40}$$

where $k = 1, \dots, M; T \leq M$.

Extremely small μ_is can cause the term $\hat{f}_k$ to be infinite. In order to prevent the unacceptable situations, we may apply the Tikhonov-Phillips filter function as shown in Equation (3.41). We can control the $\hat{f}_k$ through η.

$$\hat{x} = \left\{ \hat{x}_k : \hat{x}_k = \sum_{i=1}^{T} v_{ki} \left[\frac{\mu_i}{\mu_i^2 + \eta} \right] \sum_{j=1}^{N} u_{ji} g_j \right\} \tag{3.41}$$

where η is a regularization parameter and $k = 1, \dots, M; T \leq M$.

We can rearrange Equation (3.41) into Equation (3.42).

$$\hat{x}_k = \sum_{j=1}^{N} \left[\sum_{i=1}^{T} v_{ki} \mu_i^{-1} u_{ji} \right] g_j; \tag{3.42}$$

where $k = 1, \ldots, M$.

We can use Equation (3.43) to rewrite Equation (3.42) into Equation (3.44).

$$\tilde{A}^{+} = \left\{ \tilde{a}_{kj} : \tilde{a}_{kj} \equiv \sum_{i=1}^{T} v_{ki} \mu_i^{-1} u_{ji} \right\} \tag{3.43}$$

where $k = 1, \ldots, M; j = 1, \ldots . N$.

$$\hat{x}_{k=} \tilde{A}^{+} g \tag{3.44}$$

By arranging LORs within a sinogram into a series of LORs and using the truncated pseudo-inverse matrix $\tilde{P}^{+}$, the image estimate is obtained as a sum of the previous image estimate and one column of the matrix $\tilde{P}^{+}$. For more details, refer to [ch3-16]. The update equation is shown in Equation (3.45).

$$x_k^{(s)}(t) = x_k(t-1) + \tilde{a}_{ks} \tag{3.45}$$

where $\tilde{a}_{kj}$ is given in Equation (3.43) and the term *t* is the LOR count. The term *s* is a bin index in the measurement space.

Fig. 3-7 shows an illustration of the real time image update procedure. The new image is the sum of the previous image and one column of $\tilde{A}^{+}$. The one column of A^{+} is obtained from a single LOR as shown in Fig. 3-7. Therefore the image is updated on an event-by-event basis.

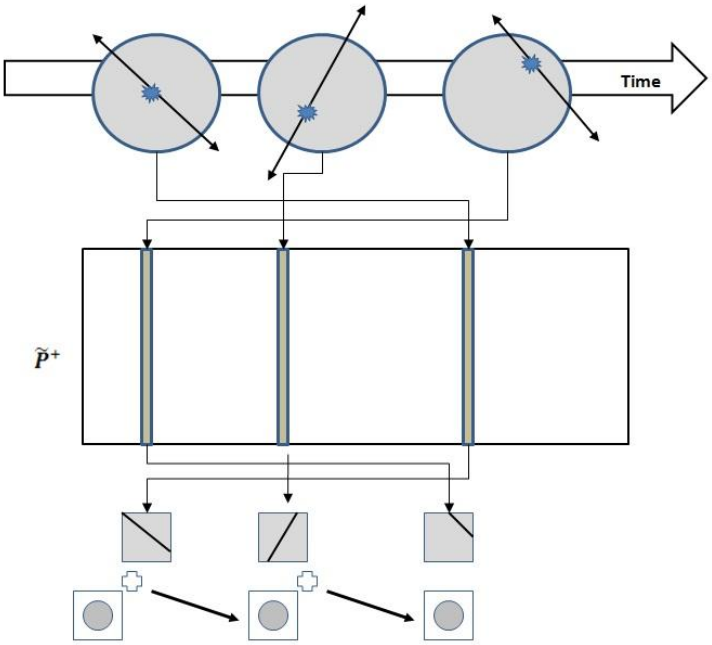

Figure 3-7. Illustration of event-by-event update. This picture was adapted from [83].

Fig. 3-8 shows the comparison of incrementally reconstructed images from the regularized pseudo inverse matrix method and images from MLEM. We can see the streak-like artifacts in the reconstructed images from the regularized pseudo inverse matrix method.

One of the drawbacks is that this method requires a huge amount of memory for matrix operations in order to obtain $\tilde{P}^+$ from the singular values. In particular, high resolution images require smaller voxels, resulting in bigger matrix sizes.

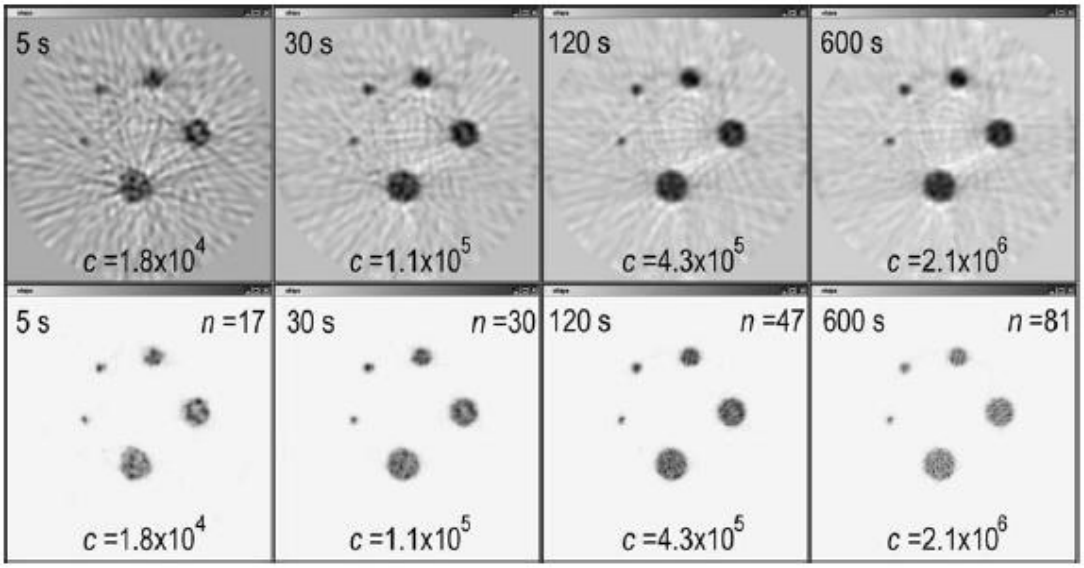

Figure 3-8. Image sequence obtained with the incremental (truncated singular value decomposition) TSVD-based reconstruction (upper row) and with the ML-EM without regularization (lower row). These pictures are from [83].

3 .7 **Geometrical Sorting of Subsets**

The conventional OSEM algorithm takes advantage of geometrically ordered subsets. However in list mode data, data are usually stored chronologically. Further data processing is required to order the chronological list mode data into geometrically ordered subsets. To take advantage of fast convergence of OSEM, random access to the list mode data for obtaining geometrical ordered subsets has been considered [ch3-17, 84]. We can take advantage of the speed-up of the original OSEM by sorting the subsets geometrically in list mode data.

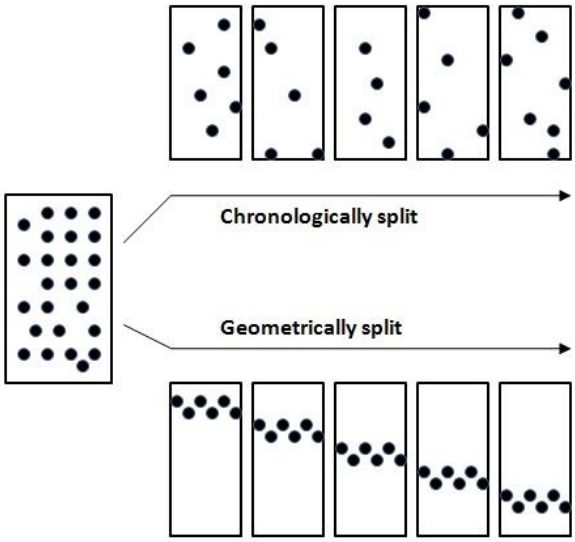

Figure 3-9. Illustration of sorting sinogram data into either chronological subsets or geometrical subsets. This picture was adapted from [84].

The intra-operative PET imaging probe takes coincidence data between the probe and the partial ring detector. Therefore subsets from different angles have different geometrical information albeit LORs in each subset are stored chronologically. The LORs in a subset are confined to a small space variation. Therefore coincidence data in each subset of the PET imaging probe are sorted geometrically to some extent even though the data are stored in list mode. This characteristic can help take advantage of the speed-up of original OSEM.

3 .8 Incorporating OPL-ML, RAMLA, and a Gaussian Back-projection Kernel for Real Time Image Reconstruction

The proposed iterative image reconstruction algorithm aimed to display reconstructed images during surgery or diagnosis in real time. In the proposed algorithm, the image update is applied to each subset, which is a projection view. The subset size is

confined to a small number of LORs. Incrementally reconstructed images are provided to the clinician or surgeon on the fly. The new image is then used for an initial image for the next update. The proposed image update algorithm is described below in detail.

List mode row-action maximum likelihood algorithm was obtained from Equation (3.46) by setting $g_l = 1$. List mode data goes through the data one time as in OPL-EM. Therefore we set the iteration number *k* to 1.

$$x_j^{(k=1,i)} = x_j^{(k=1,i-1)} + \lambda_{k=1} x_j^{(k=1,i-1)} \cdot \sum_{l \in S_i} a_{lj} \left(\frac{1}{\sum_{j=1}^{M} a_{lj} x_j^{(k=1,l-1)}} - 1 \right) \tag{3.46}$$

where $0 < \lambda_k c_{lj} \leq 1$ $(if\ c_{lj} \neq 0)$ and $c_{lj} = \sum_{l \in S_i} a_{lj}$

Equation (3.46) can be rewritten into Equation (3.47) to show affinities to conventional OSEM [73]. Equation (3.47) becomes an OSEM update equation as in Equation (3.48) when $\lambda_k = \frac{1}{c_{lj}}$. Equation (3.48) is the same as the original OSEM update equation except that each subset in RAMLA consists of one projection view [73].

$$x_j^{(i)} = x_j^{(i-1)}(1 - \lambda_k c_{lj}) + \lambda_k x_j^{(i-1)} \cdot \sum_{l \in S_i} \left(\frac{a_{lj}}{\sum_{j=1}^{M} a_{lj} x_j^{(i-1)}} \right) \tag{3.47}$$

$$x_j^{(i)} = x_j^{(i-1)} \cdot \frac{1}{c_{lj}} \sum_{l \in S_i} \left(\frac{a_{lj}}{\sum_{j=1}^{M} a_{lj} x_j^{(i-1)}} \right) \tag{3.48}$$

Since we intend to use list-mode data and a Gaussian kernel for image reconstruction, list mode RAMLA is derived from the bin mode RAMLA. Intra-operative PET imaging probe system has *continuous coordinates* of LORs, rather than finite possible coordinates, because the PET imaging probe is designed to move around lesions.

Therefore we can use some properties of list mode MLEM derived from the *list mode* likelihood function [ch3-18, 85]. We can compare list mode MLEM derived from *bin mode* likelihood with list mode MLEM derived from a *list mode* likelihood function. Equation (3.49) is a list mode MLEM update equation derived from *bin mode* likelihood. Equation (3.50) is the list mode MLEM derived from the *list mode* likelihood function [85].

$$x_j^{(k,i)} = x_j^{(k,i-1)} \cdot \frac{1}{\sum_{l=1}^{M} a_{lj}} \sum_{l \in S_i} \left(\frac{a_{lj}}{\sum_{j=1}^{M} a_{lj} x_j^{(k,i-1)}} \right) \tag{3.49}$$

$$x_j^{(k,i-1)} = x_j^{(k,i-1)} \cdot \frac{1}{Q_j} \left(\sum_{l \in S_i} \frac{p(A_l|j) Q_j}{\sum_{j=1}^{M} p(A_l|j) Q_j x_j^{(k,i-1)}} \right) \tag{3.50}$$

where A_l is an LOR with an attribute A (two end-points, time, and energy, etc.). The term Q_j is the sensitivity. $p(A_l|j)$ is the probability density that a detected event generated in bin j leads to a measurement A_l [85].

From the two equations, we can see that Q_j identifies with $\sum_{l=1}^{M} a_{lj}$ [86]. Therefore we can replace $\sum_{l=1}^{M} a_{lj}$ with Q_j. Equation (3.51) is a list mode RAMLA derived from *bin mode* RAMLA. The $\sum_{j=1}^{M} a_{lj}$ in Equation (3.51) is replaced with Q_j. The resulting equation is shown in Equation (3.52).

$$x_j^{(i)} = x_j^{(i-1)} + \lambda_{k=1} x_j^{(i-1)} \cdot \left(\sum_{l \in S_i} \frac{a_{lj}}{\sum_{j=1}^{M} a_{lj} x_j^{(i-1)}} - \sum_{l \in S_i} a_{lj} \right) \tag{3.51}$$

$$x_j^{(i)} = x_j^{(i-1)} + \lambda_{k=1} x_j^{(i-1)} \cdot \left(\sum_{l \in S_i} \frac{a_{lj}}{\sum_{j=1}^{M} a_{lj} x_j^{(i-1)}} - Q_j^{(i)} \right) \tag{3.52}$$

A similar expression of list mode RAMLA including the back ground count density $\mu_b(g_n)$ is given as follows [84].

$$x_j^{(k,i-1)} = x_j^{(k,i-1)} + \lambda x_j^{(k,i-1)} \cdot \left(\sum_{y_n \in Y_S} \frac{a_j(g_n)}{\mu_t(y_n | x^{(k,i-1)}) + \mu_b(g_n)} - Q_j^{(i)} \right) \tag{3.53}$$

where $Q_j^{(s)} = \int_{D_s} a_j(g) dg, \quad D = \cup_{s=1}^{S} D_S,$ and $\mu_t\left(g_n \middle| x^{(k,i-1)}\right) = \sum_{j=1}^{I} a_j(g_n) x_j.$ The term D_s is a subset and the term $a_j(\boldsymbol{g})$ is the probability density of detecting an emission from a voxel *j* with attributes of $\boldsymbol{g_n}$.

To incorporate a Gaussian kernel, p_{lj} is replaced with $p(A_l|j)Q_j$ [85]. The resulting list mode RAMLA for this study is shown in Equation (3.54).

$$x_j^{(i)} = x_j^{(i-1)}(1 - \lambda \ Q_j^{(i)}) + \lambda \ x_j^{(i-1)} \cdot \left(\sum_{l \in S} \frac{p(A_l|j)Q_j}{\sum_{j=1}^{M} p(A_l|j)Q_j x_j^{(i-1)}} \right) \tag{3.54}$$

We then need to calculate the ratio of $p(A_l|j)Q_j$ to $\sum_{j=1}^{M} p(A_l|j)Q_j x_j$. We used a method from [85]. List mode MLEM derived from the *list mode* likelihood function is shown in Equation (3.55) and its rewritten formula is shown in Equation (3.56).

$$x_j^{(k+1)} = \sum_{l=1}^{N} \frac{p(A_l|j)x_j^{(k)}}{T\sum_{i=1}^{M} p(A_l|i)Q_i x_i^{(k)}} \tag{3.55}$$

$$x_j^{(k+1)} = x_j^{(k)} \frac{1}{Q_j} \sum_{l=1}^{N} \frac{p(A_l|j)Q_j}{\sum_{i=1}^{M} p(A_l|i)Q_i x_i^{(k)}} \tag{3.56}$$

$p(A|j)$ can be calculated by using Bayes' rule.

$$p(A|j) = p(A)p(j|A)/p(j) \tag{3.57}$$

By using $p(j) = Q_j$, we can replace $p(A|j)Q_j$ with $p(A)p(j|A)$.

$$p(A|j)Q_j = p(A)p(j|A) \tag{3.58}$$

The $p(A)p(j|A)$ term can be approximated as follows [85]. For more detail, refer to [85].

$$p(A|j)Q_j \propto p(A)G(d, \sigma_{s_{eff}}) \tag{3.59}$$

where $G\left(d, \sigma_{s_{eff}}\right) = \left(\frac{1}{\sqrt{2\pi\sigma}}\right) \exp\left(-\frac{d^2}{2\sigma^2}\right)$ is a Gaussian kernel and the term d is the perpendicular distance from a pixel to a LOR.

The term d is shown in Fig. 3-10. The mearsured two end-points as an LOR are (U_1, U_2). U_1 has two dimensional coordinates (u_{1_x}, u_{1_y}) and U_2 has two dimensional coordinates (u_{2_x}, u_{2_y}). The two end-points for atual events are (U_1', U_2'). The perpendicular distance d from the center z_i of pixel i to the mesaured LOR is given by

$d = \|\vec{\boldsymbol{m}}\big(\vec{\boldsymbol{m}} \cdot (z_i - U_i)\big) - \big((z_i - U_i)\big)\|$. The term $\vec{\boldsymbol{m}} = ((U_2 - U_1)/\|(U_2 - U_1)\|)$ is the unit vector along a mearued LOR. The term σ is given as FWHM/2.35. The value of FWHM is set to the detector crystal width.

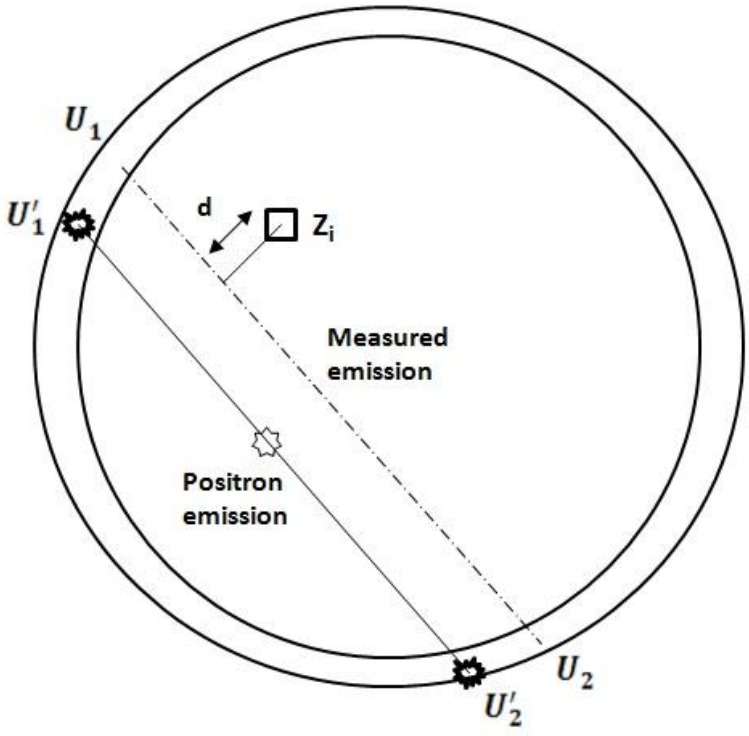

Figure 3-10. Gaussian kernel in the list mode ML algorithm. This picture was adapted from [85].

For the sensitivity $Q_j^{(s)}$, we used a roughly approximated value by taking advantage of the small ROI compared to the whole body PET system. We computed the joint solid angle subtended by the imaging probe and the partial ring detector for each voxel. The joint solid angle was multiplied by the detector sensitivity and the photo fraction. This final result was used for the sensitivity $Q_j^{(s)}$.

The image update equation is applied to each subset. Each subset consists of small number of LORs. For example, each subset contains 16 consecutive LORs. The new estimates from a set of 16 LORs become initial values for the next update. The reconstructed image is provided to the clinician or surgeon on the fly.

Based on the provided images, surgeons or clinicians can decide where to move to locate lesions. Because this process should be done in real time, we tested the update algorithm using a graphics processing unit (GPU). The GPU implementation of the proposed algorithm is discussed in Chapter 4.

3 .9 **Other Update Equations Using a Relaxation Parameter**

Other update equations using a relaxation parameter are also available [83]. Equation (3.60) is a relaxation version of OSEM and Equation (3.61) is a relaxation version of the conventional MLEM algorithm.

$$x_j^{(k+1)} = x_j^{(k)} + xf_j^{(k)} \times \left(\frac{1}{Q_j^{(s)}} \sum_{g_n \in Y_s} \frac{a_j(g_n)}{\mu_t(g_n|x^{(k)}) + \mu_b(g_n)} - 1 \right) \tag{3.60}$$

$$x_j^{(k+1)} = x_j^{(k)} \left(\frac{1}{Q_j^{(s)}} \sum_{g_n \in Y_s} \frac{a_j(g_n)}{\mu_t(g_n|x^{(k)}) + \mu_b(g_n)} \right)^{\lambda} \tag{3.61}$$

where $\mu_t(g_n|x) = \sum_{j=1}^{J} a_j(y)x_j$ and $a_j(g)$ is the probability density function of detecting an event from a voxel i with g attributes. $\mu_b(g_n)$ is the density of random coincidences and scatters.

3 .10 **Simulation Study**

We used GEANT4 to obtain simulated data for the image reconstruction. Attenuation correction was not included in the study. Fig. 3-11 shows the simulation geometry. The partial ring detector consists of a 125×51 array of BGO crystals. The small imaging probe consists of an 11×11 array of LSO crystals. Each BGO crystal measures 5mm×5mm, 30mm thick. Each LSO crystal measures 2mm×2mm, 3mm thick. The 128mm radius sphere represents patient's body. The diameter of the partial rings is 400mm. The partial ring was moved to the sphere in order to reduce the separation between the partial ring and the sphere.

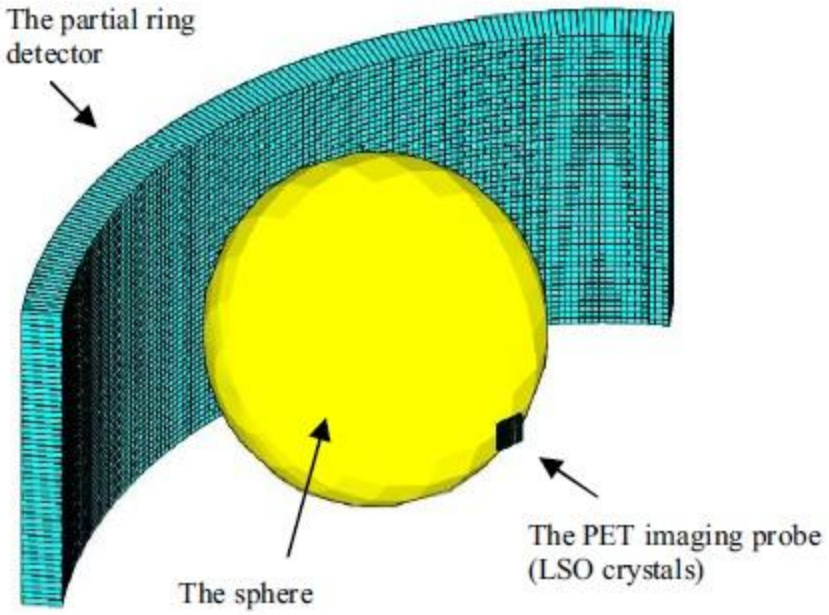

Figure 3-11. Simulation geometry of the intra-operative PET imaging probe system.

We have two small spheres along the horizontal line as shown in Fig. 3-12. The small sphere on the right-hand side is at the focal point of probe rotation and the other small sphere to the left is out-of-focus. The right-hand source serves as the pivot of a cylindrical arc. We tend to image the single point source at the focal point (closer to the imaging probe), but the out-of-focused sphere is also imaged because the ROI includes the out-of-focused sphere. Each sphere measures 1mm in radius.

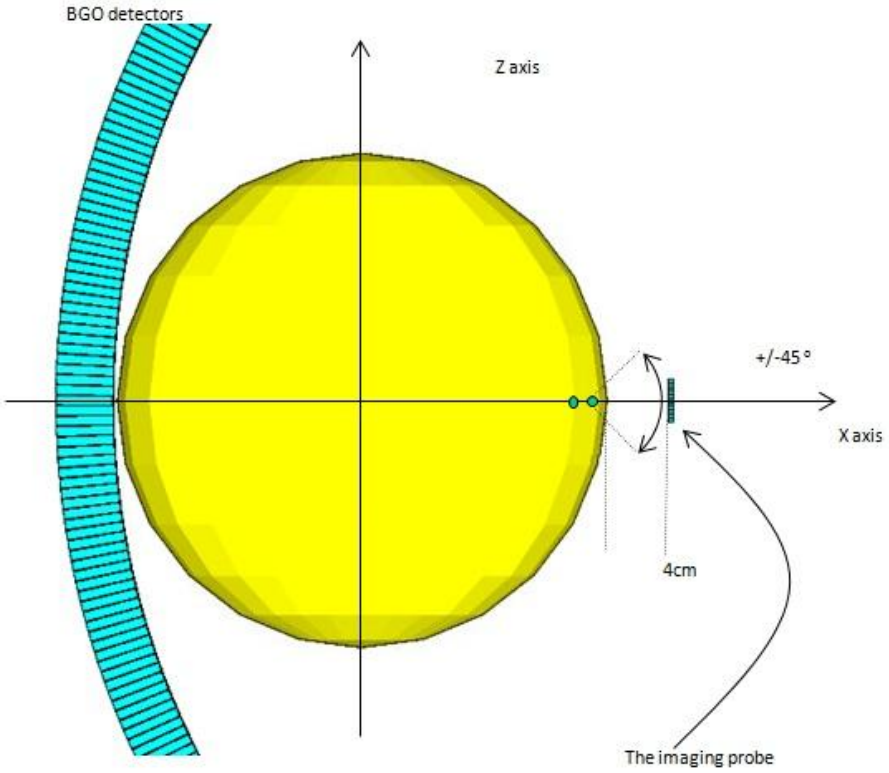

Figure 3-12. Transverse view of the simulation geometry.

The FOV included both of the two small spheres to investigate the effect of out-of-focused sphere source. The unfocused sphere source is located at the coordinate x=106 mm. The sphere source at the focal point is located at x=116 mm. The two sphere sources are enclosed in a medium size sphere, 10mm in radius, as shown in Fig. 3-13. The distance between the focused sphere and the front of the imaging probe is 40mm.

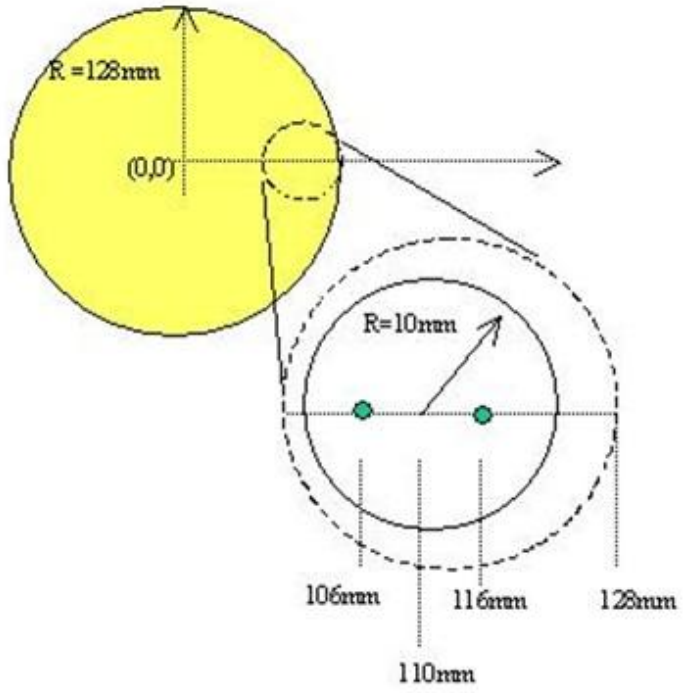

Figure 3-13. Zoomed in view of the region around the two small spheres.

The medium size sphere (the 10mm-radius sphere) is filled with background tracer activity. 80 % of 3 million positrons are placed in the 10mm radius background sphere. 10 % of 3 million positrons are in the small sphere on the left-hand side, and the rest 10% is in sphere on the right-hand side. In order to visualize the two sphere sources, the birth coordinates of simulated positrons were collected and were projected onto the z-x plane of Figure 3-13. We can see two hot spots in Fig. 3-14.

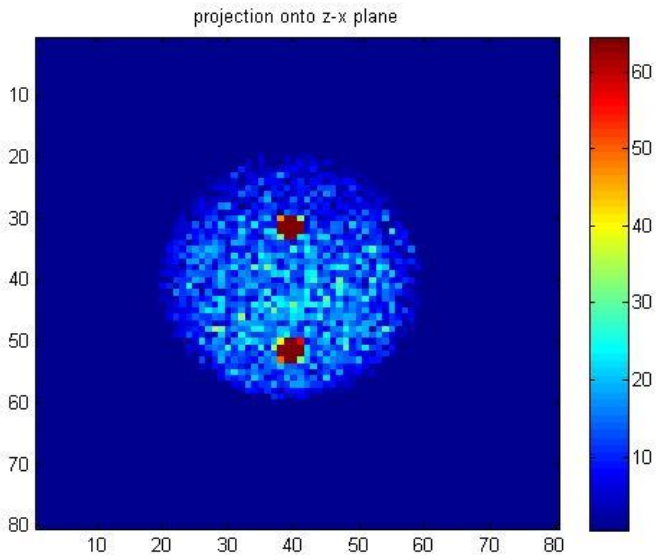

Figure 3-14. Two hot spots surrounded by background activity.

True coincidences were taken from +45° through -45° at intervals of 5° along the cylindrical arc shown in Fig. 3-12 and 3-15. Therefore the angles at which the data are taken are +45°, +40°, +35°, +30°, +25°, +20°, +15°, +10°, +5°, 0°, -5°, -10°, -15°, -20°, -25°, -30°, -35°, -40°, and -45°.The first interaction coordinates in each detector were chosen as the true interaction position. This removes uncertainty from position error. Only three sets of angle data were used for image reconstruction. The data set from angle 0° contained 804 LORs. 956 LORs were collected at +45° and 967 LORs at -45°.

True coincidence events were divided into very small size subsets. For instance, each subset contains 16 LORs. The update equation shown in Equation (3.50) was applied to each subset. Therefore we had new estimates after each subset. Attenuation correction was not included in the study.

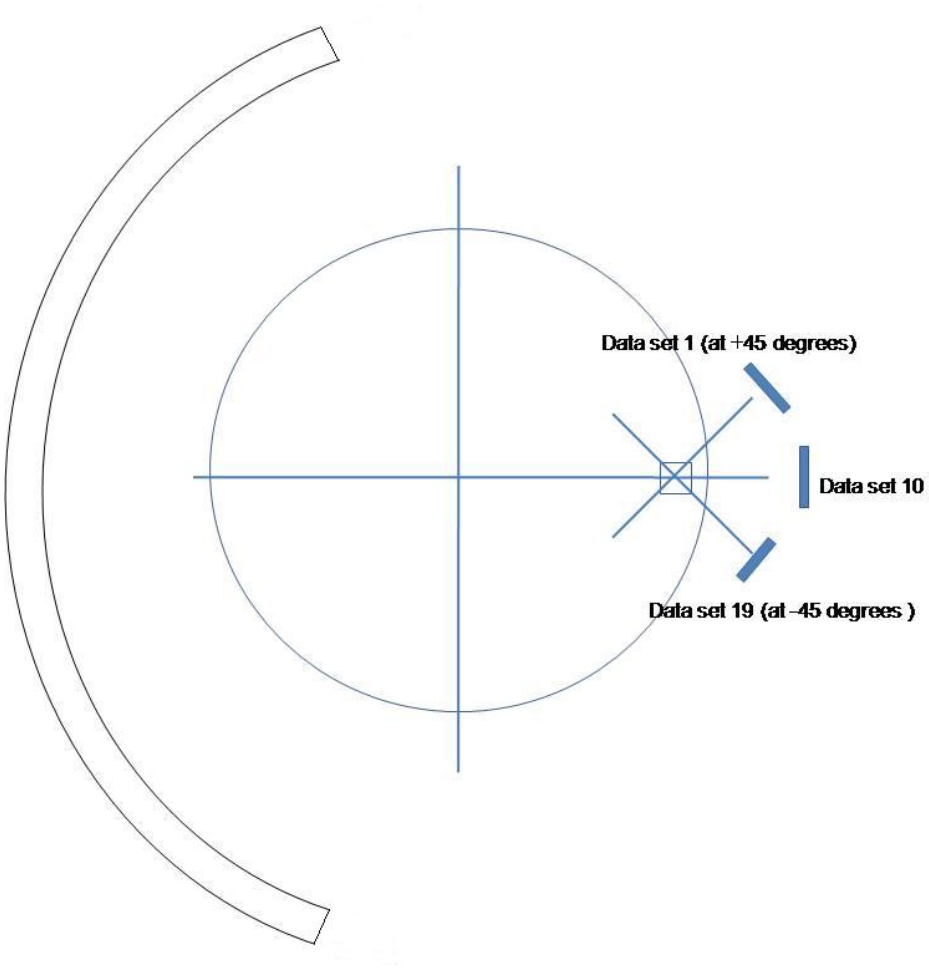

Figure 3-15. Three sets of data at different angles.

The final image of a row action ML algorithm is affected by the input sequence of subsets. The data set taken at 0° was processed first, and the data set taken at +45° was then processed. The subset taken at -45° degree was last processed. Fig. 3-16 shows a center slice of a reconstructed 3-dimensional image using three sets of data taken at 0° (total 804 LORs), +45° (total 956 LORs), and -45° (total 967 LORs).

The image update algorithm was tested by using a graphics processing unit (GPU). The GPU for image reconstruction is discussed in Chapter 4. Fig. 3-16 shows a center slice of a reconstructed 3-dimensional image using Equation (3.62) with $\lambda_s = \frac{0.5}{Q_j}$.

$$x_j^{(s)} = x_j^{(s-1)}(1 - \lambda_s Q_j^{(s)}) + \lambda_s x_j^{(s-1)} \cdot \left(\sum_{l \in S} \frac{G_n(d_j, \sigma)}{\sum_{i=1}^{M} G_n(d_i, \sigma) x_i^{(s-1)}} \right) \quad (3.62)$$

where $\sigma = \frac{FWHM}{2.35}$ and FWHM = 2mm. $G(d, \sigma) = 0, if\ d > 4 \times \sigma$. $G_n(d, \sigma)$ is a normalize Gaussian function.

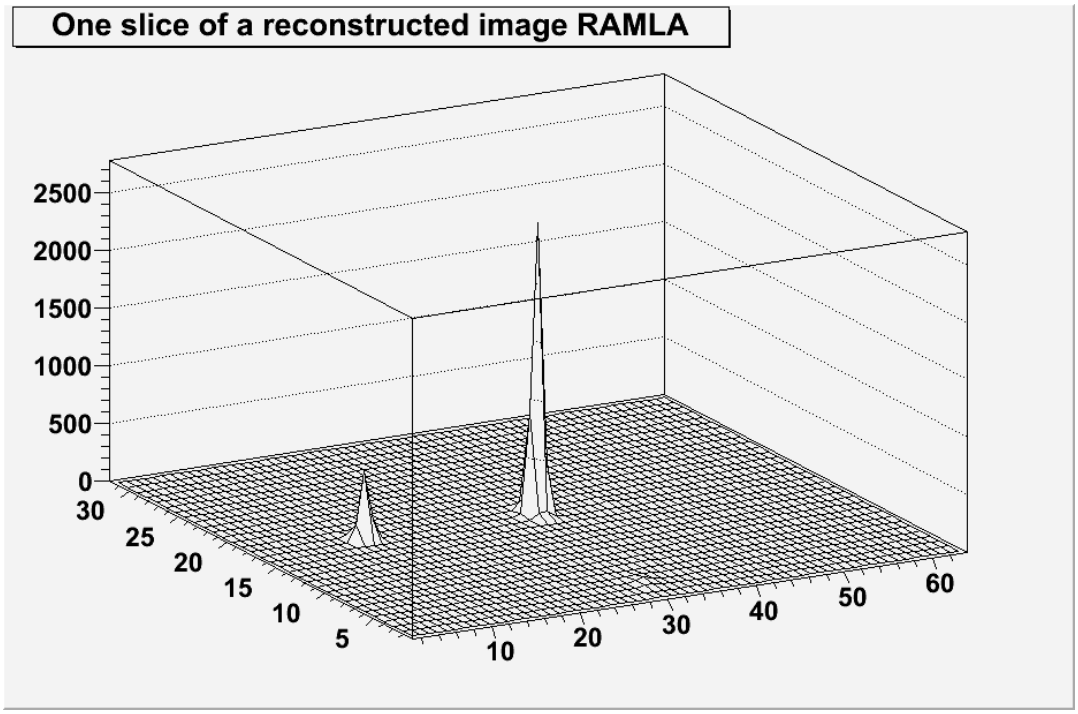

Figure 3-16. Center slice of a reconstructed 3-dimensional image using $\lambda_s = 1/(2Q_j)$.

Equation (3.62) was rewritten into Equation (3.63) with $\lambda_s = 1/(2Q_j)$.

$$x_j^{(s)} = x_j^{(s-1)} \times (0.5) + \frac{0.5}{Q_j} x_j^{(s-1)} \cdot \left(\sum_{l \in S} \frac{G_n(d_j, \sigma)}{\sum_{i=1}^{M} G_n(d_i, \sigma) x_i^{(s-1)}} \right) \quad (3.63)$$

To observe the role of the relaxation parameter, the relaxation parameter was reduced to $\lambda_s = \frac{1}{100*Q_j}$. Fig. 3-17 shows a center slice of a reconstructed 3-dimensional image using Equation (3.64).

$$x_j^{(s)} = x_j^{(s-1)} \times (0.99) + \frac{0.01}{Q_j} x_j^{(s-1)} \cdot \left(\sum_{l \in S} \frac{G_n(d_j, \sigma)}{\sum_{i=1}^{M} G_n(d_i, \sigma) x_i^{(s-1)}} \right) \tag{3.64}$$

We can see that the relaxation parameter λ is used to control convergence rates. As the value of λ is reduced, the convergence rate becomes slower. The term λ is almost a fixed value for this study because the term Q_j does not change dramatically over different angles, but it can be set to a different value for each subset [81]. Investigation of this variable λ is beyond the scope of this dissertation; refer to [73] for more details.

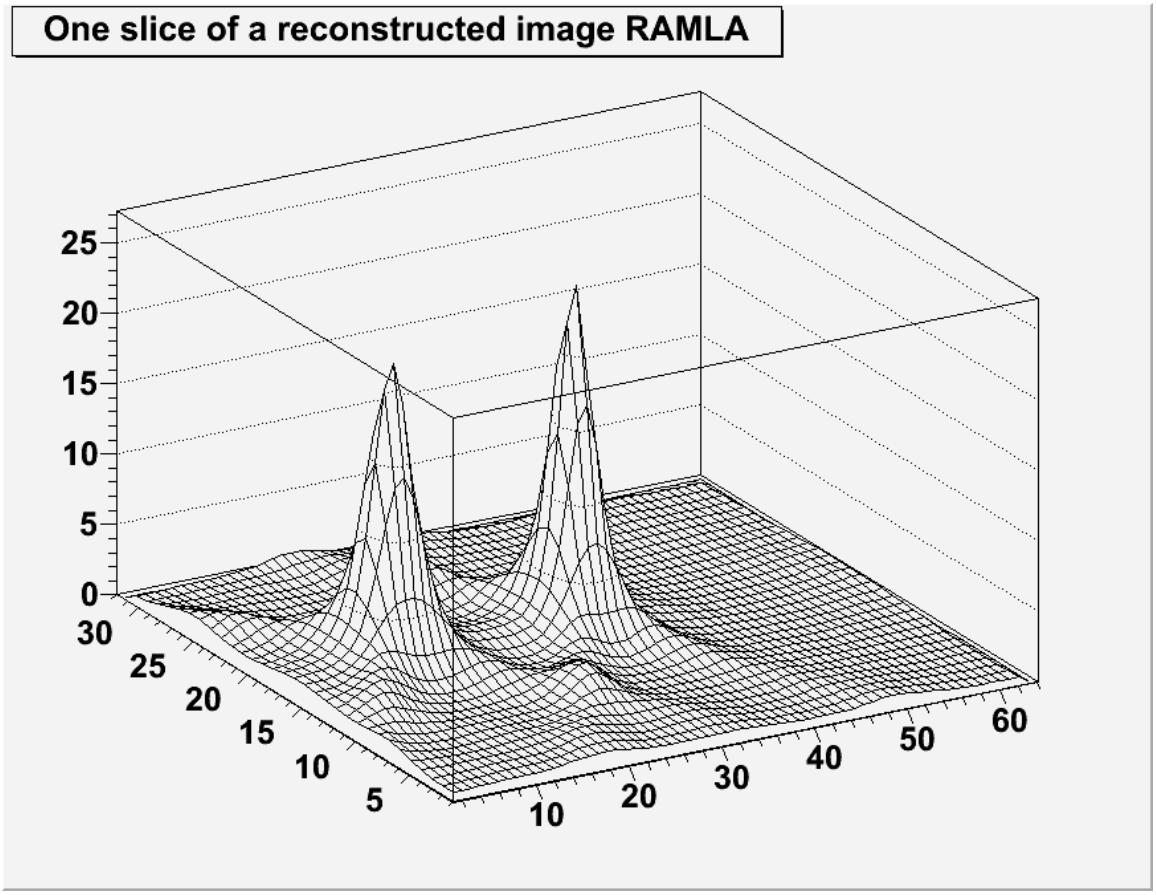

Figure 3-17. Center slice of a reconstructed 3-dimensional image using$\lambda_s = 1/(100 * Q_j)$.

3 .11 **Summary**

In this chapter, an image reconstruction algorithm that was dedicated to the intra-operative PET imaging probe was introduced. A RAMLA algorithm, an OPL algorithm, and a Gaussian kernel were integral to the proposed algorithm. Since this algorithm is based on a RAMLA with a relaxation parameter, each subset can have one projection view. Reconstructed images from simulated data showed promising results with mitigated effects of limited angle tomography.

Chapter 4
Parallel Image Reconstruction Based on a Graphics Processing Unit (GPU)

In this chapter, the proposed iterative image reconstruction algorithm is tested using a graphics processing unit (GPU) with CUDA™ (Compute Unified Device Architecture). Graphics processing units contain many streaming processors (SP) for parallel processing. By parallelizing an iterative image reconstruction, computing times are dramatically reduced. One drawback is lack of enough cache memory.

4 .1 Introduction to graphics processing units (GPUs)

Real time image reconstruction requires huge computing power. Even quad core CPUs are not sufficient for real time image reconstruction. Recently graphic process units (GPUs) emerged as one of candidates for faster image reconstruction. Originally, GPUs were dedicated to video data processing for 3-dimensional graphics. GPU devotes more number of transistors to arithmetic logic units rather than to control units as shown in Fig. 4-1. Consequently parallel data processing, which is termed as single instruction multiple data (SIMD), is used to speed up computation time. One drawback is the shrunk cache memory, resulting in longer memory access time.

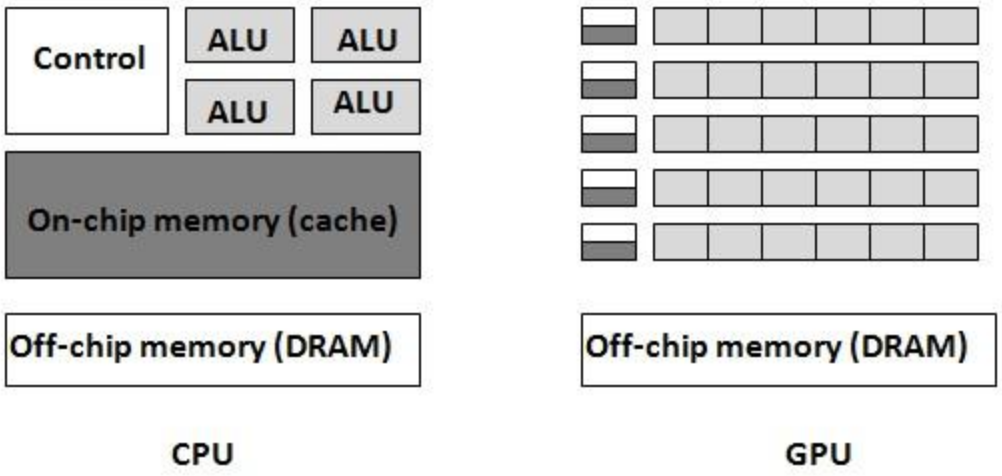

Figure 4-1. Comparison of CPUs and GPUs. This picture was adapted from [87].

Comparison of floating-point operations per second is shown in Fig. 4-2. We can notice the rate of speed-up in GPUs is faster than that of CPUs. In addition, theoretical computation speed of GPUs reaches over one tera-flop/s. Therefore we can see that programmable GPUs are candidates for hardware for faster image reconstruction.

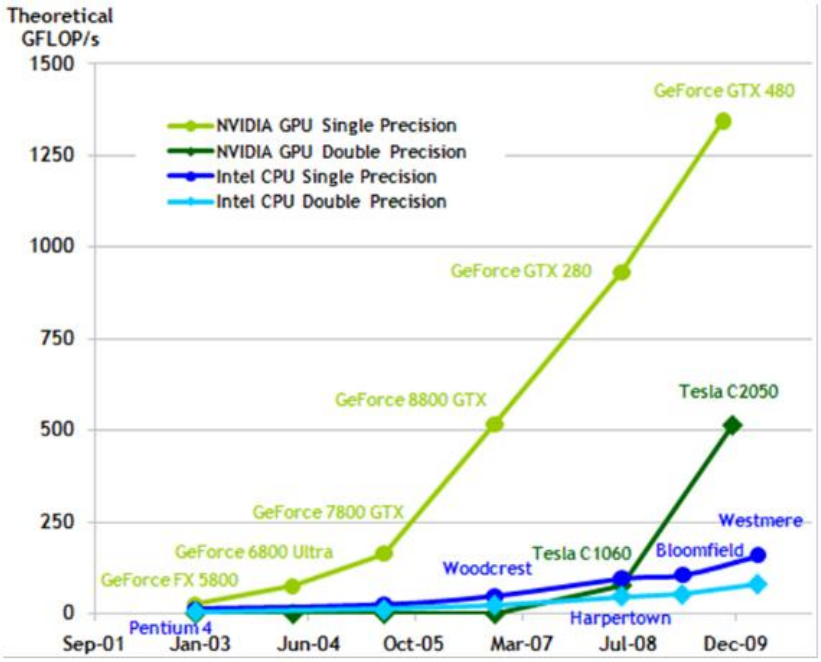

Figure 4-2. Floating-point operations/second of GPUs and CPUs. This picture is from [87].

4 .2 **CUDA Programming**

4. 2 .1 **Main concepts**

One of programming tools for GPU programming is CUDA C (a C-extension for CUDA). Conventional C code should be rewritten for parallel processing. Fig. 4-3 shows a well known for-loop example for comparison. The same instruction is executed 100 times sequentially on CPU.

```
for(int i=0; i<100; i++){
    A[i] = B[i]+C[i];
}
```

Figure 4-3. For-loop for comparison of GPUs and CPUs.

In parallel processing, we can take advantage of executing the same instruction. For example, 100 ALUs can be used to execute the same instruction concurrently in order to execute the for-loop. GPU parallel computing using multiple ALUs is shown Fig. 4-4. Each ALU can execute the same instruction concurrently.

Each ALU in Fig. 4-4 is termed as a *streaming processor* (SP) in the CUDA architecture. A group of streaming processors is termed as a *streaming multiprocessor* (SM). SPs in a SM are usually constrained to execute only the same instruction. Recent GPUs are, however, capable of executing different instructions.

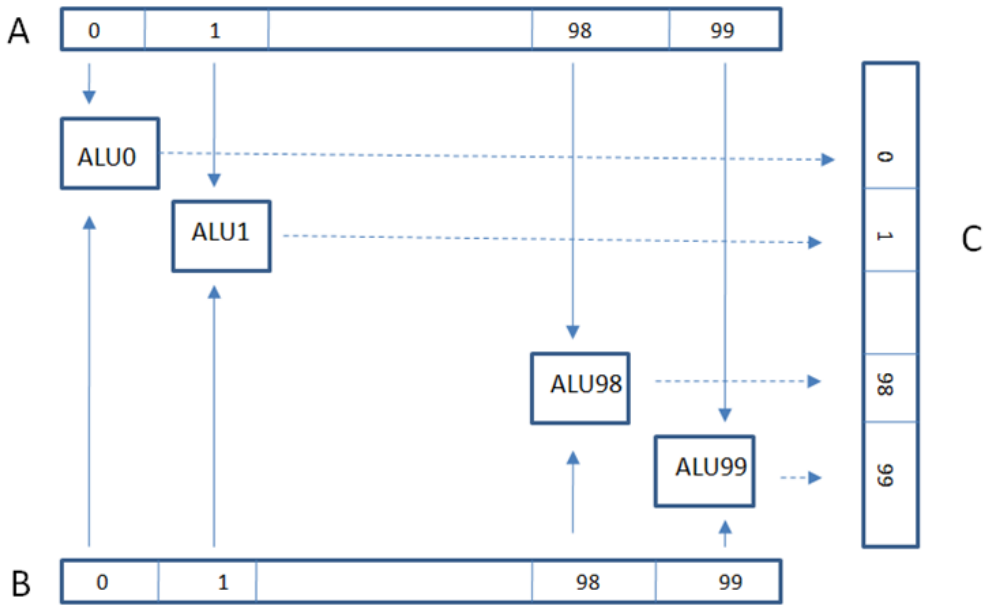

Figure 4-4. Sum operation using multiple ALUs.

4. 2 .2 **Threads and CUDA Programming**

The for-loop of sum operations in Fig. 4-3 can be rewritten as in Fig. 4-5. Each row in Fig. 4-5 is called a *thread* in CUDA programming. In order to convert conventional C

code to CUDA C code, programmers need to be aware of how threads are grouped in CUDA programming. One GPU on a graphics card is allowed to have one *grid* as shown in Fig. 4-6. The grid can have a number of *thread blocks*. Each block can also contain a number of *threads*. The maximum number of blocks/grid or threads/block is found by reading out information from graphics cards.

```
A[0] = B[0] + C[0];

A[1] = B[1] + C[1];

A[2] = B[2] + C[2];

A[3] = B[3] + C[3];
.
.
.

A[99] = B[99] + C[99];
```

Figure 4-5. Threads in a program.

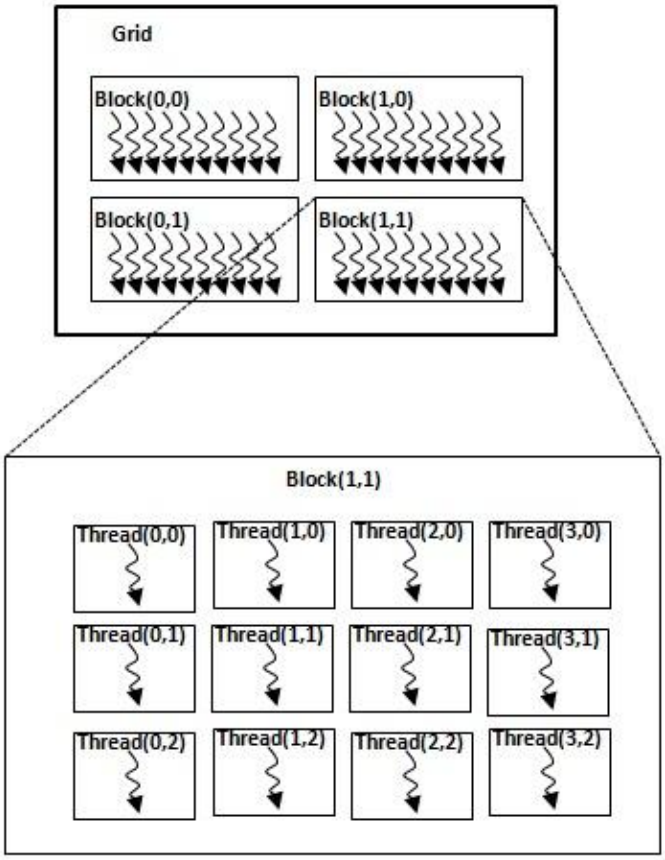

Figure 4-6. Thread assignment in CUDA programming. This picture is from [87].

Each block has a unique block *index number* as shown in Fig. 4-6. The same is true for threads. The grid in Fig. 4-6 has a 2-by-3 array of blocks. Each block contains a 3-by-4 array of threads. Therefore the grid has total 72 threads.

Each thread has a very small size of its own memory space. Threads in a block can share a special memory space, which is an on-chip shared memory. Blocks in a grid can share an off-chip global memory space (RAM). Fig. 4-7 shows memory spaces assigned to threads and blocks.

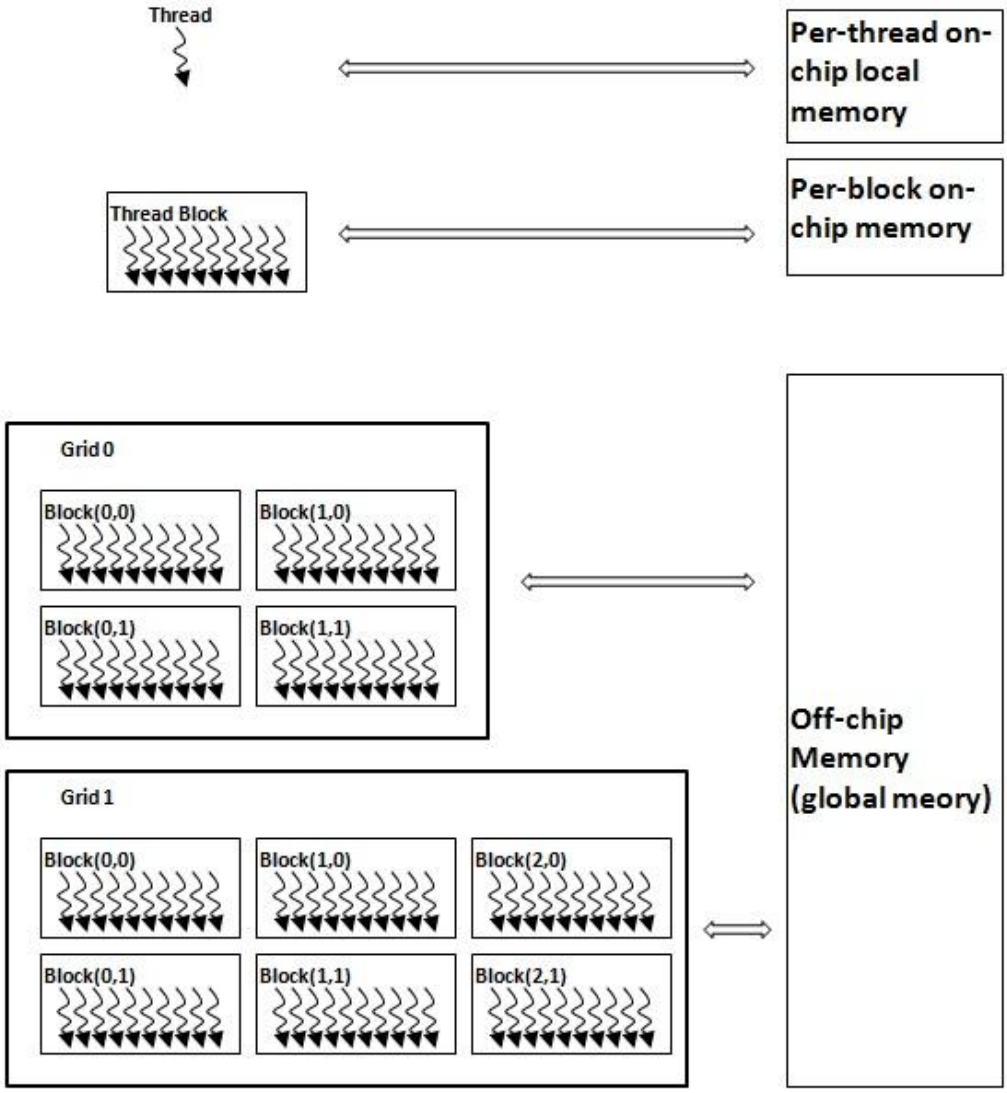

Figure 4-7. Memory space in CUDA programming. This picture is from [87].

A CUDA program can have multiple, sequential grids as shown in Fig. 4-8. In this case, the program consists of sets of serial codes for CPU and kernels for GPU. Kernels refer to the code that is executed on GPU. In recent architecture, multiple grids can be run concurrently.

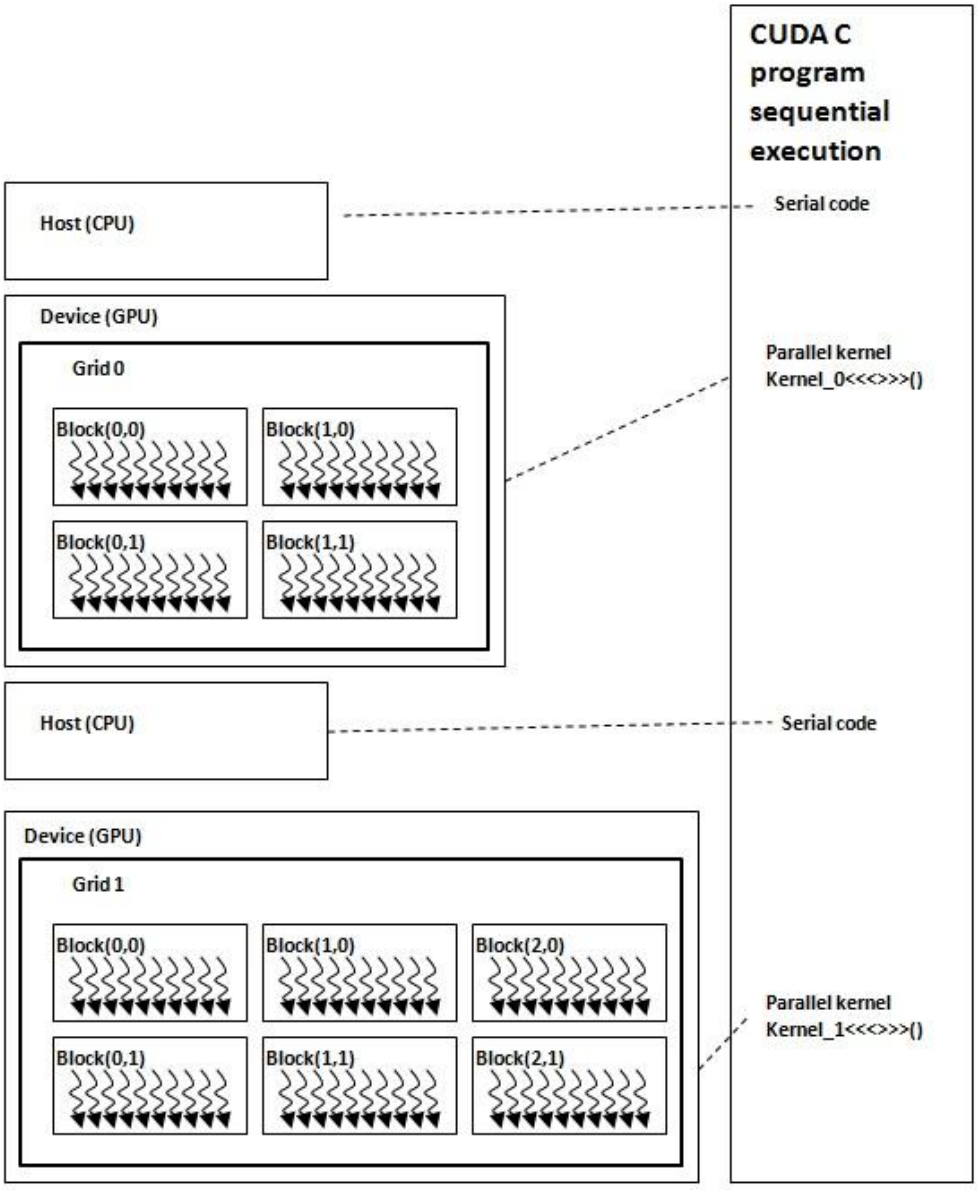

Figure 4-8. Serial codes for CPU and Kernels for GPU. This picture is from [87].

4 .3 CUDA Hardware Architecture (NVidia G80 Architecture)

Even though CUDA C can be used with a limited knowledge of the CUDA hardware architecture, it will be helpful to be aware of the CUDA hardware architecture in order to understand subtle performance difference. Table 4-1 shows the specification

of NVidia Geforce 9800GTX+. The specification shows it has 128 CUDA cores (streaming processors).

Table 4-1. GPU engine specs of NVidia GeForce 9800GTX+. This table was adapted from a specs from NVIDIA [88].

CUDA Cores (Streaming Processors)	128
Graphics Clock (MHz)	738 MHz
Processor Clock (MHz)	1836 MHz

Table 4-2. NVidia G80, GT200, and Fermi Architectures. This table is from [89].

GPU	G80	GT200	Fermi
Transistors	681 million	1.4 billion	3.0 billion
CUDA Cores	128	240	512
Double Precision Floating Point Capability	None	30 FMA ops/clock	256 FMA ops/clock
Single Precision Floating Point Capability	128 MAD ops/clock	240 MAD ops/clock	512 FMA ops/clock
Special Function Units (SFUs)/SM	2	2	4
Warp scheduler (per SM)	1	1	2
Shared Memory (per SM)	16KB	16KB	Configuration 48KB or 16KB
L1 Cache (per SM)	None	None	Configuration 16KB or 48KB
L2 Cache	None	None	768KB
ECC Memory Support	No	No	Yes
Concurrent kernels	No	No	Yes
Load/Store Address Width	32-bit	32-bit	64-bit

The Geforce® 9800GTX+ is based on the NVidia® G80 architecture. The GT200 and the Fermi architecture have 240 SPs and 512 SPs, respectively [89]. In Fermi architecture, each streaming multiprocessor has a programmable L1 cache (Parallel

DataCache®) to implement fast read/write operations and an additional L2 cache is also available [90]. The bigger cache size is likely to minimize the data accessing time.

The nVidia® G80 architecture is discussed in detail because a GeForce® 98000GTX+ graphics card, which is used for this study, is based on the G80 architecture.

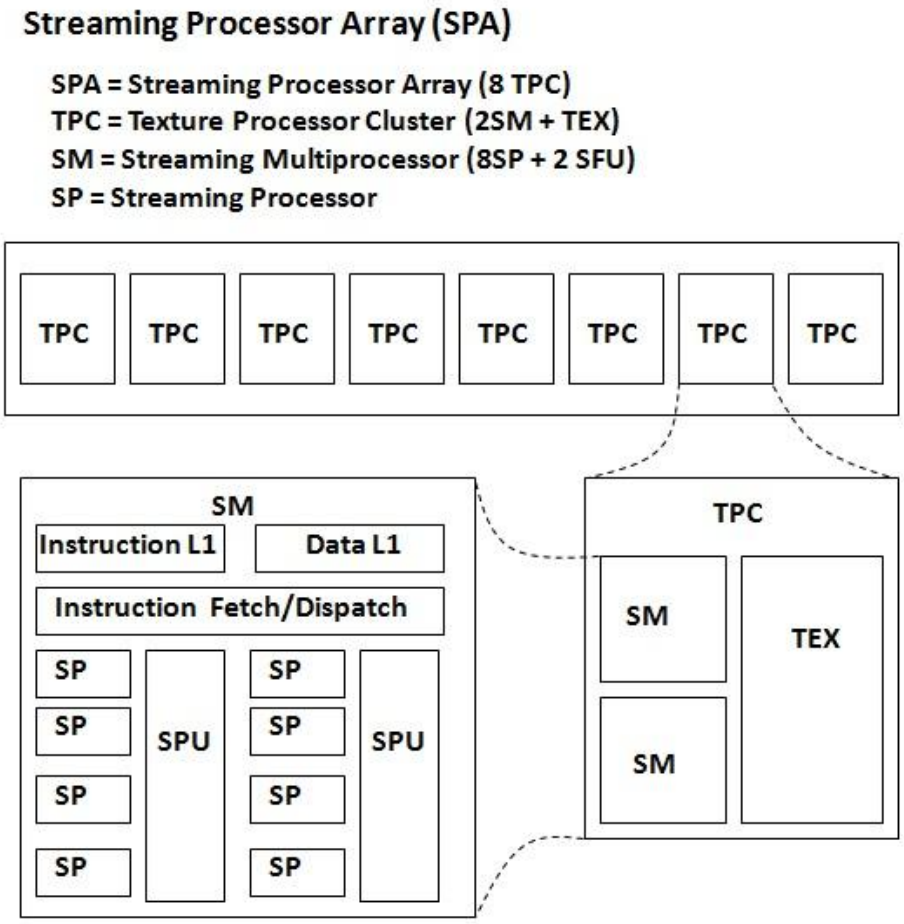

Figure 4-9. G80 Architecture and Streaming Processor Array. This picture is from [91] [92].

A typical GPU based on the G80 architecture has one streaming processor array (SPA) as shown in Fig. 4-9. One SPA contains 8 texture processor clusters (TPCs). Each TPC has 2 streaming multiprocessors (SMs) and one texture unit (TEX). Each streaming multiprocessor has 8 streaming processors (SPs) and two super function units (SFUs).

From the Table 4-2, a Geforce® 9800GTX+ has a 16 KB shared memory space for each streaming multiprocessor (SMs).

A TEX (texture unit) in Fig. 4-9 is in charge of sophisticated operations. [93]. A desired 2-dimensional image can be wrapped around a 3-dimensional object and be displayed on the screen by using the TEX. The special function units (SFUs) on each SM implement functions like trigonometry and square roots [93].

Although thousands of threads can be run on a GPU, a typical GPU with the G80 architecture has only 128 streaming processors [94]. A *warp scheduler* divides the threads within a block into a group of threads and is in charge of assigning threads to SMs (streaming processors). A resulting group of threads is termed as a *warp*. In the G80 architecture, it is known that each warp consists of 32 threads [95].

Fig. 4-10 shows details of a block diagram of a G80 SM (streaming multiprocessor). Eight SPs share one 16KB shared memory. Eight CUDA cores (SPs) are grouped into a streaming multiprocessor (SM). G80-class GPUs have 128 streaming processor cores (CUDA cores); 16 SMs x 8 CUDA cores/SM = 128 cores/GPU.

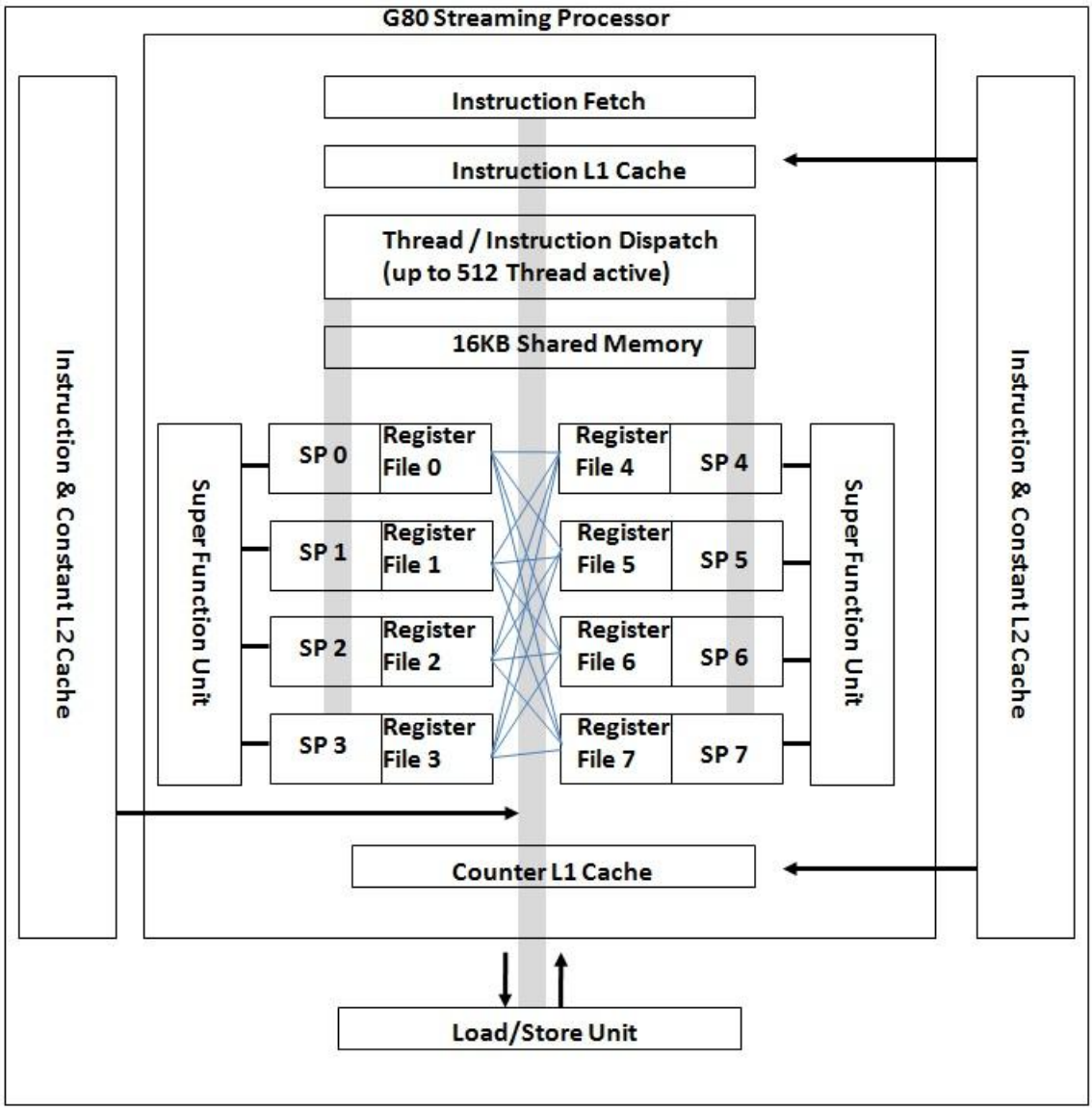

Figure 4-10. Details of a G80 streaming processor. This picture is from [96].

4 .4 GPU Applications on Image Reconstruction

4. 4 .1 Speed-Up of Image Reconstruction

Prototypes of nuclear medicine imaging systems using CUDA-enabled GPUs are gaining ground. Miller *et al*. used GPUs for a single-photon SPECT system that required

intensive computational load [97]. They built a real time data acquisition and processing system by incorporating GPUs into their SPECT system.

Dieckman *et al*. studied how to improve memory access efficiency in GPU programming [98]. They also compared CPU-only image reconstruction (a HP xw8400 workstation with two dual-core Intel Xeon 5130 CPUs at 2.0 GHz) with GPU-based image reconstruction (an NVIDIA Tesla® S1070-400 system with Fermi architecture) for motion compensated list mode OSEM. They used the cache memory for read operations for forward projection and shared memory for intermediate sums. For back-projection, a CUDA-provided addition function, atomicADD( ), was used to avoid illegal memory updates by concurrently running threads, i.e., a race condition [99]. A drawback of using the CUDA-provided sum function is that it operates only on unsigned integers. Voxel values and scale factors are, however, usually in the form of floating-point during updating. Consequentially, programmers need to pay more attention in order to avoid rounding error. Table 4-3 shows comparison of CPU-only image reconstruction and GPU-based image reconstruction. The speed-up is about 40 fold based on the number of LORs that were processed per second.

Table 4-3. Comparison of CUP-only and GPU-based. This table is from [98].

Module	Events/sec CPU -only	Events/sec GPU-accelerated
Forward Proj. (single-events/block)	9,770	396,000
Back-projection	8,561	167,001
OSEM Forward-Backward (1 Kernel)	4,550	39,062
OSEM Forward-Backward (2 Kernels)	4,550	48,543

They also investigated the execution time of each part of image reconstruction with respect to threads/block configurations. Table 4-4 shows relative execution times of the forward projection section in a function of threads/block. The shortest execution time was observed when the threads/block was set to 64 in Table 4-4. Table 4-5 shows the relative execution times of the backward projection section with respect to threads/block.

Table 4-4. Run time with respect to thread/block for the forward projection. This table is from [98].

Threads per Block	Thread Distribution	Relative Run-time
256	8/8/4	2.79
128	8/8/2	2.37
64	8/8/1	1.91
128	4/4/8	1.44
32	2/2/8	1.52
64	2/2/16	1.00
128	2/2/32	1.30

Table 4-5. Run time with respect to threads/block for the backward projection. This table is from [98].

Thread per Block	Thread Distribution	Relative Run-time
256	8/8/4	1.09
128	8/8/2	1.04
64	8/8/1	1.00
128	16/4/2	1.31
128	4/16/2	1.37

Barker *et al*. also compared the performance of CPU-only image reconstruction with that of GPU-based image reconstruction for a motion compensated list mode OSEM (MOLAR) [100]. Fig. 4-11 shows the acceleration by using GPU. The processing rates with respect to the number of LORs are shown in Fig. 4-13.

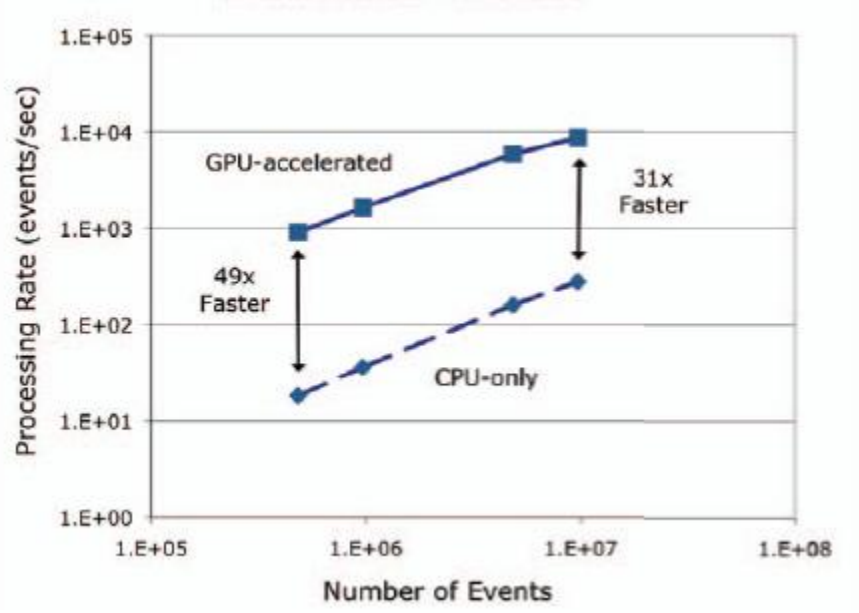

Figure 4-11. Comparison of CPU-only and GPU-based. This picture is from [100].

A conventional OSEM image reconstruction implementation on GPU is described in Fig. 4-12 [ch4-13]. It was reported that the effect of the race condition was almost negligible for a GPU using 128 CUDA streaming processors [99]. The update equation used in Fig. 4-14 is shown in Equation (4.1).

$$x_{l+1} = x_l c_l; \;\; c_l = \frac{1}{A_N^t} \sum_{i \in S_l} (A_i)^t \frac{1}{A_i x_l} \tag{4.1}$$

1. Move subsets CPU to GPU
2. A) compute a partial sum c_l
   B) Save c_l to memory
   C) thread assingments
3. Each thread/voxel computes new estimates
4. Copy new estimated back to CPU

Figure 4-12. OSEM algorithm on GPU. This picture was adapted from [99].

4. 4 .2 **Comparison of multi-processor systems**

List mode OSEM can be parallelized using hybrid clusters, cell processors, multi-core CPUs, or GPUs. The performance comparison is, however, not a straightforward task because the optimum conditions for each method are not clear [99].

Schellmann *et al*. compared the performance of multi-processor systems to a conventional hybrid cluster system [99]. Fig. 4-13 shows a comparison of the cell processor, the quad core CPU, and the two-GPU system. Each system for the comparison is shown in Table 4-6. The performance was marked compared to a typical hybrid cluster system. The image space size was 150×150×280 for list mode OSEM. 10^7 LORs were acquired for image reconstruction.

Table 4-6. The multi-processor systems for comparison. This table was adapted from [99].

Hybrid Cluster	200 Dual INTEL Xeon 3.2 GHZ nodes.
Cell Processor	A two-Cell processor system. Each cell processor contains 8 processing cores (SPEs) running at 3.2 GHz.
Quad core CPU	An Intel Quad core CPU running at 2.83 GHz.
GPU	Two NVIDIA GeForce 8800 GTX graphics cards (128 SPs / card).

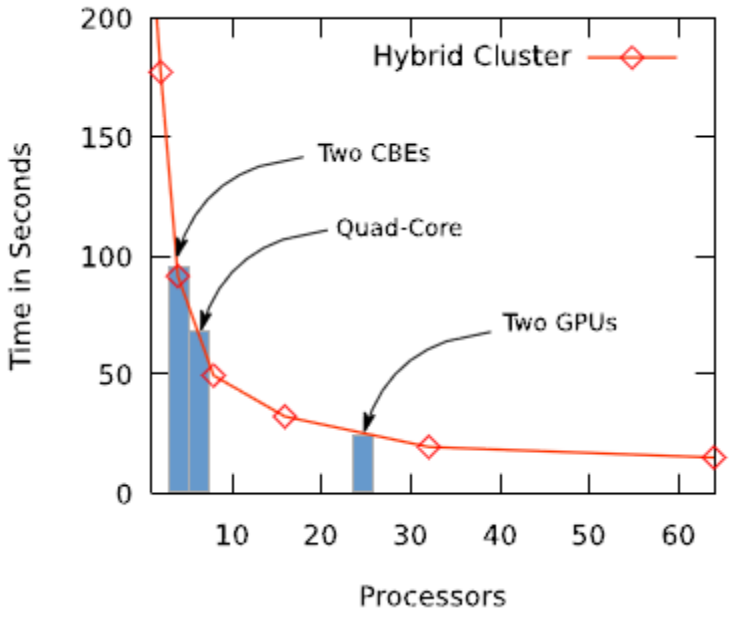

Figure 4-13. Performance comparison of parallel processing systems. This picture is from [99].

A well known drawback of cluster systems is its $\log_2$(number of processors) communication load, which is data transfer between nodes. Therefore the performance of the hybrid cluster is not linearly proportional to the number of processors as shown in Fig. 4-13. The two-GPU system is comparable to a cluster with about 25 processors.

4 .5 **Testing the proposed real time image reconstruction algorithm on GPU**

The proposed real time image reconstruction algorithm, which is termed as a *sliding window* OSEM, was tested using a GPU with 128 streaming processors. For clarity, the off-chip global memory was used for estimates instead of the on-chip shared memory. This will remove all the uncertainty of race conditions, resulting in being the source of the bottle-neck of speed-up.

4. 5 .1 **Hardware Configuration**

An nVidia Geforce® 9800GTX+ graphics card was used for this study. The GeForce® 9800GTX+ has 128 streaming processors based on the nVidia® G80 architecture. The graphics card runs at 738 MHz. Streaming processors run at 1.836 GHz. The global memory (RAM) size is 512Mbytes running at 1.1GHz.

The nVidia CUDA® Linux driver was installed on the Fedora eleven (F11) Linux with a gcc compiler (gcc 4.3 version). The C compiler was downgraded from the gcc 4.4 version, which came with the Fedora 11, to the gcc 4.3 version in order to set up a programming environment. The CPU on the system board is an Intel 3GHz single core processor.

Figure 4-14. nVida Geforce® 9800GTX+ that was installed in a DELL Optiplex GX280.

Fig. 4-14 shows an nVidia GeForce® 9800GTX+ graphics card that was installed in a PCI-e slot of a DELL Optiplex GX280 computer. The graphics card requires external

power in addition to the PCI power in order to operate and takes up 2-slot space due mostly to a cooling fan. The original power supply module in the PC was replaced with a higher capacity power supply.

4. 5 .2 **Thread Configuration**

The image space was set to a 64×32×32 array of voxels as shown in Fig. 4-15. Each voxel is a 0.5mm-side cube. Fig. 4-16 shows the superimposition of two sphere source coordinates and the image space.

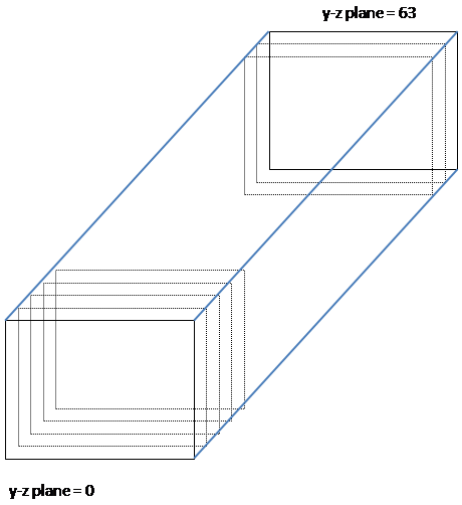

Figure 4-15. Image space for image reconstruction. Each y-z slice consists of 32-by32 voxels.

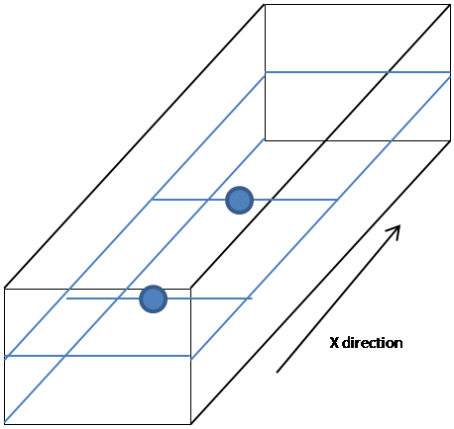

Figure 4-16. Superimposition of two sphere source coordinates and image space. The sphere source on the right hand side is at the center of the image space.

Equation (4.1) was used for image update. Refer to Chapter 3 for more details.

$$x_j^{(s)} = x_j^{(s-1)}(1 - \lambda_s Q_j^{(s)}) + \lambda_s x_j^{(s-1)} \cdot \left(\sum_{l \in S} \frac{G_n(d_j, \sigma)}{\sum_{i=1}^{M} G_n(d_i, \sigma) x_i^{(s-1)}} \right) \tag{4.1}$$

We assigned 16 LORs per subset. The CUDA® code was divided into 5 parts for image reconstruction as shown in Table 4-7. Each part requires a kernel that contains a bunch of threads. The outcome from each kernel was passed to the host computer. The outcome on CPU side was then transferred back to the GPU global memory as an input to the next step. This data transfer was done for debugging purpose. After the 5 kernels were executed, the updated image was used as initial values for the next subset.

Table 4-7. Dividing the image reconstruction algorithm into 5 parts for GPU implementation.

Grid 0	Searching intersected voxels by each LOR.
Grid 1	Calculating the joint solid angle for each voxel.
Grid 2	Assigning a Gaussian kernel for the voxels within the perpendicular distance of 4σ from each LOR.
Grid 3	Calculating the forward projection.
Grid 4	Calculating the backward projection and updating voxel values.

The grid 0 is for finding the intersected voxels by LORs within a subset as shown in Fig. 4-17. The CPU side code (serial code) for the grid 0 is shown in Fig. 4-18. The grid 0 consists of 16 blocks. Each block contains 64 threads, corresponding to 64 slices. The image space has 64 slices along the x-direction axis as shown in Fig. 4-15. For each slice, the intersection between an LOR and a slice is calculated concurrently on GPU. The whole 5 grids are shown in Fig. 4-19.

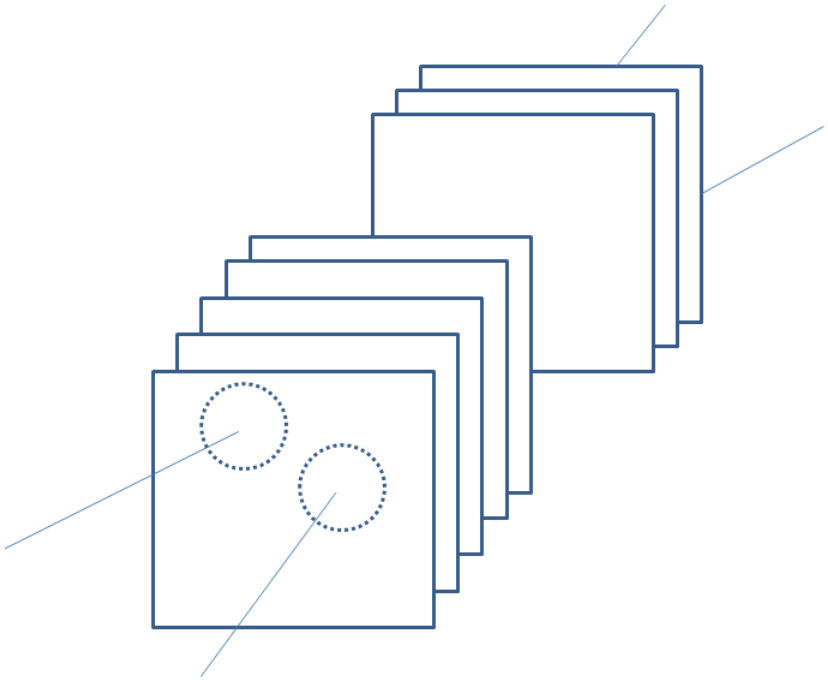

Figure 4-17. Finding intersected voxels by LORs for each subset. Only 2 LORs are shown for simplicity's sake.

```
dim3 grid0(SUB_LORs, 1);
//grid.x=SUB_LORs, grid.y=1, grid.z=1
dim3 blockLOR(64, 1);
//block.x = 64, block.y=1, block.z=1
searchLOR<<< grid0, blockLOR >>>(d_intersection,
                                 d_subset);
```

Figure 4-18. The serial code for the grid 0.

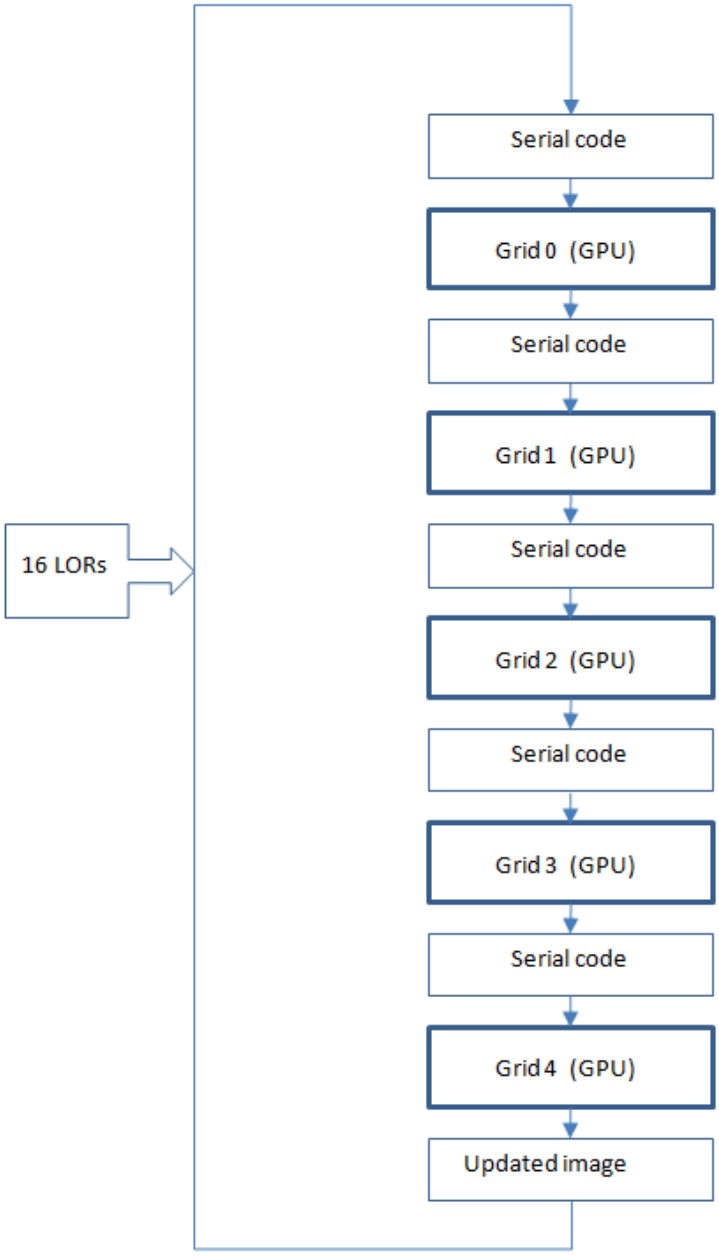

Figure 4-19. Flow diagram of 5 parts of the image reconstruction algorithm for GPU implementation.

For the grid 1, a total of 65536 voxels (64×32×32) were divided into 2×64 blocks. One thread is assigned to one voxel. Each block contains 16×16 threads. The grid with 2×64 blocks was assigned to a graphics card as shown Fig. 4-20.

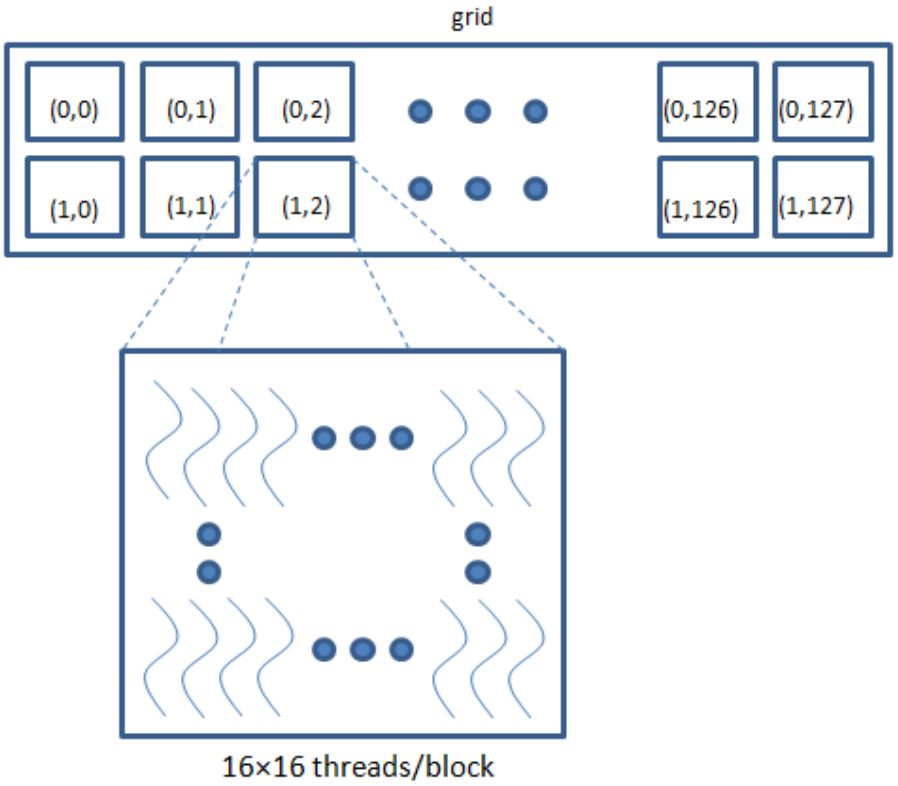

Figure 4-20. blocks and threads for the grid 1.

The mapping of thread blocks into image space is shown in Fig. 4-21. For each slice with 32-by-32 voxels, 4 thread blocks were assigned to the slice and each block contains 16-by-16 threads.

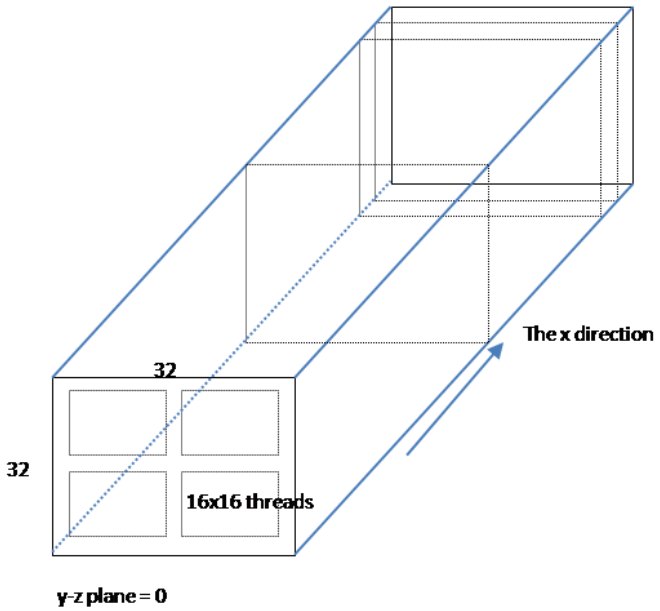

Figure 4-21. Mapping of thread blocks into the image space.

The GeForce® 9800GTX+ graphics card has only 128 streaming processors. The number of SPs is small compared to the total 65536 threads. The *warp* scheduler assigns blocks of threads, termed as *warps*, to one steaming multiprocessor. Because each thread block has 16-by-16 threads, one thread block has 8 warps (16×16 threads/32). Consequently, we have 2048 warps in the grid 1 for the solid angle calculation. The serial code for the grid 1 is shown in Fig. 4-22.

```
dim3 grid1(128, 2);
// gird1.x=128, grid1.y=2, grid1.z=1
dim3 blockSolid(16, 16);
// blockSolid.x=16, blockSolid.y=16, blockSolid.z=1
sensitivity<<< grid1, blockSolid >>>( d_Sensi,
                                      d_intersection);
```

Figure 4-22. Serial code for the grid 1.

The serial code of the grid 2 for applying a Gaussian kernel is shown in Fig. 4-23. After processing of the Gaussian kernel, the grid 3 calculates the sum for the forward projection. The serial code for the grid 3 is shown in Fig. 4-24. It has one thread block. The other thread block does nothing, only for debugging. The active thread block has 16 threads, a thread per one LOR.

```
dim3 grid2(128, 2);
// grid2.x=128, grid2.y=2, grid2.z=1
dim3 blockKernel(16, 16);
// blockKernel.x=16, blockKernel.y=16, blockKernel.z=1
gaussKernel<<< grid2, blockKernel >>>( d_SumOverJ,
                                       d_Qi,
                                       d_Map,
                                       d_GaussKernel,
                                       d_Sensi,
                                       d_A,
                                       d_B ,
                                       d_intersection,
                                       d_Snapshot);
```

Figure 4-23. Serial code of the grid 2 for assigning a Gaussian kernel.

```
dim3 grid3(2, 1);
// grid3.x=2, grid3.y=1, grid3.z=1
dim3 blockSum(SUB_LORs, 1);
// blockSum.x=SUB_LORs, blockSum.y=1, blockSum.z=1
sum_over_i<<< grid10, blockSum>>>(d_SumOverJ,
                                  d_ForwardLOR);
```

Figure 4-24. Serial code of the grid 3 for the forward projection.

Fig. 4-25 shows a serial code of the grid 4 for updating voxel values. The grid 4 has a 2-by-128 array of blocks. Each thread block contains 256 threads.

```
dim3 grid4(128, 2);
// grid4.x=128, grid4.y=2, grid4.z=1
dim3 blockUpdate(16, 16);
// blockUpdate.x=16, blockUpdate.y=16, blockUpdate.z=1
// execute the kernel <<< n_blockx, n_threads_per_block >>>
imageUpdate<<< grid3, blockUpdate >>>(  d_UpdatedImage,
                                        d_SumOverJ,
                                        d_Qi,
                                        d_Map,
                                        d_GaussKernel,
                                        d_A,
                                        d_B ,
                                        d_intersection,
                                        d_ForwardLOR);
```

Figure 4-25. Serial code of the grid 4 for updating voxel values.

4 .6 **Outcomes**

Reconstructed images using simulated data are shown in Chapter 3. Refer to Chapter 3 for the image reconstruction algorithm. Speed-up of image updating is discussed here.

4. 6 .1 **Reconstruction Time**

Fig. 4-26 shows the processing time of each part on GPU for a subset in the unit of milliseconds. We can see that the processing times for searching intersected voxels (grid 0) and sum for forward projection (grid 3) are almost negligible compared to image updating (grid 4). Most of the processing time was spent both applying a Gaussian kernel and updating estimates. This is due mainly to intensive access to the off-chip global

memory (RAM). We note that the GeForce® 9800GTX+ does not have any cache memory.

Fig. 4-27 shows a screenshot of reconstruction times for each subset. The reconstruction time for each step is also listed. The reconstruction time does not include data transfer time between the host and the GPU. The whole listed reconstruction times were spent on GPU. The *n_loop* in Fig. 4-27 refers to a subset that consists of 16 LORs.

We can also see that the processing time varied on subsets. For example, image updating time for *n_loop (subset)* 167 is 53 milliseconds while it is 42 milliseconds for *n_loop (subset)* 169. For the Gaussian kernel, *n_loop (subset)* 167 spent 15 ms for a Gaussian kernel while *n_loop (subset)* 168 spent 25 ms.

The processing time can be further reduced by using a GPU with more streaming processors. In addition, we can utilize the cache memory. The Fermi architecture in Table 4-2 has a total of 64KB shared memory per SM and additional L2 cache memory. Once the cache memory size is large enough for image processing, the processing time will be reduced dramatically.

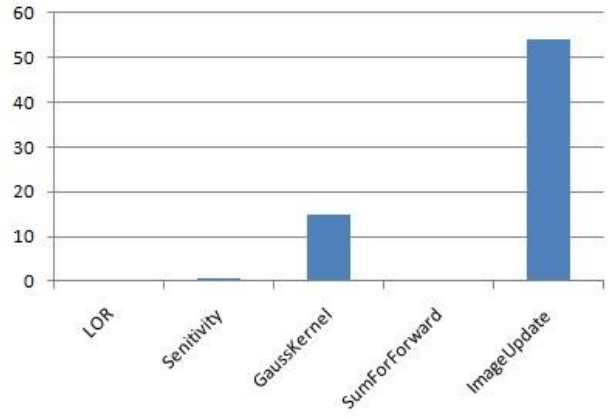

Figure 4-26. Processing time of each step for subset #167. The processing time is in the unit of milliseconds.

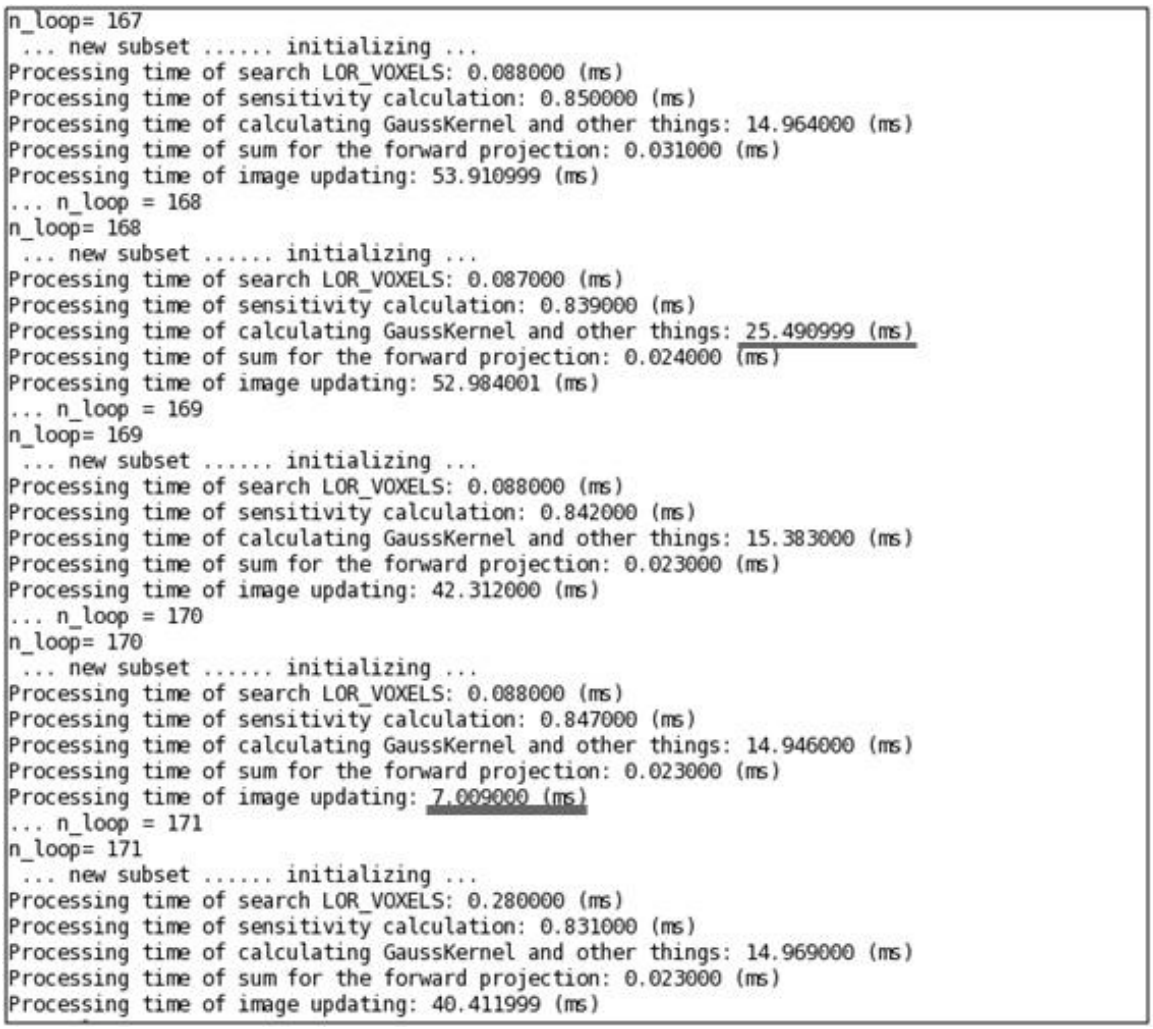

Figure 4-27. Screenshot of reconstruction times.

4 .7 **Summary**

In this chapter, the proposed image reconstruction algorithm was tested on a CUDA-enabled GPU. The test showed significant improvement in reducing reconstruction times. Further improvement is expected in the future work since the off-chip memory (DAM) access time takes up a great portion of the image reconstruction time.

Chapter 5
Prototype of the PET Imaging Probe System

In this chapter, a first-generation prototype of the PET imaging probe system is presented. The prototype system consists of a pixilated NaI(Tl) detector (a probe) and a cluster of BGO block detectors (a partial ring detector). The coincidences between the NaI(Tl) detector and the BGO block detectors were taken and stored in list mode. The image reconstruction algorithm presented in Chapter 3 was used for image reconstruction.

5 .1 A Pixilated NaI(Tl) Detector for a High Resolution Imaging Probe

A pixelated NaI(Tl) detector was built to be used as the high resolution imaging probe. An array of pixelated NaI(Tl) crystal was coupled to a 2-by-2-inch position sensitive PMT (Hamamatsu® H8500). Optical grease was used to couple the NaI(Tl) module and the PSPMT. The PSPMT has 64 uniformly pitched anode outputs that are routed to a charge division circuit that is followed by a front end readout circuit.

5. 1 .1 Testing the PSPMT with Green LED Light

Fig. 5-1 shows an illustration of a position sensitive PMT. The Hamamatsu® H8500 PSPMT has an 8-by-8 array of anodes. 8-by-8 metal channels are visible through

the glass window. Fig. 5-2 shows the illustration of metal channel dynodes. Electrons are multiplied in each channel. The dimensions are $52\times52\times28mm^3$ and the effective front area is $49\times49mm^2$. The pitch is 6.08mm and each pixel size is $5.8\times5.8mm^2$.

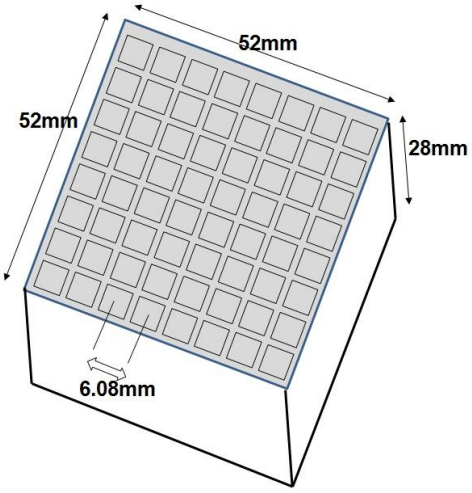

Figure 5-1. HAMAMATSU H8500 PSPMT. This picture was adapted from [101].

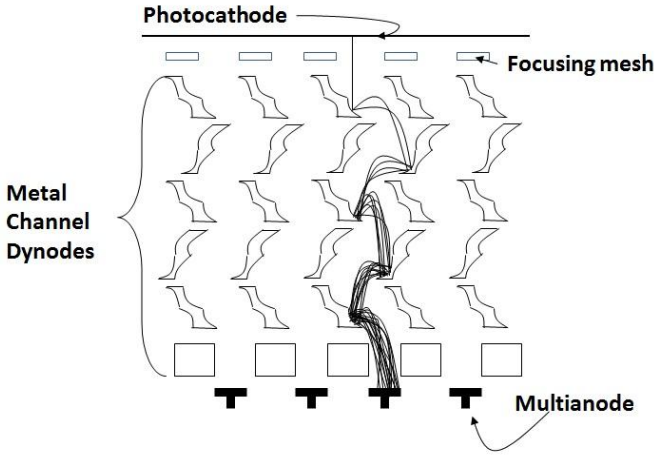

Figure 5-2. Metal channel dynodes type multi-anode PMT. This picture was adapted from [102].

The flat panel PSPMT was tested using LED light. Green LED light was directly illuminated to the PSPSMT front window. The peak intensity of NaI(Tl) emission is approximately 410nm. The spectrum of green light ranges from 495 through 570nm. A

typical spectral response of a Hamamatsu H8500 PSPMT is shown in Fig. 5-3. Some properties of NaI(Tl) are shown in Table 5-1.

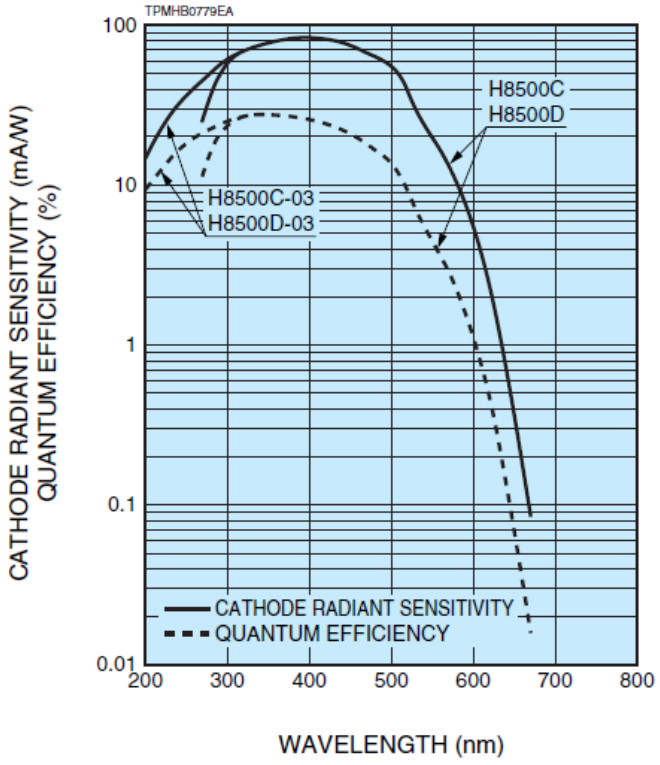

Figure 5-3. Typical H8500 spectral response. [101].

Table 5-1. Properties of NaI(Tl). This table was adapted from [103].

Density	$3.67 g/cm^3$
Melting Point	6.46Å
Hardness	2Mohs
Hydroscopicity	Little
Decay constant	Fast620ns, Slow250 ns
Radiation length	2.6cm
Emission Wavelength	Fast310nm, Slow410nm
Light yield	$52 – 56 \times 10^3$ photons/MeV
Refractive Index (Maximum emission wavelength)	1.85
Linear attenuation coefficient	(for 511keV γ-rays) $0.34 cm^{-1}$
Light yield	Fast 6.5×10^3, Slow4×10^4 photon/Mev
Energy resolution (for 511keV)	About 8%
Flatness	λ/4 @ 633nm
Time resolution (for Co-60; Beta, 1.2MeV, and 1.3MeV)	1000ps

The 64 anodes were coupled to a charge division circuit. The charge division circuit (CDC) consists of an array of resistors and is shown in Fig. 5-4. The charge division circuit (CDC) is a resistor array that connects between anodes and converts an 8-by-8 array of anode signals to 4 outputs for position estimation. Four outputs from the CDC are marked as A, B, C, and D in Fig. 5-4. A schematic of position estimation using the four outputs is shown in Fig. 5-5.

The four outputs from the CDC are then routed to a front-end readout circuit. The front-end readout circuit is shown in Fig. 5-6. Each output from the CDC is shaped and amplified in the front-end circuit. The front-end circuit also generates a trigger pulse. The LED module for focusing the LED light on the PSPMT is shown in Fig. 5-7. The LED module contains a green LED that is activated by a tail pulse generator.

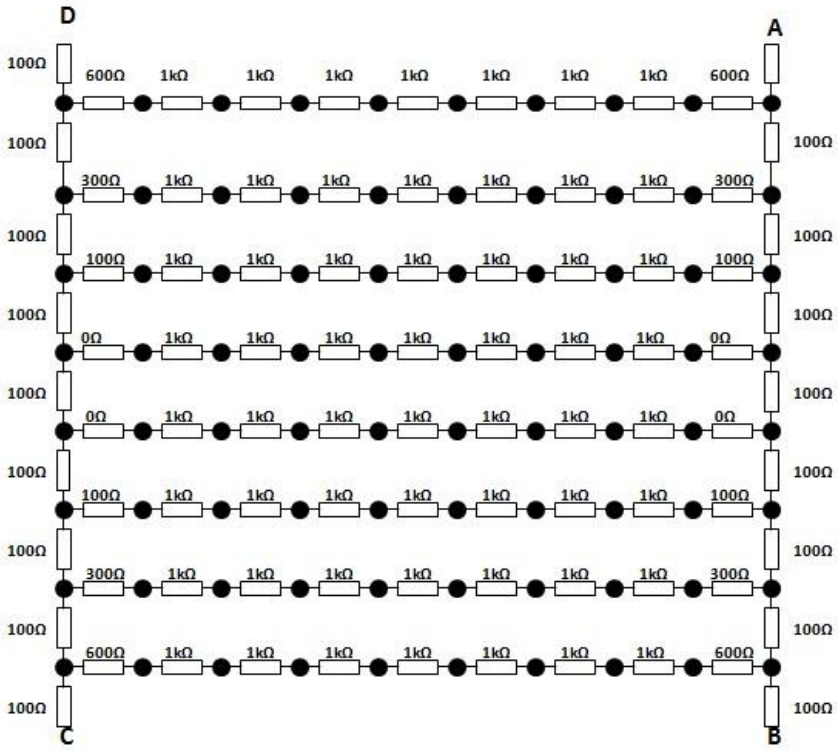

Figure 5-4. Diagram of a charge division circuit. This picture was adapted from [104].

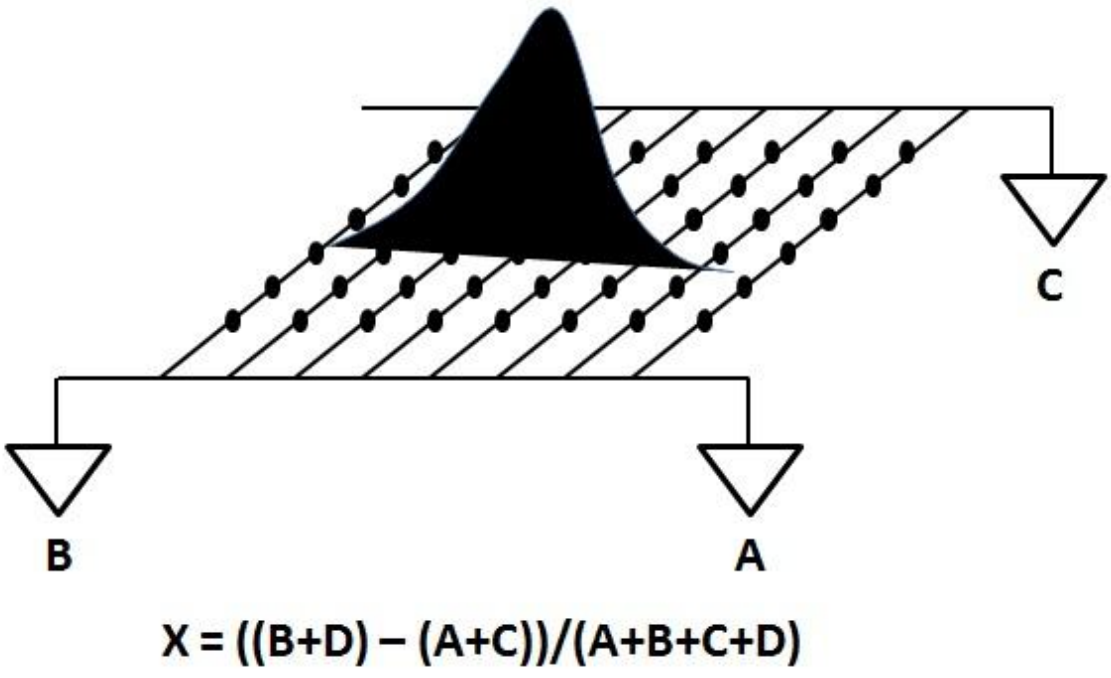

Figure 5-5. Principle of position estimation. This picture was adapted from [105].

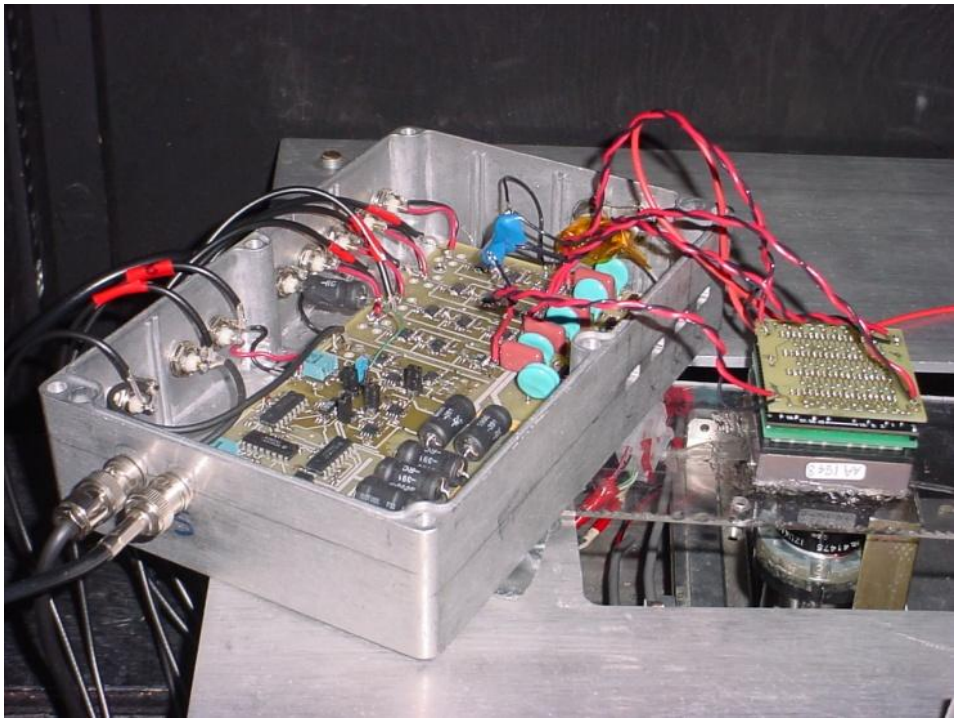

Figure 5-6. Front readout electronics and the charge division circuit inside a light-tight box.

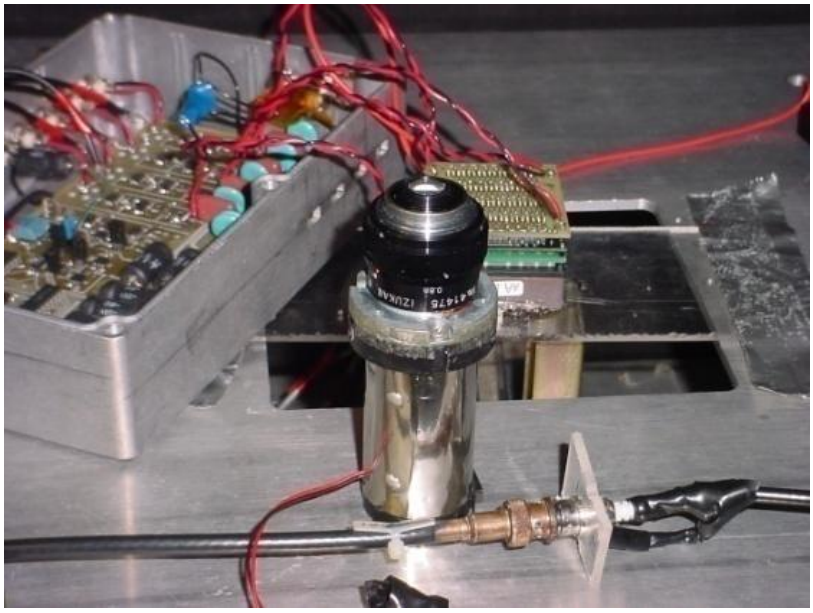

Figure 5-7. LED container that houses a green LED.

Fig. 5-8 shows a tail pulse generator. The rising time was set to 0.2 μsec and the falling time was set to 1 μsec. Fig. 5-9 shows the calibration set-up. The LED module was mounted on an x-y translator. The PSPMT, an x-y translator, and a front-end readout circuit were placed inside a light-tight black box. Green LED light was illuminated through a transparent plastic panel onto the PSPMT.

Figure 5-8. Tail pulse generator (far left). The tail pulse generator produces exponentially decaying pulses. These pulses power the LED that simulates scintillation pulses.

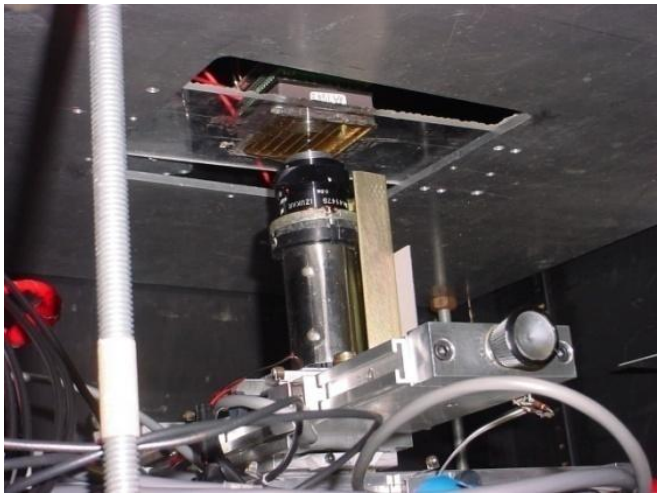

Figure 5-9. Calibration set-up inside a light-tight black box.

Fig. 5-10 shows a sum signal and a negative-active gate pulse. We used a CO 4010 NIM module to control the width of the GATE pulse. The 4 shaped outputs from the front-end electronics were routed to a peak sensing ADC (C.A.E.N.® v785). The GATE pulse is the fast NIM level signal. The input voltage range of the peaking sensing ADC is 0 ~4 V.

Figure 5-10. Sum signal of 4 outputs from the CDC circuit (the positive analog signal). The gate pulse for the peak-sensing ADC (the negative pulse).

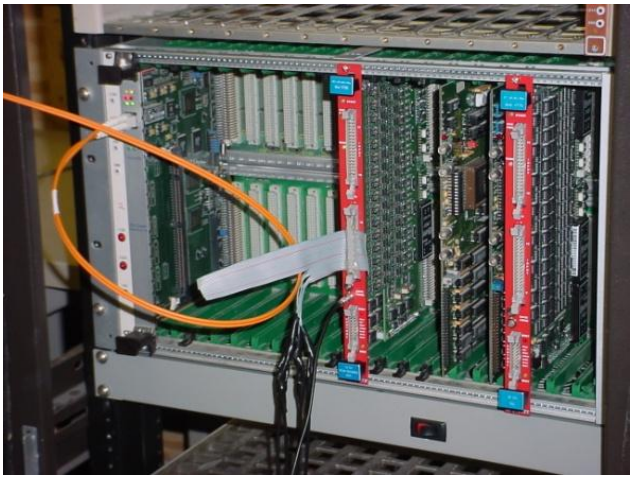

Figure 5-11. VME (Versa Module European) interface card (far left) and a V785 peak-sensing ADC card (the second one from the left).

Fig. 5-12 shows the peak-detection operation of V785. The peak signal within the active GATE pulse is detected and held. The sustained peak value is then digitized after the GATE pulse is inactivated.

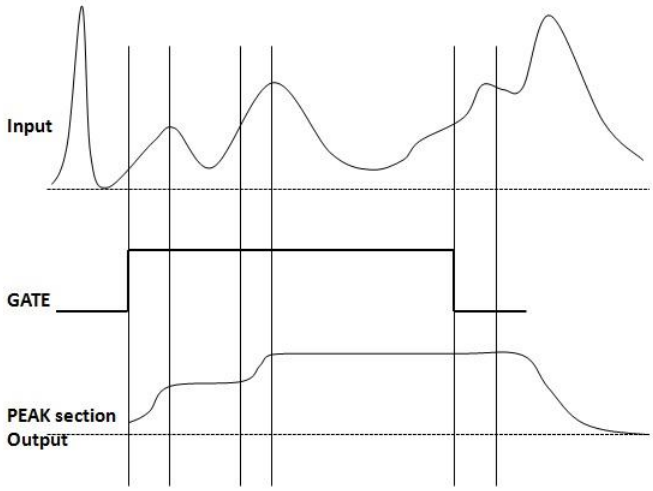

Figure 5-12. Detection of the peak signal. This picture was adapted from [106].

The LED module was translated along the horizontal and vertical axes at intervals of ¼ in. as shown Fig. 5-13. The interaction positions were estimated at each translated coordinates. The position estimation was based on the centroid of 4 peak-sensing ADC values. Five histograms from 5 translated coordinates were then superimposed to show the relative distance and intensities. The superimposition of 5 histograms is shown in Fig. 5-14. The PSPMT requires a high voltage bias. The bias voltage was set to -800V for the PSPMT.

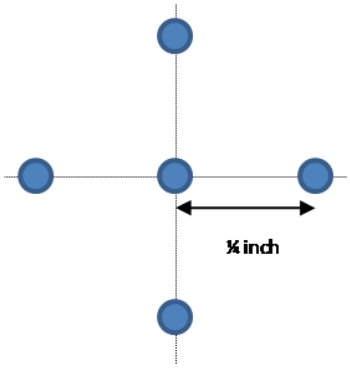

Figure 5-13. Translations of the green LED focal spot at intervals of ¼ in.

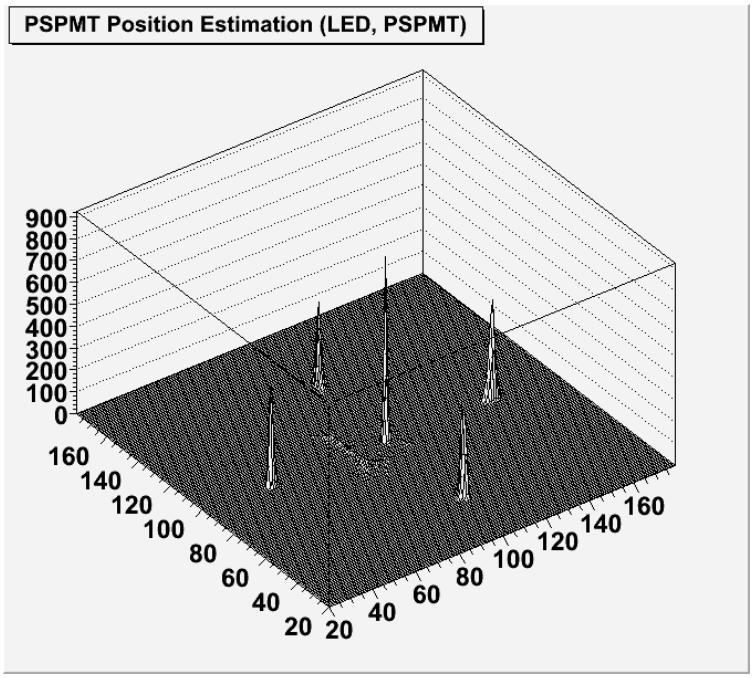

Figure 5-14. Superimposition of the 5 count-histograms. The distance between two peaks along an axis is ¼ in.

In order to observe finer separations, the distance between LED focal spots was reduced to 1/8 in. The superimposition of count-histograms is shown in Fig. 5-15. The translation pitch was then further reduced to 1/16 in. and the histograms are shown in Fig. 5-16.

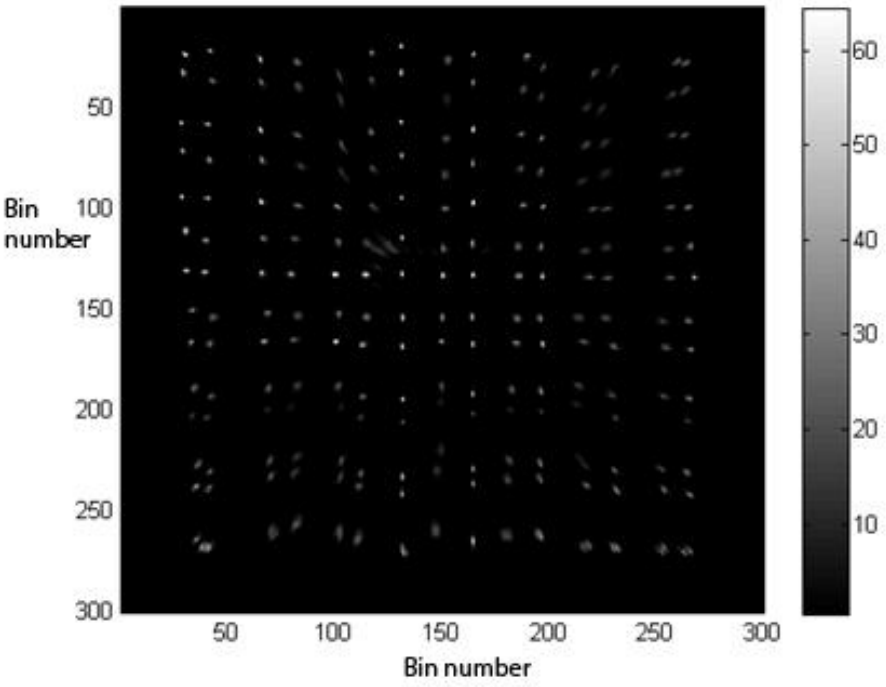

Figure 5-15. The superimposition of counts histograms. The actual distance two peaks along an axis 1/8 in.

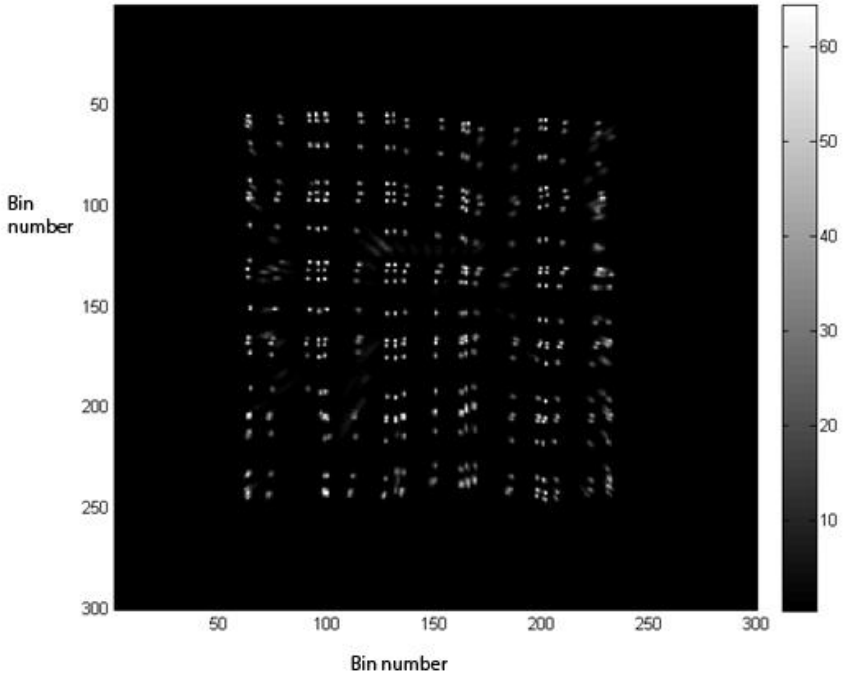

Figure 5-16. The superimposition of counts histograms. The sampling locations are at intervals of 1/16 in.

Fig. 5-16 shows clusters of interaction positions. A similar phenomenon was observed in a flood image. Fig. 5-17 shows a flood field irradiation image of YAP(Ce). The raw image shows clusters of estimated crystals. The clusters appeared due to the square-shaped metal channels in the PSPMT.

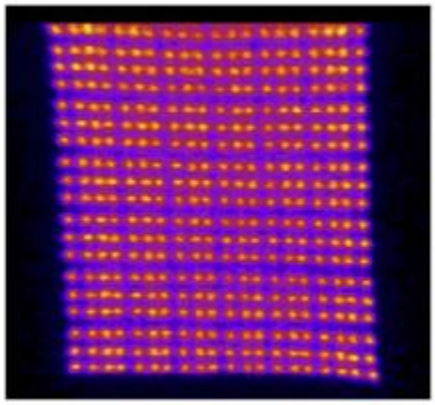

Figure 5-17. Position estimation from an H8500 PSPMT coupled to $2\times2\times25mm^3$ YAP:Ce. This picture is from [107]. A Na-22 flood image was taken at the distance of 15cm.

Table 5-2 shows characteristics of YAP and NaI(Tl). We can see YAP has higher energy resolution and higher density than NaI(Tl). Therefore NaI(Tl) flood images may show different raw images.

Table 5-2. Comparison of characteristics of crystals. This table is from [108].

Detector	Effective atomic no (Z)	Density (g/cm^3)	Scintillation decay time (ns)	Photon yield (per keV)	Linear attenuation coefficient (cm^{-1}) of 511keV	Energy Resolution (% at 511kev)
NaI(Tl)	51	3.67	250	38	0.34	7.8
BGO	74	7.13	300	6	0.96	10
BaF2	54	4.89	0.6	2	0.44	11.4
GSO	59	6.71	50	10	0.67	9.5
LSO	66	7.40	40	29	0.87	10.1
YSO	34	4.53	70	46	0.39	12.5
LYSO	65	7.2	50	25	0.87	20
YAP	39	5.4	27	18	0.46	2.5
LaBr3	-	5.3	5	61	-	5.3

Fig. 5-18 shows another flood field irradiation image of NaI(Tl). Each crystal measures $1.8\times1.8\times6mm^3$. In this raw image, the clusters are not shown. This could be due to lack of crystal-separation capability due to lower density and lower energy resolution than YAP.

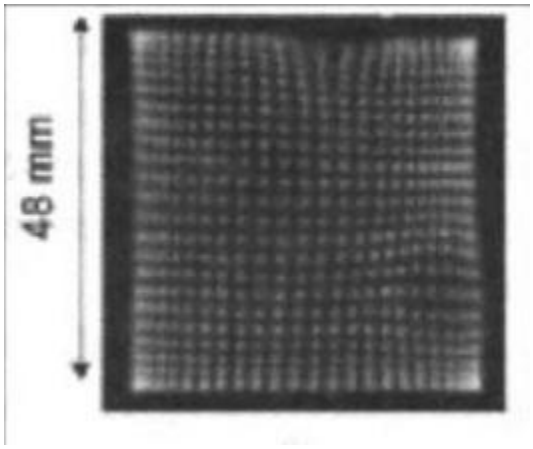

Figure 5-18. Co-57 flood field irradiation image of NaI(Tl). The NaI(Tl) module was coupled to a Flat Panel PSPMT. This picture is from [105, Chapter 9].

5. 1 .2 Assembling of a NaI(Tl) Crystal module with the PSPMT

5.1.2.1 Na-22 Energy Spectrum in NaI(Tl)

Na-22 source disks are easy to handle compared to F-18 FDG solutions. F-18 FDG is obtained from a nearby cyclotron facility due to its 110 minutes decay time. In this study, Na-22 was used for calibrations. A typical Na-22 pulse height spectrum in NaI(Tl) is shown in Fig. 5-19. Equation (5.1) shows the kinetic energy of recoil electron due to Compton scattering.

$$E_e = E_{in}\left[\frac{\frac{E_{in}}{511KeV}(1-\cos\theta)}{1+\frac{E_{in}}{511KeV}(1-\cos\theta)}\right] \tag{5.1}$$

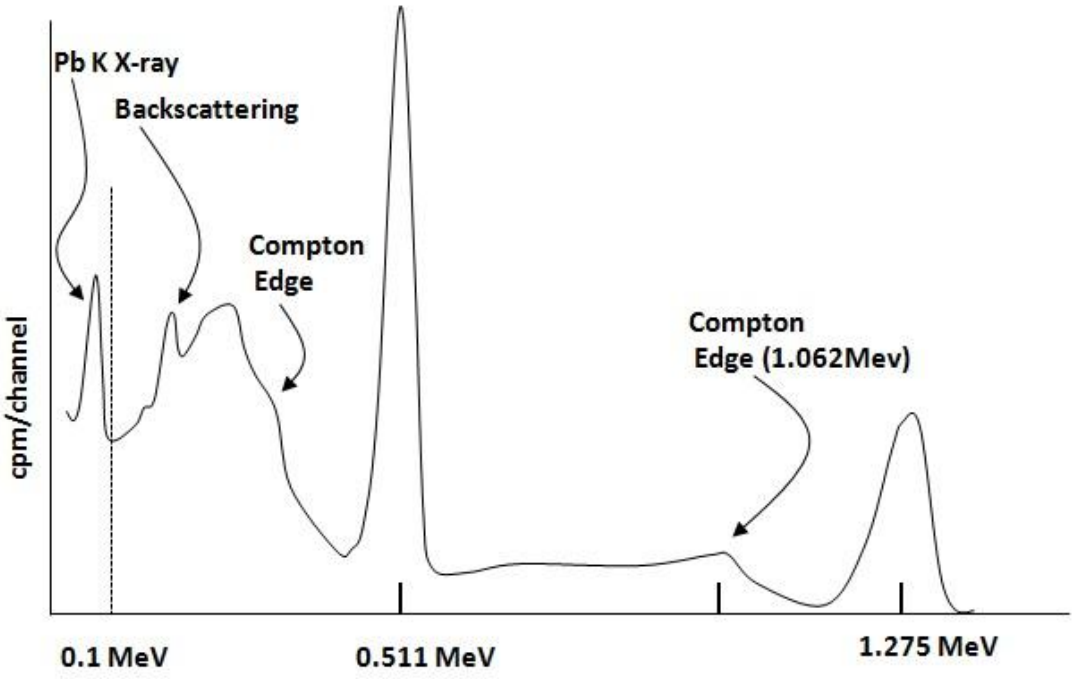

Figure 5-19. Typical Na-22 pulse height spectrum in NaI(Tl). This picture was adapted from [109].

5.1.2.2 **Assembling of the NaI(Tl) Detector Module**

A 4-inch-diameter NaI(Tl) crystal array that was coupled to a 2 inches-by-2 inches PSPMT is shown in Fig. 5-20. Each NaI(Tl) crystal measures 2mm-by-2mm, 10mm thick. Optical grease was applied between the PSPMT and the NaI(Tl) crystal array. The PSPMT covers only part of the NaI(Tl) array as shown in Fig. 5-21.

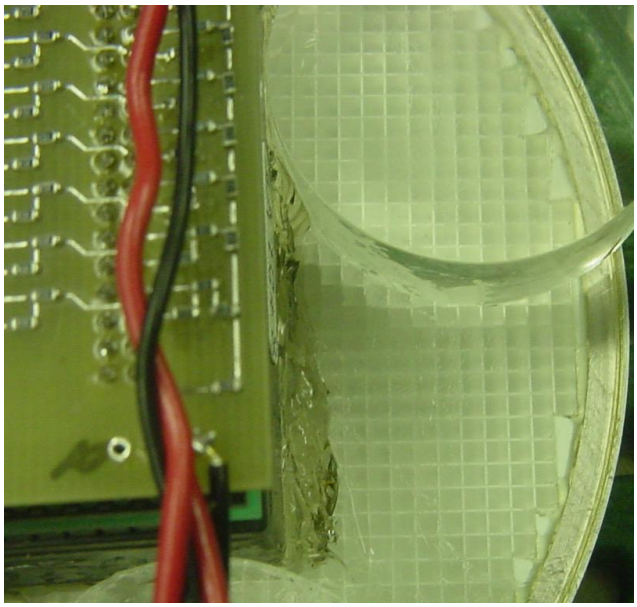

Figure 5-20. An array of 2mm×2mm, 10mm thick NaI(Tl) crystals.

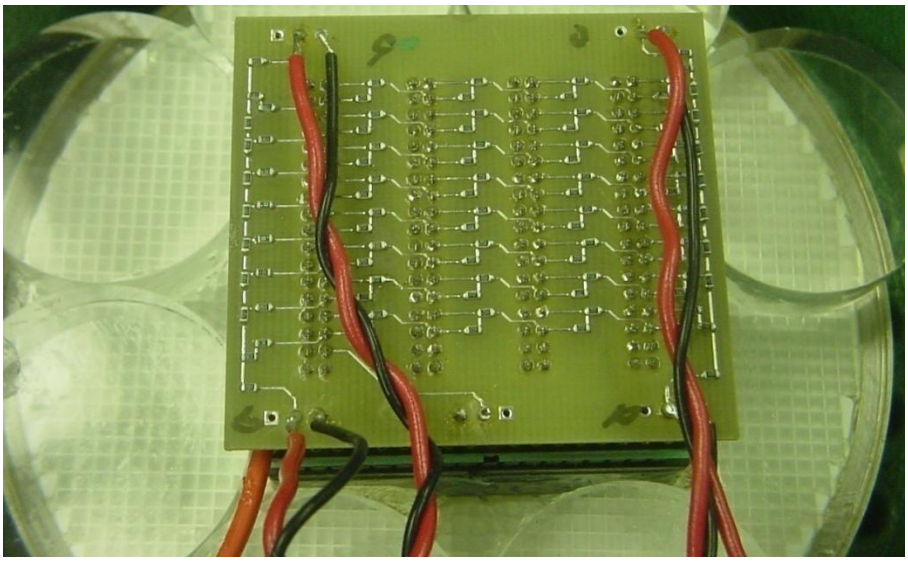

Figure 5-21. The NaI(Tl) crystal array and the PSPMT assembly.

The final housing of both NaI(Tl) crystals and the PSPMT is shown in Fig. 5-22. One of the 4 shaped-signals and the trigger signal were observed. The trigger pulse was sufficiently ahead of the peak of the shaped NaI signal in Fig. 5-23.

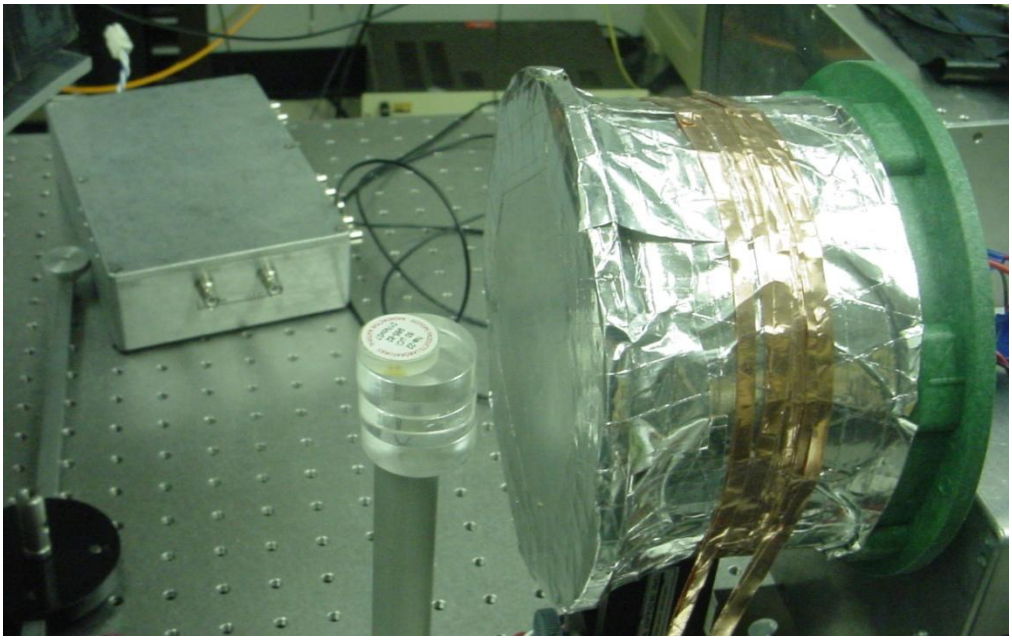

Figure 5-22. Light-tight container that houses the NaI(Tl) crystal array and the PSPMT.

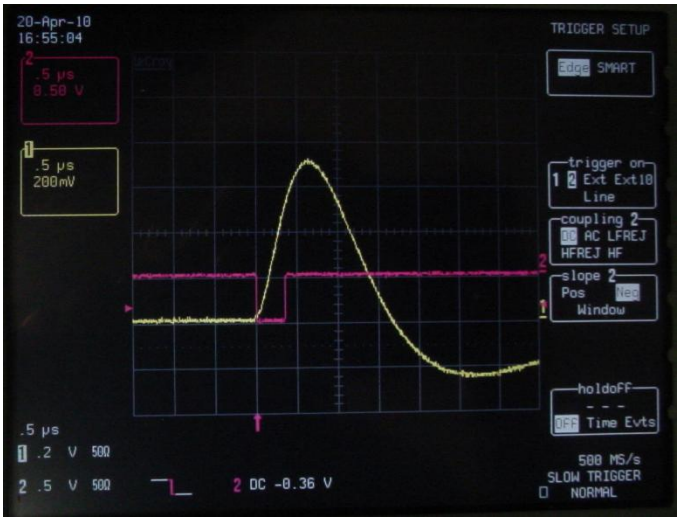

Figure 5-23. Trigger pulse and a shaped channel signal (analog).

5 .2 **Gain Adjustment of BGO (bismuth germinate, $Bi_4Ge_3O_{12}$) Block Detectors**

The position-sensitive BGO block detectors are designed to operate in coincidence with the hand-held intra-operative PET imaging probe for tumor imaging. The spatial resolution of the BGO block detector is lower than that of the NaI(Tl) detector.

A BGO block detector consists of 4 PMTs that are coupled to a block of BGO cuts as shown in Fig. 5-24. Each PMT of the BGO block detector has an adjustable gain. The gain of each PMT was adjusted to produce the same amplitude signal.

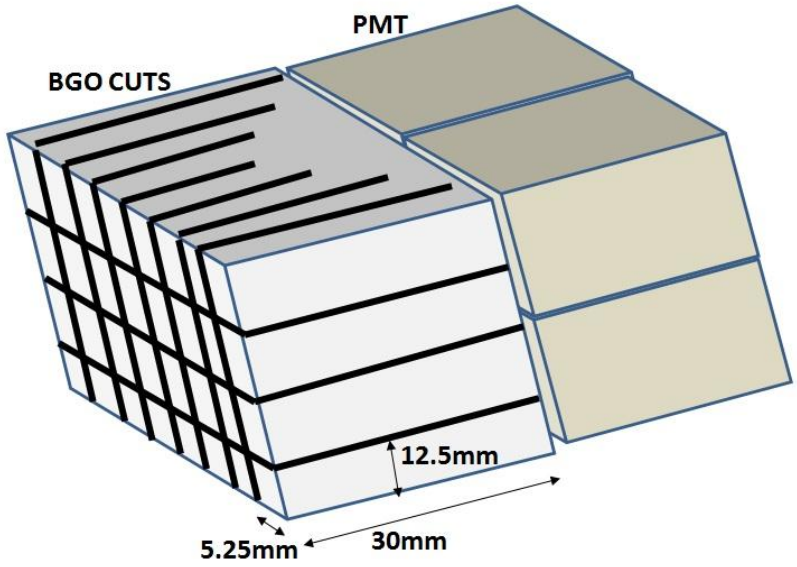

Figure 5-24. 4 PMTs in a BGO block detector. This picture is not to scale. Each cut measures $5.25 \times 12.5 \times 30 mm^3$.

5. 2 .1 **Characteristics of BGO**

Fig. 5-25 shows typical pulse height spectra of Cs-137 (662keV) and Na-22 (511keV and 1275keV) in BGO.

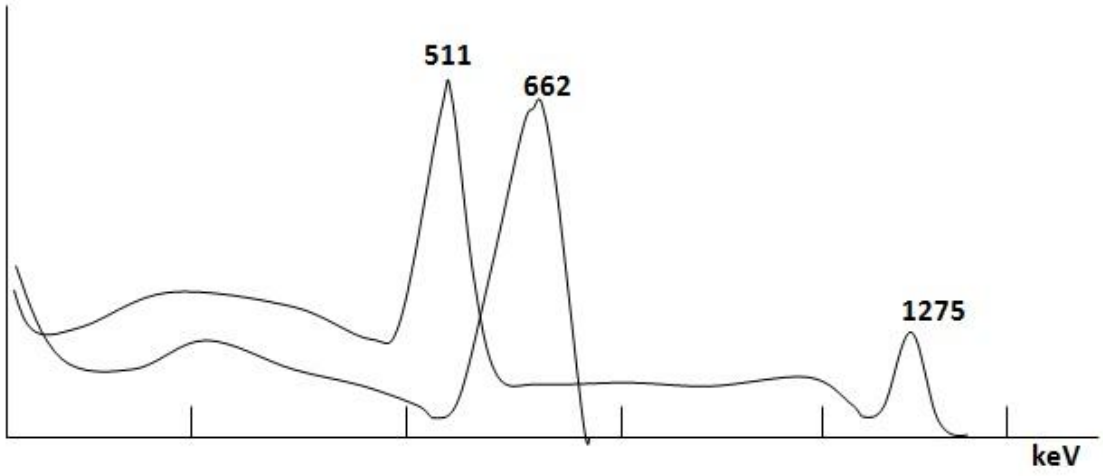

Figure 5-25. Pulse height spectra of Cs-137 and Na-22 in BGO. This picture was adapted from [110].

The linear attenuation coefficient μ, in cm^{-1}, and photo-fraction ϕ for lutetium oxyorthosilicate doped with cerium (LSO), bismuth germinate (BGO) crystals, and NaI(Tl) are listed in Table 5-3.

Table 5-3. Typical characteristics of LSO, BGO, and NaI(Tl). This table was adapted from [111].

	LSO(Ce)	BGO	NaI(Tl)
μ at 140 keV (cm^{-1})	9.7	12.1	2.4
μ at 511 keV (cm^{-1})	0.86	0.95	0.33
ϕ at 511 keV	0.33	0.41	0.18

The rise time of BGO pulse shape is shown in Fig. 5-26. The timing spectrum of BGO is shown in Fig. 5-27. The start of the timing measurement was triggered by a CsF crystal and the trigger from a BGO crystal stopped the measurement. Na-22 was used as a radioactive source.

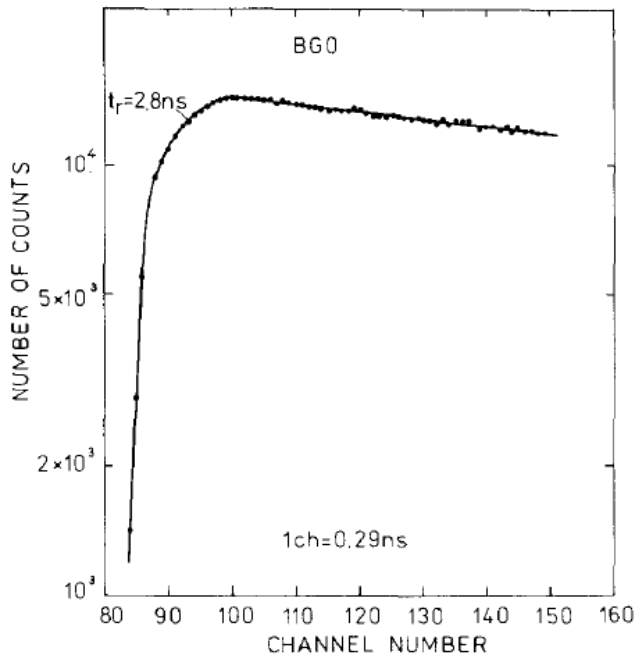

Figure 5-26. Initial part of BGO light pulse shape. This picture is from [110].

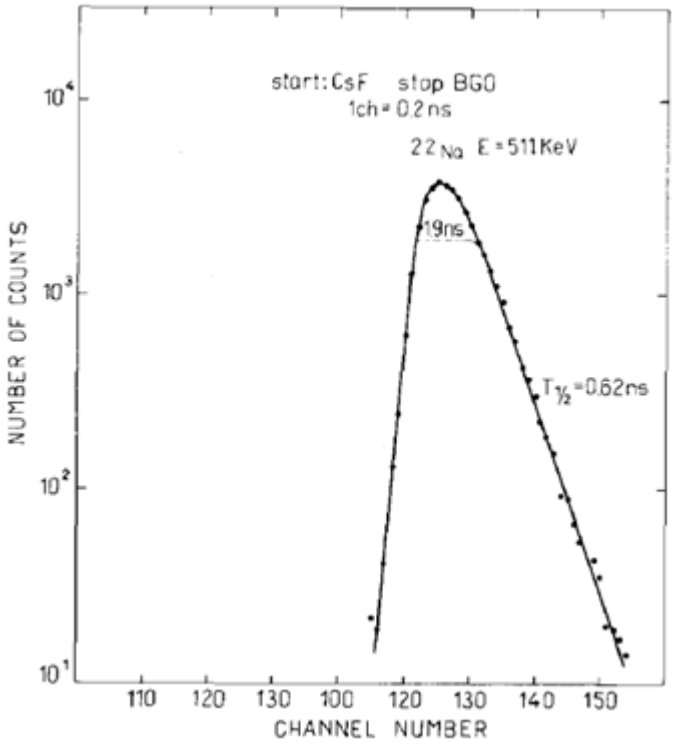

Figure 5-27. Timing spectrum between BGO and CsF using Na-22 (511KeV). This picture was adapted from [110].

The FWHM of the timing spectra of BGO and NaI(Tl) are shown in Table 5-4. The FWHM of the Na-22 timing spectrum was roughly 2.1 ns for BGO. The timing resolution of NaI(Tl) was better than that of BGO.

Table 5-4. Timing resolution of BGO and NaI(Tl). This table is from [110].

Energy		BGO		NaI(Tl)	
		FWHM (ns)	FWTM (ns)	FWHM (ns)	FWTM (ns)
Na-22	511keV	1.9		0.75	
	≥ 100keV	2.1	4.4	0.9	2.0

5. 2 .2 **Na-22 Source Disk**

Na-22 source disks were used as radio-active sources for calibrations. Na-22 disintegrates in two ways; beta decay and electron capture. The level diagram of the Na-22 decay is shown in Fig. 5-28 [107]. Beta decay has its own two paths as shown in Fig. 5-28 [112] [113].

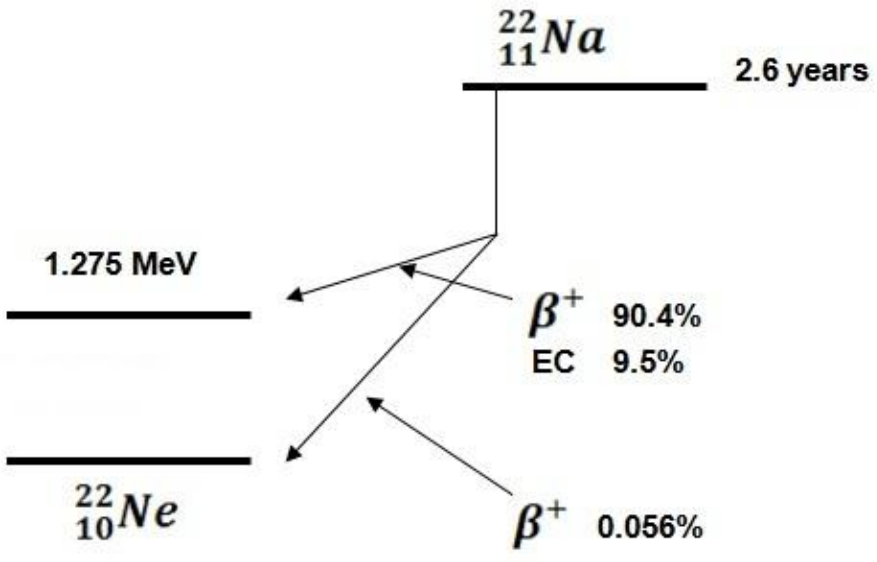

Figure 5-28. Level diagram of Na-22 disintegration. This picture was adapted from [114].

The endpoint energy of Na-22 positrons is 545keV [113]. The kinetic energy of positrons from Na-22 is higher than that of F-18. Even though the Na-22 source is enclosed in an acrylic container, the positron can penetrate the container. The positron range of F-18 in water and the positron range of Na-22 in Lucite are compared in Fig. 5-29 [113]. Fig. 5-29 (a) shows the scatter plot of positron end-points of F-18 in water and Fig. 5-30 (b) shows the scatter plot of positron end-points of Na-22 in Lucite. Fig. 5-29 (c) shows the projection of the end-points onto one axis. The dashed line represents the projection of Na-22. Fig. 5-29 (d) shows absolute end-points from the origin. The broken-line shows the end-point distribution of Na-22 positrons in Lucite. We can see some degree of similarity of the two distributions in Fig. 5-29 (d). This positron range of Na-22 in Lucite will further blur reconstructed images.

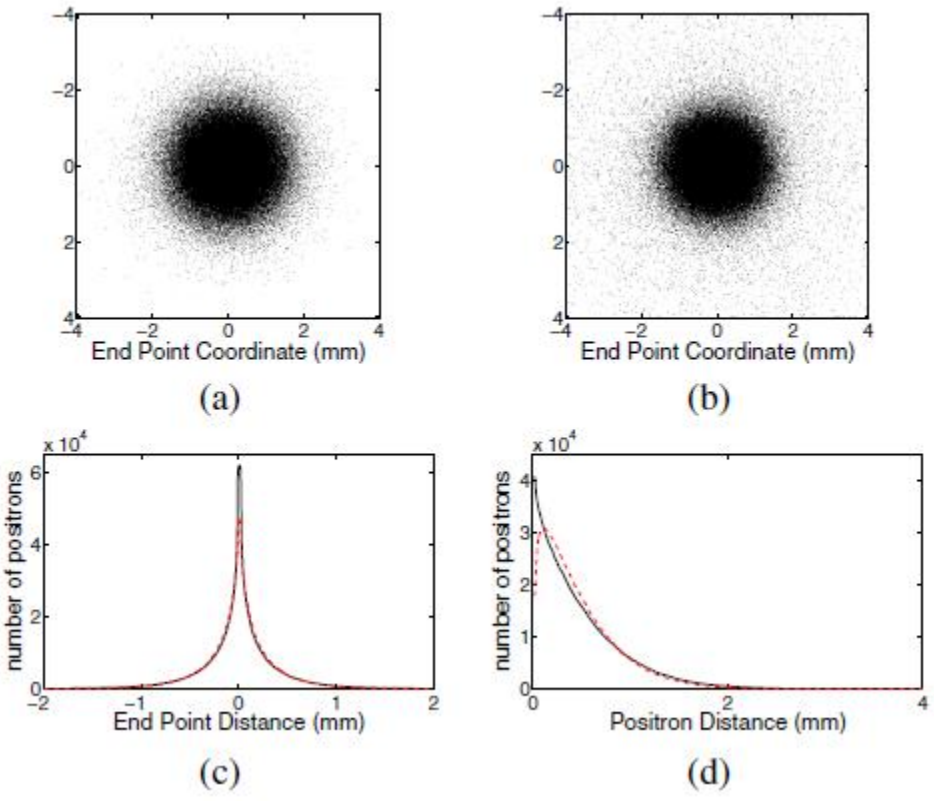

Figure 5-29. Na-22 in Lucite and F-18 in water. These pictures are from [115].

5. 2 .3 **BGO Gain Adjustment in Coincidence with a Single LSO Crystal**

Each BGO block detector has 4 PMTs. Each PMT is coupled to an array of 4×2 BGO cuts. A single small LSO coupled to a PMT was aligned with a BGO block detector in order to make electronic collimation. The gain of PMTs in the BGO block detectors was adjusted by taking coincidences between the single LSO crystal and one of 4×2 cuts.

5.2.3.1 **A Single LSO Crystal Detector**

A single LSO crystal was coupled to a 12-stage PMT. The PMT was coupled to an ORTEC® photo-multiplier base 265A. The photomultiplier base was operated at -2700V.

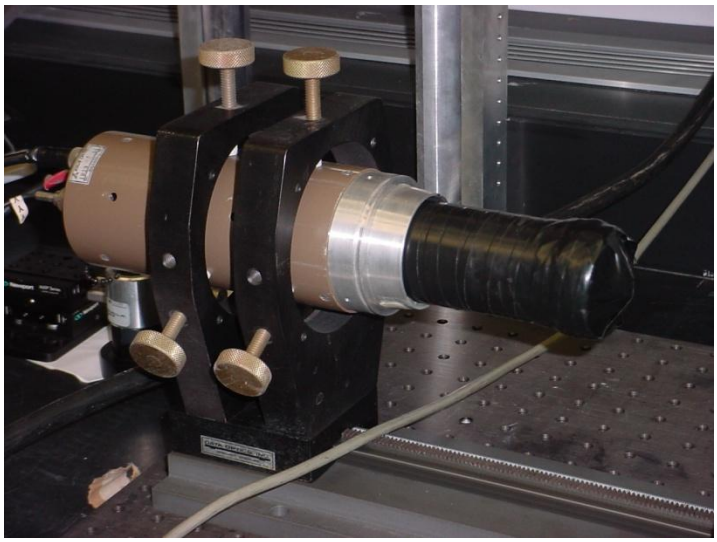

Figure 5-30. Assembly of a PMT base, a PMT, and an LSO crystal wrapped in light-tight tape.

Fig. 5-31 shows the anode signal and the dynode signal from the LSO detector. The lower negative tail pulse signal is the anode signal. The anode signal was routed to a constant fraction discriminator (CFD). A trigger pulse from the CFD is shown in Fig. 5-32. The lower NIM level signal is the trigger pulse from the CFD. The trigger pulse lags

behind the dynode signal, but the dynode signal is to be shaped and amplified. After the shaping stage, the peak position lags behind the trigger pulse.

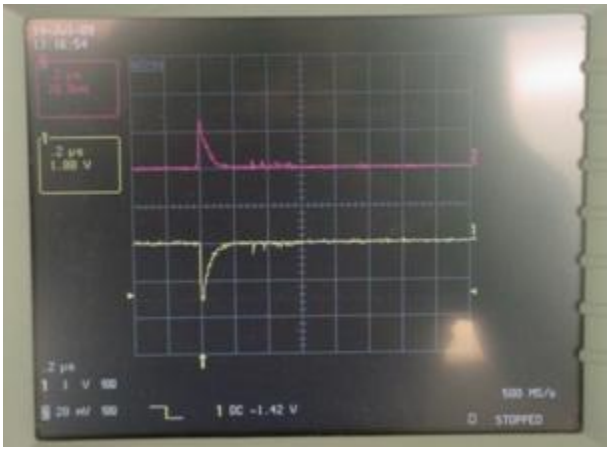

Figure 5-31. Anode (negative) and dynode (positive) signal from the LSO detector.

Figure 5-32. LSO dynode signal and the trigger signal from a constant fraction discriminator. The trigger pulse is about 250 ns behind the dynode signal.

5.2.3.2 Translation Stage for BGO Block Detectors

The BGO block detectors were mounted on an x-y translator to align a BGO crystal with a *single* LSO crystal. The BGO block detector was connected to the front-end electronics. The high bias voltage of BGO block detectors was set to +1500V. The maximum bias voltage is +1600V.

Fig. 5-33 shows a BGO block detector connected to its front-end electronics. The BGO block detector was mounted on the arm of an x-y translator. A Na-22 source disk was placed in between the BGO block detector and the LSO detector. Fig. 5-34 shows a Na-22 source disk that is inserted in a cylindrical holder. Fig. 5-35 shows the single LSO crystal detector, a Na-22 source disk holder, and the BGO block detector mounted on an x-y translator.

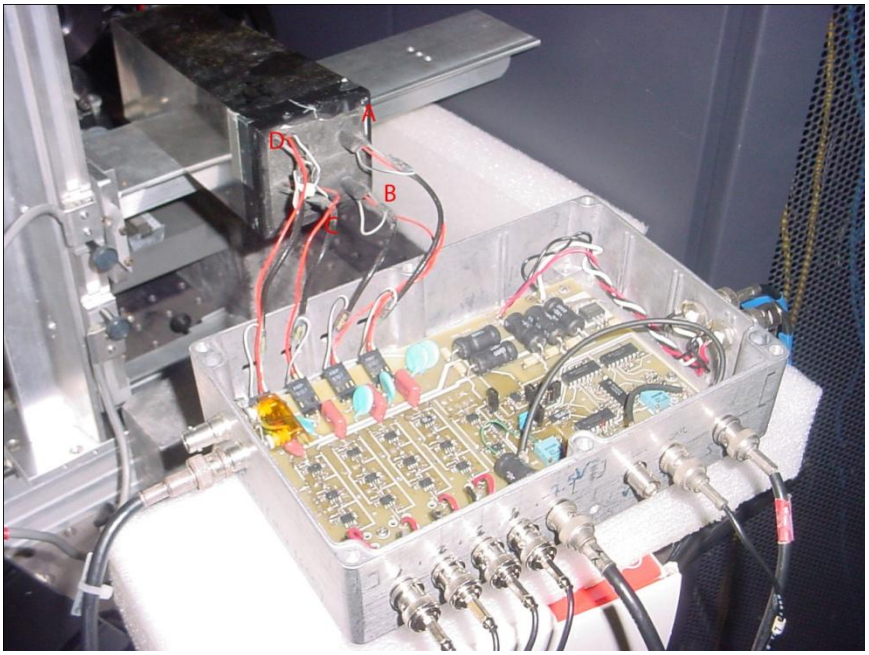

Figure 5-33. BGO block detector that is connected to a front-end readout.

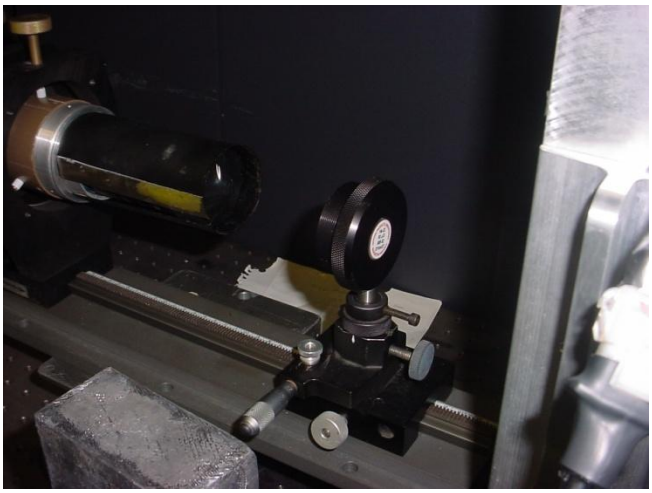

Figure 5-34. Na-22 source disk (60uCi) in the cylindrical holder.

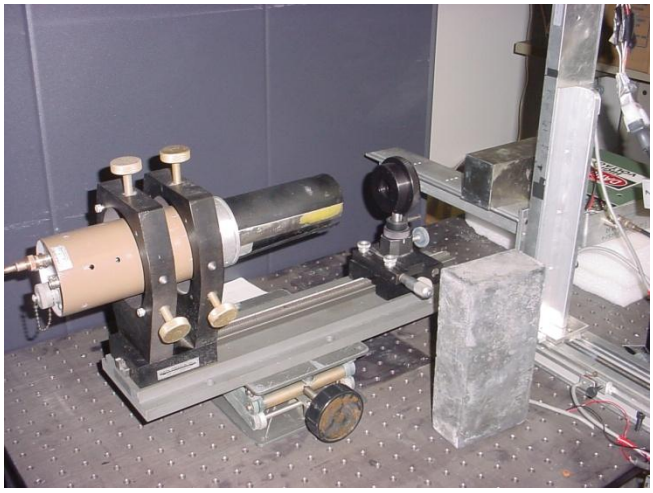

Figure 5-35. Coincidence set-up for the gain adjustment.

5.2.3.3 **Coincidence Pulse Circuit**

Fig. 5-36 shows the block diagram of the coincidence set-up for the gain calibration. NIM Amplifiers and a constant fraction discriminator (CFD) are shown in Fig. 5-37.

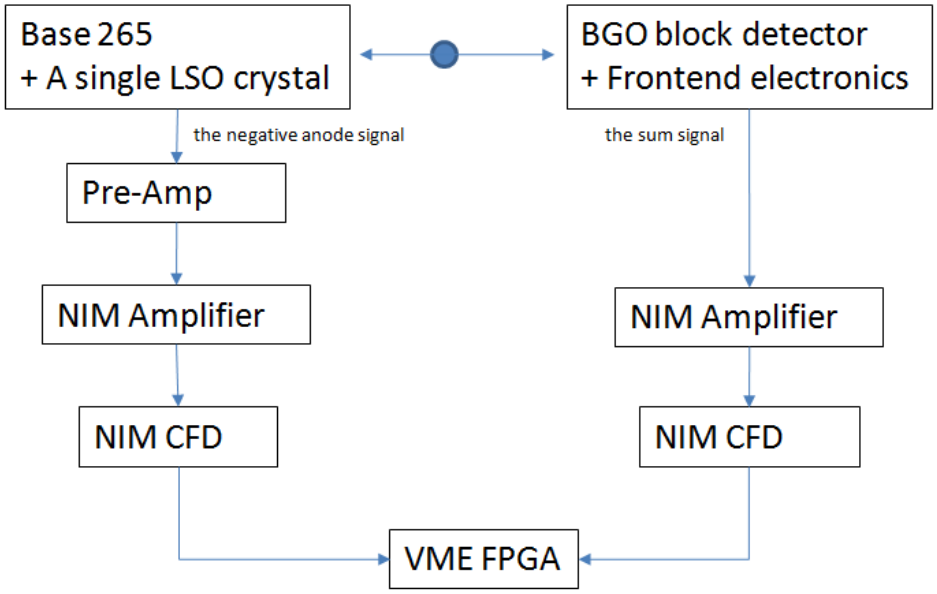

Figure 5-36. Block diagram of the coincidence control.

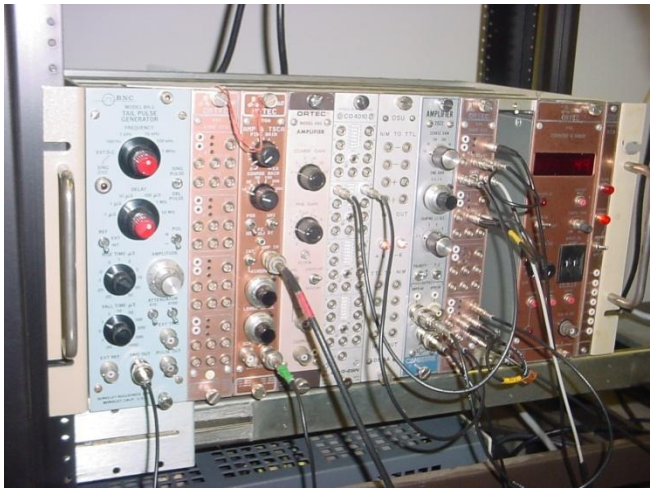

Figure 5-37. NIM amplifiers and constant fraction discriminators (CFDs).

The trigger pluses from the LSO detector and the BGO detector were routed to a pulse delay circuit. Delay was set to zero for this gain adjustment. The two trigger pulses were then routed to a VME field-programmable gate array (FPGA) board. The FPGA board (C.A.E.N.® v1495) is shown in Fig. 5-39. The FPGA board identifies coincidence

pulses from incoming LSO triggers and BGO triggers and interfaces with the host computer through a VME-PCI interface card. The width of the coincidence gate pulse is controlled by the FPGA and the host computer can enable/disable the coincidence gate pulse. The synchronization of the host computer and the FPGA was accomplished by disabling the coincidence pulse while reading out the peak values from the peak-sensing ADC.

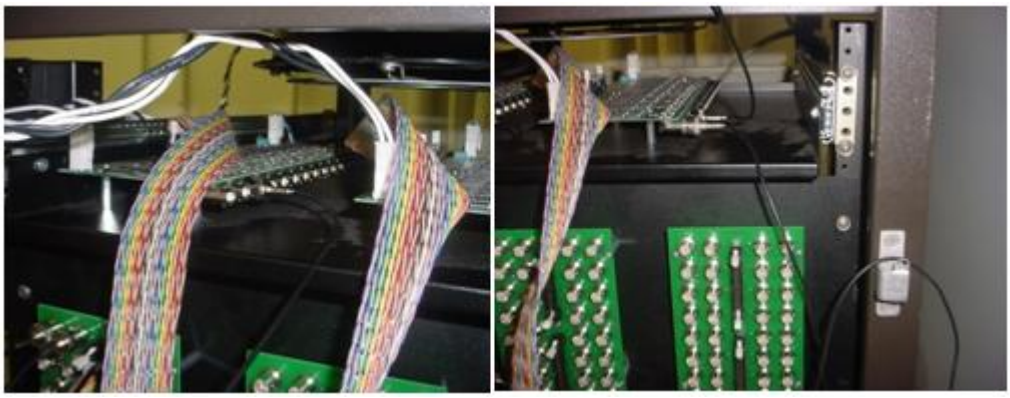

Figure 5-38. Two delay-line boards.

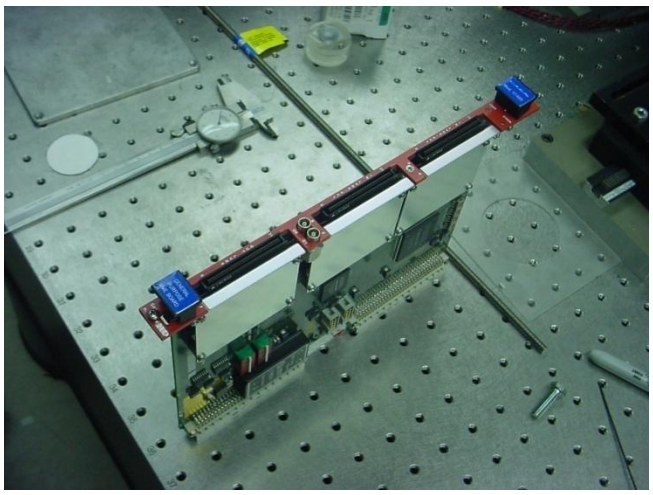

Figure 5-39. VME FPGA v1495®.

5.2.3.4 **Trigger Pulses and Coincidence Gate Pulses**

Fig. 5-40 shows BGO trigger pulses and shaped BGO signals from one of 4 channels. The viewing mode was set to a persistent mode in order to superimpose multiple outputs. The falling edge of the BGO trigger pulse is ahead of the peaks of shaped BGO signals. The trigger pulse width is about 200ns. Fig. 5-41 shows LSO trigger pulses and shaped BGO signals that are from one of 4 BGO channels. The falling edge of the LSO trigger pulse is barely ahead of the peaks of shaped BGO signals.

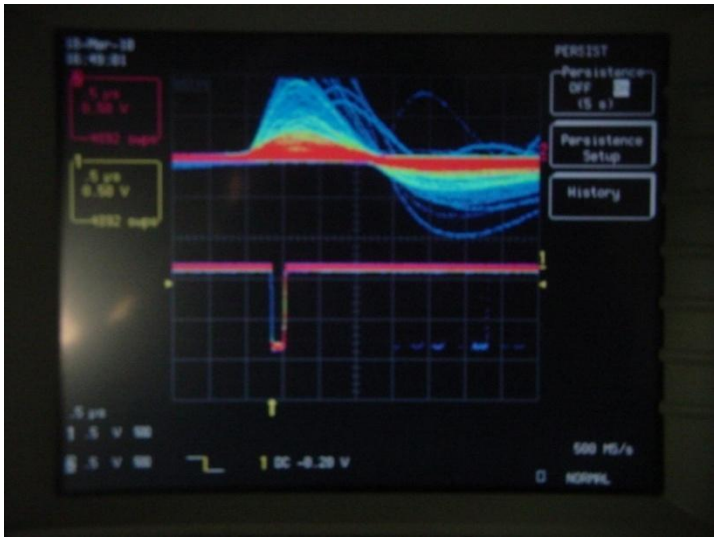

Figure 5-40. One of 4 BGO channel shaped-signals (upper) and BGO trigger pulses (lower).

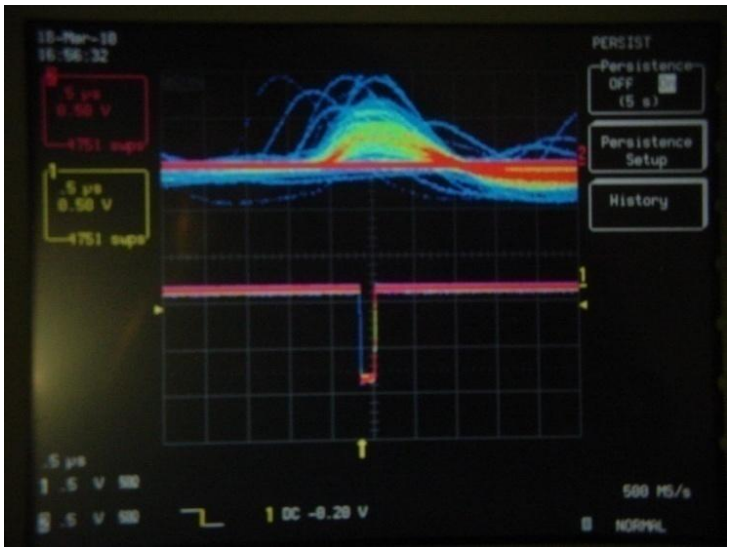

Figure 5-41. One of 4 BGO channel shaped-signals (upper) and LSO trigger pulses (lower).

The timing of the BGO and LSO trigger pulses were compared as illustrated in Fig. 5-42. The two triggers are shown in a persistent (superimposed) mode. The upper pulses are BGO triggers and the lower pulses are LSO triggers. Since the BGO surface area is wider than the LSO surface area, BGO traces are denser than LSO traces.

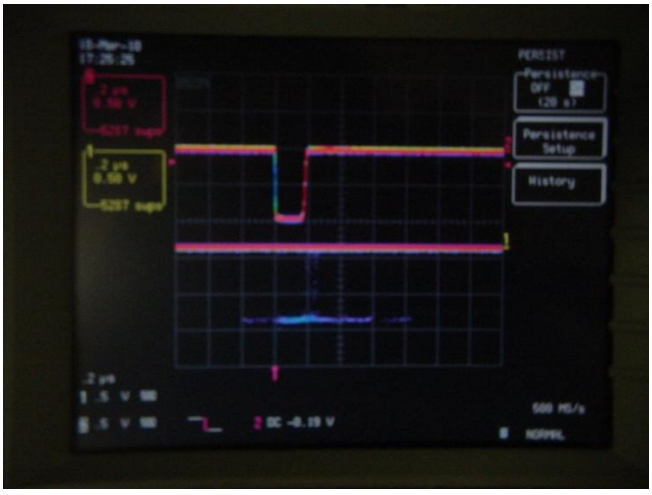

Figure 5-42. BGO triggers (the upper pulses) and LSO triggers (the lower pulses) in the persistent (superimposed) mode.

A coincidence pulse is generated in the VME FPGA when a pair of BGO and LSO triggers overlaps in time. Fig. 5-43 shows shaped BGO signals and coincidence pulses. Falling edges of the coincidence pulses begin just before the peak of shaped BGO signals.

The coincidence pulses were routed to the peak-sensing ADC. The peaks of the 4 channel shaped-signals from BGO frontend electronics were detected using the peak-sensing ADC. The peak value of each shaped signal was sustained while a gate pulse (coincidence pulse) was activated. The peak value was then sampled just after the end of the coincidence gate pulse.

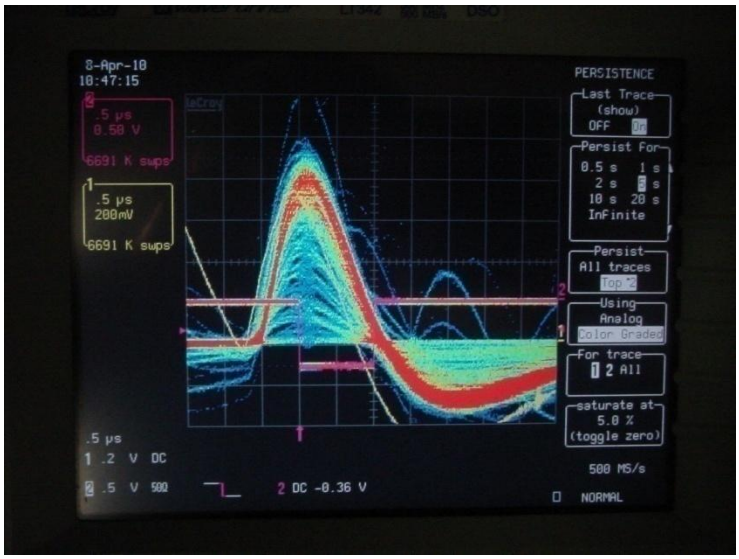

Figure 5-43. Coincidence gate pulses and shaped BGO signals from one channel.

5. 2 .4 **Data Analysis**

The acquired peak values were processed using an on-line data acquisition/analysis program. The on-line data acquisition program is discussed later in detail. The histogram in the oval in Fig. 5-44 shows the pulse height spectrum of the sum of 4 digitized peak values. The histogram peak between the two vertical lines is the

511keV photo-peak. The 1275keV photo peak was not detected in the pulse height spectrum because the data acquisition was limited to coincident events. The lower square window shows estimated interaction positions in the 4-by-8 BGO cuts. Coincidence events that fell into the energy window in the upper oval were processed to obtain estimated interaction positions. A centroid method was used to estimate the horizontal and vertical interaction positions. A 50-by-50 array of finite (logical) pixels was used to display estimated positions. The effective BGO detector front surface is about 43mm by 50 mm. A cluster of finite pixels in Fig. 5-44 shows a single illuminated BGO crystal in coincidence mode.

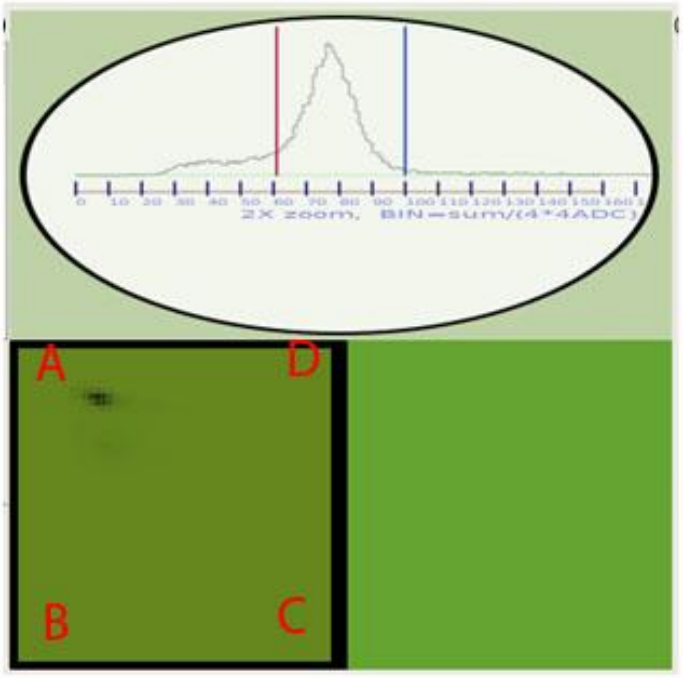

Figure 5-44. Pulse height spectrum (upper) and the estimated interaction positions (lower). A BGO cut in the upper left corner was imaged. Energy resolution is roughly 20%. Since each BGO cut was imaged, spatial resolution was not measured.

The BGO detector was vertically translated so that one of the crystals in the lower left corner was illuminated with gamma rays in coincidence mode. Fig. 5-45 shows the illuminated BGO cut in the bottom left-hand corner. The gain adjustment screw was turned to adjust the gain.

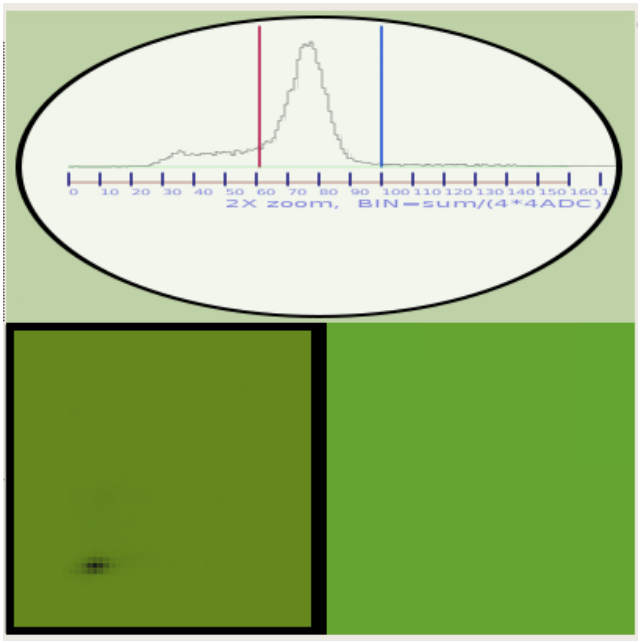

Figure 5-45. A crystal in the lower left-hand corner was imaged. Energy resolution is roughly 20%. Since each BGO cut was imaged, spatial resolution was not measured.

After a horizontal translation, a crystal in the lower right-hand corner was illuminated in Fig. 5-46. Finally, the gain adjustment of one crystal in the upper right-hand corner is shown in Fig. 5-47.

The peak location of each pulse height spectrum in the oval window was adjusted to have almost the same value. The pulse height spectra from Fig. 5-45 to Fig. 5-48 showed similar photo-peak locations after the gain adjustments.

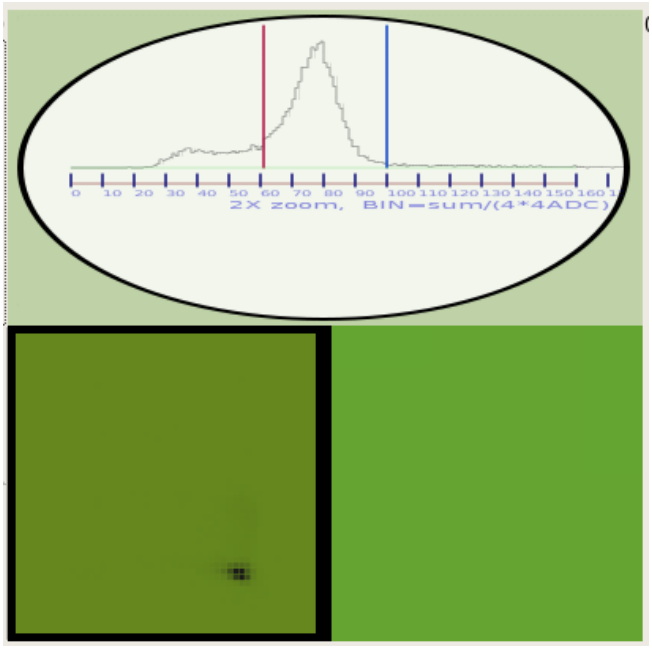

Figure 5-46. A crystal in the bottom right-hand corner was imaged. Energy resolution is around 20%.

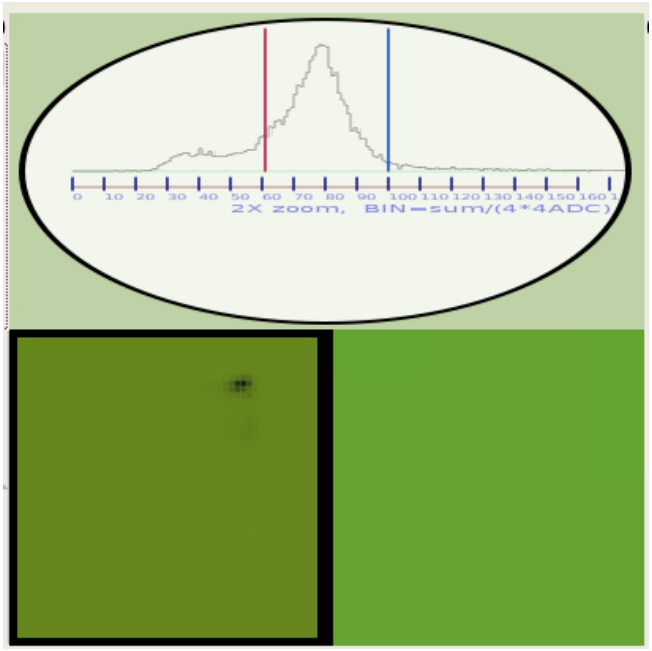

Figure 5-47. A crystal in the upper right-hand area was imaged. Energy resolution is around 25%.

5 .3 Custom-made On-Line Data Acquisition and Analysis Program

5. 3 .1 Integrating Graphical User Interface with Threads Using libSigCX

An online data acquisition/analysis program was developed. The developed program runs on Linux Fedora 5 and is based on libSigCX [116] and gtkmm [117]. The libSigCX is useful for incorporating threads and graphical user interface. Fig. 5-48 shows the outline of the developed data acquisition/analysis program. The first thread is in charge of controlling the peak-sensing ADC. There is another thread that is in charge of drawing the acquired data on screen.

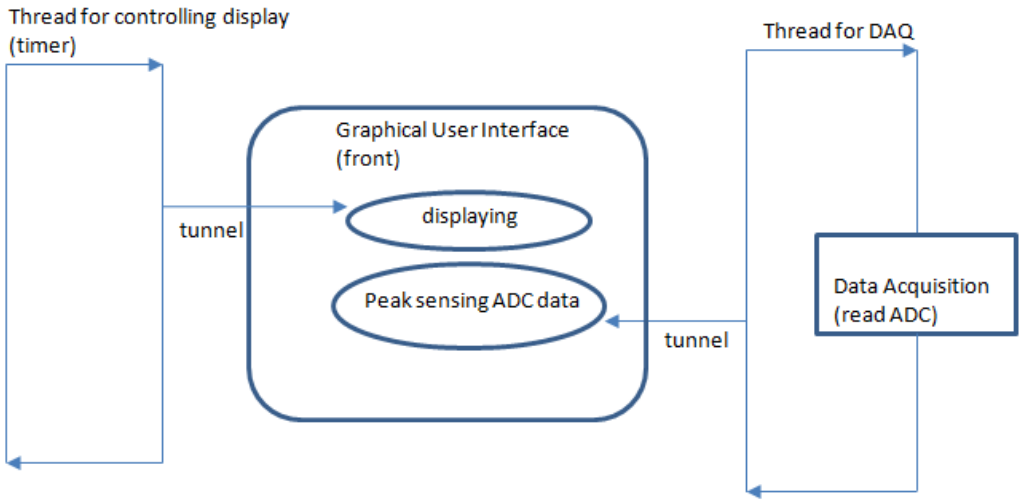

Figure 5-48. Outline of the on-line data acquisition and analysis program.

5. 3 .2 Na-22 Flood Field Irradiation Images in BGO

Estimated interaction positions in Fig. 5-47 were obtained without the pedestal subtraction. Different baseline values in 4 channels can degrade the accuracy of position estimation. Therefore baseline subtraction was included for better position estimation.

The pedestal level in each channel was measured by using asynchronous artificial trigger pulses while the high bias voltage of BGO detectors was set to zero.

Fig. 5-49 shows a pulse height spectrum and a flood image from a flood field irradiation. A flood image of Na-22 in a BGO detector using the given energy window in the oval is shown in the lower square window. A Na-22 source disk was placed a few inches apart from a BGO block detector. Only BGO trigger pulses were used to obtain flood images. The pulse height spectrum shows the 511keV photo-peak (between the two vertical bars) and the 1275keV photo-peak to the right of the 511keV photo-peak. Only the events that fell into the given energy window (the two vertical bars in the pulse height spectrum) were processed to draw the flood image. The flood image is a 50-by-50 array of finite pixels.

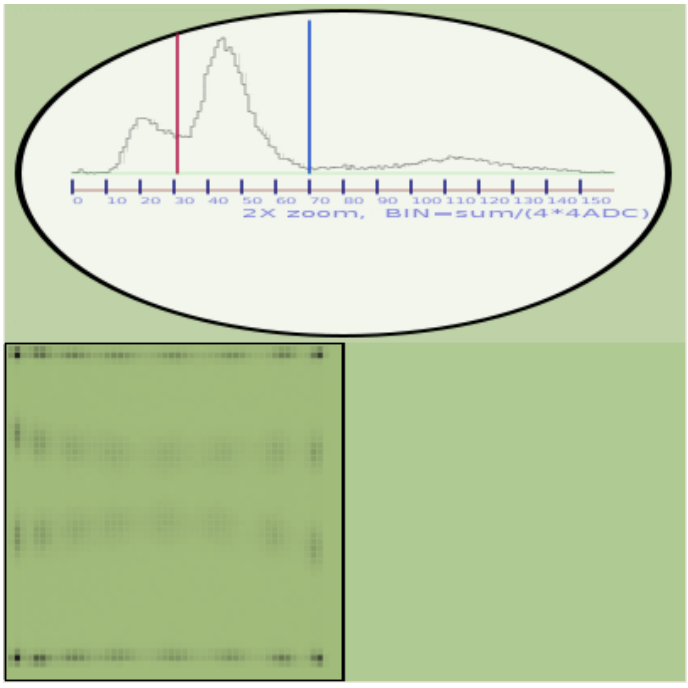

Figure 5-49. Low resolution flood image of Na-22 in BGO. A 50-by-50 array of pixels.

In order to clearly identify crystals in a flood image, a higher resolution flood image was used. A few physical pixels of the computer screen were grouped to represent a logical pixel in the flood image. The higher resolution flood image has a 128-by128 array of logical pixels as shown in Fig. 5-50. Each dark area represents a BGO cut. Each BGO cut measures $5.25 \times 12.5 mm^2$.

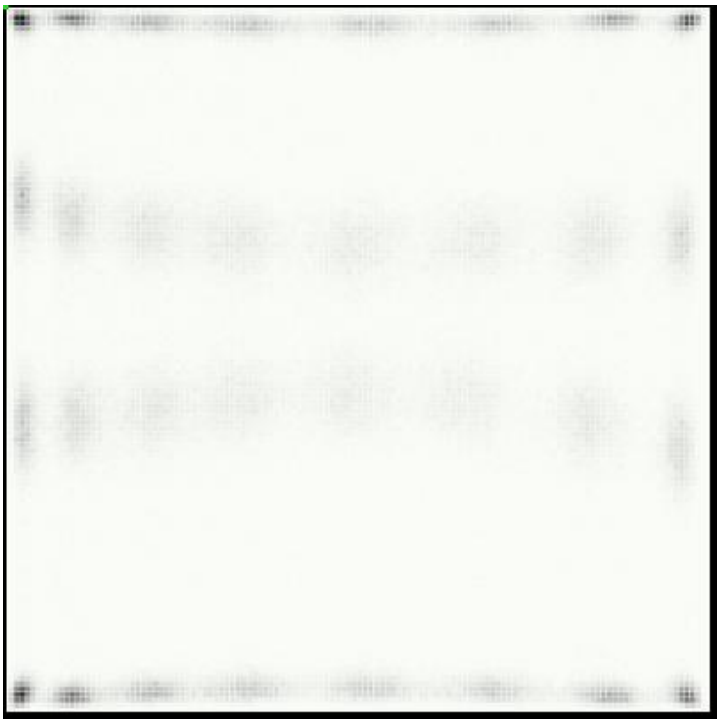

Figure 5-50. Na-22 flood field radiation raw image of a 4-by-8 array of BGO cuts. The high resolution flood image has a 128-by-128 array of enlarged pixels. Each BGO cut measures $5.25 \times 12.5 mm^2$.

Each BGO block detector has different sensitivity and gain. Fig. 5-51 shows another set of a pulse height spectrum and a flood image from another BGO block detector that has the same 4-by-8 cuts. The two center rows in the flood image are out of alignment to some degree. A higher resolution flood image is shown in Fig. 5-52.

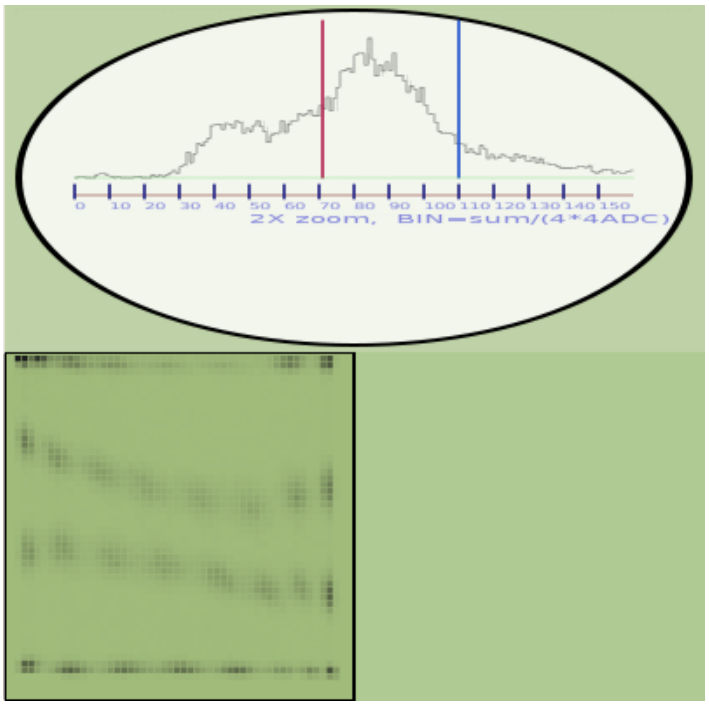

Figure 5-51. Another low resolution flood image of Na-22 in another BGO detector.

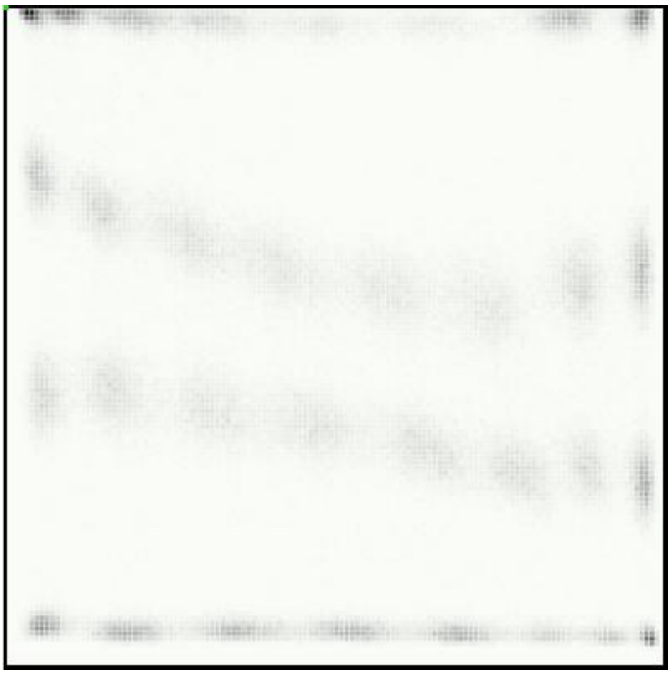

Figure 5-52. Another 128×128 pixel Na-22 flood image in BGO from a different detector than shown in Fig. 5-50. A 128-by-128 array of finite pixels.

5. 3 .3 **Estimated Interaction Positions in NaI(Tl)**

5.3.3.1 **140keV Gamma Rays**

Incident gamma rays interact in thallium-activated sodium iodide, NaI(Tl), crystals and deposit some energy. Linear attenuation coefficients for NaI(Tl) with respect to incident gamma energy are shown in Fig. 5-53. For 511KeV gamma rays, Compton scattering is dominant over the photoelectric effect in NaI(Tl). However 140keV (Tc-99m) gamma rays result in more photoelectric effect events than Compton events in NaI(Tl).

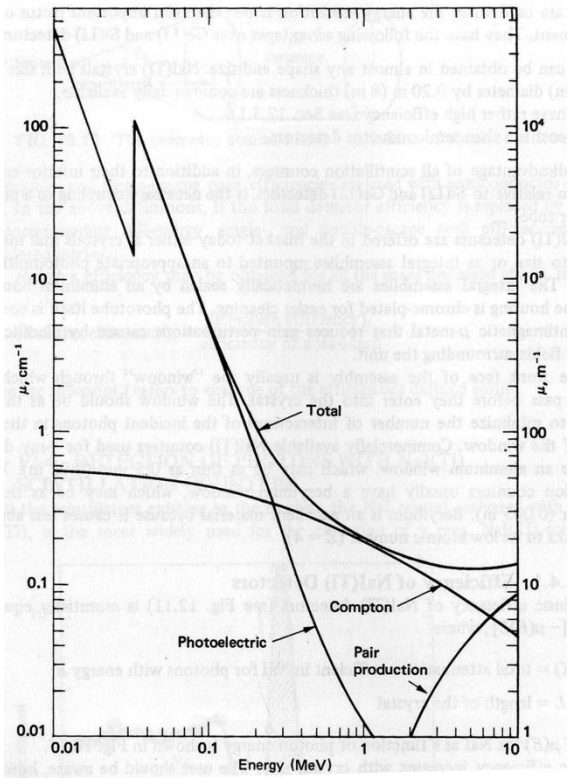

Figure 5-53. Linear attenuation coefficients in NaI(Tl) with respect to incident gamma ray energy. This picture is from [114].

A comparison of crystal identification using Na-22 and Tc-99m was reported [118]. Four H8500 PSPMTs were coupled to each pixelated NaI(Tl) crystal array. Fig. 5-

54 shows the crystal identification of NaI(Tl) crystals. Each NaI(Tl) crystal measures $1.4\times1.4\times6mm^3$. The crystal pitch is 1.6mm. The left picture is a Tc-99m flood image and the right picture is a Na-22 flood image. We can see all the crystals were identified in the Na-22 flood image. The crystals around the boundary were not clearly identified in the Tc-99m flood image. We note that energy resolution is related to the inverse of the square root of the number of photo-electrons. Therefore energy resolution improvement of 511keV over 140keV is approximately $\sqrt{511/140}$. This energy resolution discrepancy can affect spatial resolution near the boundary. Since four PSPMTs were coupled to an array of NaI(Tl) crystals, we can also see some spots between the PMT boundaries were blurred.

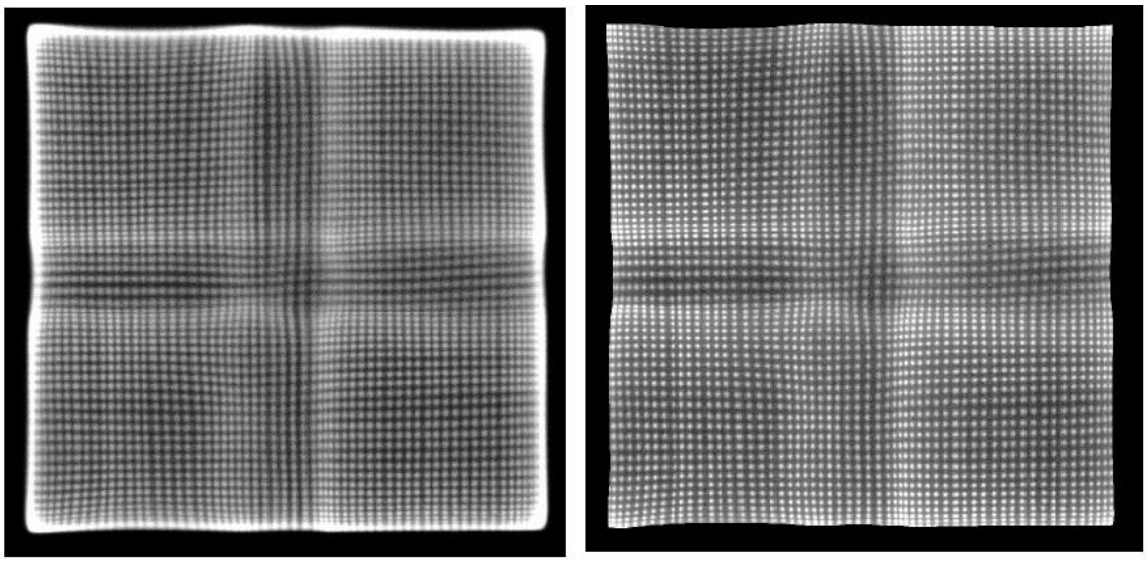

Figure 5-54. Tc-99m flood image (left) and Na-22 flood image (right) in NaI(Tl). These pictures are from [118].

5.3.3.2 **511keV Gamma Rays**

Since each NaI(Tl) crystal has different sensitivity and each metal channel in PSPMT also has a slightly different gain, we used coincidence events between the NaI

detector and the BGO block detector in order to draw the pulse height spectrum showing a 511keV photo-peak. A Na-22 source disk was placed close to the NaI detector to reduce the joint solid angle, consequently illuminating just a few NaI(Tl) crystals in coincidence mode.

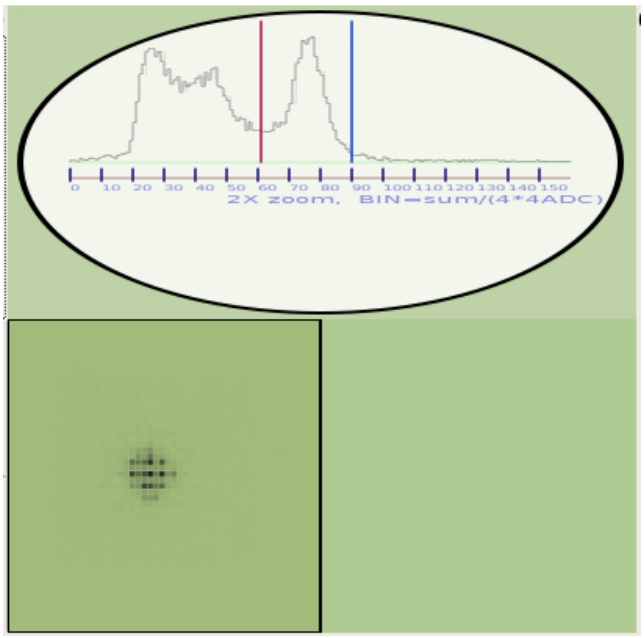

Figure 5-55. Coincidence pulse height spectrum of Na-22 in NaI(Tl). The high bias voltage was set to -700V. Energy resolution is approximately 17%.

Only a few NaI(Tl) crystals were imaged in Figure 5-55 because we took the coincidences between a single BGO crystal (one of 4×8 BGO cuts) and the NaI(Tl) detector. The pulse height spectrum in the oval shows the 511keV photo-peak that has roughly 17% energy resolution.

In order to illuminate all the NaI(Tl) crystals, flood images of Na-22 were taken. A flood image of Na-22 in the NaI(Tl) detector is shown in Figure 5-56. The 511keV photo-peak was not distinguishable. This may be due to the non-uniform Thallium (Tl)

distribution and different sensitivity to gamma rays in NaI crystals. Another conceivable reason is that the 4-inch-diameter NaI(Tl) crystal array extends beyond the 2 inch×2 inch PSPMT front surface. Therefore part of the emission light is not collected in the PSPMT.

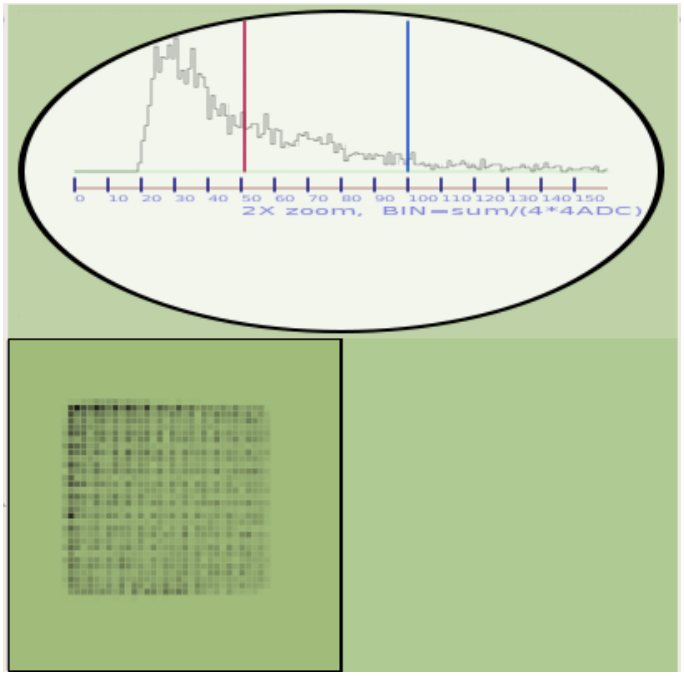

Figure 5-56 Flood image of Na-22 in NaI (lower) and a pulse height spectrum (upper). The bias voltage was set to -700V.

The high bias voltage was increased to negative 750V in order to make the bias voltage closer to the nominal bias voltage of -1100V. Fig. 5-57 shows a set of a pulse height spectrum and a coincidence image at -750V. Baseline subtraction was applied to estimate interaction positions in Fig. 5-57. Only the events that fell into the given energy window (the two vertical bars) were processed to draw the image in the square window.

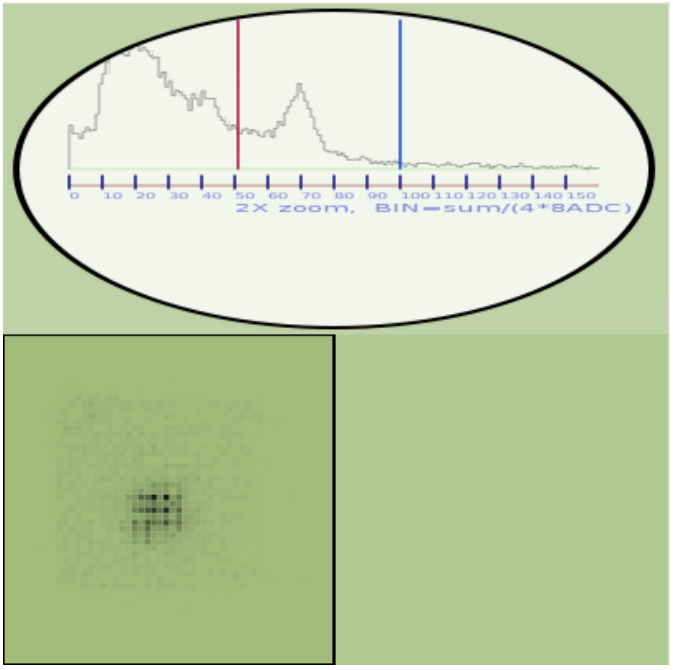

Figure 5-57. Pulse height spectrum at a higher bias voltage. The bias voltage was increased to negative 750V.

Fig. 5-58 shows the flood image when the bias was set to -750V. As can be seen in Fig. 5-58, the NaI(Tl) crystals are not clearly identified in the 50-by-50 array of pixels. The image size was increased to a 512-by-512 array. With the bigger image size, the crystals were clearly identified. Fig. 5-59 shows a flood image of Na-22 in NaI(Tl).

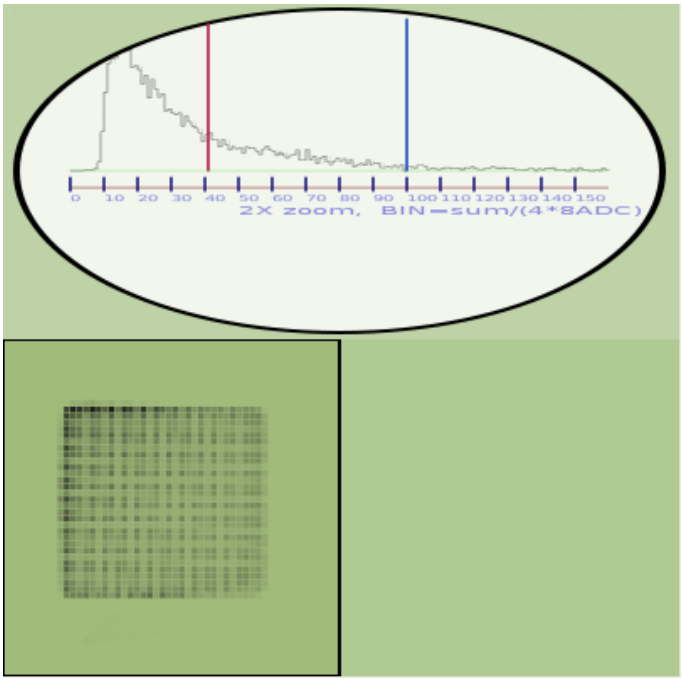

Figure 5-58. Flood image of Na-22 in NaI(Tl) at -750V. The image array size is 50×50 pixels.

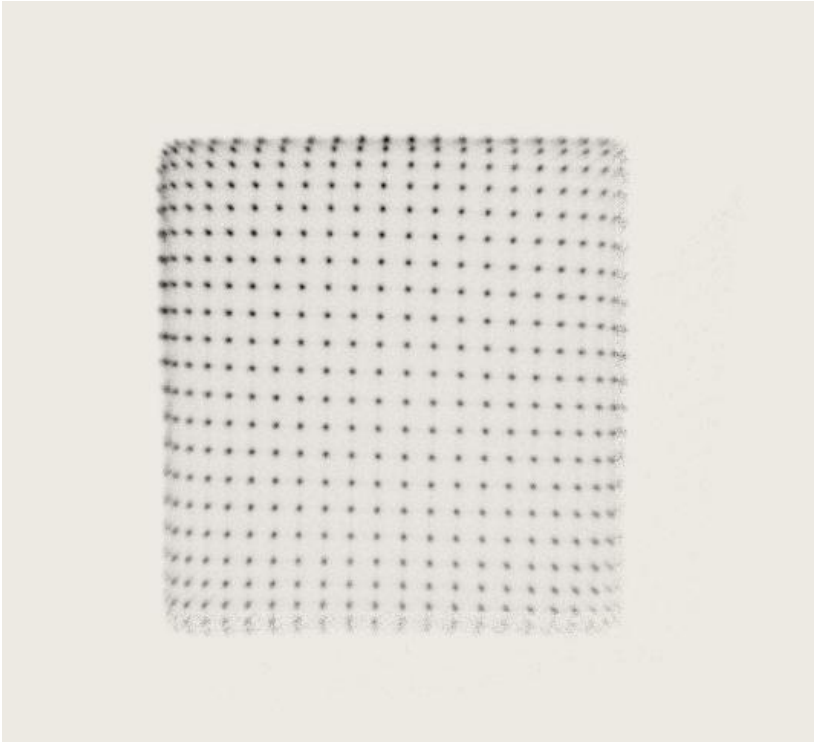

Figure 5-59. Flood image of Na-22 in NaI(Tl) at -750V. The image size is a 512-by-512 array of pixels.

5. 3 .4 Mapping Estimated Interaction Positions to True Positions

Flood images of Na-22 in BGO showed distortion of crystal positions. These distorted crystal positions are not directly used for image reconstruction. The estimated interaction positions need to be mapped to true crystal positions.

5.3.4.1 BGO Crystal Identification

If we can identify a crystal in a flood image, we can then assign true coordinates to the estimated crystal by comparing the actual BGO cuts and the flood image. Therefore we first need to identify crystals in the flood image [119].

Fig. 5-60 shows a Na-22 flood image in BGO. A few physical pixels of the computer screen were grouped into a logical pixel. The image has a 128-by-128 array of finite-size logical pixels. The pixel size was reduced to oversample the image and allow the centroid to be estimated. The estimated interaction positions scatter around the center of each crystal. The center of each cluster was roughly picked up without accurate calculation. This method introduces error, but it will not significantly affect the whole performance. A single dot was then placed at the center of each cluster using interactive user interface.

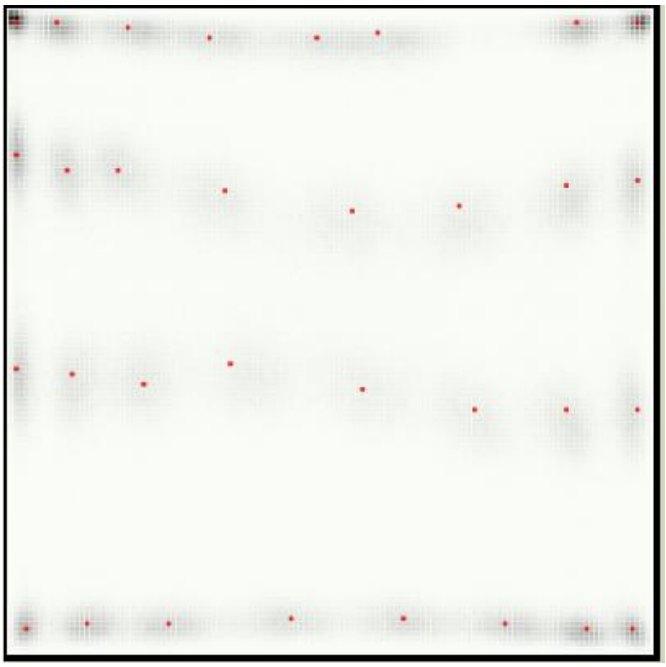

Figure 5-60. Flood image of Na-22 in BGO. Each center of a cluster is marked by a dot. The image size is 128-by-128.

The dots at the cluster centers were used to draw boundaries between estimated crystals. The middle point of four neighbor dots was calculated. The middle points were then connected to visualize the boundaries. The borders between adjacent crystals are shown in Fig. 5-61.

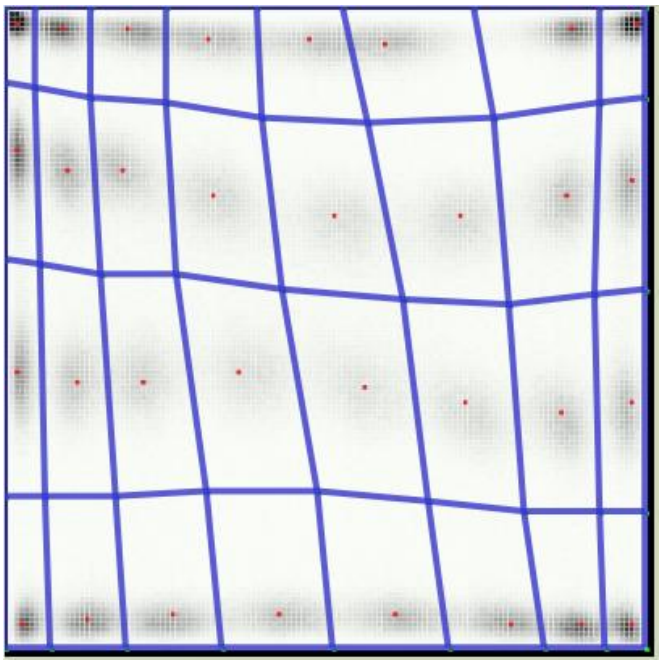

Figure 5-61. Borders between estimated crystals.

Another flood image was obtained from a different BGO block detector. Fig. 5-62 shows the estimated crystals and boundaries.

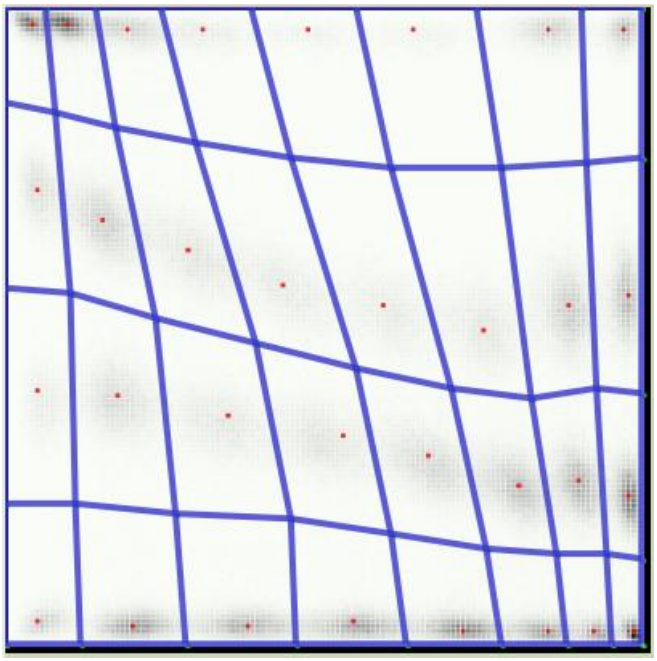

Figure 5-62. Different BGO detector showing different borders.

5.3.4.2 NaI(Tl) Crystal Identification

The NaI(Tl) detector needs more attention to identify crystals because the crystal array is inside the light-tight container and the alignment information is not clearly available. To find a way to do the mapping, a single NaI(Tl) crystal was illuminated in a coincidence set-up. The Na-22 single source disk for the coincidence set-up is shown in Fig. 5-63 and Fig. 5-64. The source disk has 30μCi (1.1MBq) activity.

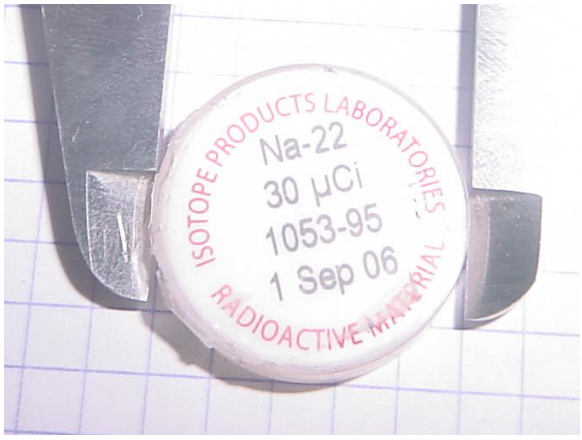

Figure 5-63. Single Na-22 source disk. The source disk contains a point source with 30μCi (1.1MBq) activity. The diameter is roughly one inch.

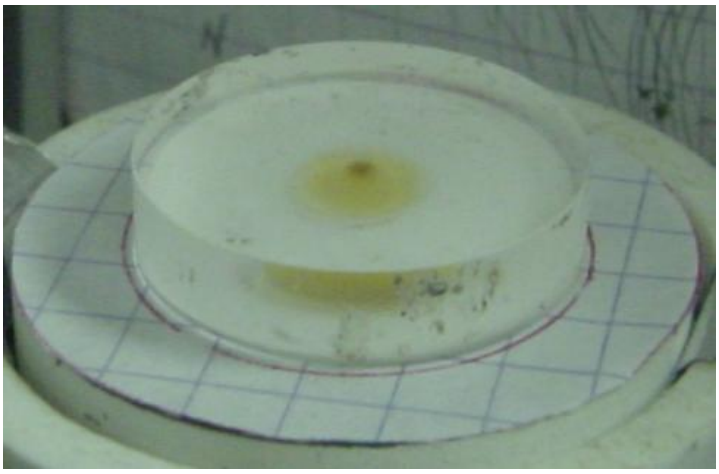

Figure 5-64. Single Na-22 source disk. The single point source is shown at the center of the disk.

In order to illuminate a single NaI(Tl) crystal in coincidence with the BGO detector, we need to select only one BGO crystal to reduce the joint solid angle. The grid drawn in Fig. 5-62 was used to identify a single BGO crystal. For each event that fell into the given energy window, a point-in-polygon test was applied [120]. The point-in-polygon test is a procedure that determines whether a given point belongs to a selected polygon. If the estimated interaction position belongs to a grid element, the true interaction position is assigned to the corresponding crystal. The oval in Fig. 5-65 shows a pulse height spectrum in BGO. A rectangle is shown in the lower square window. The rectangle represents a 5.25mm-by-12.5mm BGO cut. Only one quadrilateral was enabled for the point-in-polygon test in order to display a BGO crystal in Fig. 5-65. All other coincidence events were excluded from further processing.

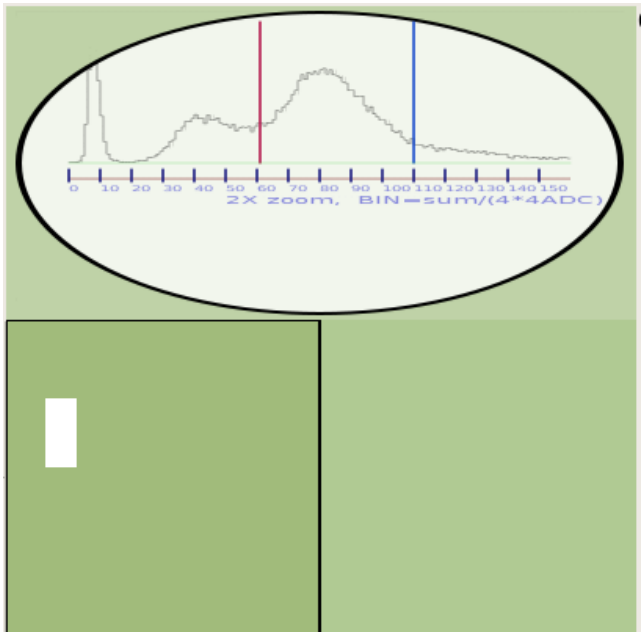

Figure 5-65. One BGO crystal was enabled for further processing.

Fig. 5-66 shows the source disk on the front of the NaI(Tl) detector. We need to minimize the solid angle in order to illuminate one single NaI(Tl) crystal in coincidence mode. The coincidences between the single BGO crystal and the NaI(Tl) detector were taken.

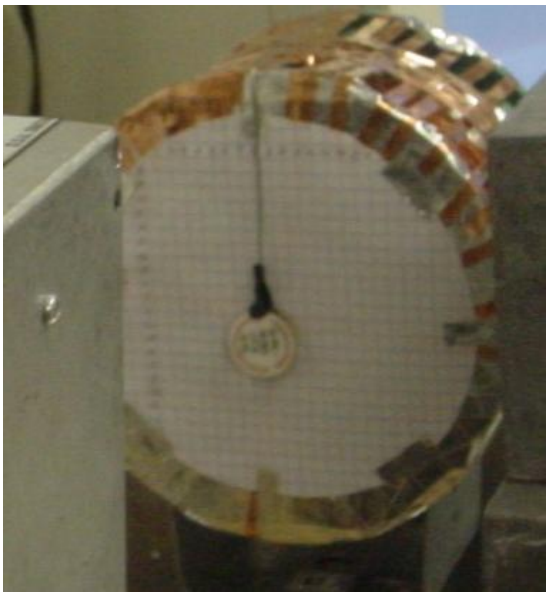

Figure 5-66. Na-22 source disk (30uCi) on the front of the NaI(Tl) detector.

The coincidence image of Na-22 in NaI(Tl) between the single BGO crystal and the NaI(Tl) detector is shown in Fig. 5-67. The 511keV photo-peak is shown more clearly. Only two NaI(Tl) crystals collected most of coincidence events. The pixel on the left-hand side has more counts than the other pixel on the right hand side.

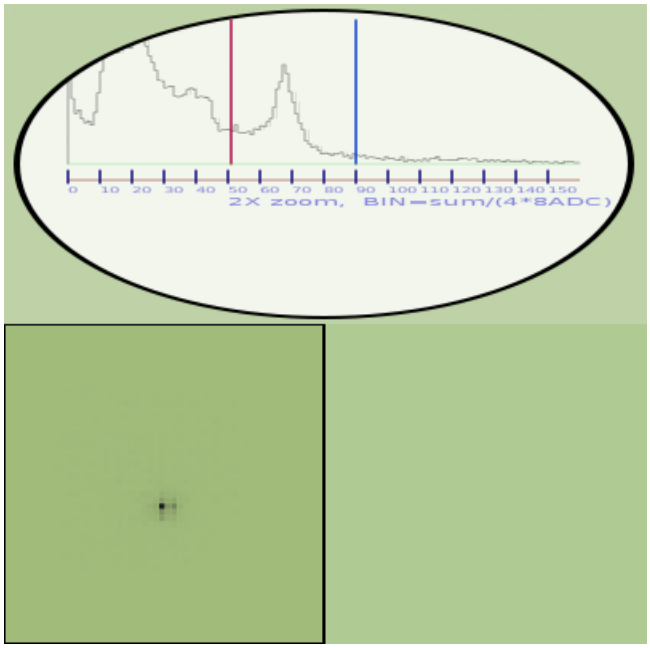

Figure 5-67. Pulse height spectrum in the NaI(Tl) detector in coincidence with a single BGO crystal. The bias voltage was set to -750V.

The single Na-22 source disk was moved to the right in order to illuminate the dimly illuminated NaI(Tl) crystal. After the adjustment, the right hand side pixel showed more coincidence counts in Fig. 5-68.

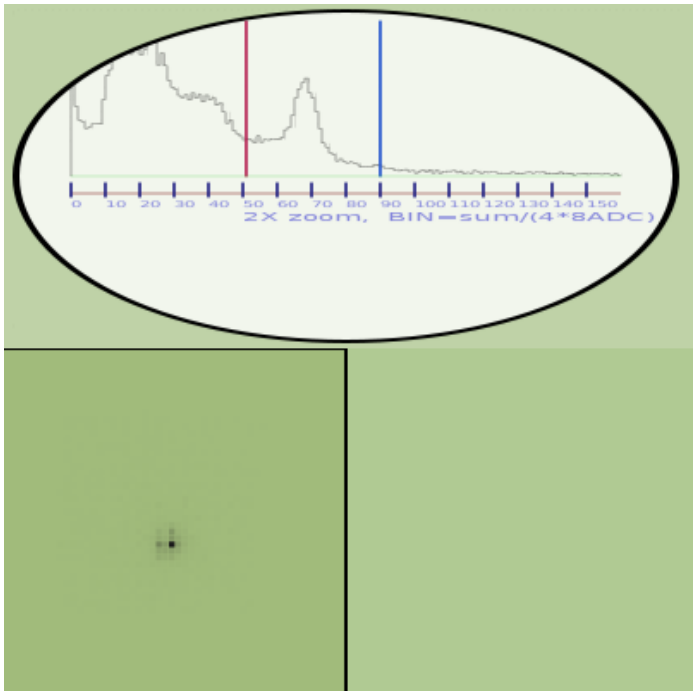

Figure 5-68. Source disk was moved to the right. The bias voltage was set to -750V.

After further fine adjustment, Fig. 5-69 shows a high count pixel that adjoins a dim pixel to the right. A higher resolution image was used to make sure we have only one crystal illuminated. Fig. 5-70 shows a high resolution version of the same image. It turned out that most of the counts belong to one crystal in the high resolution image in Fig. 5-70.

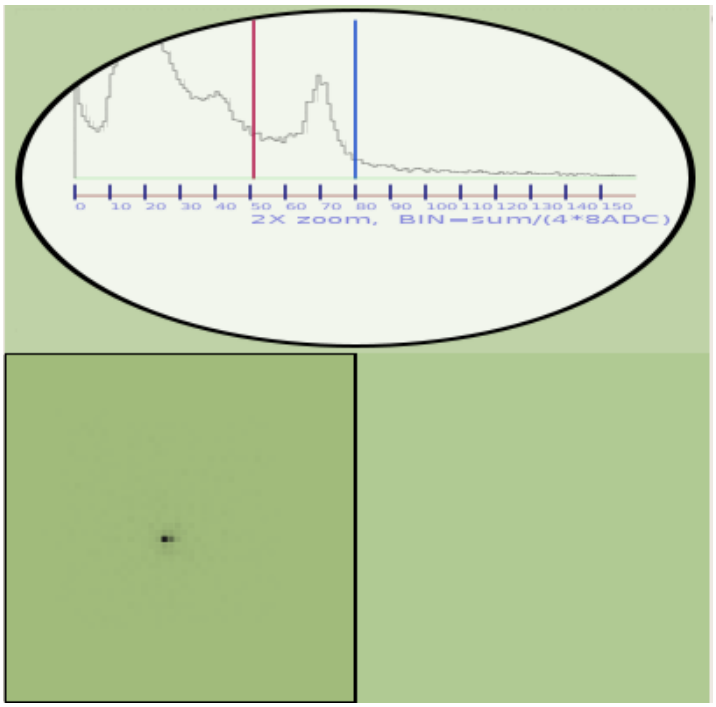

Figure 5-69. Low resolution image of the single crystal coincidence set-up.

Figure 5-70. High resolution image from the single crystal coincidence set-up. The image array is 512-by-512.

Once a single crystal is identified, the circumference of the source disk was delineated as shown in Fig. 5-71. Based on the circumferences in Fig. 5-71, the NaI(Tl) crystals appeared to be a little down-sloped to the right. The NaI(Tl) detector was later turned a bit counter clockwise when it was used to image a source disk.

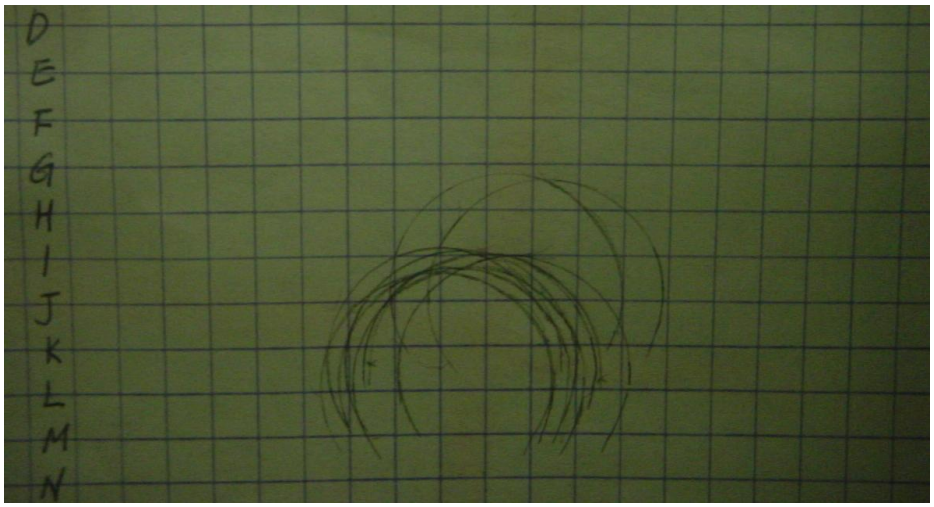

Figure 5-71. Circumference of the source disk. The centers of the circles indicates NaI(Tl) crystal centers.

Since we can locate the actual crystal positions, flood images were obtained in order to map estimated crystal positions to the actual crystal positions. Fig. 5-72 shows a Na-22 flood image in the NaI(Tl) detector. An 11-by-13 array of estimated crystals were chosen, marked by " ┌ ". The middle of four neighbor centers was marked by a dot.

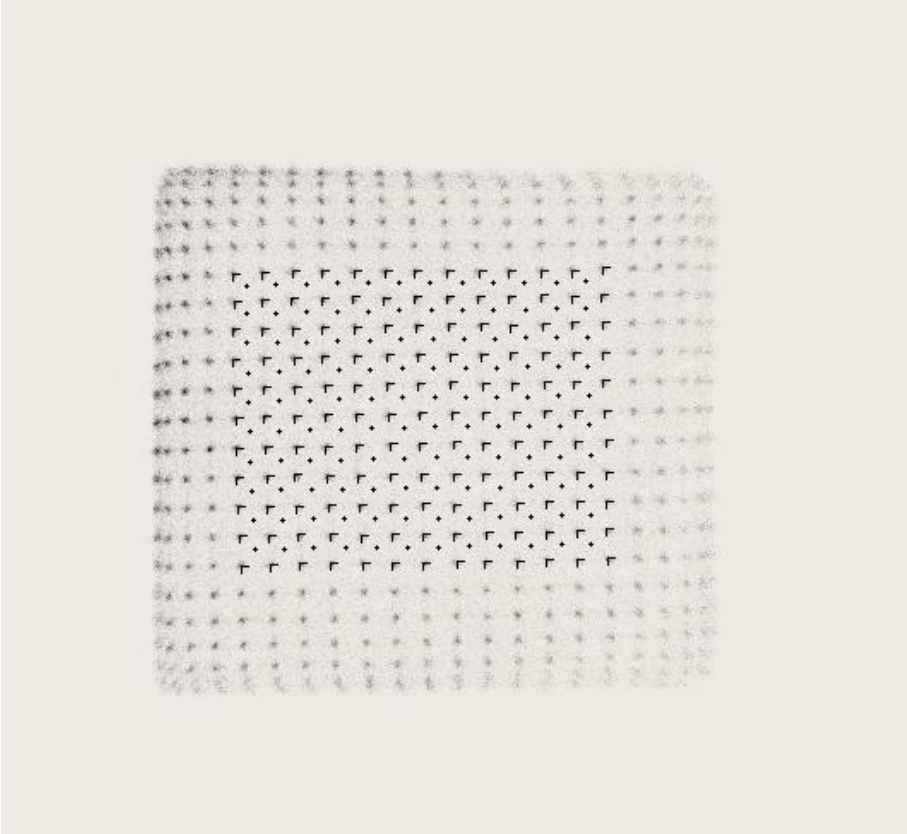

Figure 5-72. Na-22 flood image in the NaI(Tl) detector.

The middle dots in Fig. 5-72 were connected as shown in Fig. 5-73. The quadrilateral made by four middle dots represents an estimated crystal boundary. We have a 9-by-11 array of estimated crystals that are surrounded by quadrilaterals as shown in Fig. 5-73. Each of the 9-by-11 estimated crystals can be enabled or disabled for further data analysis by using the point-in-polygon test.

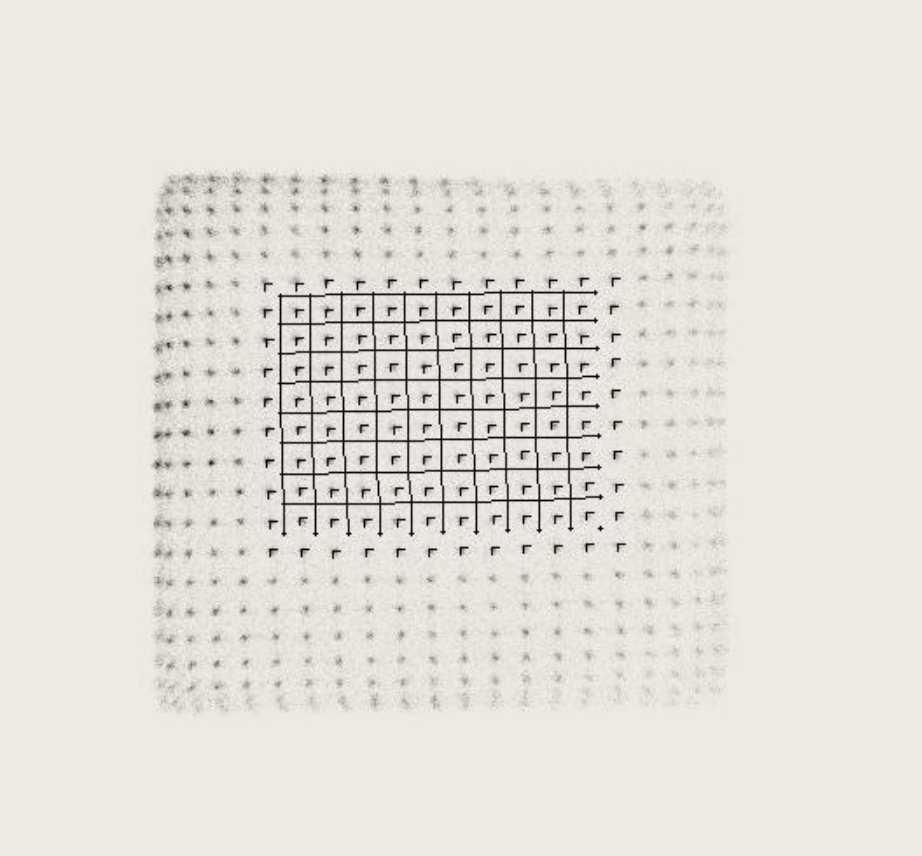

Figure 5-73. 9-by-11 estimated-crystals with boundaries.

Fig. 5-74 shows some enabled estimated-crystals. Only the events that belonged to the enabled crystals were further processed. The coincidence events that were further processed are shown on the right-hand side in Fig. 5-74. Another set of enabled-crystals is shown in Fig. 5-75.

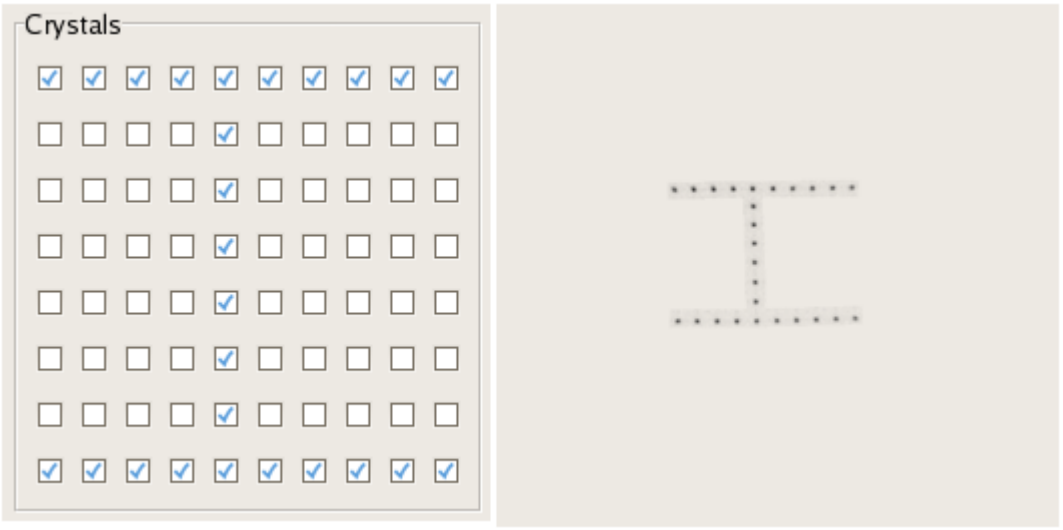

Figure 5-74. Enabled crystals and estimated crystals.

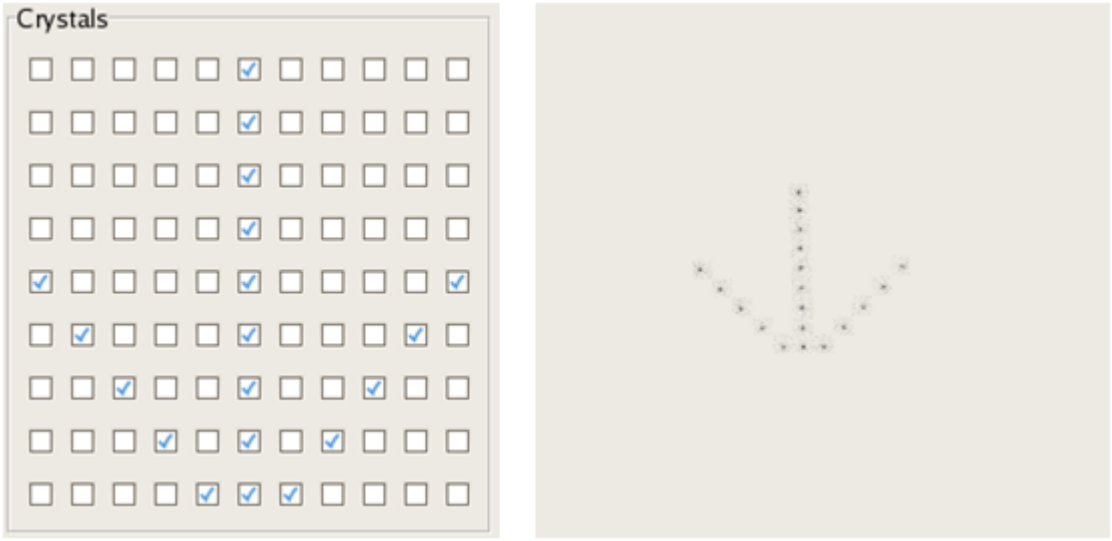

Figure 5-75. Another set of enabled crystals and estimated crystals.

5 .4 **BGO – NaI(Tl) Coincidence Set-Up for 2-Dimensional Data Acquisition**

Two dimensional coincidence data were taken in order to verify whether or not the experimental set-up was in good alignment. Each estimated-crystal can be enabled or disabled for further processing by the user interface. The estimated-crystals need to be mapped to real coordinates of the experimental set-up.

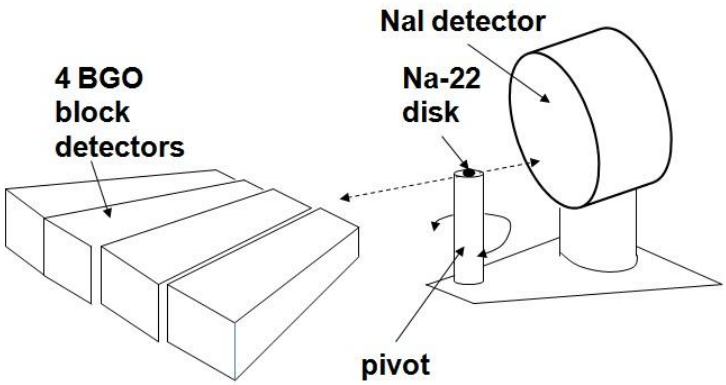

Figure 5-76. NaI(Tl) detector, 4 BGO block detects, and the source disk.

5. 4 .1 Mapping Estimated Positions to True Positions

Fig. 5-76 shows the NaI(Tl) detector and a pivot cylinder. The NaI(Tl) detector is rotated around the pivot cylinder in order to take data at different angles. Fig. 5-77 shows a calibration set-up to obtain actual coordinates of an estimated crystal. A single Na-22 source disk was propped up against the front surface of the NaI(Tl) detector. A laser was used to align the center of the pivot cylinder with the center of the point source.

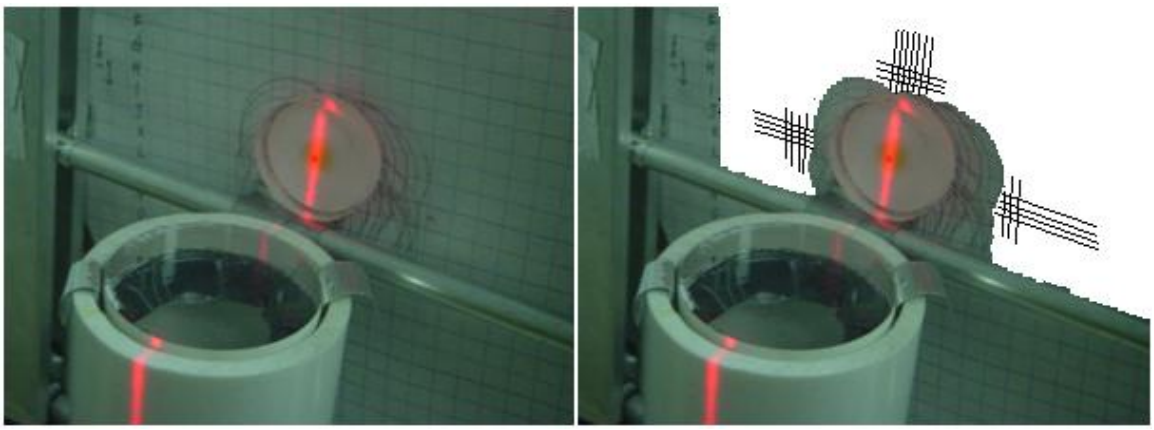

Figure 5-77. Grid and NaI(Tl) crystals.

Only one or two BGO crystals were enabled to take data in coincidence with the NaI(Tl) detector. The coincidence image of the NaI(Tl) detector was obtained from the small solid angle set-up. Fig. 5-78 and Fig. 5-79 show a single estimated NaI(Tl) crystal in low resolution and in high resolution, respectively. Most of the coincidence events occurred in one crystal.

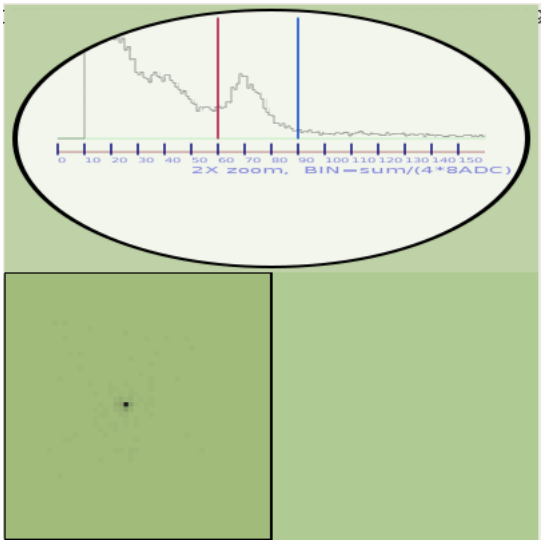

Figure 5-78. Image of a single NaI(Tl) crystal.

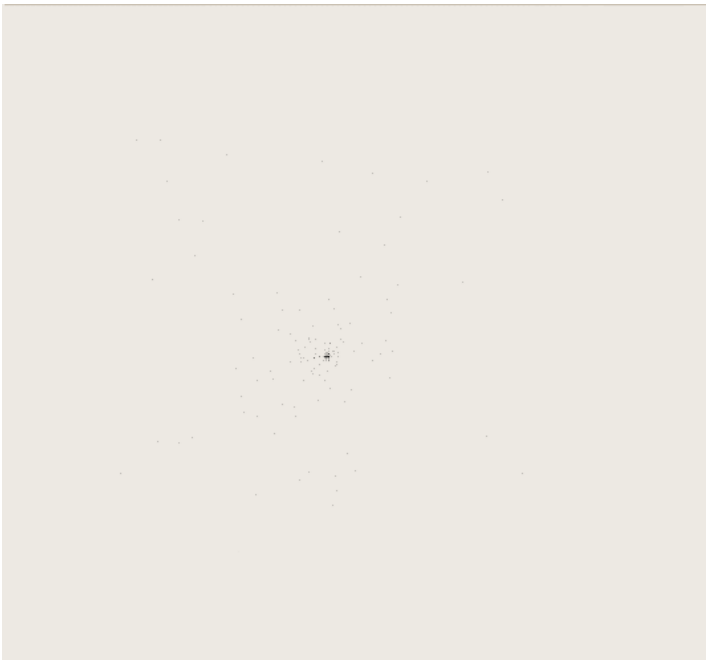

Figure 5-79. One NaI(Tl) crystal that has most of the coincidence events. The image size is 512-by-512.

Fig. 5-80 shows the alignment in the horizontal direction. We found that the NaI(Tl) alignment in the horizontal direction was a bit sloped. Therefore, the NaI(Tl) detector was rotated counter-clockwise in order to align the NaI(Tl) crystals levelly.

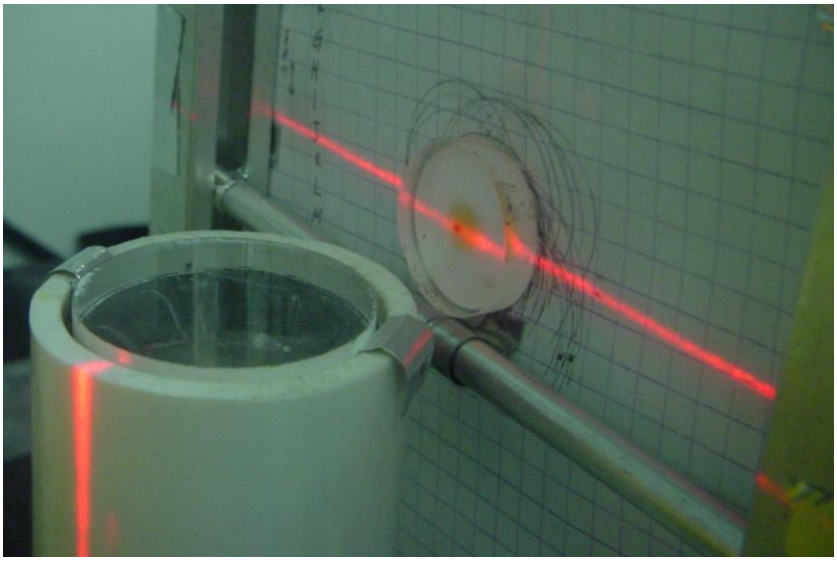

Figure 5-80. Mechanical alignment in the horizontal direction. The NaI(Tl) detector was rotated counter –clockwise.

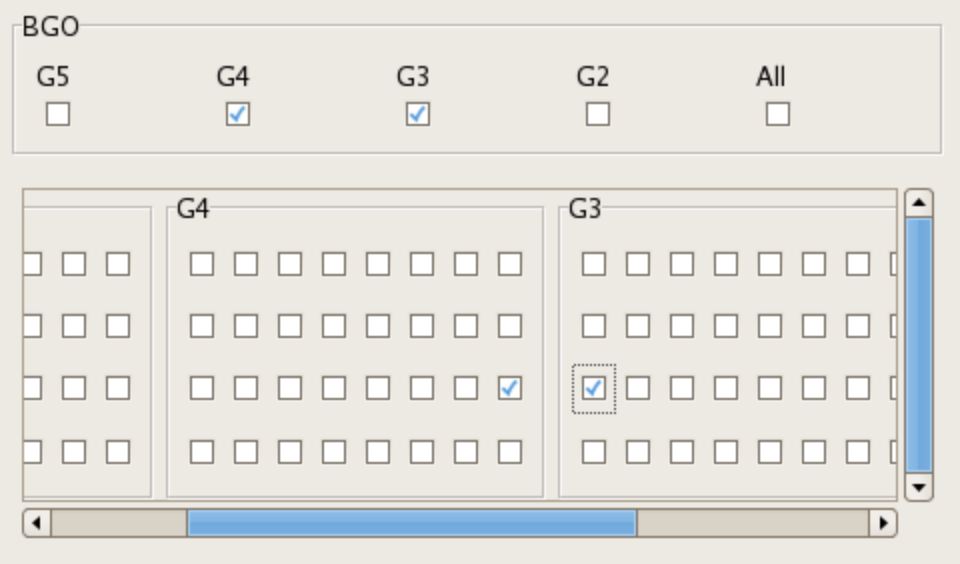

Figure 5-81. Two enabled BGO crystals.

Fig. 5-81 shows two enabled BGO crystals for further data processing and Fig. 5-82 shows a 4-by-7 array of enabled NaI(Tl) crystals for further data processing. The coincidences between two BGO crystals and 28 NaI(Tl) crystals were taken for further data processing. Fig. 5-83 shows two NaI(Tl) crystals from the acquired coincidence data. Fig. 5-84 shows the two NaI(Tl) crystals in a higher resolution image. The right-hand crystal has higher counts than the left-hand crystal.

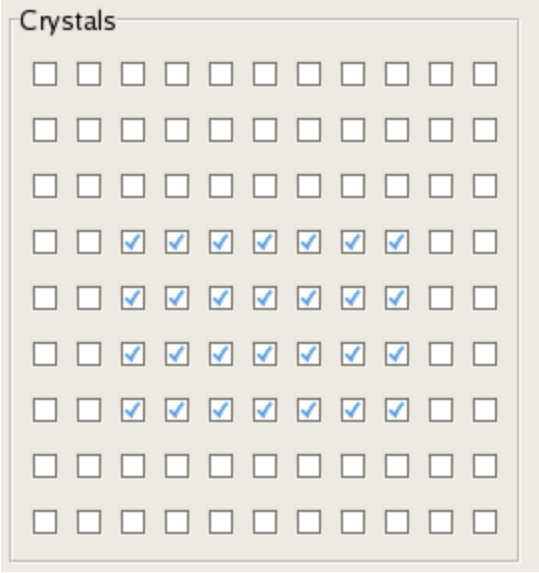

Figure 5-82. A 4-by-7 array of enabled NaI(Tl) crystals.

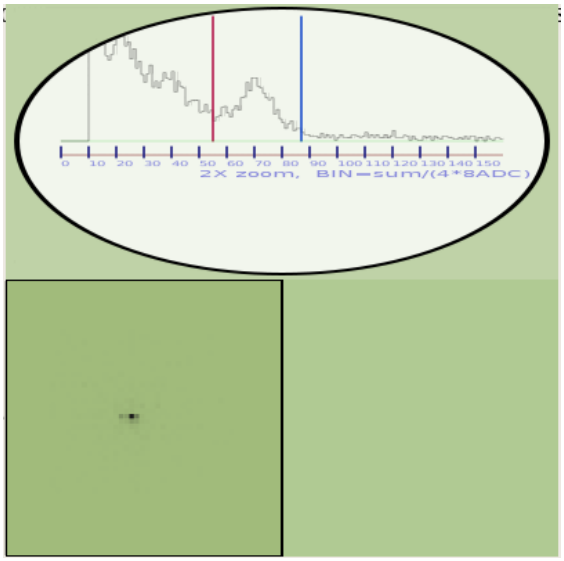

Figure 5-83. Two crystals that collect the coincide events.

Figure 5-84. Two crystals that collect the coincidence events are shown in a higher resolution image (512x512).

We had two NaI(Tl) crystals collecting most of coincidences in Fig. 5-84. The other 26 NaI(Tl) crystals did not collect many counts. The number of enabled NaI(Tl) crystals were then reduced sequentially until we had only two enabled NaI(Tl) crystals left.

Finally, Fig. 5-85 shows two enabled crystals in the user interface panel. The low resolution image shows coincidence events mostly occurred in one of the two crystals. The high resolution image shows only two crystals; the right-hand crystal has higher counts. From the high resolution image showing two crystals, we can identify which pixel in the user interface is mapped to the crystal that has higher counts. In addition, we

know where the estimated crystal is actually located in the NaI(Tl) detector from the calibration set-up.

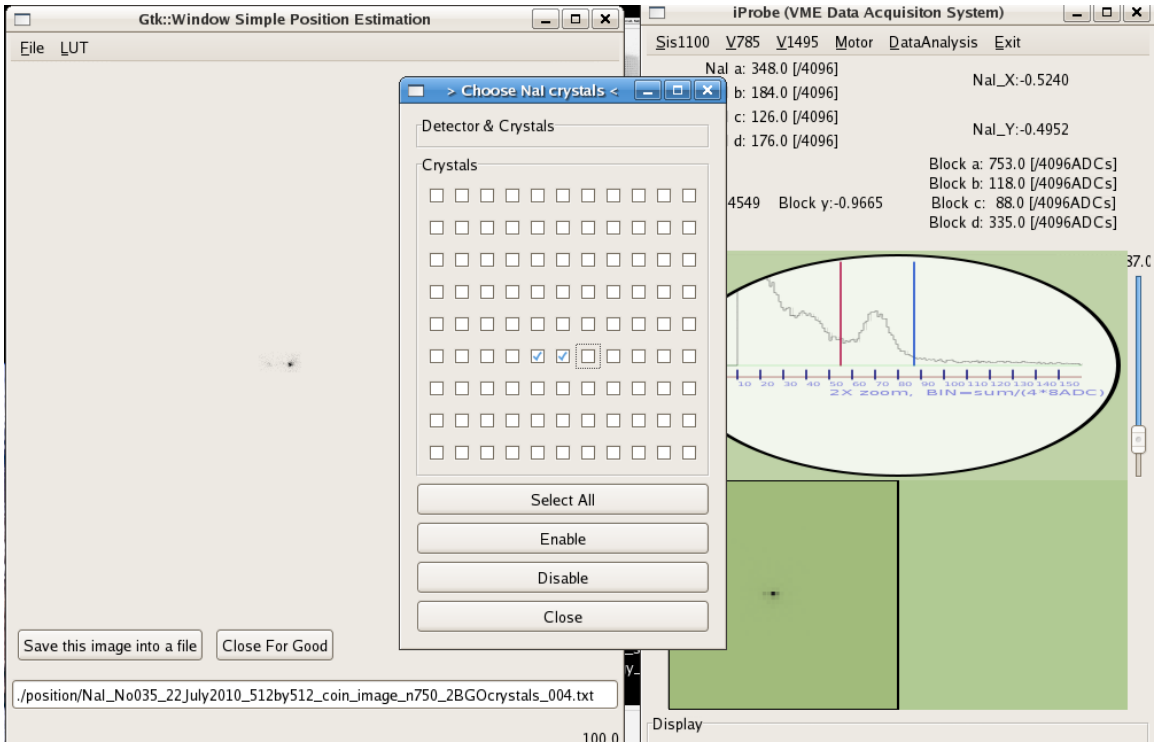

Figure 5-85. Two enabled NaI(Tl) crystals and two imaged NaI(Tl) crystals.

5. 4 .2 **Data Acquisition Conditions**

The illustration of the experimental set-up is shown in Fig. 5-86. Calibration parameters of the data acquisition set-up are briefly described. Fig. 5-87 shows the illustration of top view of the experimental set-up. Four BGO block detectors were placed side by side along an arc that has a roughly 50cm radius. Each BGO block detector contains 8 cuts per row. 11 NaI(Tl) crystals per row are shown in the NaI(Tl) detector.

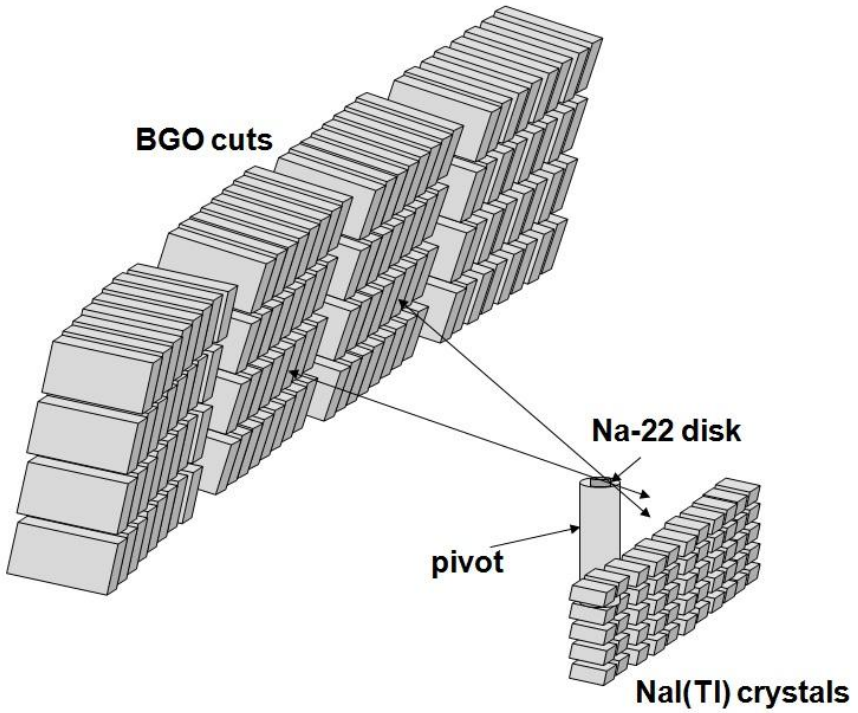

Figure 5-86. Illustration of the experimental set-up.

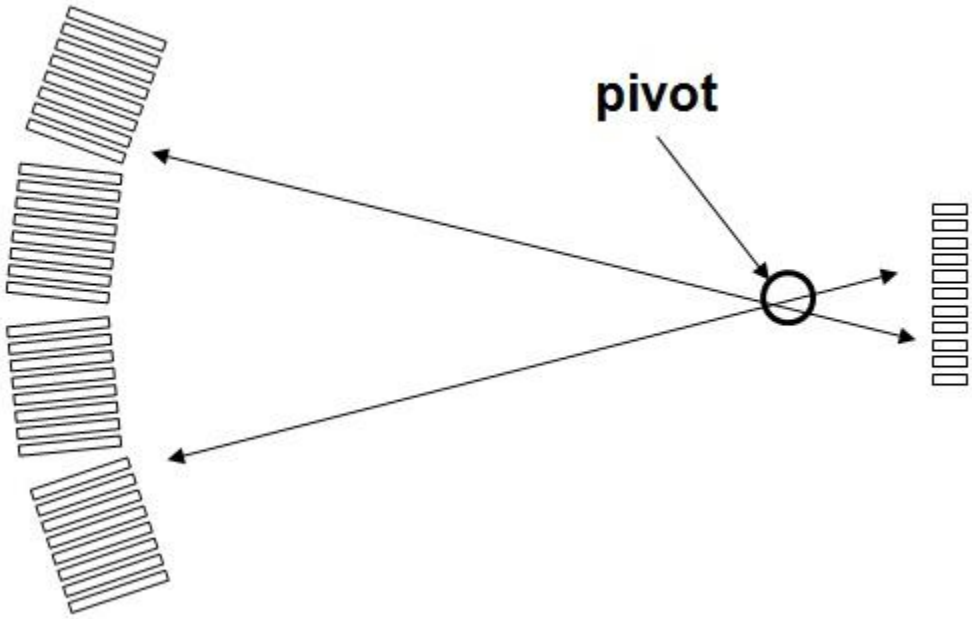

Figure 5-87.Top view of the experimental set-up. The drawing is not to scale.

Fig. 5-88 shows the illustration of side view of the experimental set-up. 4 rows of BGO crystals are shown on the left-hand side and 9 rows of NaI(Tl) crystals are shown on the right-hand side. BGO crystals stands 12.5mm tall and NaI(Tl) crystals stands 2mm tall. The distance from the BGO to the pivot center is 280mm and the NaI(Tl) detector is 40mm apart from the pivot center.

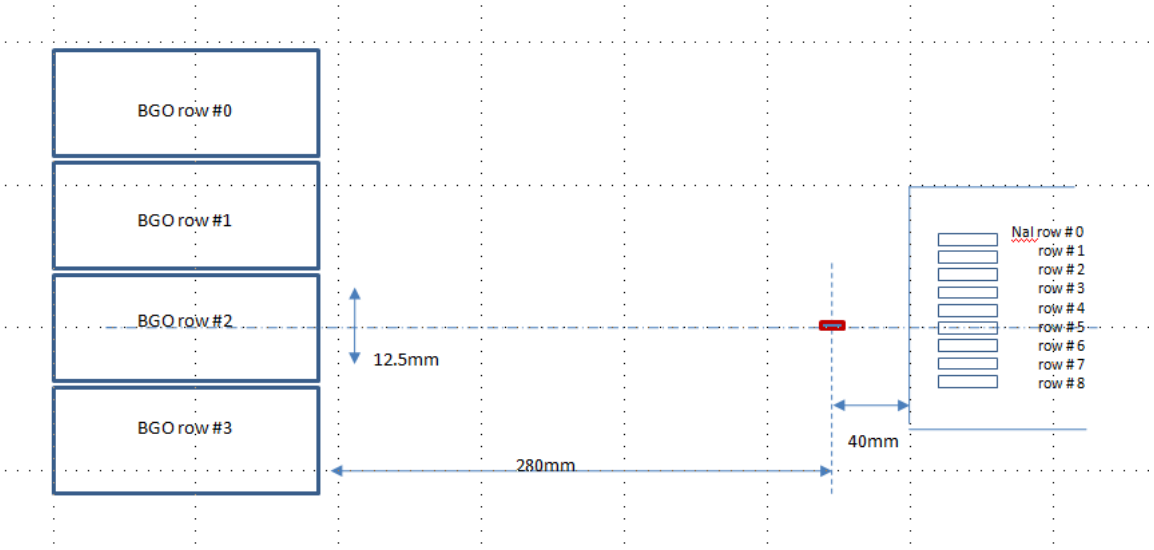

Figure 5-88. Illustration of side view of the experimental set-up. The drawing is not to scale.

BGO row #2 is aligned with NaI(Tl) row #5 as shown in Fig. 5-88. In order to collect coincidences between one row of BGO elements and the NaI(Tl) detector, only one row of BGO pixels was enabled for further data processing in Fig. 5-89. The enable row is the “BGO row #2” in Fig. 5-88. A single Na-22 source disk was placed at the pivot center and coincidence data between the single row of BGO crystals and the NaI(Tl) detector were acquired. Fig. 5-90 shows a coincidence-count image in the NaI(Tl) detector.

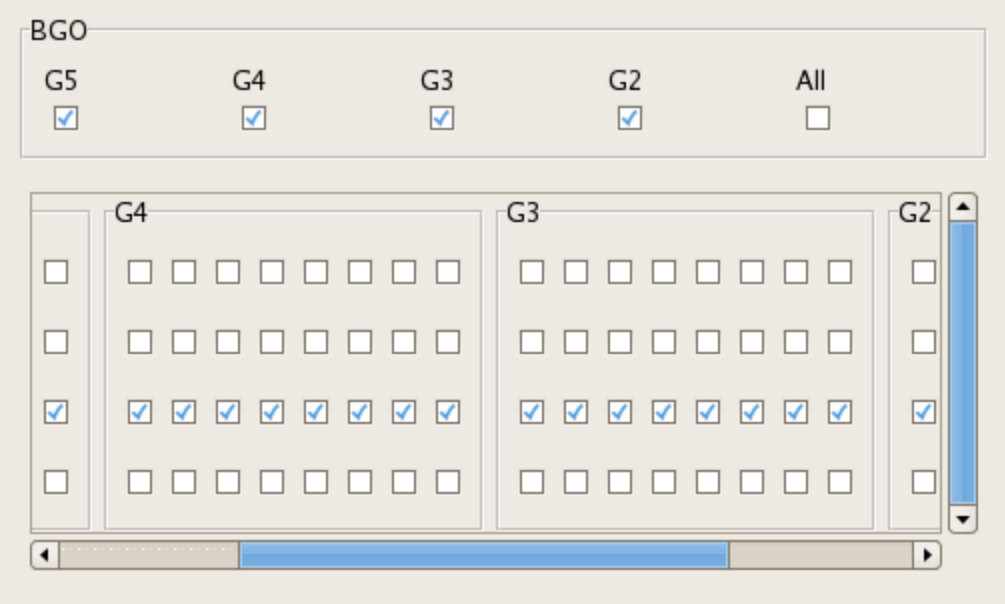

Figure 5-89. One row of BGO crystals was enabled.

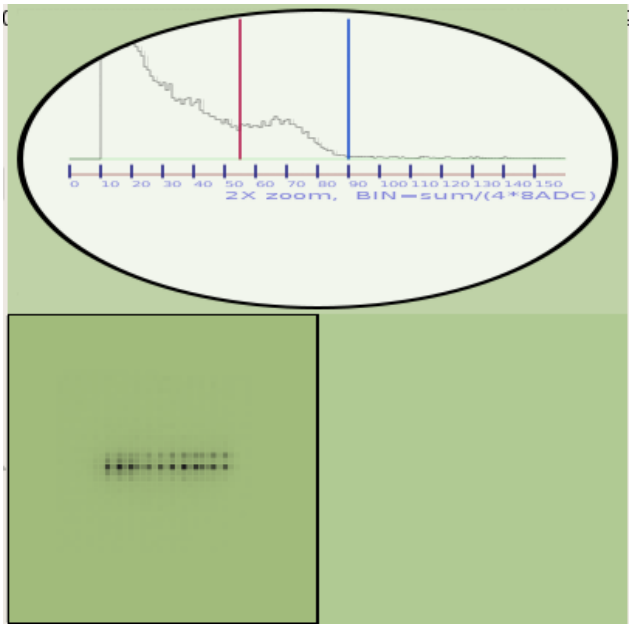

Figure 5-90. Coincidence image in the NaI(Tl) detector.

Two or three rows of NaI(Tl) crystals were collecting most of the coincidence events. We stored coincidence events from only one of the three NaI(Tl) rows by enabling only one row as shown in Fig. 5-91.

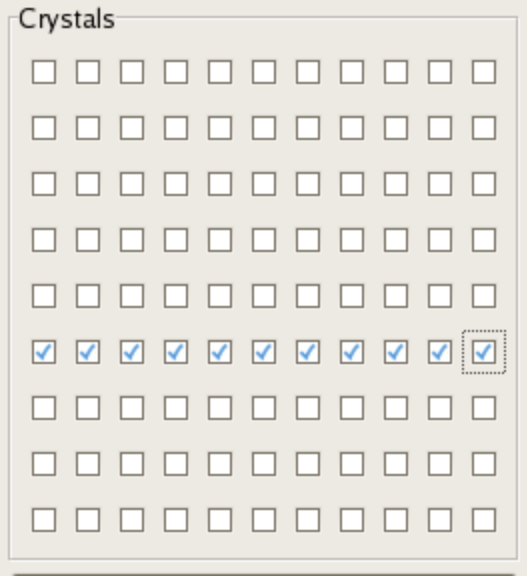

Figure 5-91. Enabled one row of NaI(Tl) crystals.

The selected NaI(Tl) crystals by the user interface in Fig. 5-90 are shown in a high resolution image in Fig. 5-92. As a result, we can collect coincidence events from one row of BGO crystals and one row of NaI(Tl) crystals.

Figure 5-92. Selected one row of NaI(Tl) crystals.

Fig. 5-93 shows an illustration of rotation of the NaI(Tl) detector around the pivot cylinder. The coincidence data were taken at 3 different angles; at the 0° reference position, at 12° counter-clockwise, and at 14° clockwise.

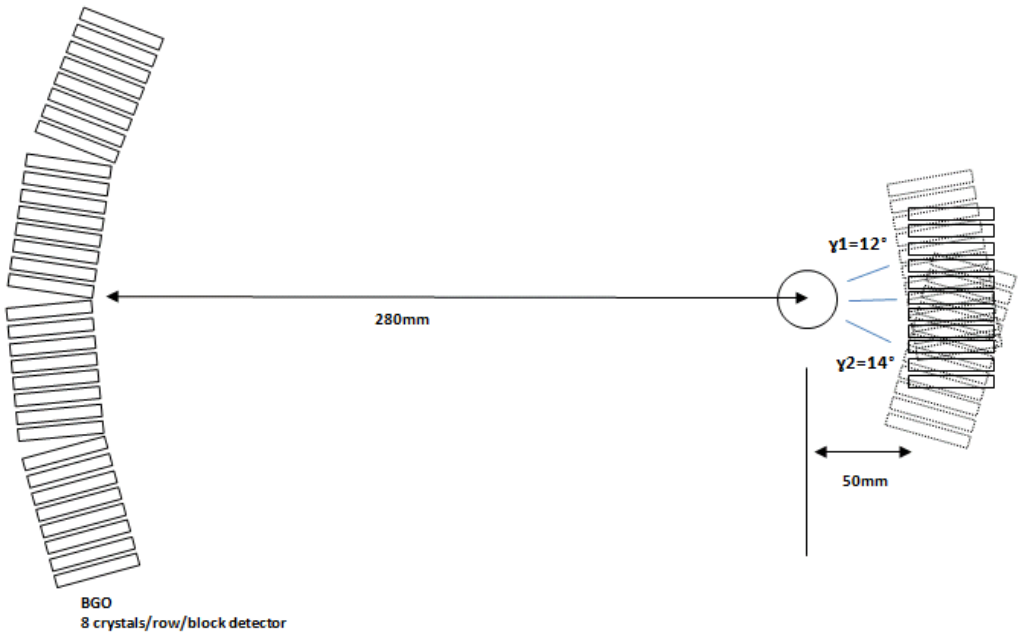

Figure 5-93. Illustration of rotation of the NaI(Tl) detector around the pivot cylinder. The drawing is not to scale.

Fig. 5-94 shows the experimental set-up in which the NaI(Tl) detector was at the 0° reference position. Fig. 5-95 shows the experimental set-up in which the NaI(Tl) detector was rotated by 12° counter-clockwise. The 14° clockwise rotation of the NaI(Tl) detector is shown in Fig. 5-96.

Figure 5-94. NaI(Tl) detector at the 0° reference position.

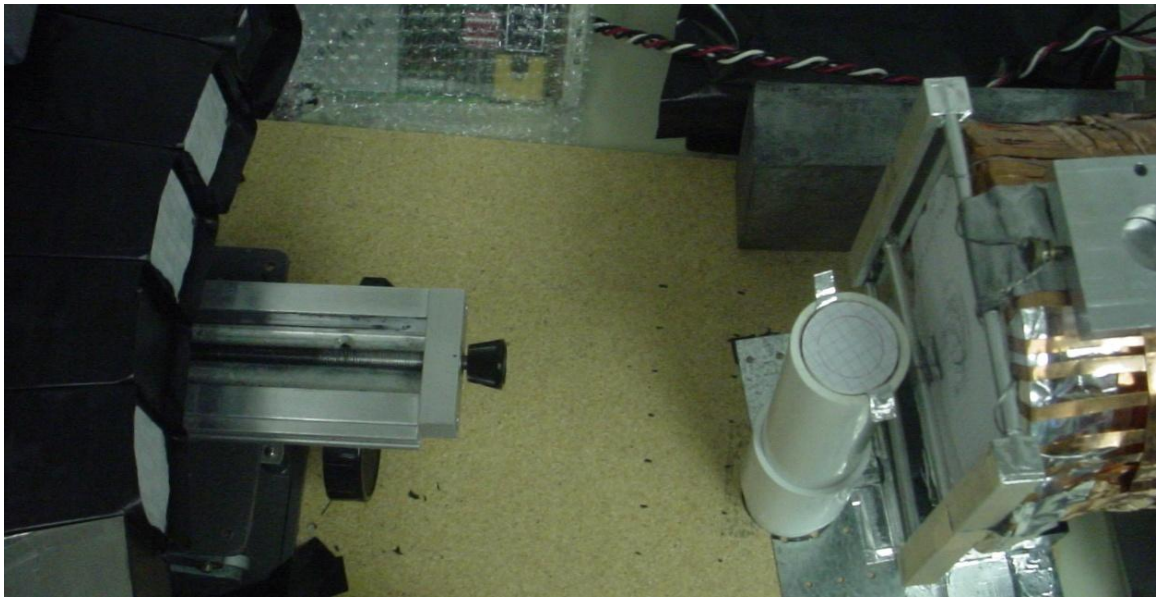

Figure 5-95. NaI(Tl) detector that is rotated by 12° counter clockwise.

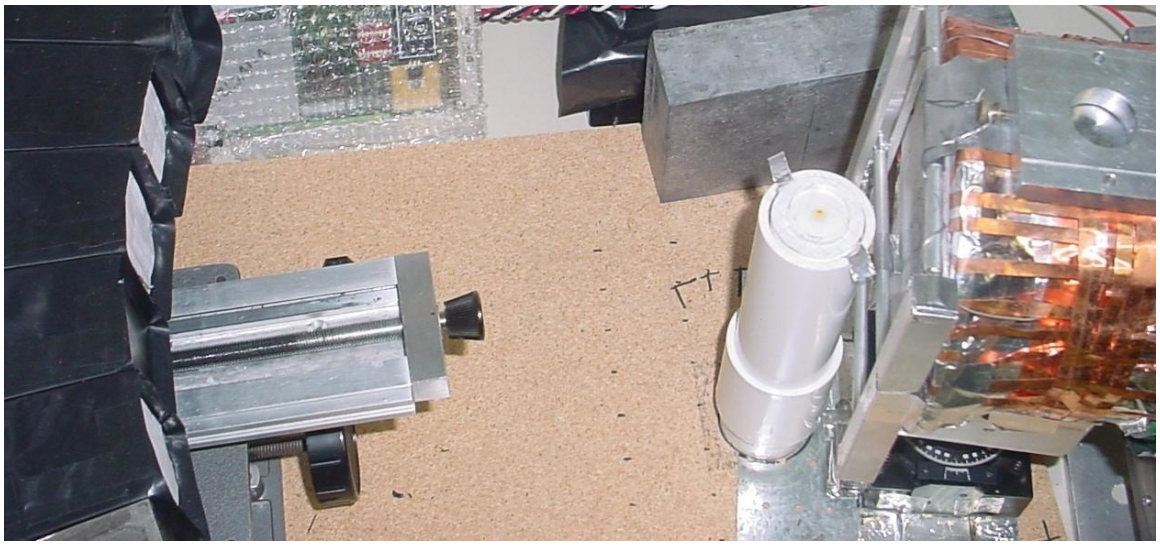

Figure 5-96. NaI(Tl) detector that is rotated by 14° clockwise.

5. 4 .3 **Coincidence Data Acquisition**

The experimental set-ups shown in Fig. 5-94, Fig. 5-95, and Fig. 5-96 were used for coincidence data acquisition. One row of BGO crystals and one row of NaI(Tl) crystals were enabled to take coincidence data for further data processing. A single Na-22 source disk and a double Na-22 source disk were used as radio-active sources. The coincidence data were taken at 3 different angles.

5.4.3.1 **Single Point Source Disk (Set-up N08)**

A single Na-22 point source disk was used as a radioactive source. The source disk is shown in Fig. 5-97. The coincidence data between one row of BGO crystals and one row of NaI(Tl) crystals were taken at three different angles.

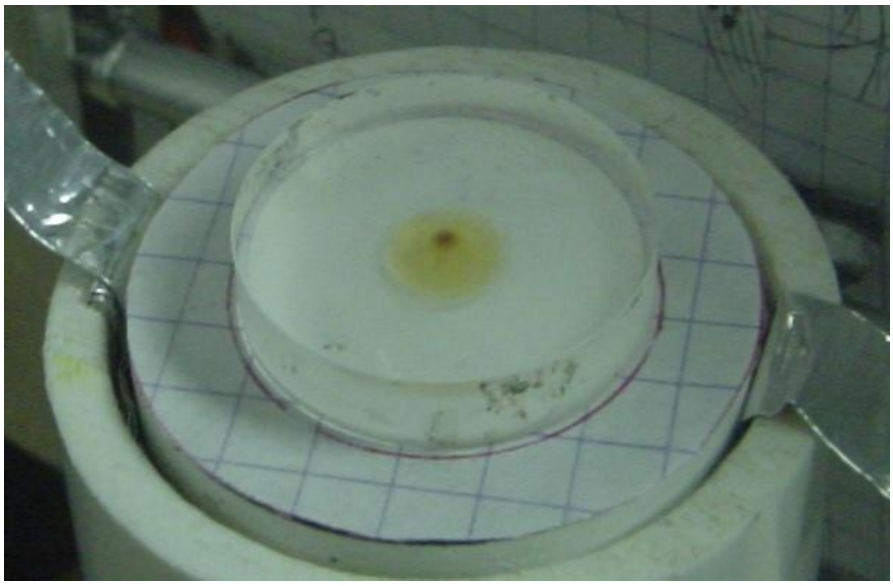

Figure 5-97. The single Na-22 point source disk.

Only the first 2000 LORs in each data set at the given angle were used to draw the back-projection. The center region of a back-projection image is shown in Fig. 5-98. The zoom-in view shows a 12mm-by-6mm center region. The bin number 24 in the horizontal direction was chosen to draw a cross-section profile of the back-projection. The cross-section profile is shown in Fig. 5-99. FWHM of the profile is roughly 2.7mm.

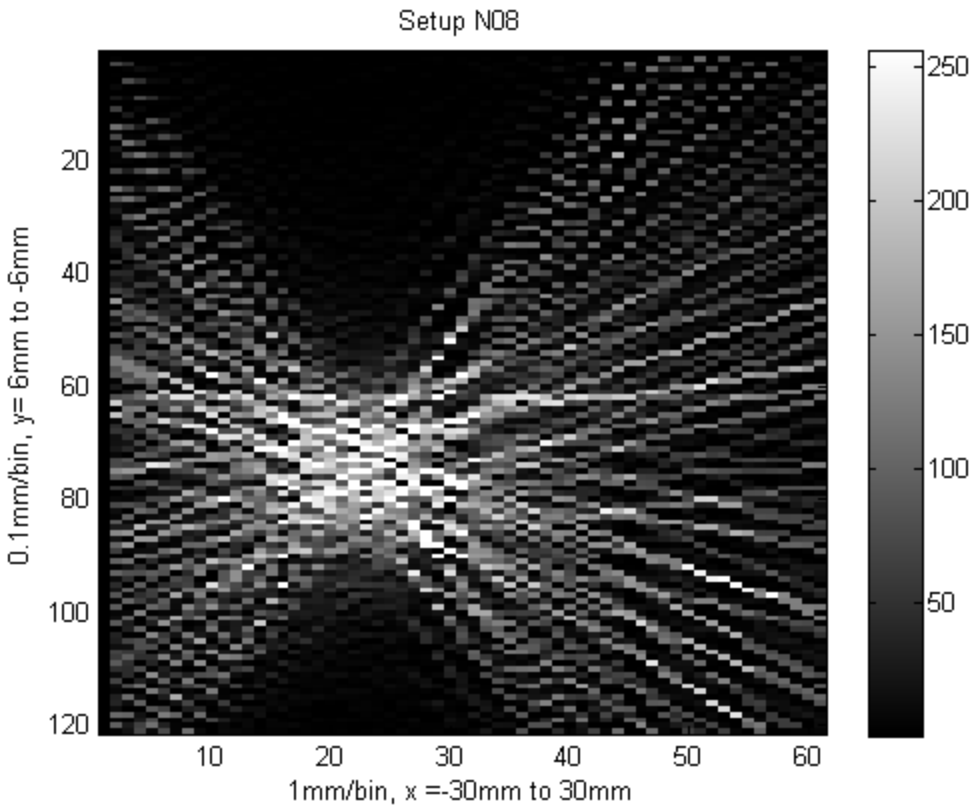

Figure 5-98. Zoom-in view of a simple back projection image. A single Na-22 point source was used.

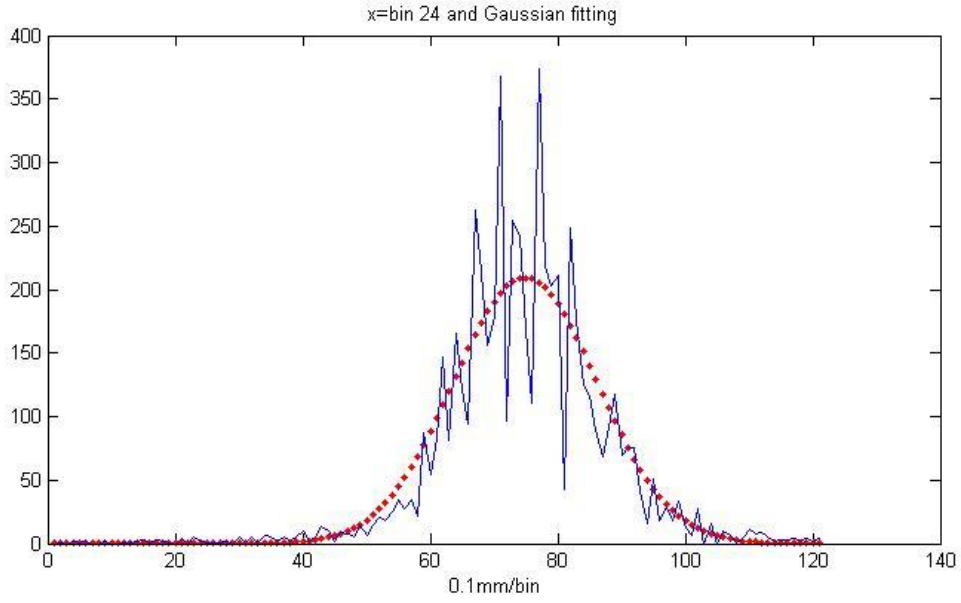

Figure 5-99. Cross-section profile of the back projection at bin 24.

5.4.3.2 **Double Point Source Disk (Setup N11)**

A source disk with two Na-22 point sources was used for data acquisition as shown in Fig. 5-100. Each point source is a Na-22 source with 30μCi activity. The disk was placed at the pivot center. The distance between the two point sources was measured as shown in Fig. 5-101. The separation is roughly 1.5mm.

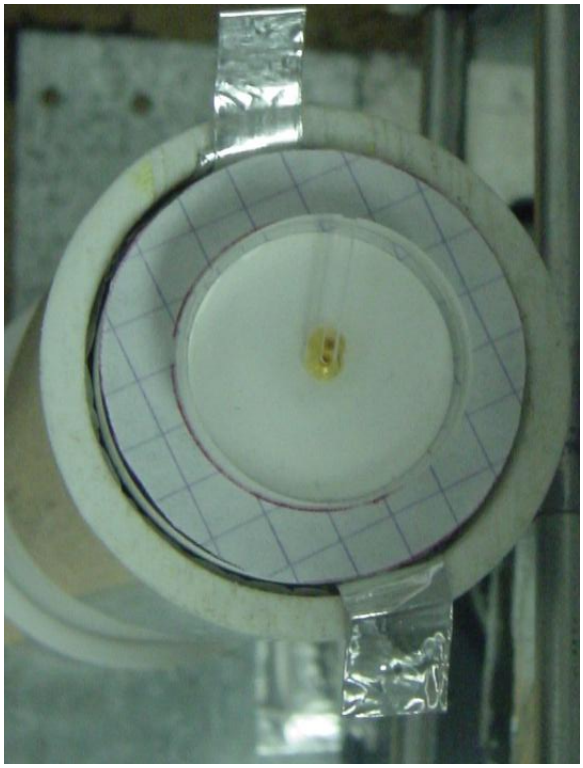

Figure 5-100. Na-22 double source disk at the pivot center (60μCi).

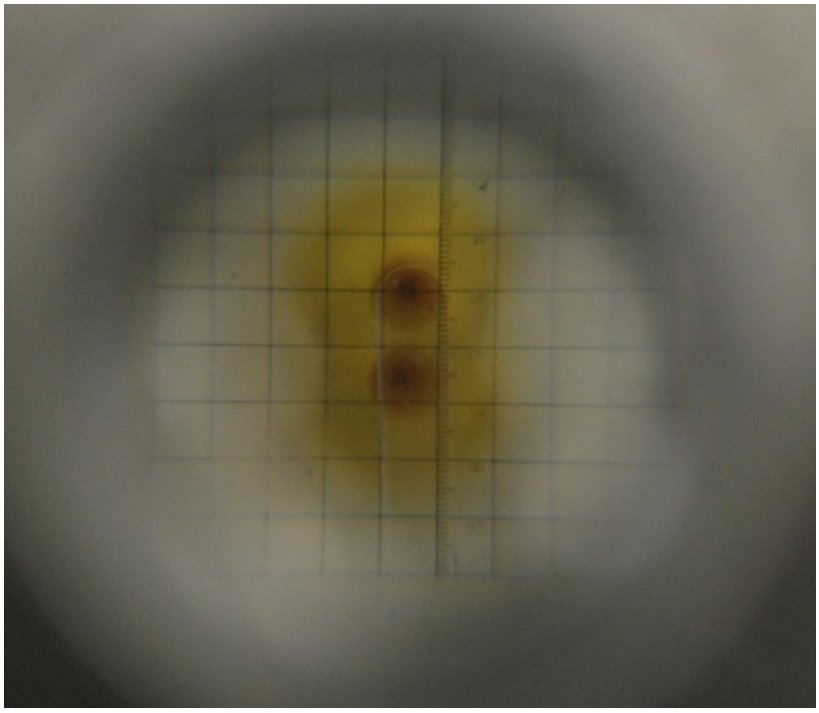

Figure 5-101. Zoom-in view of the Na-22 double source disk. The grid consists of squares of $1mm^2$.

The two point sources were aligned parallel to the front surface of the NaI(Tl) detector. One row of BGO crystals and one row of NaI(Tl) were enabled to take coincidence data for further data processing. The LORs from the double source disk are shown in Fig. 5-102. The zoom-in view of the crisscrossed region is shown in Fig. 5-103. The bin number of 24 was chosen to draw the cross-sectional profile. The profile is shown in Fig. 5-104. FWHM of the profile is roughly 4mm. When the two cross-section profiles are compared, the width of profile from the double source disk is wider than that from a single source disk as shown in Fig. 5-105.

Figure 5-102. Back-projection from the Na-22 double source disk.

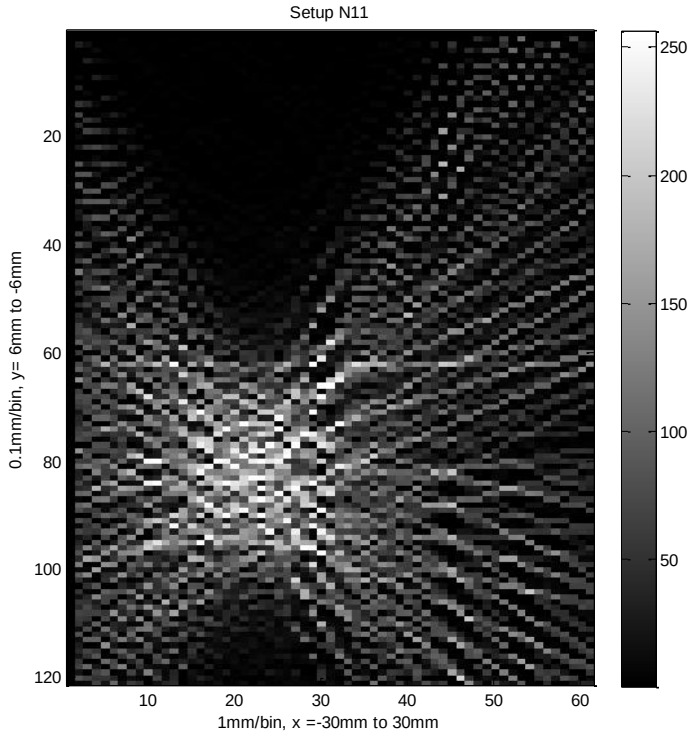

Figure 5-103. Zoom-in view of the back-projection.

.

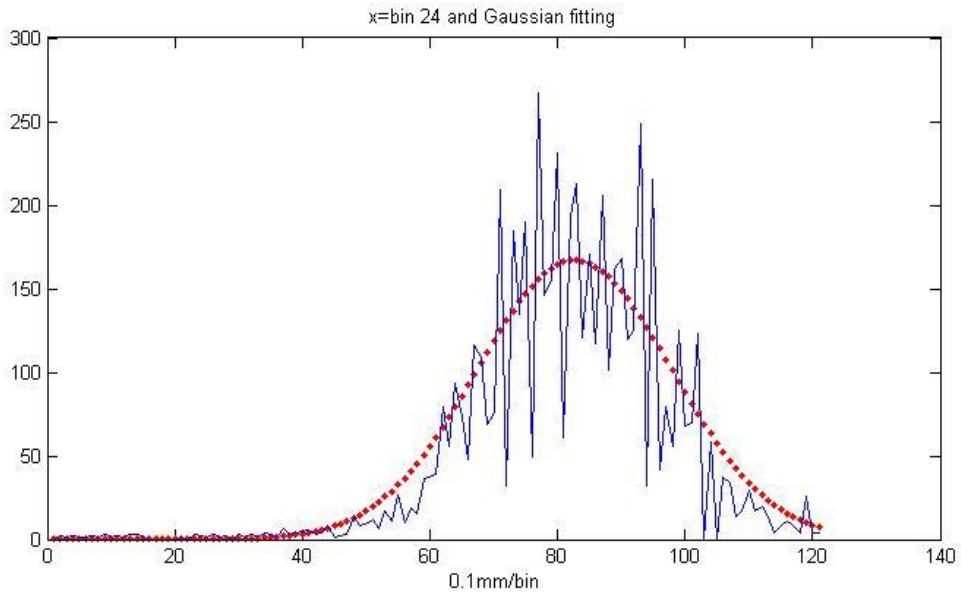

Figure 5-104. Cross-section profile of the back-projection from the double Na-22 source disk.

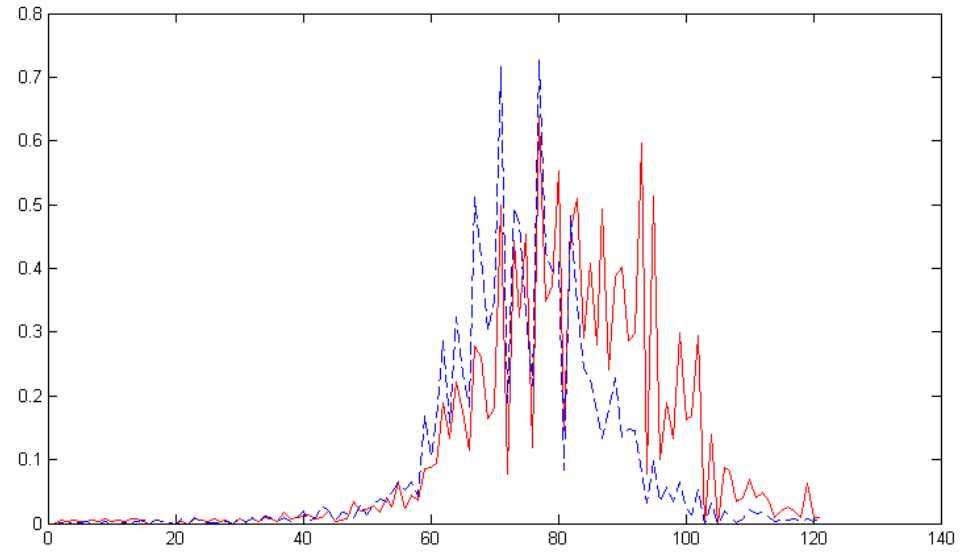

Figure 5-105. Superimposition of the two normalized cross-section profiles.

5 .5 BGO-NaI Coincidence Set-Up for 3 Dimensional Data Acquisition

5. 5 .1 Na-22 Double Source Disk

The experimental set-up for the 2-dimensional data acquisition collected coincidence data between one row of BGO crystals and one row of NaI(Tl) crystals. The data acquisition set-up was expanded to a 3-dimensional set-up. For 3-dimensional data acquisition, we used 3 rows of BGO crystals. The Na-22 double source was used as a radioactive source.

As a first step, the coincidence events between the 3 rows of BGO crystals and the NaI(Tl) detector were acquired. Fig. 5-106 shows the selected 3 rows of BGO crystals in the user interface. Selected 5-by-11 NaI(Tl) crystals are also shown in Fig. 5-106. The coincidence events between the 3 rows of BGO crystals and the 5-by-11 NaI(Tl) crystals were acquired. The square below the oveal shows the acquired coincidence events in the NaI(Tl) detector. Only a few NaI(Tl) rows collected most of the coincidence events.

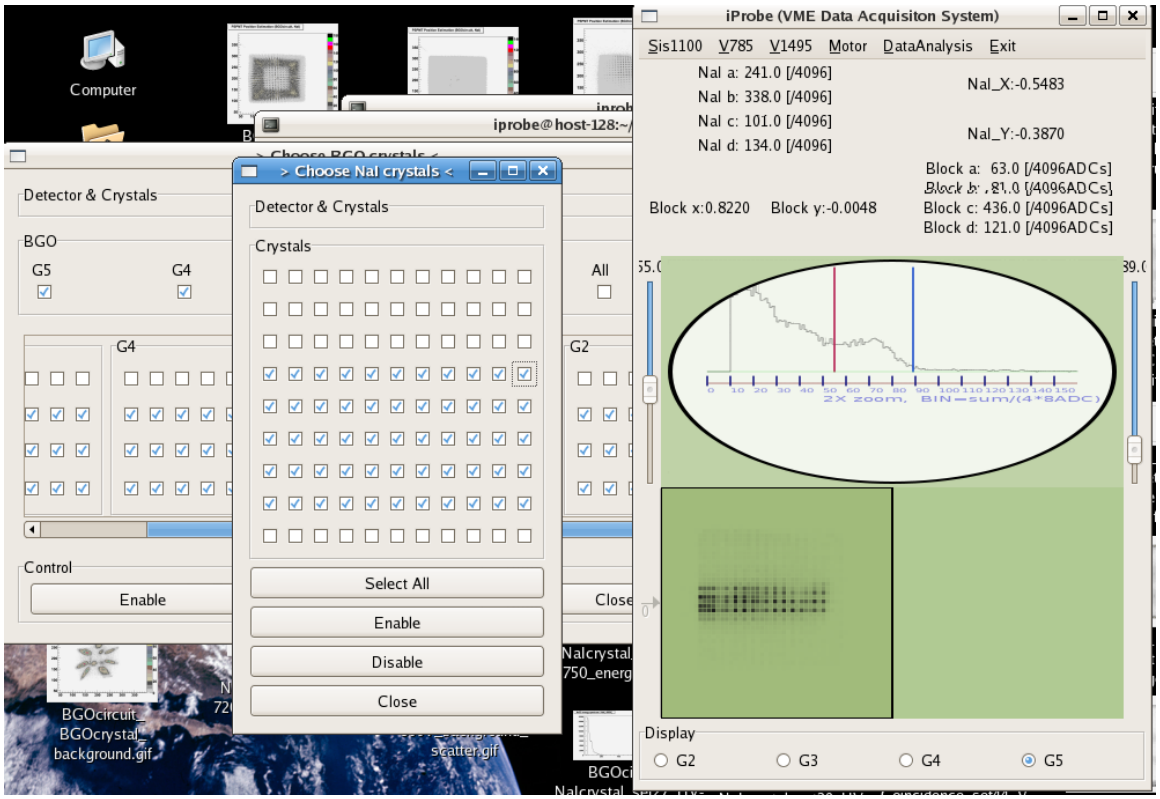

Figure 5-106. Graphical user interface for 3D dimensional data acquisition.

Since only a few NaI(Tl) were illuminated in coincidence mode, we enabled 5 rows of NaI(Tl) crystals for further data processing. The chosen 5 rows of NaI(Tl) crystals were imaged in the high resolution coincidence image. Fig. 5-107 shows the high resolution coincidence image in NaI(Tl) when the NaI(Tl) detector is at the 0° reference position. We can see a 5-by-11 array of estimated NaI(Tl) crystals in the high resolution coincidence image.

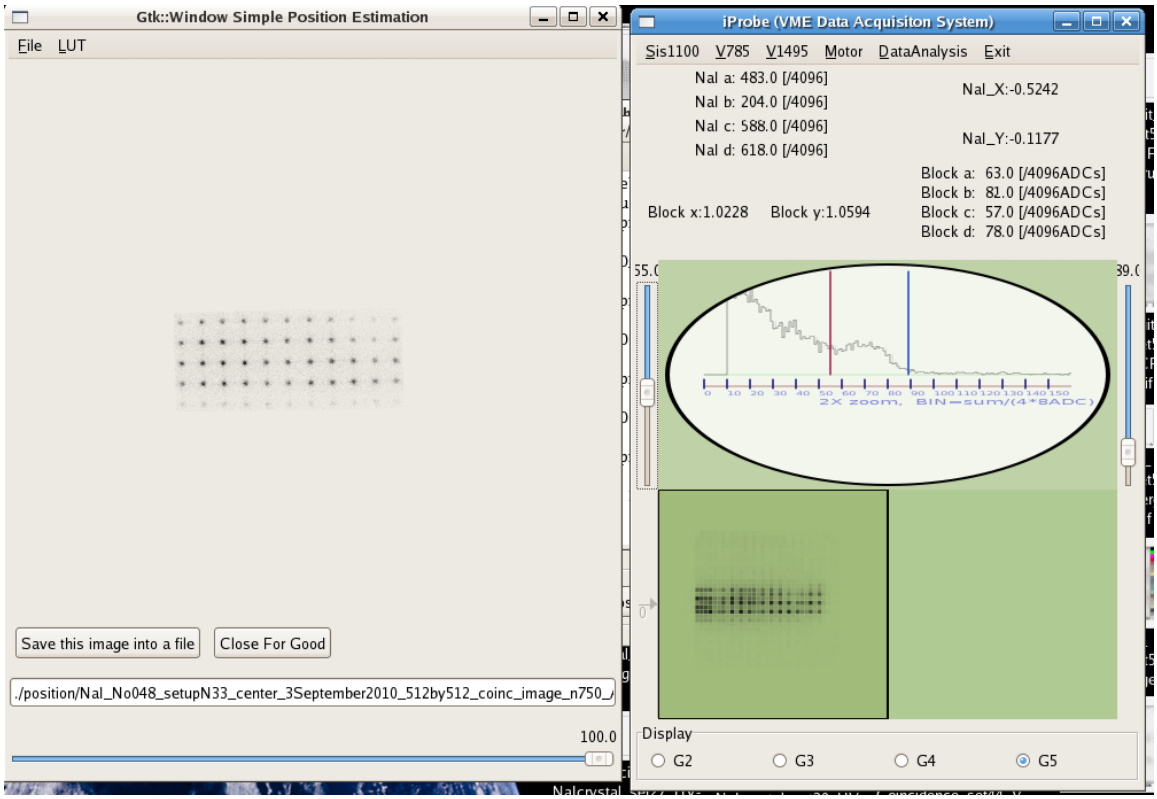

Figure 5-107. Coincidence image in NaI(Tl) when 3 rows of BGO crystals were enabled. The NaI(Tl) detector was at the 0 ° reference position. A 5-by-11 array of NaI(Tl) crystals were enabled in the high resolution image.

To take data from a different angle, the NaI(Tl) detector was rotated counter clockwise by 12 degrees. Fig. 5-108 shows the corresponding coincidence image in the NaI(Tl) detector. The low resolution image shows a different hit-map than that in Fig. 5-107 because the NaI(Tl) detector was rotated.

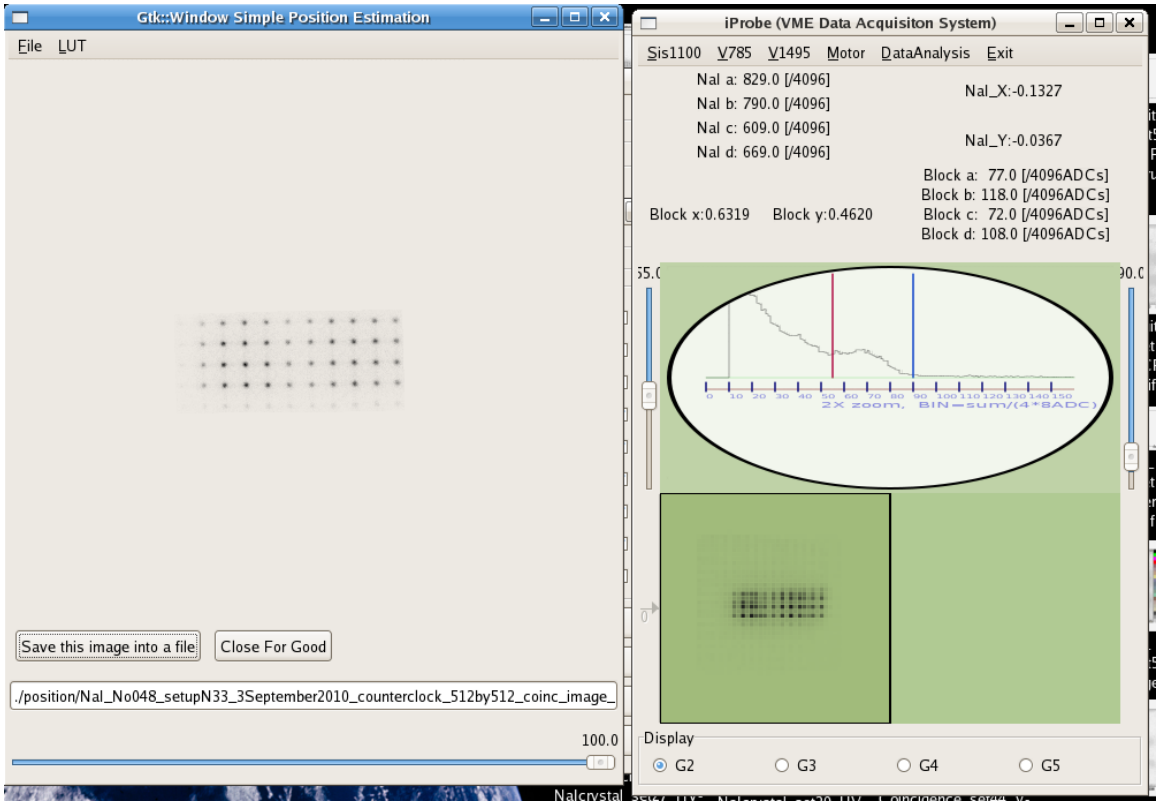

Figure 5-108. Coincidence image in NaI(Tl). The NaI(Tl) detector was at the 12° counter-clockwise position.

5 .6 **Image Reconstruction Using a Graphics Processing Unit**

The coincidence events between a 3-by-24 array of BGO crystals and a 5-by-11 array of NaI(Tl) crystals were acquired using the experimental set-up. The point-in-polygon test was performed for each coincidence events; refer to section 5.3.4. As a result, the acquired coincidence data contained the BGO crystal identification numbers (IDs) and NaI(Tl) crystal identification numbers. The crystal IDs were converted into 3-dimensional coordinates in an off-line analysis program. The 3-dimensinal coordinates represent actual crystal locations. The converted 3-dimensional coordinates were used for 3-dimensional image reconstruction.

5. 6 .1 **Differences between True LORs and Measured LORs**

The acquired 3-dimensional data were coincidence events between 3 rows of BGO crystals and 5 rows of NaI(Tl) crystals. One problem arose when the *quantization* of the end-points of LORs were considered. Fig. 5-109 shows an illustration of side view of the experimental set-up. The BGO crystals are 12.5mm tall and NaI crystals are 2mm tall. We note that the ratio of the BGO crystal to the NaI(Tl) crystal height is roughly 6. Fig. 5-109 (a) shows a line-of-response 1 (LOR1). The LOR1 is a line that connects the center of the BGO #2 and the center of the NaI #5. In the measurement space, the LOR 1 represents all lines-of-response between the BGO row #2 and the NaI row #5 because all the coincidences are *quantized* to the nominal LOR. Therefore a large number of true LORs can result in the measured LOR 1, consequently containing some position error.

Fig. 5-109 (b) shows a true line-of-response LOR 2 between BGO row #1 and the NaI row #5. The LOR 3 connects the center of the BGO #1 and the center of NaI #5. The LOR3 is the measured line-of-response that represents the true LOR2. The measured LOR3 deviates from the true LOR2 and does not pass through the point source. Another line-of-response is shown in Fig. 5-109 (c). The true line-of-response LOR 4 between the BGO row #3 and the NaI row #5 is the dished line. The measured LOR 5 (solid line) represents the true LOR4. The measured LOR also deviates from the true LOR.

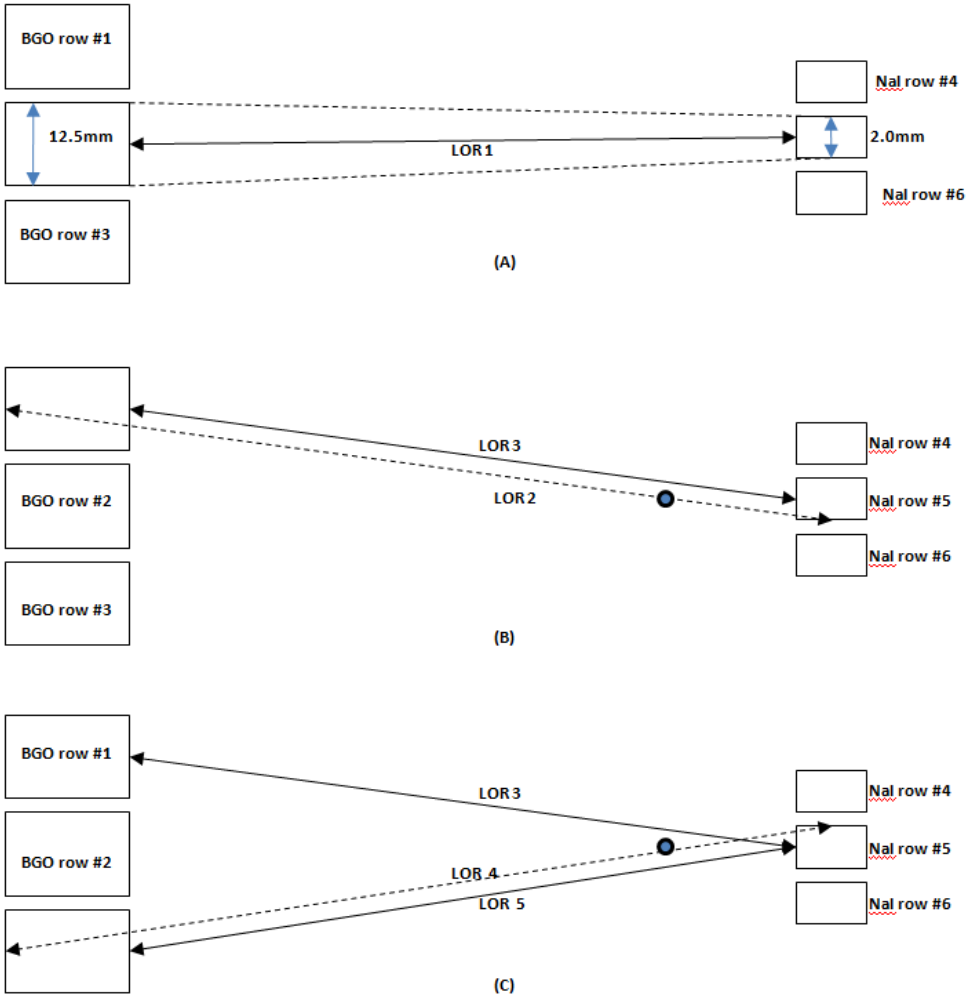

Figure 5-109. Illustration of side view of the experimental set-up. Dashed lines are for true LORs and solid lines are for measured LORs.

The correction of mean depth penetration was not used. The front face location was used for the end-point coordinates. This effect will be investigated in future studies. The effect of measured LORs is shown in Fig. 5-110. The true line-of-responses, the dashed line LOR2 and LOR4, pass through the point source. On the contrary, the measured LORs neither pass through the point source nor crisscross near the point source. Therefore we excluded the set of LORs between BGO row #1 and NaI row #5 and the set of LORs between BGO row #3 and NaI row #5.

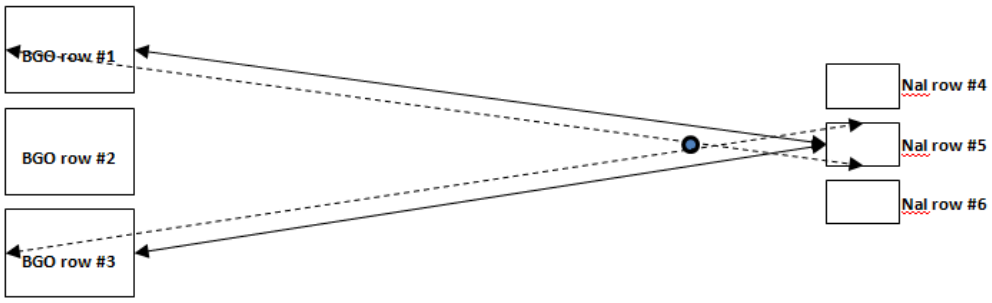

Figure 5-110. Illustration of side view of the experimental set-up. Measured LORs do not crisscross near the point source.

There are some lines-of-response that have less discrepancy between true LORs and measured LORs. Fig. 5-111 shows a measured LOR between BGO row #3 and NaI row #4. The measured LOR (solid line) represents all the possible true LORs between BGO row #3 and NaI row #4. In the same way, another measured LOR between BGO row #1 and NaI row #6 represents all the possible true LORs between BGO row #1 and NaI row #6 as a consequence of quantization of the interaction positions. The measured LORs in Fig. 5-111 crisscross near the point source.

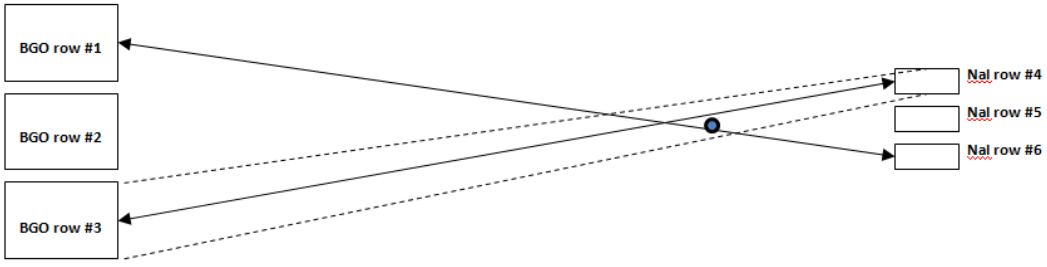

Figure 5-111. Less discrepancy between true LORs and measured LORs.

Fig. 5-112 shows the illustration of side view of the experimental set-up and the measured LORs that were used for image reconstruction. Other types of LORs are left out in order to reduce image distortion due to position error.

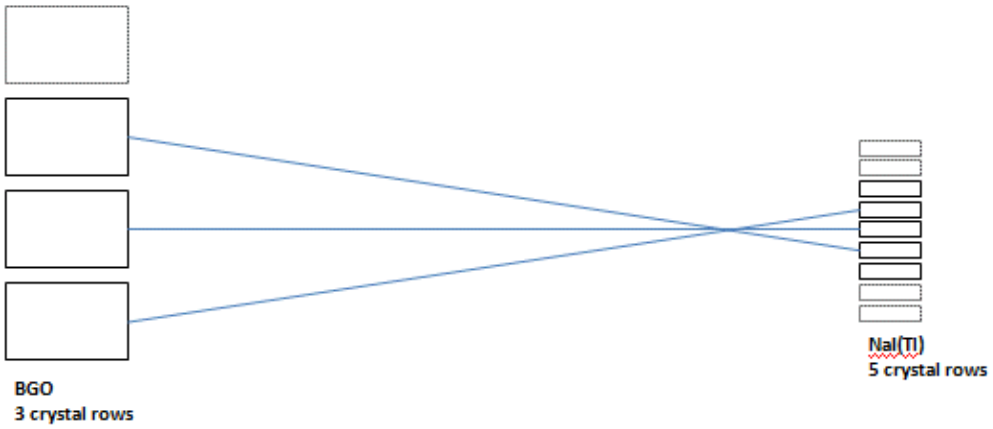

Figure 5-112. Side view of the experimental set-up. Measured LORs that were included for image reconstruction are shown.

5. 6 .2 **3-dimensional Image Reconstruction**

5.6.2.1 **A Na-22 Double Source Disk at the Pivot Center (setup N33)**

The Na-22 double source disk was placed at the center of the pivot cylinder. The two point sources were aligned parallel to the front surface of the NaI(Tl) detector so that the NaI(Tl) detector could see the two point sources. The coincidence data between the NaI(Tl) detector and the BGO block detectors were acquired at 3 different angles. The interaction positions in the detectors were estimated using a centroid method and were mapped to true crystal positions using the point-in-polygon test. Each crystal has a crystal

identification number. The online data acquisition/analysis program stored the crystal identification numbers for further processing.

A variant of one-pass list mode ML algorithm discussed in Chapter 3 was used for image reconstruction. In addition, a graphics processing unit discussed in Chapter 4 was used to speed up image reconstruction.

The coincidence data were acquired at three different angles (at -12° for the counter-clockwise rotation, at 0° for the reference position, and at 14° for the clockwise rotation). In the simulated data study discussed in Chapter 3, the number of LORs per angle was fewer than 1000. To use approximately the same number of LORs, roughly 900 LORs were cut out of each angle data set. Each subset was then confined to 16 LORs.

The sequence of input data to the row action ML algorithm is also important. The coincidence data from the 0° reference position were processed first for image reconstruction. The acquired data from the counter-clockwise rotation set-up were then processed. Finally, the LORs from the clockwise rotation set-up were last fed to the image reconstruction program.

Fig. 5-113 shows a center slice of a 3-dimensional reconstructed image. The image space has a 128×64×64 array of voxels. Each voxel is a 0.25mm-side cube. The big hump at the center is from the Na-22 double source. The relaxation parameter λ of the image reconstruction algorithm was set to $0.5/Q_i$. The sensitivity factor Q_i is approximately calculated at the given image voxel on the fly. Small humps around the big hump are artifacts due to both position error and the image reconstruction algorithm.

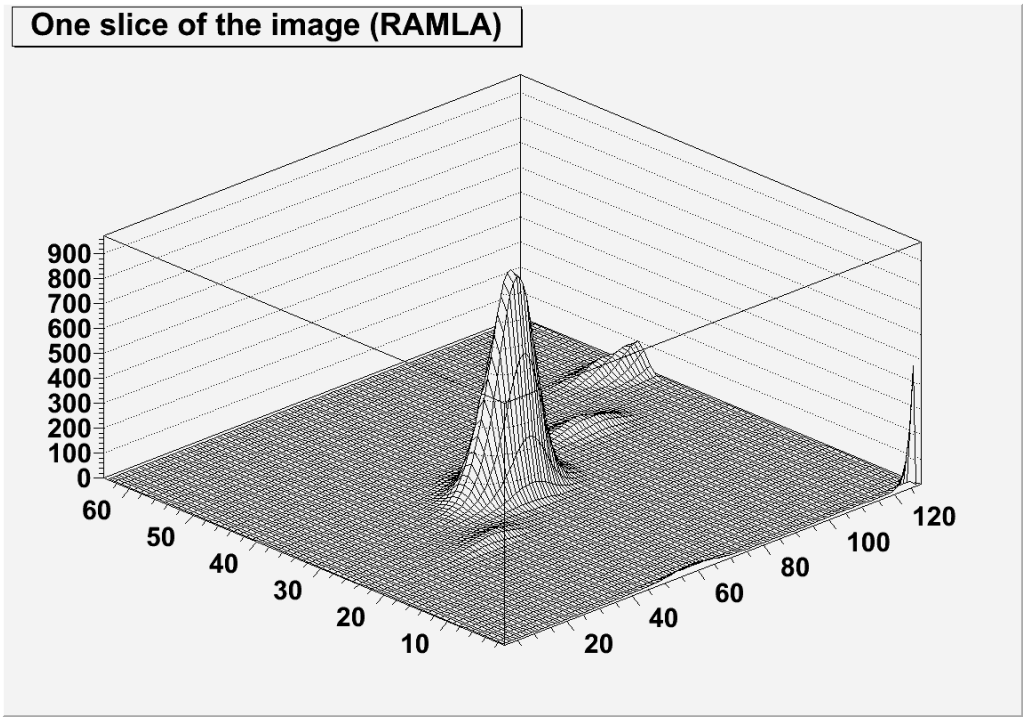

Figure 5-113. Center slice of a 3-dimensional reconstructed image; surface mapping $\lambda=0.5/Q_i$.

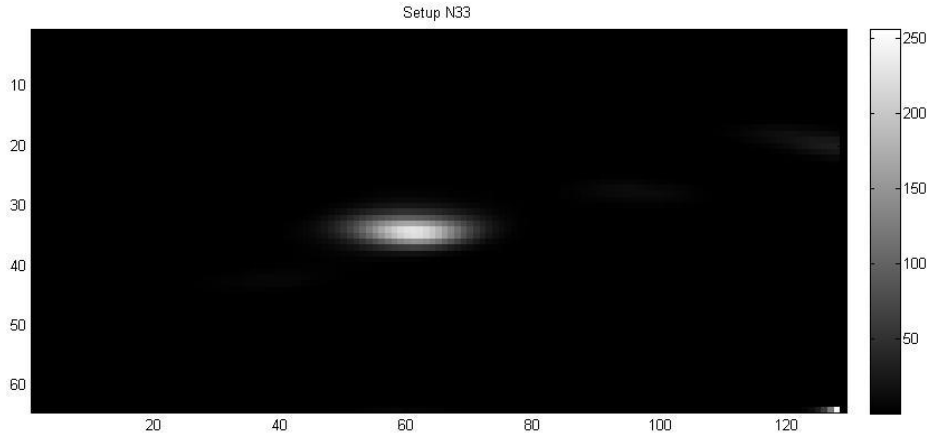

Figure 5-114. Center slice of a 3-dimensional reconstructed image; intensity map.

The count-rate of acquired coincidence events was observed. The observation was based on the acquired data by the online data acquisition/analysis program. The coincidence count-rate at the VME FPGA is expected to higher than that at the on-line

data acquisition/analysis program. Coincidence events that lay outside the energy window were left out. In addition, the online data acquisition program did not collect all the coincidence events at the VME FPGA because it took time to transfer the digitized data to the host computer and to draw raw position estimation images on the screen. It takes about 6μs to digitize the peak value for each operation. The gate width for peak-sensing is less than 1μs. Therefore the dead time could take up about 85% of the available time.

Table 5-5 shows the count rate at the data acquisition/analysis program when the NaI(Tl) probe was at the -12° counter clockwise position. The on-line data acquisition program stored about 159 coincidence events per minute. The Na-22 double source disk contains 60μCi (2.2MBq) in total. Approximately 2.2 million photon pairs per second were generated and roughly 0.00012% of the annihilation events were acquired by the data acquisition program.

Table 5-5. Coincidence count rate at the online data acquisition/analysis program.

Probe Orientation	#Coincidence Events	Acquisition Time (hours)	Rate (events/min)
Counter clockwise	162791	17	159

5.6.2.2 A Na-22 Double Source Disk Located Slightly Off-Center

5.6.2.2.1 Outward Transverse Displacement (set-up N55)

The Na-22 double source disk was displaced in the transverse direction by about 2.5mm as shown in Fig. 5-114. Data were taken at three different angles.

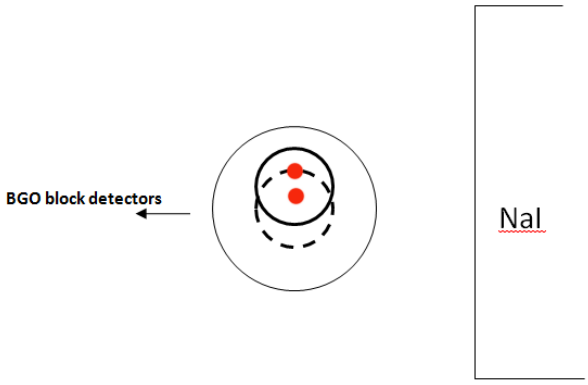

Figure 5-115. Illustration of top view of the set-up. The source disk was translated about 2.5mm off center in the outward direction.

Fig. 5-116 shows the experimental set-up for the data acquisition. The two point sources were aligned parallel to the front surface of the NaI(Tl) detector.

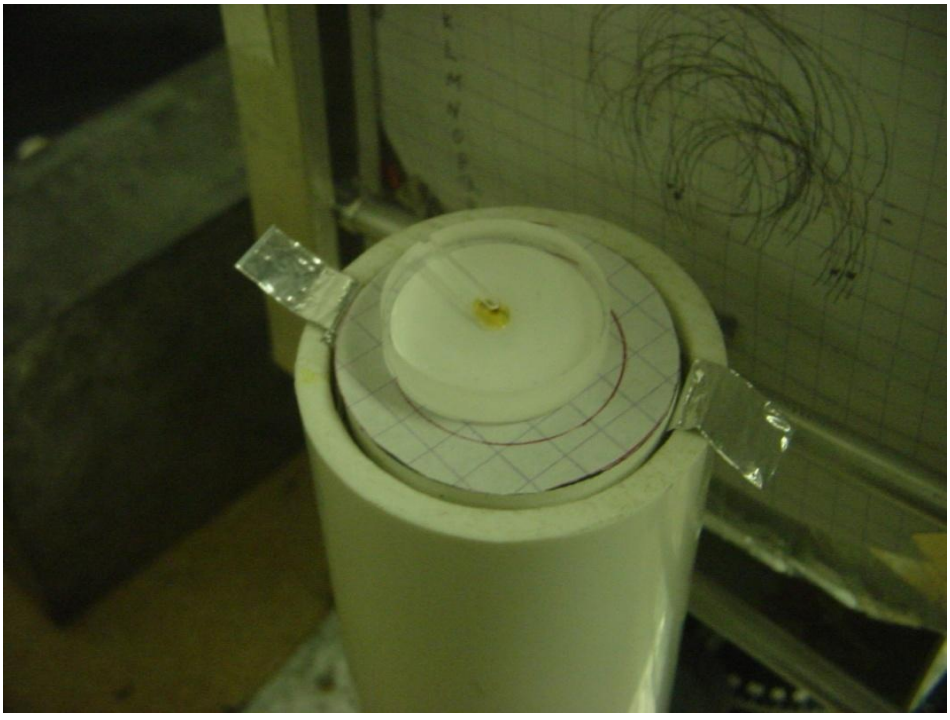

Figure 5-116. Double source disk at the pivot. The source disk was translated outward.

Fig. 5-117 shows a center slice of a 3-dimensional reconstructed image. The hump appeared to be moved outward compared to Fig. 5-113. The pixel size is 0.25mm-by-0.25mm.

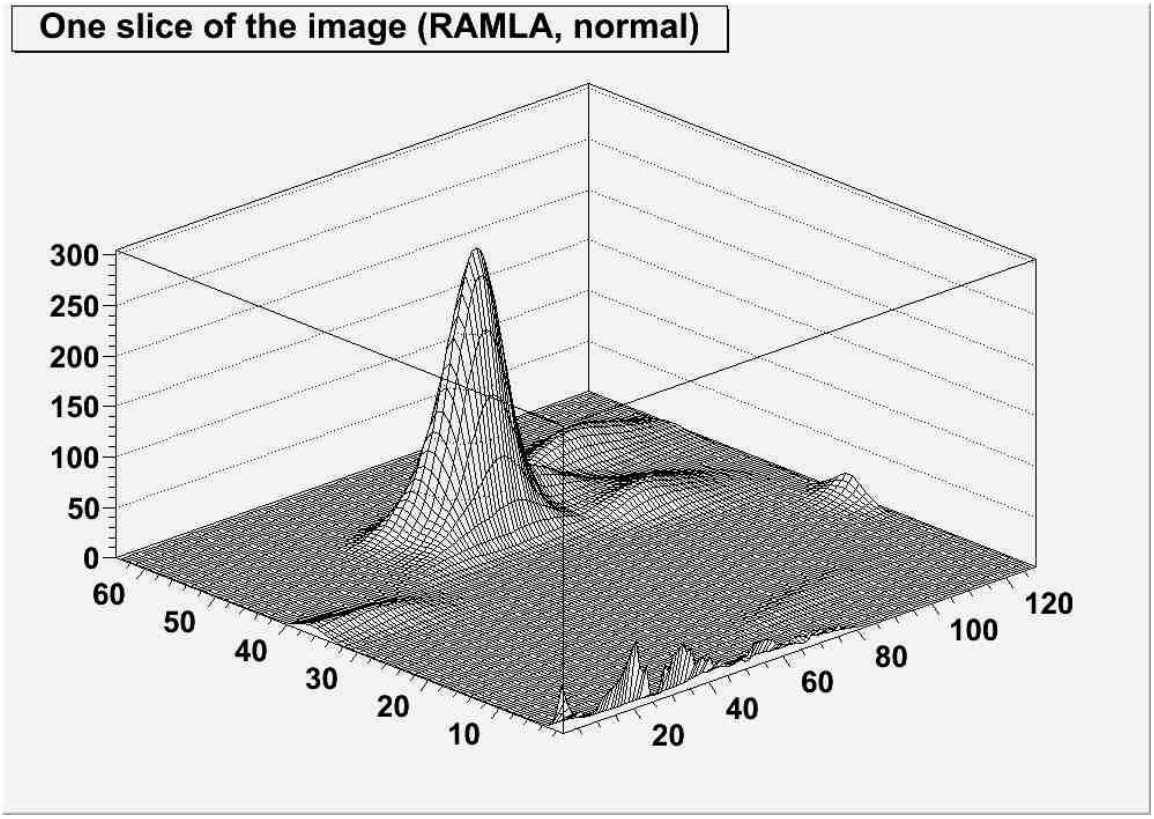

Figure 5-117. Center slice of a 3-dimensional reconstructed image. The source disk was slightly translated outward. $\lambda=0.3/Q_i$.

Fig. 5-118 shows the intensity map of the center slice image. Table 5-6 shows the count rates that were acquired at the online data acquisition program. The count rates are slightly different for each direction. This difference could be due to the different joint solid angle.

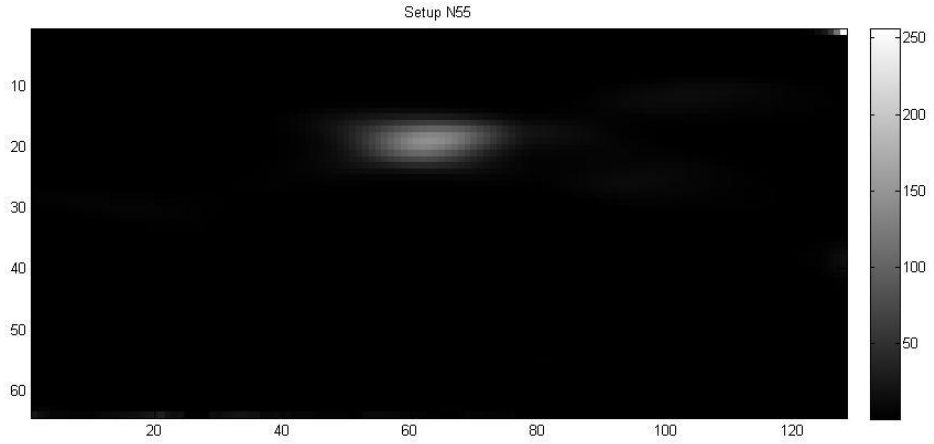

Figure 5-118. Center slice of a 3-dimensional reconstructed image; intensity map.

Table 5-6. Coincidence count-rates at the online data acquisition/analysis program. The source was slightly translated outward.

Probe Orientation	#Coincidence Events	Acquisition Time (hours)	Count Rate (events/min)
Counter clockwise	156415	16.5	158
Center (reference)	65533	8	136
clockwise	122087	18	113

5.6.2.2.2 **Longitudinal Translation toward the BGO Detector (setup N66)**

The source disk was translated toward the BGO detector by 2.5mm in Fig. 5-119. A center slice of a 3-dimensional reconstructed image is shown in Fig. 5-119. The hump in the reconstructed image was also slightly translated toward the BGO detector.

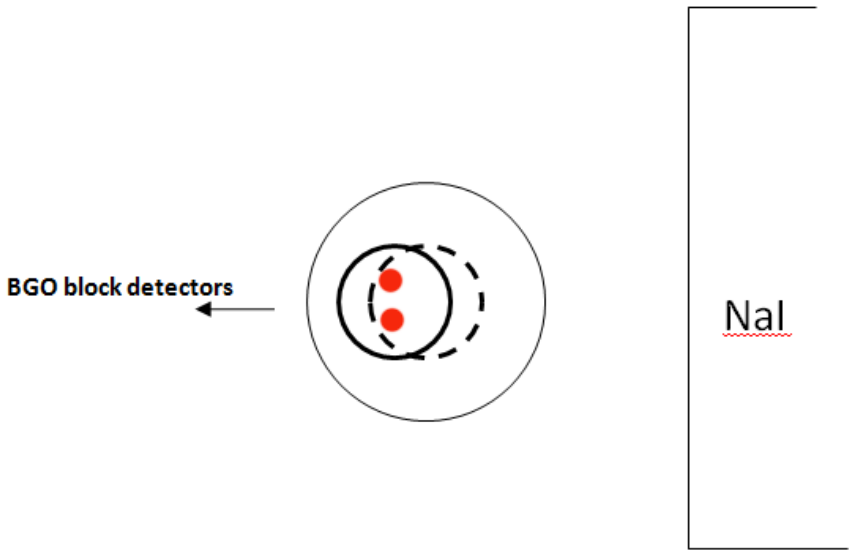

Figure 5-119. Illustration of top view. Translation of the source disk toward the BGO detector by 2.5mm.

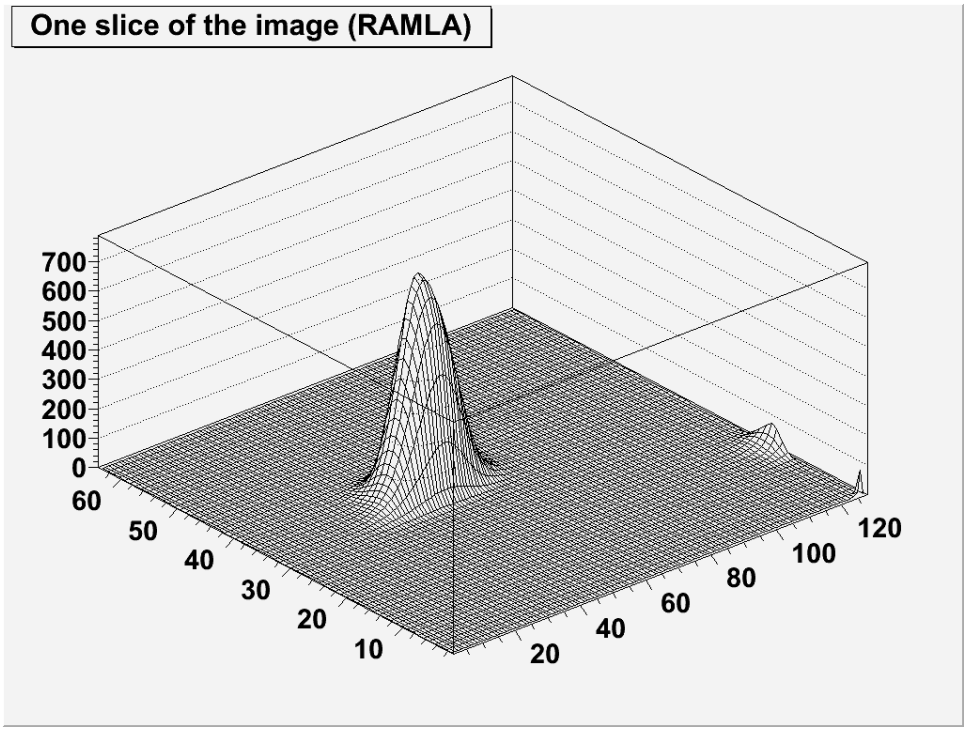

Figure 5-120. Center slice of a 3-dimensional reconstructed image. The source disk was slightly translated toward the BGO detector. $\lambda=0.5/Q_i$.

The coincidence count-rates at the online data acquisition/analysis program are shown in Table 5-7. The coincidence count-rates were less than those in Table 5-6 because the double source disk was slightly away from the NaI(Tl) detector, resulting in a reduced effective solid angle.

Table 5-7. Coincidence count-rates at the online data acquisition/analysis program. The source disk was slightly translated toward the BGO detector.

Probe Orientation	#Coincidence Events	Acquisition Time (hours)	Rate (events/min)
Center (reference)	31700	10	53
Clockwise	36602	7.5	81

5.6.2.2.3 **Longitudinal Translation toward the NaI(Tl) Detector (setup N77)**

Fig. 5-121 shows the illustration of the source translation toward the NaI(Tl) detector by 2.5mm.

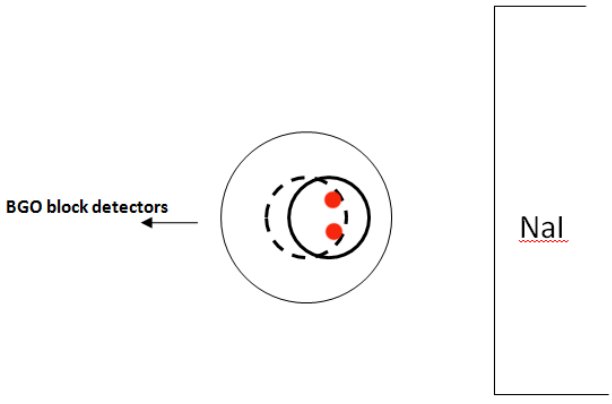

Figure 5-121. Illustration of the translated source disk toward the NaI(Tl) detector.

The experimental set-up is shown in Fig. 5-122. A center slice of a 3-dimensional reconstructed image is shown in Fig. 5-123. The reconstructed image in Fig. 5-123 shows two humps in the longitudinal direction. The two humps look like realization of incorrect LORs due mainly to position error as the source disk gets closer to the NaI(Tl) detector.

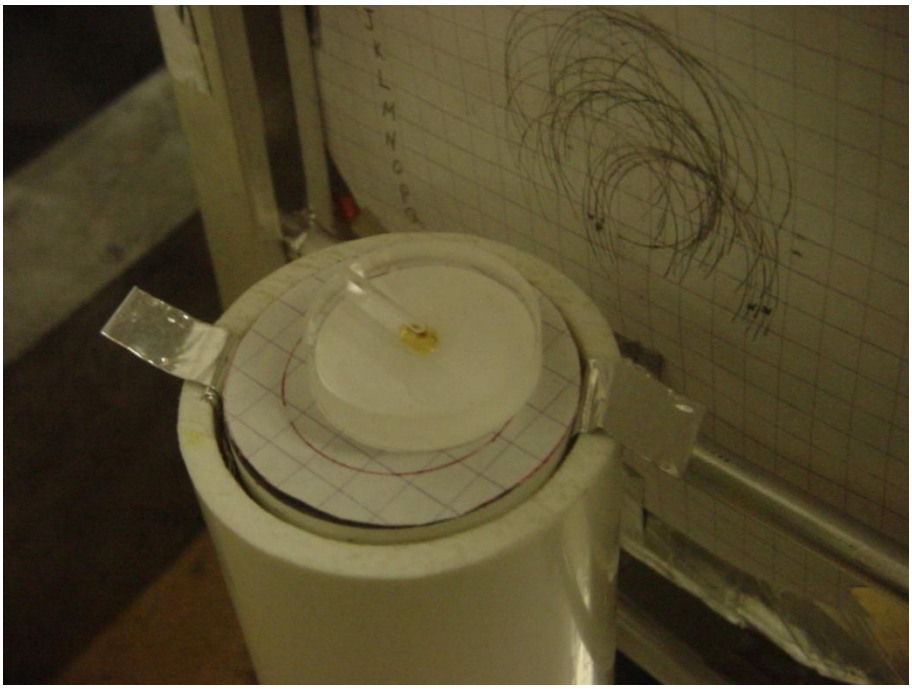

Figure 5-122. Double source disk that was translated toward the NaI(Tl) detector.

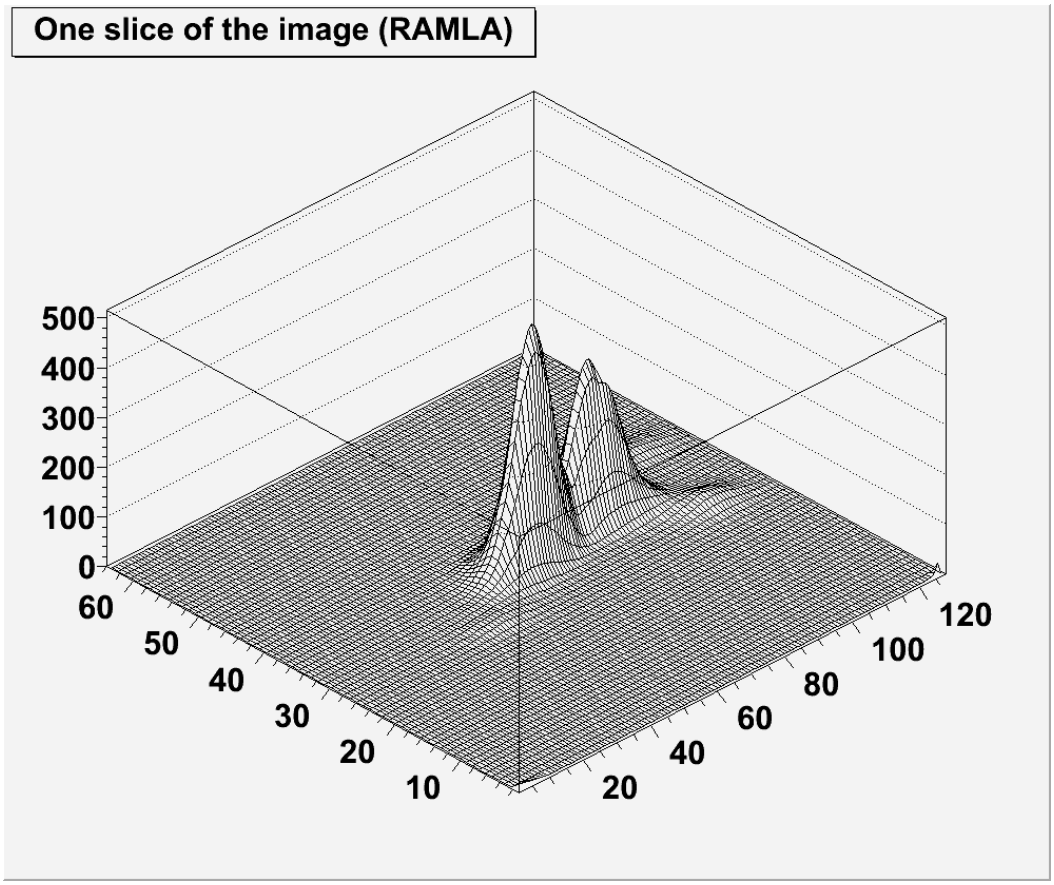

Figure 5-123. Center slice of a 3-dimensional reconstructed image. The source disk was translated toward the NaI(Tl) detector by 2.5mm.

Table 5-8 shows the count rates that were acquired by the online data acquisition program. We can notice that the count rates are higher than those from the set-up of translation toward the BGO detector.

Table 5-8. Coincidence count-rates at the on-line data acquisition/analysis program. The source disk was slightly translated toward the NaI(Tl) detector.

Probe Orientation	#Coincidence Events	Acquisition Time (hours)	Rate (events/min)
Counter clockwise	143301	17	140
Center (reference)	49447	5.85	141
Clockwise	89790	11.7	128

5 .7 **High Resolution Small Animal PET**

We have been also investigating a high resolution small animal PET system and *high resolution* PET imaging probes. A prototype device has been built and consists of silicon pixel detectors and BGO block detectors. The silicon detectors are located between the two banks of BGO block detectors and just as for the probe reported in this dissertation, the high resolution detectors are close to the region of interest. Therefore we can acquire multi-resolution coincidence events. Silicon-silicon events provide the highest resolution coincidence events.

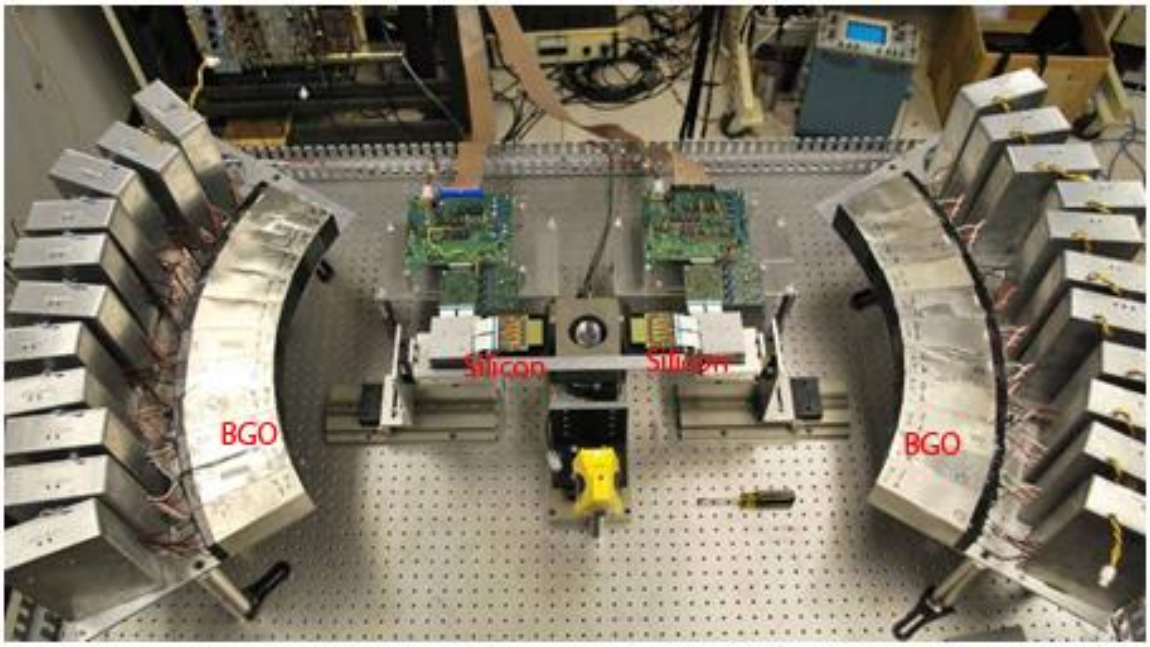

Figure 5-124. High resolution PET imaging system, by the courtesy of Dr. Clinthorne at University of Michigan.

The rotation stage at the center of the experimental set-up is shown in Fig. 5-125. The pixel silicon detector module is shown next to the rotation stage hemmed in by the tungsten slit collimators. Each silicon pixel measured 1.4mm×1.4mm.

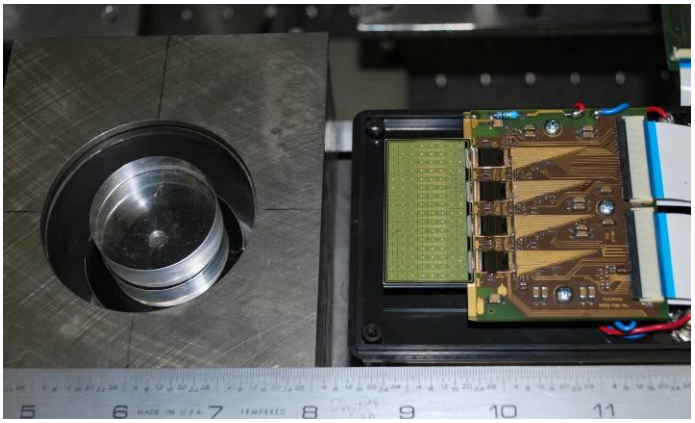

Figure 5-125. Rotation stage and the silicon detector module.

5. 7 .1 Imaging a Na-22 Double Source Disk

The Na-22 double source disk was imaged using the high resolution PET imaging system and MLEM. The silicon-silicon events were used for image reconstruction since the separation between the two point sources is 1.5mm. Fig. 5-126 shows the two point sources were clearly identified in the reconstructed images. The whole 360° data were used for the image reconstruction.

This high resolution PET imaging system also uses high-resolution detectors and low-resolution BGO block detectors. Therefore, this system can be rearranged and have a similar geometry to the proposed intra-operative PET imaging probe system.

Since the reconstructed image from 360° clearly shows the two-point source, if we use this silicon pixel detector as the imaging probe, we can expect better spatial resolution than the proposed intra-operative PET imaging probe system.

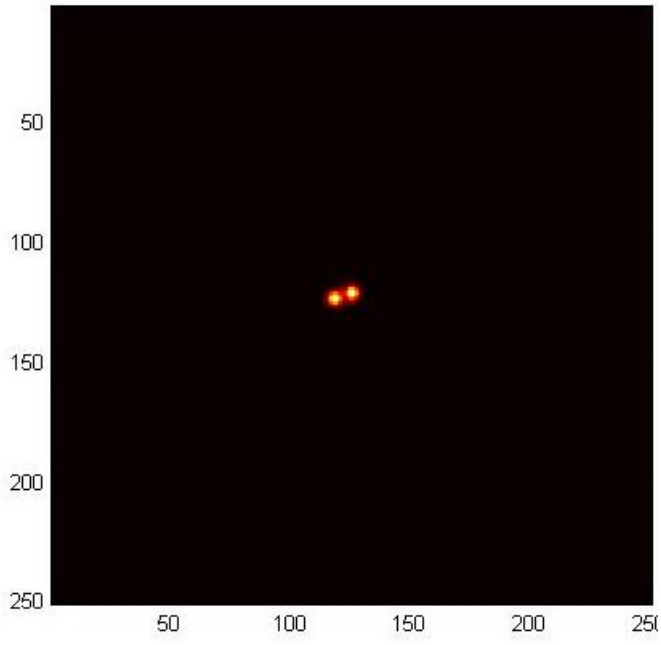

Figure 5-126. MLEM reconstructed image using 360 degree data and silicon-silicon coincidence events. 0.2mm/bin.

5. 7 .2 **Imaging a Resolution Phantom**

A 4cm diameter resolution phantom was also imaged using the high resolution PET system and MLEM. Rod diameters are 4.8mm, 4.0mm, 3.2mm, 2.4mm, 1.6mm, and 1.2mm. The silicon-silicon coincidence events from the whole 360° were used for image reconstruction. We can see that 1.2 diameter rods were identified.

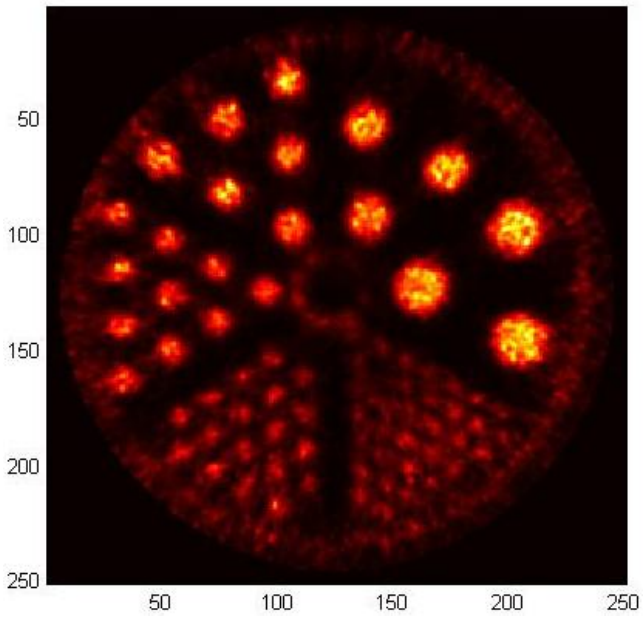

Figure 5-127. Reconstructed image of a 4cm diameter resolution phantom. Silicon-silicon events were used.

We note again that the proposed intra-operative PET imaging probe system uses high spatial resolution detector elements in coincidence with low spatial resolution detector elements. In the same way, silicon-BGO coincidence events were used for image reconstruction. Fig. 5-128 shows a reconstructed image using only silicon-BGO coincidence events. The small rods were not distinguishable and 2.4mm diameter rods were separated.

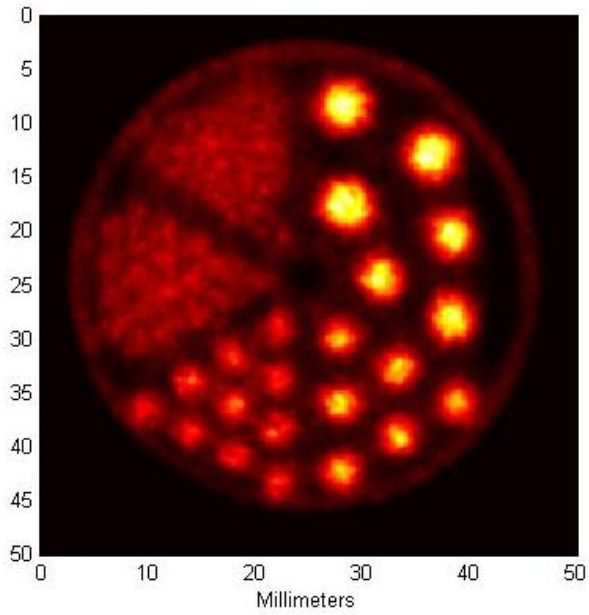

Figure 5-128. Reconstructed image using only silicon-BGO coincidence events.

5 .8 **Summary**

In this chapter, a first-generation prototype of the surgical PET imaging probe system was built to test the feasibility and potential performance of a positron imaging system consisting of a high resolution hand-held NaI(Tl) imaging probe operating in coincidence with a lower resolution partial ring of BGO detectors.

A pixilated ($2\times2\times10mm^3$) NaI(Tl) detector that was coupled to a PSPMT was used for the high resolution imaging probe. BGO block detectors were used for the partial ring detector. A Na-22 double source disk was used as a radioactive source. A position tracker was not included in the prototype system for the sake of simplicity. Instead, the imaging probe was rotated around a pivot point to predetermined locations.

A preliminary test of system resolution was made using a Na-22 double point source with the two source separated by 1.5mm. The source disk was located about 4mm from the imaging probe. The proposed image reconstruction algorithm that included

RAMLA, one-pass OSEM, and a Gaussian kernel was used to obtain 3-dimensional reconstructed images.

Reconstructed images did not show two point sources. The two point sources blurred together in the images. The single hump measured roughly 2mm in FWHM in the transverse direction and roughly 4mm in FWHM in the longitudinal direction. Fig. 5-129 shows the convolution of two point sources with 1.5mm separation. FWHM of 2mm detector response function and additional 0.5mm FWHM positron range were included.

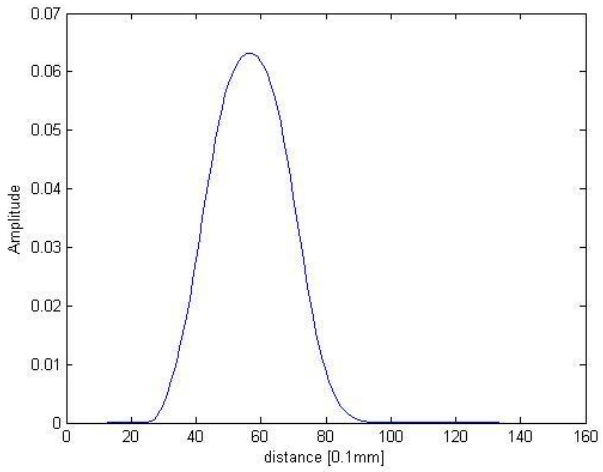

Figure 5-129. Two point sources with 1.5mm separation. The probe response function of 2mm FWHM and the positron range of 0.5mm FWHM were used.

Fig. 5-130 and Fig. 5-131 show the convolution outcomes of 2mm separation and 3mm separation, respectively. We can see two point sources with 2mm separation are separable. To find out the separation capability of the experimental set-up, we may need a Na-22 double source disk with 3mm separation because the spatial resolution of the PET imaging probe system is roughly determined by the width of the detector element. $2\times2\times10mm^3$ NaI(Tl) crystals were used for the experimental set-up.

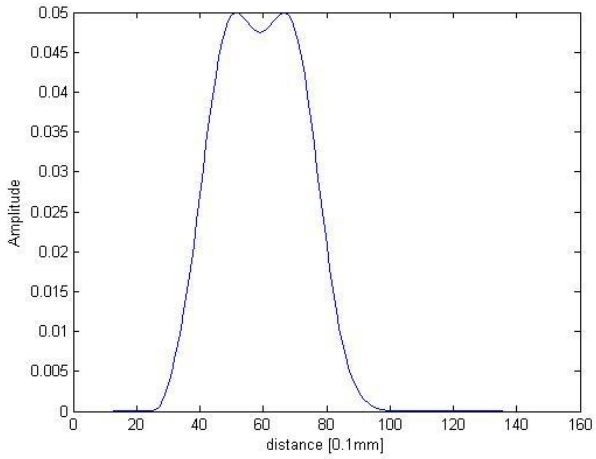

Figure 5-130. Two point sources with 2.0mm separation. The probe response function of 2mm FWHM and the positron range of 0.5mm FWHM were used.

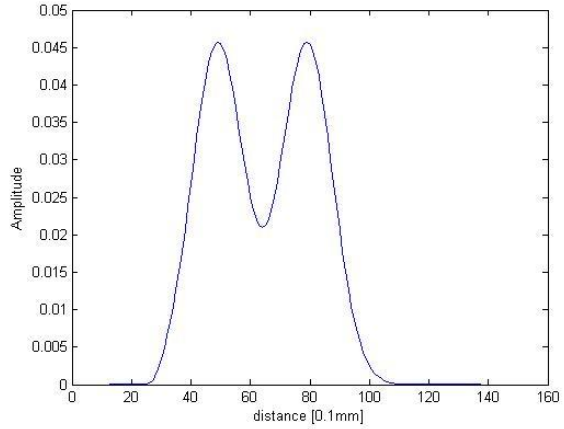

Figure 5-131. Two point sources with 3.0mm separation. The probe response function of 2mm FWHM and the positron range of 0.5mm FWHM were used.

The coincidence rate by the data acquisition program was about 159 coincidence events/minute. Since the source activity of the Na-22 double point source is 2.2MBq, the measured coincidence detection efficiency is roughly 0.00012%.

In the simulation study using BGO and LSO detectors, 804 coincidence events were acquired form 0.6 million annihilation photon pairs. The coincidence detection rate is roughly 0.134%. Since this coincidence rate can be achieved from a perfect, ideal

measurement system, the rate is much higher than that of the experimental set-up. In addition, the experiment set-up has dead-time because the peak sensing ADC needs 6μs to digitize the peak value. Also the data acquisition program requires time to do position estimation and display estimated positions. The experimental set-up is smaller than the simulated geometry which explains the lower detection efficiency.

We expect that the prototype PET imaging probe system can identify whether a tumor size is greater than 2mm since front surface of the detector element is $2\times2mm^2$. Detectable tumor to background ratios will be reported in a future study. Detectable tumor activity will be also investigated in a future study.

It is important to note that the reconstructed images showed that the effects of limited angle tomography were not severe in the longitudinal direction. This effect is due mainly to the NaI(Tl) detector's proximity to the target source and the proposed image reconstruction algorithm.

In future studies, smaller detector elements in the imaging probe can be employed to enhance spatial resolution. We also need to investigate effects of increased effective probe front surface as a way to increase detection sensitivity. A position tracker must be integrated to the prototype system in order to access position error due to uncertainty of the tracker itself.

Chapter 6
Conclusions and Future Work

6 .1 Conclusions

Removing detected tumors during surgery is a difficult task because the locations of lesions could be displaced due to patient's movement and the extent of the detected tumors is not clearly visible. In addition, to detect small tumors less than 1cm still remains challenging in conventional PET imaging. This difficulty in detecting small tumors is due mainly to annihilation photon acolinearity, limited linear sampling, statistical noise, and undesired radiation from surrounding tissues.

The proposed intra-operative PET imaging probe system consists of a high resolution imaging probe equipped with a position tracker and a partial ring detector. The imaging probe operates in coincidence with the partial ring detector. In addition, the surgical PET imaging probe system was designed to provide reconstructed images in real time.

One of drawbacks of the PET imaging probe system is not to collect coincidence data over 360 degrees. Due to limited angle tomography, reconstructed images are elongated in the longitudinal direction. However this distortion due to limited angle tomography was not severe when 3-dimensional images were reconstructed using a variant of one-pass list-mode ordered subsets ML algorithm. The variant of list-mode

one-pass ML algorithm is the combination of a row-action ML algorithm, a one-pass OS ML algorithm, and a Gaussian back projection kernel. The proposed algorithm was parallelized for parallel image reconstruction using a CUDA-enabled graphics processing unit. An nVidia Geforce® 9800GTX+ with 128 streaming processors was used to run the parallelized image reconstruction algorithm.

A first-generation prototype of the intra-operative PET imaging probe system was built to test the feasibility of the proposed PET imaging probe system. The prototype system consists of a pixilated NaI(Tl) detector and an array of BGO block detectors. The 3-dimensional reconstructed images showed the effect of limited angle tomography could be mitigated by using the propose image reconstruction algorithm. The spatial resolution in the transverse direction was roughly dominated by the crystal size of the imaging probe.

In conclusion, the PET imaging probe system is able to obtain high spatial resolution in the transverse direction and is able to mitigate the effects of limited angle tomography in the longitudinal direction. In addition, parallel image reconstruction using GPUs and CUDA is promising.

6 .2 **Future Work**

6. 2 .1 **Interpretation of the PET Imaging Probe System: Adaptive Imaging System**

The PET imaging probe system including surgeons' interference is similar to adaptive imaging to some extent. We assume that surgeons are roughly informed of the tumor locations from pre-operative diagnostic scans before surgery. Surgeons hold the

PET imaging probe around the tumor sites and the PET imaging probe system will then provide 3-dimensional reconstructed images in real time. Based on the on-line images, surgeons would decide where to move. Because the surgeons are integral to the whole imaging system—guiding where to make the measurements — this can be considered as an "adaptive imaging" system as described by Barrett [121] [122]. Since the adaptation should be done in an autonomous way as opposed to the PET imaging system, we are interested in analyzing the proposed intra-operative PET imaging probe system in terms of a *human intervened* adaptive system.

6. 2 .2 The Effects of Background Radiation

The amount of background radiation from surrounding tissues depends on the orientation and location of the PET imaging probe system. Scatter coincidences can be simulated in Monte Carlo simulations. Recently, GEANT4 Monte Carlo simulations using parallel processing is emerging [123]. By using a parallel Monte Carlo simulation tool kit, computations for estimating the effects of background radiation will become faster and more feasible.

6. 2 .3 The Roles of the Relaxation Factor of the Proposed Image Reconstruction Algorithm

We proposed a variant of one-pass list-mode ordered subsets ML algorithm including both a row-action ML algorithm and a Gaussian back-projection kernel. The relaxation factor in the row-action ML algorithm can affect the quality of reconstructed images. The relaxation factor can either remain constant for all the subsets or be an

adjustable variable. The optimum value of the relaxation factor can be obtained using a set of training images. Therefore by investigating the relaxation factor, we can obtain one of the best relaxation factors for the given imaging object.

6. 2 .4 Evaluation of Performance

Evaluation of the proposed intra-operative PET system and reconstructed images are also important. Quantitative assessment of performance will help improve the proposed PET imaging probe system. One of key assessment components will be how much we can reduce the effects of limited angle tomography.

6. 2 .5 Parallel Image Reconstruction Using Advanced Graphics Processing Units

Graphics processing units are evolving fast. The on-chip memory (cache) was already introduced. Using on-chip memory instead of the global memory will minimize memory access time. Floating point operation without the racing condition will significantly speed up image reconstruction.

6. 2 .6 A Second-Generation Prototype of the PET Imaging Probe System

Even with some limitations, the first-generation prototype showed promising results. The partial ring detector can be replaced with another detector with uniform 2-dimensional crystal sizes. We can then image 3-dimensionally distributed point sources.

Also a position tracker can be mounted to the imaging probe module. The limitations of the proposed PET imaging probe system will be more clearly addressed.

BLOGRAPHY

BIBLOGRAPHY

[1] Ahmedin Jemal, Rebecca Siegel, Jiaquan Xu, and Elizabeth Ward **,** "Cancer Statistics, 2010," CA: A Cancer Journal for Clinicians. Published online before print July 7, 2010**.**

[2] Peggy P. Hsu and David M. Sabatini, "Cancer Cell Metabolism: Warburg and Beyond," Cell *134*, 703-707, September 5, 2008.

[3] http://www.sparknotes.com/biology/cellrespiration/glycolysis/summary.html

[4] Peter Vaupel, Oliver Thews, and Michael Hoeckel, "Treatment resistance of solid tumors: role of hypoxia and anemia," Med Oncol, 2001;18:243-259.

[5] Carol A. Mittelstaedt, "Ultrasound as a Useful Imaging Modality for Tumor Detection and Staging," CANCER RESEARCH 40, 3072-3078. August 1980.

[6] Tobias Schaeffter, "Imaging modalities: principles and information content," Progress in Drug Research, Vol. 62, 2005.

[7] J. Anthony Seibert, and John M. Boone, "X-Ray Imaging Physics for Nuclear Medicine Technologists. Part 2: X-Ray Interactions and Image Formation," JOURNAL OF NUCLEAR MEDICINE TECHNOLOGY, Vol. 33, No. 1, March 2005.

[8] Pottumarthi V. Prasad, "Magnetic Resonance Imaging," Humana Press Inc, 2006.

[9] Ray Hashman Hashemi, William G. Gradley, and Christopher J. Lisanti, MRI: The Basics, 3rd edition, Wolters Kulwer|Lippincott Williams & Wilkins, 2010.

[10] PET and PET/CT: a clinical guide, edited by Eugene C. Lin and Abass Alavi. 2nd edition. Thieme Medical Publishers, 2009.

[11] Katrin Kaarstad, Dirk Bender, Lise Bentzen, OleLajord Munk, and Susanne Keiding, "Metabolic Fate of 18F-FDG in Mice Bearing Either SCCVII Aquamous Cell Carcinoma or C3H Mammary Carcinoma," The Journal of Nuclear Medicne, Vol. 43, No. 7, July 2002.

[12] Lugi Aloj, Corradina Coraco, Elanine Jogoda, William C. Eckelman, and Ronald D. Neumann, "Glut-1 and Hexokinase Expression: Relationship with 2-Fluoro-2-deocy D-glucose Uptake in A431 and T47D Cells in cluture," Cancer Research 59, 4709-4714, September 15, 1991.

[13] Egidio Iorio, Delia Mezzanzanica, Paola Alberti, Francesca Spadaro, Carlo Ramoni, Sandra D'Ascenzo, Sanilo Millimagi, Antonio Pavan, Vincenza Dolo, Silvana Canevari, and Franca Podo, "Alterations of Choline Phospholipid Metaoblism in Ovarian Tumor Progression," CancerRes. 2005; 65; (20). pp. 9369-9376, October 15, 2005.

[14] Eric O. Aboagye and Zaver M. Bhujwalla, "Malignant Transformation Alters Membrane Choline Phospholipid Metabolism of Human Mammary Epithelial Cells," Cancer Reserch 59, 80-84, January 1, 1999.

[15] Timothy R. DeGrado, Steven W. Baldwin, Shuyan Wang, Matthew D. Orr, Ray P. Liao, Henry S. Friedman, Robert Reiman, David T. Price, and R. Edward Coleman, "Synthesis and Evaluation of 18F-labeled Choline Analogs as Oncologic PET Tracers," The Journal of Nuclear Medicine 2001: 42: 1805-1814.

[16] Oyama N; Akino H; Kanamaru H; Suzuki Y; Muramoto S; Yonekura Y; Sadato N; Yamamoto K; Okada K; "11C-Acetate PET Imaging of Prostate Cancer," Journal of Nuclear Medicine, 2002; 43(2):181-6.

[17] Michael D. Harpen, "Positronium: Review of symmetry, conserved quantities and decay for the radiological physicist," Med. Phys. 31 (1), January 2004.
[18] W H Tait, "Radiation Detection," 1980.
[19] Martin Charron, "Pediatric PET imaging," Ch8. Fig. 8.2. Springer.
[20] DW Townsend, "Principles and Technology of PET," Annals of Academy of Medicine, March 2004, Vol.33, No. 2.
[21] M. Dahlborn, E.J. Hoffman, C.K. Hoh, C. Schiepers, G. Rosenqvist, R.A. Hawkins, and M.E. Phelps, "Whole-Body Positron Emission Tomography: Part I. Methods and Performance Characteristics," The Journal of Nuclear Medicine, Vol. 33, No. 6, June 1992.
[22] Dan J. Kadrmas and Paul E. Christian, "Comparative Evaluation of Lesion Detectability for 6 PET Imaging Platforms Using a Highly Reproducible Whole-Body Phantom with ^{22}Na Lesions and Localized ROC Analysis," The Journal of Nuclear Medicine, Vol. 43, No. 11, 1545-1554, November 2002.
[23] M. Defrise, F. Deconinck, S. Kuijk, A. Bossuyt, V. Lacroix, M. Waligorski, "Methodology for predicting the performance of different PET camera designs," Information Processing in Medical Imaging 9th Conference, beginning page. 455, Washington DC, May 1985.
[24] Craig S Levin and Edward J Hoffman , "Calculation of positron range and its effect on the fundamental limit of positron emission tomography system spatial resolution," Phys. Med. Biol. 44 (1999) 781–799.
[25] O.A. Oredipe, R.F. Barth, S.E. Tuttle, D.M. Adams, I. Sautins, D.M. Bucci, C.M. Mojzisk, G.H. Hinkle, S. Jewell, Z. Steplewsk, M.O. Thurston, and E. W. Martin Jr., "Limits of sensitivity for the radioimmunodetection of colon cancer by means of a hand held gamma probe," Nucl. Med. Biol. 15(6):595-603, 1988.
[26] Martin P. Tornai, "Small Area Beta and Gamma Detectors for Functional Nuclear Emission Imaging," the dissertation, University of California, Los Angeles, 1997.
[27] Aitken DR, Thurston MO, Hinkle GH Jr, Martin DT, Haagensen DE Jr, Houchens D, Tuttle SE, Martin EW Jr., "Portable Gamma Probe for Radioimmune localization of Experimental Colon Tumor Xenografts," Journal of surgical research, 36 480-489, 1984.
[28] J. R. Saffer, H. H. Barrett, H. B. Barber and J. M. Woolfenden, "Surgical probe design for a coincidence imaging system without a collimator," Image and Vision Computing, Vol. 10, No. 6, July/August 1992.
[29] D. N. Krag, S. J. Meijer, D. L. Weaver, B. W. Loggie, S. P. Harlow, K. K. Tanabe, E. H. Laughlin and J. C. Alex, "Minimal-access surgery for staging of malignant melanoma," Vol. 130. No. 6, Archives of Surgery, June 1995.
[30] Ismet Sarikaya, Stephen P. Povoski, Osama H. Al-Saif, Ergun Kocak, Mark Bloomston, Steven Marsh, Zongjian Cao, Douglas A. Murrey, Jun Zhang, Nathan C. Hall, Michael V. Knopp, and Edward W. Martin Jr., "Combined use of preoperative 18F FDG-PET imaging and intraoperative gamma probe detection for accurate assessment of tumor recurrence in patients with colorectal cancer," World Journal of Surgical Oncology, 5:80, 2007.
[31] Liu, F.; Saffer, J.R.; Mayers, G.M.; Kononenko, W.; Newcomer, F.M.; Karp, J.S.; Lockyer, N.S. "Performance evaluation of a 64-pixel Surgical Probe for FDG imaging," Nuclear Science Symposium Conference Record, 2003 IEEE.

[32] Martin P. Tornai, Bradley E. Patt, Jan S. Iwanczyk, Carolyn R. Tull, Lawrence R. MacDonald, and Edward J Hoffman, "A novel silicon array designed for intraoperative charged particle imaging," Medical Physics, Vol. 29, No. 11, Nov. 2002.

[33] F. E. Emery and T. A. Rabson, "Average Energy Expended Per Ionized Electron-Hole Pair in Silicon and Germanium as a Function of Temperature," Physical Review, Vol. 140, No. 6A, page(s) A2089-A2093, 1965.

[34] Claude Leroy and Pier-Giorgio Rancoita, Principles of Radiation Interaction in Matter and Detection, Chapter 1, World Scientific Publishing Co. Ltd. 2004.

[35] Lisha Zhang, "Compton gamma-ray imaging probes for prostate and breast," Dissertation at University of Michigan, Ann Arbor, 2004.

[36] S. Agostinelli *et al*, "Geant4-a simulation tool kit," Nuclear Instruments and Methods in Physics Research A 506 (2003) 250-303.

[37] L. Eriksson, D. Townsend, M. Eriksson, C. Melcher, M. Schmand, B. Bendriem, R. Nutt, " Experience with scintillators for PET: towards the fifth generation of PET scanners, "Nuclear Instruments and Methods in Physics Research A 525 (2004) 242–248.

[38] Ned C. Rouze, Matthias Schmand, Stefan Siegel, and Gary D. Hutchins, "Design of a Small Animal PET Imaging System with 1 Microliter Volume Resolution," IEEE Transactions on Nuclear Science, Vol. 51, No. 3, June 2004.

[39] W.W. Moses, P.R.G. Virador, S.E. Derenzo, R.H. Huesman, and T.F. Budinger, "Design of a High-Resolution, High-Sensitivity PET Camera for Human Brains and Small Animals," IEEE Transactions on Nuclear Science, Vol. 44, No.4, pp. 1487-1491. 1997.

[40] C. J. Thompson, S. St. James, N. Tomic, "Under-sampling in PET scanners as a source of image blurring," Nuclear instruments and Methods in Physics Research A 545 (2005) 436–445.

[41] Hongdi Li, Wai-Hoi Wong, Soonseok Kim, Shitao Liu, Rocio Ramirez, Shuping Xie, Yu Wang, Tao Xing, Jorge Uribe, Hossain Baghaei,Yuxuan Zhang, and Jiguo Liu, "A Simulation Study on Optically Decoding Reflecting Windows for PMT Quadrant Sharing Scintillation Detector Block ," IEEE TRANSACTIONS ON NUCLEAR SCIENCE, VOL. 53, NO. 5, OCTOBER 2006.

[42] Bernd J. Pichler Florian Bernecker, Guido Böning, Magdalena Rafecas, Wendelin Pimpl, Markus Schwaiger, Eckart Lorenz, and Sibylle I. Ziegler, "A 4 8 APD Array, Consisting of Two Monolithic Silicon Wafers, Coupled to a 32-Channel LSO Matrix for High-Resolution PET ," IEEE transactions on Nuclear Science, Vol. 48, No. 4, August 2001.

[43] Stephen E. Derenzo, William W. Moses, Ronald H. Huesman, and Thomas F. Budinger, "Critical instrumentation issues for resolution < 2mm, high sensitivity brain PET," in Quantification of Brain Function, Tracer Kinetics & Image Analysis in Brain PET, ed. Uemura et al, Elsevier, 1993, pp. 25-40.

[44] Christopher J. Thompson, Aleks Labuda, and Joonyoung Suk, "Improving the Spatial Resolution of the MicroPET Scanner by Wobbling the Bed," 2005 IEEE Nuclear Science Symposium Conference Record, M03-169.

[45] M. Hćon, C. Camer, J. Cadorette, P. Richard, D. Rouleau, *S* . Rodrigue, and R. Lecomte, 'A Stationary Sampling Scheme for Multilaver Positron Tomographs," IEEE Tranctions on Medical Imaging, Vol. 12, No. 2, June 1993.

[46] Zubal, I.G., Harrell, C. R., Smith, A. L. "Two dedicated software, voxel-based, anthropomorphic (torso and head) phantoms," Available on http://noodle.med.yale.edu/zubal/library/Zubal.pdf.

[47] J. S. Huber, S. E. Derenzo, J. Qi, W. W. Moses, R. H. Huesman, T. F. Budinger, " Conceptual Design of a Compact Positron Tomograph for Prostate Imaging," IEEE Transaction on Nucler Science, Vol. 48, No. 4, pp. 1506-11. 2001.

[48] J. S. Huber, W. S. Choong, W. W. Moses, J. Qi, J. Hu, G. C. Wang, D. Wilson, S. Oh, R. H. Huesman, S. E. Derenzo, and T. F. Budinger, "Initial Results of a Positron Tomograph for Prostate Imaging," IEEE Transactions on Nuclear Science, Vol. 53, No. 5, pp. 2653- 2659, October 2006.

[49] Ronald H. Huesman, Gregory J. Klein, William W. Moses, Jinyi Qi, Rryan W. Reuter, and Patrick R. G. Virador, "List-Mode Maximum-Likelihood Reconstruction Applied to Positron Emission Mammography (PEM) with Irregular Sampling," IEEE Transaction on Medical Imaging, Vol. 19, No.5, pp. 532-537, May 2000.

[50] Jeffrey A. Fessler, W. Leslie Rogers, "Spatial Resolution Properties of Penalized-Likelihood Image Reconstruction: Space-Invariant Tomographs," IEEE Transactions on Image Processing, Vol. 5, No. 9, page(s) 1346-1358, September 1996.

[51] Z. H. Cho, S. K. Hilal, J. B. Ra, K. S. Hong, R. E. Bigler, T. Yoshizumi, A. P. Wolf, and J. S. Fowler, "High-resolution circular ring positron tomography with dichotomic sampling: Dichotom-I," Phys. Med. Biol., 1983, Vol. 28, No. 11, 1219-1234.

[52] Young Huh, Seung-Oh Jin, Jung-Byung Park, "Fast image reconstruction from fan beam projections using parallel digital signal processors and special purpose processors," Proceedings of the IEEE Region 10 Conference, Vol. 2, 1558-1561, Dec. 1999.

[53] K. Kouris, E.S. Garnett, and G.T. Herman,"Sampling Properties of Stationary and Half-Rotation Rings in Positron Emission Tomogtraphy," Journal of Computer Assisted Tomography, 5(5):744-754, October 1981.

[54] D. A. Simon, "Intra-Operative Position Sensing and Tracking Devices," available at *www.ri.cmu.edu/pub_files/pub1/simon...2/simon_david_1997_2.pdf*

[55] S. Surti and J. S. Karp, "Design consideration for a limited angle, dedicated breast, TOF PET scanner," *Phys Med Biol*. 2008 June 7; 53(11): 2911–2921.

[56] Jojoni Dey and Michael A. King, "Theoretical and Numerical Study of MLEM and OSEM Reconstruction Algorithms for Motion Correction in Emission Tomography," IEEE Transactions on Nuclear Science, Vol. 56, No. 5, page(s) 2739-2749, October 2009.

[57] Heyu Wu, Debashish Pal, Joseph A. O'Sullivan, and Yuan-Chuan Tai, "A Feasibility Study of a Prototype PET Insert Device to Convert a General-Purpose Animal PET Scanner to Higher Resolution," The Journal of Nuclear Medicine, Vol. 49, No.1, pp. 79- 87, January 2008.

[58] Jian Zhou and Jinyi Qi, "Theoretical analysis and simulation study of a high-resolution zoom-in PET system," Physics in Medicine and Biology, Vol. 54, pp. 5193-5208, 2009.

[59] S. Agostinelli *et al*, "Geant4-a simulation tool kit," Nuclear Instruments and Methods in Physics Research A 506 (2003) 250-303.

[60] W. R. Nelson and J. Liu, "Sampling the Fermi Distribution for β-decay energy input to EGS4," SLAC-TN-92-1, June 1992.

[61] Marguerite T. Hays and George M. Segall, "A Mathematical Model for the Distribution of Fluorodeoxyglucose in Humans," The Journal of Nuclear Medicine, Vol. 40. No. 8. August 1999.

[62] Visser et al., "SILLY USELESS OR SMART UPTAKE VALUE," The Journal of Nuclear Medicine, Vol. 51, No. 2, February 2010.

[63] Gonca G. Bural, Drew A. Torigian, Wengen Chen, Mohamed Houseni, Sandip Basu, Abass Alavi, "Increased 18F-FDG uptake within the reticuloendothelial system in patients with active lung cancer on PET imaging may indicate activation of the systemic immune response," Hellenic J Nucl Med 2010; 13(1): 23-25.

[64] LTH Tan, KL Ong, "Semi-quantative Measurements of Normal Organs With Variable Metabolic Activity on FDG PET Imaging," Ann Acad Med Singapore 2004;33;183-5.

[65] N. K. Kononov, V. N. Potapov, S. M. Ignatov, and V. G. Nedorezov," Features of the Mechanism of Formation of X-ray Shadowgraphs in Scintillation Crystals," Russian Journal of Nondestructive Testing, 2007, Vol. 43, No. 4, pp. 211–217. Pleiades Publishing, Ltd., 2007.

[66] V. V. Avdeichikov, L. Bergholt, M. Guttormsen, J.E. Taylor, L. Westerberg, B. Jakobsson, W. Klamra, Yu. A. Murin, "Light output and energy resolution of CsI, YAG, GSO, BGO, and LSO scintillators for light ions," Nuclear Instruments and Methods in Physics Research A 349 (1994) 216-224.

[67] Lars-Eric Adam, Joel S. Karp,and Richard Freifelder, "Energy-Based Scatter Correction for 3-D PET Scanners Using NaI(Tl) Detectors," *IEEE Transactions on Medical Imaging*, Vol. 19, No. 5, pp. 513-521. May 2000.

[68] B. Hesse1, K. Tägil, A. Cuocolo, C. Anagnostopoulos, M. Bardiés, J. Bax, F. Bengel, E. Busemann Sokole, G. Davies, M. Dondi, L. Edenbrandt, P. Franken, A. Kjaer, J. Knuuti, M. Lassmann, M. Ljungberg, C. Marcassa, P. Y. Marie, F. McKiddie, M. O'Connor, E. Prvulovich, R. Underwood, B. van Eck-Smit, "EANM/ESC procedural guidelines for myocardial perfusion imaging in nuclear cardiology," European Journal of Nuclear Medicine and Molecular Imaging Vol. 32, No. 7, July 2005.

[69] Adam Alessio and Paul Kinahan, "PET Image Reconstruction," Department of Radioloy, University of Washington, To appear in Henkin et al., Nuclear Medicine 2nd edition.

[70] H. Malcolm Hudson and Richard S. Larkin, "Accelerated Image Reconstruction Using Ordered Subsets of Projection Data," IEEE Transactions on Medical Imaging, Vol. 13, No. 4, December 1994.

[71] Alain Seret, "The number of subsets required for OSEM reconstruction in nuclear cardiology, "Eur J Nucl Med Mol Imaging (2006) 33:231.

[72] Eiichi Tanaka1 and Hiroyuki Kudo, "Subset-dependent relaxation in block-iterative algorithms for image reconstruction in emission tomography, "Phys. Med. Biol. 48 (2003) 1405–1422.

[73] Jolyon Browne and Alvaro R. De Pierro, "A Row-Action Alternative to the EM Algorithm for Maximizing Likelihoods in Emission Tomography," IEEE Transactions on Medical Imaging, Vol. 15, No. 5, page(s) 687-699, October 1996.

[74] Gabor T. Herman, Fundamental of Computerized Tomography Image Reconstruction from Projections, 2nd edition, Springer, 2009.

[75] Yair Censor, Gabor T. Herman, and Ming Jiang, "A Note on the Behavior of the Randomized Kaczmarz Algorithm of Strohmer and Vershynin," J Fourier Anal Appl. 15(4), page(s) 431-436, August 2009.

[76] Johan Nuyts, "ML and MAP Reconstruction for Emission and Transmission Tomography," Belgium. This is not available any more on line.

[77] Gabor T. Herman and Lorraine B. Meyer, "Algebraic Reconstruction Techniques can be made computationally efficient," IEEE Transactions on Medical Imaging, Vol. 12, No. 3, September 1993.

[78] Richard Gordon, Robert Bender, and Gabor T. Herman, "Algebraic Reconstruction Technique Microscopy and X-ray Photography," Journal of Theoretical Biology, 29, page(s) 471-481, 1970.

[79] Beilei Wang, Kenneth Barner, Denny Lee, "Algebraic Tomosynthesis Reconstruction," Medical Imaging 2004: Image Processing. Edited by Fitzpatrick, J. Michael; Sonka, Milan. Proceedings of the SPIE, Volume 5370, pp. 711-718 (2004).

[80] Craig S. Levin, "Positron Emission Tomography I: Image Reconstruction Strategies," CE: PET Physics and Technology II 2005, AAPM Meeting, Seattle WA.

[81] Andrew J. Reader, Stijn Ally, Filippos Bakatselos, Roido Manavaki, Richard J. Walledge, Alan P. Jeavons, Peter J. Julyan, Sha Zhao, David L. Hastings, and Jamal Zweit, "One-Pass List-Mode EM algorithm for High-Resolution 3-D PET Image Reconstruction Into Large Arrays, IEEE Transactions on Nuclear Science, Vol. 49, No. 3, JUNE 2002.

[82] A. Vasko, C-H Hsu, M-C Lin, I-T Hsiao, C. Wieholt, and C-T Chen, "A Row-Action Image Reconstruction of Short Time Frame for microPET Dynamic Study," 2005 IEEE Nuclear Science Symposium Conference Record.

[83] Vitali V. Selivanov, Martin D. Lepage, Roger Lecomte, "List-mode image econstruction for real-time PET imaging," J. Vis. Commun. Image R. 17 (2006) 630–646.

[84] Lucretiu M. Popescu, Samuel Matej and Robert M. Lewitt, "Iterative image reconstruction using geometrically ordered subsets with list-mode data," Volume: 6, page(s): 3536- 3540, Nuclear Science Symposium 2004.

[85] Lucas Parra and Harrison H. Barrett, "List-Mode Likelihood: EM Algorithm and Image Quality Estimation Demonstrate on 2-D PET," IEEE Transactions on Medical Imaging, Vol. 17, No.2, April 1998.

[86] Harrison H. Barrett, Donald W. Wilson, and Benjamin M. W. Tsui, "Noise properties of the EM algorithm: I. Theory," Phys. Med. Biol. 39 (1994) 833-846.

[87] NVIDIA_CUDA_Programming_Guide_3.1. This document is available at http://developer.nvidia.com/object/cuda_3_1_downloads.html.
[88] Available at http://www.nvidia.com/object/product_geforce_9800_gtx_plus_us.html.
[89] Whitepaper, NVIDIA's Next Generation CUDA™ Compute Architecture: Fermi™ (2009). This document is available at http://www.nvidia.com/content/PDF/fermi_white_papers/NVIDIA_Fermi_Compute_Architecture_Whitepaper.pdf
[90] http://www.behardware.com/articles/772-5/nvidia-fermi-the-gpu-computing-revolution.html
[91] Erik Lindholm and Stuart Oberman, "The NVIDIA GeForce 8800 GPU," (August 2007). This document is available at www.hotchips.org/archives/hc19/2_Mon/HC19.../HC19.02.01.pdf.
[92] http://www.anandtech.com/show/2549/2
[93] Joe Stam, "NVIDIA CUDA Technology in Adobe premiere pro and the new mercury playback engine," whitepaper, NVIDIA. This document is available at http://www.nvidia.com/docs/IO/85230/CUDA_MPE_WP-05380-001_v01.pdf.
[94] http://s08.idav.ucdavis.edu/fatahalian-gpu-architecture.pdf
[95] V. Podlozhnyuk, "Histogram calculation in CUDA," NVIDIA. This document is available at http://developer.download.nvidia.com/compute/cuda/1_1/Website/projects/histogram256/doc/histogram.pdf
[96] available at pc.watch.impress.co.jp/docs/2007/0326/kaigai_4.pdf
[97] Brian W. Miller, Lars R. Furenlid, Stephen K. Moore, H. Bradford Barber, Vivek V. Nagarkar, and Harrison H. Barrett, "System Integration of FastSPECT III, a Dedicated SPECT Rodent-Brain Imager Based on BazookaSPECT Detector Technology," 2009, IEEE Nuclear Science Symposium Conference Record, M15-5.
[98] William Dieckmann, Shanthalaxmi Thada, and W. Craig Barker, "Strategies for Accelerating Forward and Backprojection in List-mode OSEM PET Reconstruction using GPUs, " 2009 IEEE Nuclear Science Symposium Conference Record, HPP-3.
[99] Maraike Schellmann, Sergei Gorlatch, Dominik Meiländer, Thomas Kösters, Klaus Schäfers, Frank Wübbeling, and Martin Burger," Parallel Medical Image Reconstruction: From Graphics Processors to Grids, PaCT 2009, LNCS 5698, pp. 457–473, 2009.
[100] W. Craig Barker, Shanthalaxmi Thada, and William Dieckmann, "A GPU-Accelerated Implementation of the MOLAR PET Reconstruction Package," 2009, IEEE Nuclear Science Symposium Conference Record. HPP-4.
[101] Flat panel type multianode photomultiplier tube assembly H8500, H8500B: Hamamatsu.
[102] Photomuliplier tubes: Basics and Applications, third edition, HAMAAMTSU, 2006. Available at http://sales.hamamatsu.com/assets/applications/ETD/pmt_handbook_complete.pdf.
[103] Available at http://www.optical-components.com/NaI-CsI-crystal.html.

[104] Stefan Siegel, Robert W. Silverman, Yiping Shao, Simon R. Cherry, "Simple Charge Division Readouts for Imaging Scintillator Arrays using a Multi-Channel PMT," IEEE Transactions on Nuclear Science, Vol. 43, No. 3, June 1996.
[105] Alberto Del Guerra, Ionizing Radiation Detectors for Medical Imaging, World Scientific Publishing Co. Ltd. 2004.
[106] http://www.caen.it, Home / Products / Front End / VME / ADCs (Peak Sensing) / V785 32 Channel Multievent Peak Sensing ADC.
[107] Deborah Herbert, Nicola Belcari, Manuela Camarda, Alberto Del Guerra, "A comparison of the imaging performance of different PSPMTs for PET applications," Nuclear Instruments and Methods in Physics Research A 518 (2004) 399–400.
[108] Gopal B. Saha, "Basics of PET imaging" second edition, Springer.
[109] Glen F. Knoll, "Radiation Detection and Measurement," John Wiley and Sons Inc., 1979.
[110] From M. Moszynski, C. Gresset, J. Vacher and R. Odru, "Timing properties of BGO scintillator," Nuclear Instruments and Methods 188 (1981) 403-409.
[111] J. Seidel, W.R. Gandler and M. V. Green, "Characteristics of a Pair of Small Field-of-View LSO Scintillation Cameras," IEEE Transactions on Nuclear Science, Vol. 43, No. 3, June 1996.
[112] available at http://www.nucleide.org/DDEP_WG/Nuclides/Na-22_tables.pdf.
[113] available at http://community.middlebury.edu/~PHManual/gamma.html.
[114] Nicholas Tsoulfanidis, "Measurement and Detection of Radiation," 1983.
[115] Adam M. Alessio, Paul E. Kinahan, Robert L. Harrison, and Thomas K. Lewellen, Measured Spatially Variant System Response for PET Image Reconstruction, 2005 IEEE Nuclear Science Symposium Conference Record, M07-92.
[116] available at http://libsigcx.sourceforge.net/docs/index.html.
[117] available at http://www.gtkmm.org/en/
[118] A. V. Stolin, M. B. Williams, B. K. Kundu, S. Majewski, V. Popov, A. G. Weisenberger, "Characterization of imaging gamma detectors for use in small animal SPECT," Nuclear Science Symposium Conference Record, Vol. 3, page(s) 2085-2089, October 2003.
[119] J. G. Rogers, A. J. Taylor, M. F. Rahimi, R. Nutt, M. Anderaco, C. W. Williams, "An improved multicrystal 2-D BGO detector for PET," IEEE Transactions on Nuclear Science, Vol. 39, No. 4, pp. 1063-1068, Aug. 1992.
[120] http://alienryderflex.com/polygon/
[121] Eric Clarkson, Matthew A. Kupinski, Harrison H. Barrett, and Lars Furenlid, "A Task-Based Approach to Adaptive and Multimodality Imaging:
Computation techniques are proposed for figures-of-merit to establish feasibility and
optimize use of multiple imaging systems for disease diagnosis and treatment-monitoring." *Proc IEEE Inst Electr Electron Eng*. 2008 March ; 96(3): 500–511.
[122] George A. Kastis, Lars R. Furenlid, Donald W. Wilson, Todd E. Peterson, H. Bradford Barber,and Harrison H. Barrett*,"* Compact CT/SPECT Small-Animal Imaging System," *IEEE TRANSACTIONS ON NUCLEAR SCIENCE*, VOL. 51, NO. 1, pp. 63-67. FEBRUARY 2004.

[123] Lennart Jahnke's work on Monte Carlo Simulations on GPU, he is with RUPRECHT-KARLS-UNIVERSITÄT HEISELBERG, Germany.